

The Pennsylvania State University

The Graduate School

College of Engineering

**A NOVEL ACTUATOR PHASING METHOD FOR ULTRASONIC DE-ICING OF
AIRCRAFT STRUCTURES**

A Dissertation in

Engineering Science and Mechanics

by

Cody J. Borigo

© 2014 Cody J. Borigo

Submitted in Partial Fulfillment

of the Requirements

for the Degree of

Doctor of Philosophy

December 2014

The dissertation of Cody J. Borigo was reviewed and approved* by the following:

Joseph L. Rose
Paul Morrow Professor of Engineering Science and Mechanics
Dissertation Adviser
Chair of Committee

Cliff J. Lissenden
Professor of Engineering Science and Mechanics

Bernhard R. Tittmann
Schell Professor of Engineering Science and Mechanics

Edward C. Smith
Professor of Aerospace Engineering

Judith A. Todd
Professor of Engineering Science and Mechanics
P.B. Breneman Head of the Department of Engineering Science and Mechanics

*Signatures are on file in the Graduate School.

ABSTRACT

Aircraft icing is a critical concern for commercial and military rotorcraft and fixed-wing aircraft. In-flight icing can lead to dramatic decreases in lift and increases in drag that have caused more than a thousand deaths and hundreds of accidents over the past three decades alone. Current ice protection technologies have substantial drawbacks due to weight, power consumption, environmental concerns, or incompatibility with certain structures. In this research, an actuator phasing method for ultrasonic de-icing of aircraft structures was developed and tested using a series of finite element models, 3D scanning laser Doppler vibrometer measurements, and experimental de-icing tests on metallic and composite structures including plates and airfoils.

An independent actuator analysis method was developed to allow for practical evaluation of many actuator phasing scenarios using a limited number of finite element models by properly calculating the phased stress fields and electromechanical impedance curves using a complex coupled impedance model. A genetic algorithm was utilized in conjunction with a series of finite element models to demonstrate that phase inversion, in which only in-phase and anti-phase signal components are applied to actuators, can be utilized with a small number of phasing combinations to achieve substantial improvements in de-icing system coverage. Finite element models of a 48"-long airfoil predicted that phase inversion with frequency sweeping can provide an improvement in the shear stress coverage levels of up to 90% compared to frequency sweeping alone. Experimental evaluation of the phasing approach on an icing grid showed a 189% improvement in de-icing coverage compared to frequency sweeping alone at comparable power levels. 3D scanning laser Doppler vibrometer measurements confirmed the increased variation in the surface vibration field induced by actuator phasing compared to unphased frequency sweeping.

Additional contributions were made to facilitate actuator phasing and to advance the state-of-the-art in ultrasonic de-icing technology. These contributions include the development of improved frequency optimization, reduction in the size of the system hardware, and improvements in actuator bonding techniques. It was demonstrated that a dynamic frequency selection method is critical to effectively implementing the actuator phasing method. A miniaturized relay system was also designed and implemented to facilitate actuator phasing in conjunction with a phase splitter circuit and a single amplifier. An improved frequency tuning method was adopted and

implemented in the de-icing system to eliminate the need for an impedance analyzer and to provide more accurate frequency selection by directly measuring the forward and reflected power between the amplifier and the de-icing actuators.

Overall, it was demonstrated that this novel method can greatly improve the efficiency and effectiveness of the ultrasonic de-icing system by effectively redistributing the shear stress fields at the ice-structure interface, and that this method can be practically implemented in the de-icing system with an overall reduction in size and weight compared to previous versions of the technology.

TABLE OF CONTENTS

LIST OF FIGURES	ix
LIST OF TABLES	xix
ACKNOWLEDGEMENTS	xx
 Chapter 1: INTRODUCTION.....	 1
1.1 Problem Description.....	1
1.2 Literature Survey – Aircraft De-Icing Technologies	4
Fluid Anti-Icing/De-Icing Systems	4
Electro-Thermal Anti-Icing/De-Icing Systems	5
Pneumatic Boot De-Icing Systems.....	5
Electro-Impulsive De-Icing Systems.....	6
Electro-Vibratory De-Icing Systems	7
Microwave Anti-Icing/De-Icing Systems.....	7
Shape Memory Alloy De-Icing Systems	8
Hot Bleed Air Anti-Icing/De-Icing Systems	8
Summary of Anti-Icing and De-Icing Systems	9
1.4 Literature Survey - Ultrasonic De-Icing Research	10
1.5 Research Objectives	13
1.6 Overview of Chapters.....	15
Chapter 1: Introduction.....	15
Chapter 2: Foundational Principles	15
Chapter 3: Actuator Design	15
Chapter 4: Impedance Analysis.....	16
Chapter 5: Actuator Phasing Method	16
Chapter 6: Ultrasonic De-Icing System Design	16
Chapter 7: Concluding Remarks	16
 Chapter 2: FOUNDATIONAL PRINCIPLES.....	 17
2.1 Ice Adhesion.....	17
Physical Mechanisms of Ice Adhesion.....	18
Interfacial Strength of Ice	21
Interfacial Shear Stress	23
2.2 Forced Structural Vibration.....	25

Chapter 3: ACTUATOR DESIGN	29
3.1 Transduction Mechanisms – Piezoelectric versus Magnetostrictive.....	29
Piezoelectric Materials	30
3.2 Disk Actuator Axial Resonances.....	33
Piezoelectric Disk Actuator Axial Resonances	33
3.3 Actuator Configuration	37
3.4 Actuator Wiring and Bonding Methods	39
3.5 Integrating Actuators into Composite Sandwich Panel Structures	47
3.6 Summary	51
Chapter 4: IMPEDANCE ANALYSIS.....	52
4.1 Mechanical, Electrical, and Electromechanical Impedance	52
4.2 Electrical Impedance Matching.....	53
Impedance Matching Theory.....	54
Impedance Matching with a Single-Winding Autotransformer	56
4.3 Electromechanical Impedance Analysis of a Coupled-Actuator System.....	62
Simple Independent Impedance Combinations	62
Equivalent Impedance of a Complex Coupled-Component System	63
Implementation of Coupled-Impedance Calculations	67
Finite Element Verification of Coupled-Impedance Calculations	68
Multi-Port Electrical Network Impedance Matrix	70
4.4 Automatic Frequency Tuning (AFT) Method	72
Chapter 5: ACTUATOR PHASING METHOD.....	79
5.1 The Role of Phasing	79
5.2 Finite Element Modeling Details	80
Direct-Solution Steady-State Dynamic Analysis	81
Airfoil Model Overview	83
Material Properties	85
Elements and Meshing	86
Constraints between Materials at Interface Layers	88
Piezoelectric Modeling Conditions	88
Model Output Variables	89
Independent Actuator Analysis Method.....	92
Validation of the Quality of the Airfoil Finite Element	98

5.3 Phasing Optimization with a Genetic Algorithm	100
Genetic Algorithm	100
Results of the Analysis	103
5.4 Phasing Evaluation of an Airfoil	106
Actuator Configuration Comparison	106
Phase Inversion Effectiveness	113
Excitation Frequency Selection during Phase Inversion	126
Comparison of Phase Inversion and Frequency Sweeping	132
Summary of Airfoil FE Modeling Results	137
5.5 3D Scanning Laser Doppler Vibrometer Phasing Measurements.....	138
3D Scanning Laser Doppler Vibrometer Experimental Setup	138
Laser Vibrometer In-Plane Surface Vibration Field Results.....	141
Laser Vibrometer Results Analysis	144
5.6 De-Icing Grid Phasing Experiments.....	149
De-Icing Grid Phasing Experiment Setup and Procedure	149
De-Icing Grid Phasing Experiment Results and Analysis.....	152
Phasing Experiment Conclusions	157
5.7 Composite Sandwich Panel Airfoil De-Icing Experiments.....	158
Chapter 6: ULTRASONIC DE-ICING SYSTEM HARDWARE AND SOFTWARE.....	162
6.1 Ultrasonic De-Icing System Functionality	162
6.2 Hardware Components	162
Amplifiers.....	163
Impedance Matching Networks.....	164
Cabling	165
Phasing Relays and Splitter	166
Analog and Digital I/O	168
Relay Control PCB	169
6.3 Control Software	177
Chapter 7: CONCLUDING REMARKS	178
7.1 Summary of Research	178
7.2 Research Contributions	181
7.3 Recommendations for Further Research	183
REFERENCES	185

Appendix A:

MATLAB CODES FOR AIRFOIL FINITE ELEMENT MODEL PHASING ANALYSIS 193

A.1 Part.....	193
A.2 Materials	194
A.3 Assembly	195
A.4 Step	195
A.5 Boundary Conditions.....	196
A.6 Meshing	196
A.7 Modify Imported Model	196
A.8 Input File Modification	197
A.9 Job Submission and Analysis	198

Appendix B:

MATLAB CODES FOR AIRFOIL FINITE ELEMENT MODEL PHASING ANALYSIS 199

B.1 datFileReader_v5_pt1.m.....	199
B.2 datFileReader_v5_pt2.m.....	206
B.3 FESpecimen_analysis_initial.m	221
B.4 FESpecimen_analysis_phasing.m	223

Appendix C:

MATLAB CODES FOR GENETIC ALGORITHM FINITE ELEMENT MODEL PHASING
OPTIMIZATION..... 238

C.1 PhasingGA_Optimization_Master.m	238
C.2 PhasingGA_Optimization_Function.m	241
C.3 PhasedFieldFunction.m	242
C.4 PhasingGA_ConstraintFunction.m.....	245

Appendix D:

POWER-NORMALIZED VERSIONS OF AIRFOIL FEM RESULTS..... 246

NON-TECHNICAL ABSTRACT..... 259

LIST OF FIGURES

Figure 1 Severe in-flight icing on a small turboprop aircraft. Icing such as this has been responsible for a great number of accidents and fatalities over the past few decades. (Source: Langley Flying School [13]).	2
Figure 2 A Royal Air Force Sea King helicopter, grounded due to icing conditions (Source: BBC News [14]).	3
Figure 3 Pneumatic boot de-icing system on a small fixed-wing aircraft; the system shown in deflated state (left) and inflated state (right) (Source: FlightLearnings.com [18]).	6
Figure 4 Diagram of an electro-impulsive de-icing system (Source: Goraj [5]).	7
Figure 5 Concept of shape memory alloy de-icing system (Source: Ingram, et al. [22]).	8
Figure 6 SH wave dispersion curves showing regions of high interfacial shear stress coefficient (ISSC) values (Source: Palacios [15]).	11
Figure 7 An iced plate before (left) and after (right) ultrasonic excitation (Source: Palacios [15]).	12
Figure 8 Ultrasonic ice protection results from Goodrich's wind tunnel (Source: Palacios [15]).	12
Figure 9 (Left) Tailored waveguide (TWG) and (right) predicted stress field with (Source: Zhu [24]).	13
Figure 10 Two types of icing common on airfoil structures are (right) rime ice, which is more granular, rough, and opaque, and (left) glaze ice, which is translucent, smooth, and dense (Source: New Scientist [31]).	17
Figure 11 Illustration of five water molecules and the hydrogen bonds between them (Source: Wikimedia Commons [36]).	19
Figure 12 Illustration of hydrogen bonding between water molecules that forms a hexagonal crystal lattice of ice (Source: Wikimedia Commons [37]).	19
Figure 13 An illustration of Van der Waals forces; (Top) two unpolarized atoms generally have balanced charge distributions; (center) one atom may become an instantaneous dipole due to probabilistic electron field distributions; (bottom) the instantaneous dipole may induce a nearby atom to become a dipole, which creates an interaction force between the two dipoles.	20
Figure 14 Coordinate system for ice-substrate structure.	24

Figure 15 (Left) Stress tensor component definitions (Source: Cook, et al. [56]); (right) traction on a plane (Source: Wikimedia Commons [57]).	24
Figure 16 Diagram of a uniform rod.	26
Figure 17 (Left) Piezoelectric crystal ceramic above the Curie temperature and (right) below the Curie temperature; the blue spheres represent large divalent metals, the red spheres represent the smaller anions, and the green spheres represent the small tetravalent metals. The arrow indicates the direction of polarization that occurs in the state below the Curie temperatures.	31
Figure 18 (Left) Unpoled piezoelectric ceramic with randomly aligned domains, (center) polarization of the ceramic under large DC voltage near Curie temperature, and (right) residual polarization after the DC current is removed and the ceramic returns to cooler temperatures.	32
Figure 19 Various piezoelectric actuator geometries, poling configurations, and actuation configurations, as well as the piezoelectric coupling coefficient that each mode of operation depends on.	32
Figure 20 Illustration of a piezoelectric disk actuator.	34
Figure 21 Illustration of a radially-constrained disk actuator operating in the radial mode, in which the constraint stiffness of the boundary, k_{str} , is frequency-dependent.	38
Figure 22 Photograph of fractured and debonded piezoelectric actuators after an ultrasonic de-icing test (Source: Palacios [15]).	40
Figure 23 Actuator wiring and bonding method developed by Overmeyer.	41
Figure 24 Layout of materials used to wire and bond a single actuator using the method developed by Overmeyer.	41
Figure 25 Diagram of the improved actuator bonding method.	43
Figure 26 Comparison of the shifts caused by previous and new bonding method; note that the differences in the initial curves are due to the fact that two different size discs were compared here, but that does not significantly influence the effect of the bonding.	44
Figure 27 Comparison of a single actuator wired and bonded using the improved method (top) and a single actuator wired and bonded with the method developed by Overmeyer (bottom); bottom image from (Source: Overmeyer [66]).	45
Figure 28 Comparison of multiple actuators wired and bonded using the improved method (top) and actuators wired and bonded with the method developed by Overmeyer (bottom); bottom image from (Source: Overmeyer [66]).	46

Figure 29 A carbon fiber and Nomex honeycomb sandwich panel structure.	47
Figure 30 Bonding the copper tabs to the electrodes (a) and (b), curing the tabs under pressure in a rat trap (c), and an actuator with attached electrode tabs (d).	48
Figure 31 Laying up the actuators for bonding to the exterior carbon fiber panel.	48
Figure 32 Vacuum bagged and cured carbon fiber panel with four actuators.	49
Figure 33 Transferring the pattern from to a transparent sheet and then to reverse the pattern and transfer it to a honeycomb panel.	49
Figure 34 Removing honeycomb material to accommodate the thickness of the actuators and wiring.	50
Figure 35 Vacuum bagged and completed sandwich panel with integrated actuators.	50
Figure 36 Exploded model of a carbon fiber sandwich panel with various imbedded actuators.	51
Figure 37 (Left) L-network, (center) pi-network, and (right) T-network impedance matching circuits are highlighted in the dashed boxes; capacitors and inductors may be interchanged depending on matching requirements.	56
Figure 38 Impedance magnitude and phase of a set of four 2"-diameter PZT actuators bonded in a carbon fiber sandwich panel.....	57
Figure 39 Impedance magnitude and phase of a set of four 2"-diameter PZT actuators bonded on a titanium panel.....	58
Figure 40 Circuit diagram of a source and load impedance matched with a transformer; here the load impedance must be larger than the source impedance because a step-down transformer is used.	58
Figure 41 A single-winding autotransformer circuit similar to the ones used for matching the amplifier impedance to the actuator impedance in the ultrasonic de-icing system.	59
Figure 42 Comparison of system impedance of four actuators in a carbon fiber sandwich panel without and with appropriate 25Ω impedance matching via an autotransformer.....	60
Figure 43 Comparison of forward, reflected, and net load power with and without the appropriate 25Ω impedance matching network.	61
Figure 44 Comparison of efficiency with and without the appropriate 25Ω impedance matching network.	61
Figure 45 Circuit diagram of N impedances in parallel.....	63
Figure 46 Drawing of a plate with two piezoelectric actuators bonded to its surface.	64

Figure 47 Representative circuit of the two-actuator system in Figure 46, in which the actuators have coupled electromechanical impedances.	64
Figure 48 Drawing of a finite element model of a four-actuator de-icing system used to evaluate the accuracy of the indirect impedance calculation method detailed by equation (4.21).	69
Figure 49 The ten individual impedance curves calculated from the finite element model illustrated in Figure 48, as well as the directly-calculated system impedance from this model and the system impedance predicted using equation (4.21). Figure 50 is a version of this plot with only the system impedance curves.....	69
Figure 50 A comparison of the directly-calculated system impedance from the model illustrated in Figure 48 and the system impedance predicted using equation (4.21) and ten individually calculated impedance curves from the same model.....	70
Figure 51 Diagram of a multi-port network, for which the equivalent impedance calculations are very similar to those of an electromechanical system with multiple coupled elements.	71
Figure 52 Diagram of a bi-directional coupler circuit in the form of cross-connected transformers.	73
Figure 53 Comparison of the impedance and power data as a function of frequency for a four-actuator carbon fiber sandwich panel specimen with 25Ω impedance matching.	76
Figure 54 Comparison of measured forward and reflected power using the manufacturer-calibrated front panel display and the retrofitted data ports.	78
Figure 55 Meshed airfoil model, isometric view.	84
Figure 56 Meshed airfoil model, back view; note that this image shows 2” actuators, while 2.5” actuators were used for the final analysis.	84
Figure 57 8-node linear brick element [81]	87
Figure 58 Meshed airfoil model, edge view.	87
Figure 59 Surface and point node sets upon which the equation constraints are applied to ensure common voltage across the entire electrode surface [66].	89
Figure 60 Illustration of the “normal surface” (green) and “primary vector” (red) used to define the local coordinate systems (black) for each element in the designated set; the global coordinate system is shown in the lower right corner for reference.	91

Figure 61 Drawing of the finite element model of a four-actuator de-icing system on a 2-mm aluminum plate with a 3-mm layer of accreted ice used to evaluate the accuracy of the independent actuator analysis method.	94
Figure 62 Image of the meshed model shown in the previous figure.	94
Figure 63 Comparison of the stress fields calculated from (left) a finite element model with direct phasing applied and (right) the independent actuator analysis predictions.	95
Figure 64 Comparison of the experimentally measured impedance minima (red) for each actuator on the airfoil and the values predicted from the finite element model (blue).	99
Figure 65 Comparison of the 90% coverage stress level results from the four-actuator finite element model using genetic algorithm optimization for each phasing increment and phasing vector length considered.	104
Figure 66 Relative improvement in the 90% coverage stress level for the model considered here using only phase inversion combinations (i.e. 180° phasing increments).	105
Figure 67 Airfoil actuator configuration 1 and the impedance curve for this configuration.	107
Figure 68 Airfoil actuator configuration 2 and the impedance curve for this configuration.	108
Figure 69 Airfoil actuator configuration 3 and the impedance curve for this configuration.	109
Figure 70 Comparison of the average shear stress, as a function of frequency, for each of the actuator configurations.	110
Figure 71 Stress coverage threshold levels, as a function of frequency, with no phasing or frequency sweeping, for actuator configuration 1.	111
Figure 72 Stress coverage threshold levels, as a function of frequency, with no phasing or frequency sweeping, for actuator configuration 2.	112
Figure 73 Stress coverage threshold levels, as a function of frequency, with no phasing or frequency sweeping, for actuator configuration 3.	113
Figure 74 Illustration of all 30 unique non-redundant phasing combinations for the airfoil model, in which green indicates in-phase operation and red indicates phase inversion.	114
Figure 75 Illustration of the 8 selective phasing combinations out of the 30 unique non-redundant phasing configurations for the airfoil model, in which green indicates in-phase operation and red indicates phase inversion.	115
Figure 76 Average interface shear stress at the phased impedance minimum for all 30 phasing combinations for actuator configuration 1.	116

Figure 77 Average interface shear stress at the phased impedance minimum for all 30 phasing combinations for actuator configuration 2.....	117
Figure 78 Average interface shear stress at the phased impedance minimum for all 30 phasing combinations for actuator configuration 3.....	118
Figure 79 Coverage threshold shear stress levels for various phasing groups, actuator configuration 1.....	118
Figure 80 Coverage threshold shear stress levels for various phasing groups, actuator configuration 2.....	119
Figure 81 Coverage threshold shear stress levels for various phasing groups, actuator configuration 3.....	119
Figure 82 The shear stress fields induced on the ice-airfoil interface by the eight selective phasing combinations while driving the actuators at the phased impedance minimum for actuator configuration 1.....	121
Figure 83 The shear stress fields induced on the ice-airfoil interface by the eight selective phasing combinations while driving the actuators at the phased impedance minimum for actuator configuration 2.....	122
Figure 84 The shear stress fields induced on the ice-airfoil interface by the eight selective phasing combinations while driving the actuators at the phased impedance minimum for actuator configuration 3.....	123
Figure 85 Comparison of the net stress field for the unphased system, selective phasing, and all phasing for actuator configuration 1.....	124
Figure 86 Comparison of the net stress field for the unphased system, selective phasing, and all phasing for actuator configuration 2.....	125
Figure 87 Comparison of the net stress field for the unphased system, selective phasing, and all phasing for actuator configuration 3.....	125
Figure 88 Average shear stress field values for each phasing combination using the dynamic frequency selection approach (blue) and the static frequency selection approach (red) for actuator configuration 1.....	127
Figure 89 Average shear stress field values for each phasing combination using the dynamic frequency selection approach (blue) and the static frequency selection approach (red) for actuator configuration 2.....	128

Figure 90 Average shear stress field values for each phasing combination using the dynamic frequency selection approach (blue) and the static frequency selection approach (red) for actuator configuration 3.	128
Figure 91 Average of the average shear stress values across all phasing combinations using the dynamic frequency selection approach (blue) and the static frequency selection approach (red) for actuator configuration 1.	129
Figure 92 Average of the average shear stress values across all phasing combinations using the dynamic frequency selection approach (blue) and the static frequency selection approach (red) for actuator configuration 2.	130
Figure 93 Average of the average shear stress values across all phasing combinations using the dynamic frequency selection approach (blue) and the static frequency selection approach (red) for actuator configuration 3.	131
Figure 94 Shear stress coverage threshold levels for six combinations of phasing and frequency sweeping for actuator configuration 1.	133
Figure 95 Shear stress coverage threshold levels for six combinations of phasing and frequency sweeping for actuator configuration 2.	134
Figure 96 Shear stress coverage threshold levels for six combinations of phasing and frequency sweeping for actuator configuration 3.	135
Figure 97 Comparison of the stress fields with only frequency sweeping (left) and only selective phasing (right), for actuator configuration 1.	136
Figure 98 Comparison of the stress fields with only frequency sweeping (left) and only selective phasing (right), for actuator configuration 2.	136
Figure 99 Comparison of the stress fields with only frequency sweeping (left) and only selective phasing (right), for actuator configuration 3.	137
Figure 100 Polytec PSV-500-3D scanning laser Doppler vibrometer system [86].	138
Figure 101 Basic laser Doppler vibrometer mechanism [87].	139
Figure 102 Illustration of two frequencies f_b (red) and f_D (blue) generating a frequency modulated signal (purple) with a carrier frequency f_b+f_D and a modulation frequency f_b-f_D	140
Figure 103 In-plane velocity fields on carbon fiber sandwich panel surface at seven frequencies during ultrasonic de-icing system frequency sweeping.	142

Figure 104 In-plane velocity fields on carbon fiber sandwich panel surface with four phasing combinations during ultrasonic de-icing system phasing.	143
Figure 105 Effective vibration fields after frequency sweeping (left) and phasing (right).	144
Figure 106 Relative normalized two-dimensional cross-correlations of the velocity fields compared to the baseline field with frequency sweeping (left) and phasing (right).....	146
Figure 107 Relative average velocity across the panel surface as a function of frequency sweeping (left) and phasing (right).	147
Figure 108 Velocity coverage thresholds for frequency sweeping and phasing.	148
Figure 109 Percent improvement in coverage thresholds when switching from frequency sweeping to phasing.	148
Figure 110 The 12" x 12" titanium plate with a 100-point grid of circular 1/2"-diamter cutouts in a PTFE tape covering.	150
Figure 111 (Left) 0.2 mL of water applied to each grid point and (right) the frozen grid of ice dots.	150
Figure 112 The 12" x 12" titanium plate with four 2"-diameter PZT actuators bonded to the reverse side.	151
Figure 113 Compiled results of full ice dot delamination for the single frequency, frequency sweeping, and combined phasing and frequency sweeping test schemes versus input voltage.	154
Figure 114 Compiled results of full and partial ice dot delamination for the single frequency, frequency sweeping, and combined phasing and frequency sweeping test schemes versus input voltage.	155
Figure 115 Compiled results of full ice dot delamination for the single frequency, frequency sweeping, and combined phasing and frequency sweeping test schemes versus load power. ...	156
Figure 116 Compiled results of full and partial ice dot delamination for the single frequency, frequency sweeping, and combined phasing and frequency sweeping test schemes versus load power.	157
Figure 117 (Left) The composite specimen with sections of honeycomb removed, and the specimen with the actuators bonded into the cavities (right).	159
Figure 118 (Left) Strips of ice were created and filled in to cover the leading edge; (middle) top view of leading edge covered with ice; (right) side view of leading edge covered with ice.	160

Figure 119 (1-3) Initial cracking and delamination of ice on the airfoil leading edge during de-icing system operation with frequency sweeping and no phasing employed; (4-6) further cracking and delamination of ice on the airfoil leading edge during actuator phasing using 4 unique phasing combinations; (7-9) shattered ice easily being removed from airfoil with a compressed air nozzle.	161
Figure 120 Electronics & Innovation, Ltd. (E&I) 1040L broadband solid state class AB amplifier.	163
Figure 121 A single-winding autotransformer impedance matching network utilized in the de-icing system.	165
Figure 122 Simplified illustration of a phase splitter circuit using a transformer.	166
Figure 123 Phase splitter circuit employed in the ultrasonic de-icing system.	167
Figure 124 Comparison of the miniature relay and socket (left) and standard relay and socket (right).	168
Figure 125 Transistor switching circuit used to control the relays.	169
Figure 126 National Instruments USB-6361 analog and digital I/O device [89].	169
Figure 127 Photograph of the four-layer PCB used to control the relays for actuator phasing..	170
Figure 128 A microstrip PCB trace above a plane.	171
Figure 129 Design of the de-icing PCB for phasing.	173
Figure 130 PCB signal layer 1.	174
Figure 131 PCB ground plane.	174
Figure 132 PCB DC power plane.	175
Figure 133 PCB signal layer 2.	175
Figure 134 The various components of the ultrasonic de-icing system with actuator phasing and power monitoring. Note that the overall size of the system could be reduced by combining the components into a single housing.	176
Figure 135 Power-normalized version average interface shear stress at the phased impedance minimum for all 30 phasing combinations for actuator configuration 1.	246
Figure 136 Power-normalized average interface shear stress at the phased impedance minimum for all 30 phasing combinations for actuator configuration 2.	247
Figure 137 Power-normalized average interface shear stress at the phased impedance minimum for all 30 phasing combinations for actuator configuration 3.	247

Figure 138 Power-normalized coverage threshold shear stress levels for various phasing groups, actuator configuration 1.	248
Figure 139 Power-normalized coverage threshold shear stress levels for various phasing groups, actuator configuration 2.	248
Figure 140 Power-normalized coverage threshold shear stress levels for various phasing groups, actuator configuration 3.	249
Figure 141 Power-normalized average shear stress field values for each phasing combination using the dynamic frequency selection approach (blue) and the static frequency selection approach (red) for actuator configuration 1.	250
Figure 142 Power-normalized average shear stress field values for each phasing combination using the dynamic frequency selection approach (blue) and the static frequency selection approach (red) for actuator configuration 2.	251
Figure 143 Power-normalized average shear stress field values for each phasing combination using the dynamic frequency selection approach (blue) and the static frequency selection approach (red) for actuator configuration 3.	252
Figure 144 Power-normalized average of the average shear stress values across all phasing combinations using the dynamic frequency selection approach (blue) and the static frequency selection approach (red) for actuator configuration 1.	253
Figure 145 Power-normalized average of the average shear stress values across all phasing combinations using the dynamic frequency selection approach (blue) and the static frequency selection approach (red) for actuator configuration 2.	254
Figure 146 Power-normalized average of the average shear stress values across all phasing combinations using the dynamic frequency selection approach (blue) and the static frequency selection approach (red) for actuator configuration 3.	255
Figure 147 Power-normalized shear stress coverage threshold levels for six combinations of phasing and frequency sweeping for actuator configuration 1.	256
Figure 148 Power-normalized shear stress coverage threshold levels for six combinations of phasing and frequency sweeping for actuator configuration 2.	257
Figure 149 Power-normalized shear stress coverage threshold levels for six combinations of phasing and frequency sweeping for actuator configuration 3.	258

LIST OF TABLES

Table 1 Comparison of blade anti-icing & de-icing systems for a Bell 412 [15].	9
Table 2 Typical properties of various types of adhesive forces.	21
Table 3 Comparison of measured shear adhesion strengths for impact ice.	22
Table 4 Comparison of measured shear adhesion strengths for freezer ice.	22
Table 5 Minimum number of impedance measurements required to calculate the net impedance of a given number of actuators in a single set.	67
Table 6 Summary of the isotropic material properties used in the finite element analyses [28, 66].	85
Table 7 Orthotropic elastic and piezoelectric material properties used for modeling APC-841 ..	86
Table 8 Number of impedance measurements required to calculate the net impedance of a given number of actuators in a single set.	96
Table 9 Phasing increments and the number of unique phasing combinations that could be utilized in a four-actuator system.	97
Table 10 Comparison of the measured and predicted impedance minima for the airfoil actuators.	98
Table 11 Summary of total population set sizes for the various parameters considered during the genetic algorithm optimization of the phasing combination problem for the four-actuator de-icing panel model.	102
Table 12 De-icing grid phasing test scheme details.	151
Table 13 Actuator phasing combinations used during the de-icing grid phasing tests.	152
Table 14 De-icing grid phasing experiment results.	153
Table 15 Specifications of the E&I 1040L amplifier and the new custom amplifier design.	164

ACKNOWLEDGEMENTS

I would first like to express my gratitude to my wife, Jennifer Borigo, for her constant support and encouragement during the process of writing this dissertation and for tolerating my absence during so many hours of that work. My success through the course of graduate school and my career would not have been possible without her support.

I would like to thank my advisor Dr. Joseph Rose, for his continued guidance and advice through the course of my Master's and Doctoral programs at Penn State, and for leading me down the path of research that led to this dissertation.

I would like to acknowledge the prior research contributions in the field of ultrasonic de-icing by Dr. Edward Smith and Dr. Jose Palacios, both of the Aerospace Engineering department at Penn State. I would also like to thank them for their guidance and recommendations early in the course of my research.

I would like to acknowledge the support of the United States Air Force via Phase I and Phase II SBIR funding of much of the research included in this dissertation, particularly the technical point of contact for these SBIRs at Wright-Patterson AFB, Dr. Elizabeth Berman.

Finally, I would like to thank the Penn State students and FBS, Inc. employees that assisted me in specimen preparation, data collection, software development, and experimentation during this research. I would like to specifically acknowledge the assistance of Alex Reese and Russell Love for their assistance during this process.

Chapter 1

INTRODUCTION

1.1 Problem Description

From the onset of critical all-weather flight operations by the U.S. Air Mail Service between New York and Chicago in the mid-1920s, aircraft icing has been a serious concern [1]. The inability to avoid icing conditions due to various causes eventually led to the commencement of significant icing research efforts in the 1940s and 1950s [2], particularly at the National Advisory Council for Aeronautics (NACA) Icing Research Tunnel (IRT) and later at the NASA Lewis Icing Research Tunnel [1]. The advent of computers in the late 1970s marked the onset of theoretical icing analysis at NASA Lewis in the US and the Royal Aerospace Establishment in the UK [2]. During the more than eight decades of icing research that followed, a plethora of experimental tests, computational models, and engineered systems have arisen, yet there is much to be achieved in the field of aircraft icing research as the problem is still of utmost concern for modern aviation.

In the time period spanning 2006-2010, more than 40 icing accidents occurred that lead to dozens of deaths. Over the years of 1982-2000, FAA statistics report a total of 583 icing-related accidents resulting in 819 deaths in the U.S. [3], and over the period of 1975-1988, 803 accidents occurred, about half of which involved fatalities [4]. Between 1990 and 1999, U.S. commercial air carriers experienced an overall icing accident rate of 0.00668%, with 1.7% of all accidents being icing related [5]. Fortunately, the total number of icing-related aviation accidents has declined over the past several decades, which can be primarily attributed to advances in icing condition forecasting and ice protection equipment [3]. Yet even with these technological advances, icing remains a serious aviation hazard for aircraft, particularly for rotorcraft due to a number of unique factors including their normal operating regime [6], the impact of rotor icing in comparison to fixed-wing icing [7], and the incompatibility of some current de-icing technologies with rotorcraft systems. Additionally, modern composite aircraft construction techniques can limit or prohibit the use of some de-icing technologies, particularly those based on thermal de-icing principles. Fortunately, the development and implementation of smart icing

systems with integrated ice detection, de-icing/anti-icing, and warning systems could likely prevent many icing accidents [9].

The potential for ice accretion exists on various regions of an aircraft; the most critical of which are engine nacelles, windshields, wing leading edges, and rotor blades [7]. The hazards of wing leading edge and rotor blade icing arise in several forms including direct concerns such as altered aerodynamic properties, changes in pitch-moments, the obstruction of flaps and other mechanical systems, and mass imbalance, as well as indirect concerns such as decreased controls sensitivity, shedding, excessive vibration, and increased power and torque demands [2, 7, 10, 11]. Any one of these complications could potentially lead to an accident.

The specific changes in aerodynamic characteristics of an airfoil during icing depend on the details of the airfoil design as well as the properties and shape of the accreted ice. A number of experimental and numerical studies have been conducted to predict accreted ice shapes and analyze the aerodynamic effects of accreted ice on various airfoil designs in a multitude of icing conditions [10, 11, 12]. It has been shown that for commercial aircraft airfoils, glaze icing can reduce the maximum lift coefficient by 24-44%, decrease the stall angle by up to 32%, and increase section drag coefficient by up to 14 times. On the other hand, rime icing was shown to cause a decrease in lift coefficient of about half that observed for glaze icing, but only caused a small increase in section drag as well as no noticeable difference in stall angle [10].



Figure 1 Severe in-flight icing on a small turboprop aircraft. Icing such as this has been responsible for a great number of accidents and fatalities over the past few decades. (Source: Langley Flying School [13]).



Figure 2 A Royal Air Force Sea King helicopter, grounded due to icing conditions (Source: BBC News [14]).

It should be noted that significant performance decreases were measured within as little as two minutes of operation in icing conditions. The aerodynamic penalties that arise due to glaze icing are primarily due to the dramatic ice shapes that grow from the leading edge, which cause premature separation of flow and increased drag, while the aerodynamic penalties associated with rime icing are primarily a product of the increased surface roughness of the ice, since a relatively streamlined airfoil shape is retained [7, 6, 11].

Indirect effects of these aerodynamic changes include decreased vehicle performance capabilities, increased demands on the powertrain, and decreased controls sensitivity. For instance, the decreased lift-to-drag ratio of the rotors or wings, as well as the increased mass, creates a rapid increase in power required by the engines in order to maintain altitude and airspeed, which can lead to exceedance of operational limits in the engine and transmission [2, 7, 3]. Icing on wing, rotor, and horizontal tail surfaces can also lead to decreased controls effectiveness [2, 7].

Other negative effects of icing for rotorcraft include rotor mass imbalance, which can lead to excessive vibration and increased stress loads on fatigue-critical components [2]. Shedding is an additional concern for both fixed-wing aircraft and rotorcraft. Shedding can occur from rotor blades when the centrifugal forces due to the mass of the accreted ice and the high rotor angular

velocity exceed the shear strength of the ice-rotor interface, which leads to the sudden release of ice at high velocities. Shedding can occur on fixed-wing aircraft and engine nacelles when aerodynamic forces can remove partially or completely disbanded ice. Shedding can cause sudden changes in mass balance, torque, and aerodynamic forces that can compromise aircraft flight stability, and shed ice can cause airframe damage or catastrophic engine damage if ingested by a turbine engine [2, 7, 12].

All of these factors combine to provide sufficient reasons to conclude that icing is not permissible and can critically endanger aircraft during flight, and that appreciable ice accretion must be either prevented or effectively countered in flight.

1.2 Literature Survey – Aircraft De-Icing Technologies

A variety of systems have been developed to address the icing problem. These include anti-icing (i.e. ice prevention) systems and de-icing (i.e. ice removal) systems. The primary systems currently in use for de-icing and anti-icing are fluid, electro-thermal, pneumatic boots, electro-impulsive, electro-vibratory, microwave, shape memory alloy, and hot bleed air systems. These various systems are briefly discussed here including basic principles of operation and benefits and drawbacks with respect to operation on an aircraft.

Fluid Anti-Icing/De-Icing Systems

Fluid systems distribute anti-icing chemicals (such as ethylene glycol and isopropyl alcohol) that reduce the freezing point of water [5, 7]. These fluids must be continuously distributed over the surfaces of concern in order to maintain ice-free conditions. Fluid anti-icing systems on fixed-wing aircraft typically consist of porous leading edge panels, while rotor anti-icing requires more complex systems including slinger rings. Fluid de-icing systems provide very effective anti-icing even at low temperatures and are only one of two systems that can maintain truly ice-free conditions at all times during flight. Additionally, they require little power to operate. However, operation times during flight are limited by the amount of de-icing fluid that can be carried on board; typical operation times range from 3.5 hours for some single-engine turboprop aircraft to less than 1.5 hours for some helicopters, which is impractical for many operations [7, 1]. Aircraft de-icing fluids are also notoriously environmentally harmful and difficult to remove from wastewater [16], leading to restrictions on their use.

Electro-Thermal Anti-Icing/De-Icing Systems

Electro-thermal de-icing systems utilize thermal energy to increase the temperature of the aircraft components to exceed the freezing point of water. This is typically achieved via electric coils embedded in the aircraft component in the region in which ice mitigation is required. Electro-thermal systems may be designed to operate in a running wet (de-icing) or an evaporative (anti-icing) arrangement. Running wet systems simply melt the interface of the ice at the leading edge, causing liquid water to run back along the aft portion of the airfoil, while evaporative systems utilize a significantly higher heat flux to achieve instantaneous evaporation of impinging water [7]. Electro-thermal de-icing systems have high power demands, which decrease aircraft efficiency and limits their operation to relatively short duty cycles on rotorcraft, and can allow ice to accrete up to 7.5 mm during system downtime [17]. Additional limitations include the significant weight of such systems (in excess of 160 lbs), the issue of refreezing runback, and the potential for thermal damage to composite or polymer blade materials. Despite the limitations of electro-thermal systems for rotor de-icing applications in particular, they are the only de-icing method approved by the Federal Aviation Administration (FAA) and the Department of Defense (DoD), and continue to be the most prominent de-icing system on rotorcraft [15, 17]. Due to the high temperatures induced by such systems, they cannot be applied to temperature-sensitive composite aircraft structures, which account for an increasingly large proportion of new aircraft designs due to the strength-to-weight ratio benefits of such designs.

Pneumatic Boot De-Icing Systems

Pneumatic boots systems are popular on small fixed-wing aircraft, and have been utilized on rotorcraft in some instances [4]. Pneumatic boot de-icing devices rely on the principle of mechanical deformation of the ice in a manner that creates stresses in the ice in excess of the interfacial strength. This deformation is achieved by inflating rubber bladders on the leading edge of the airfoil. Once the ice is removed, the rubber boots are deflated under vacuum. Additional methods of inflating the leading edge bladders exist, including electro-explosive methods and pneumatic impulse methods which activate much more rapidly [5, 7]. Although the pneumatic boot method comes with a low weight and power cost, as well as a relatively thin minimum thickness requirement (roughly 3 mm), the rubber boots do change the shape of the airfoil, particularly when inflated, which can lead to aerodynamic degradation and higher engine

power requirements [7]. Palacios et al. [8] were recently able to demonstrate a centrifugally-powered version of a pneumatic de-icing system for rotor blades, which functions on a similar principle to those system deployed on aircraft wings.

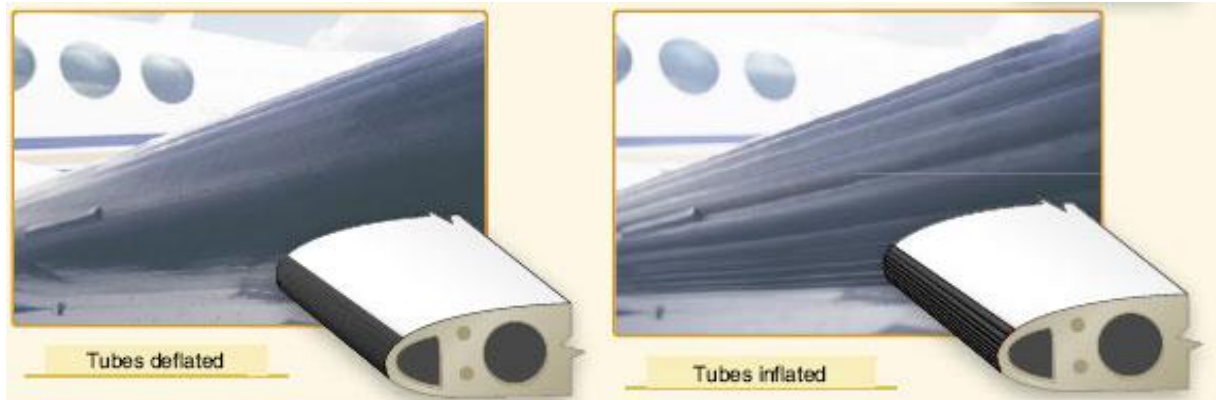


Figure 3 Pneumatic boot de-icing system on a small fixed-wing aircraft; the system shown in deflated state (left) and inflated state (right) (Source: FlightLearnings.com [18]).

Electro-Impulsive De-Icing Systems

Electro-impulsive de-icing systems rely on electromagnetic forces to accelerate the leading edge surface and debond any accreted ice beyond a threshold thickness [5]. Wound coils are installed just below the surface of the leading edge and a short-duration high-power pulse is delivered through them via a bank of capacitors. This high current pulse induces eddy currents in the metal leading edge, which cause a forceful repulsion of the leading edge from the electromagnetic coil [5, 7]. This impulsive force is sufficient to expel ice with thicknesses as small as 1.27 mm [19]. Such systems require little power, but are somewhat heavy (over 100 pounds) and can cause significant fatigue of the airfoil skin [7, 15]. It has also been shown that in composite wings and blades, electro-impulsive de-icing systems can be a considerable source of electromagnetic interference in the aircraft [7, 19].

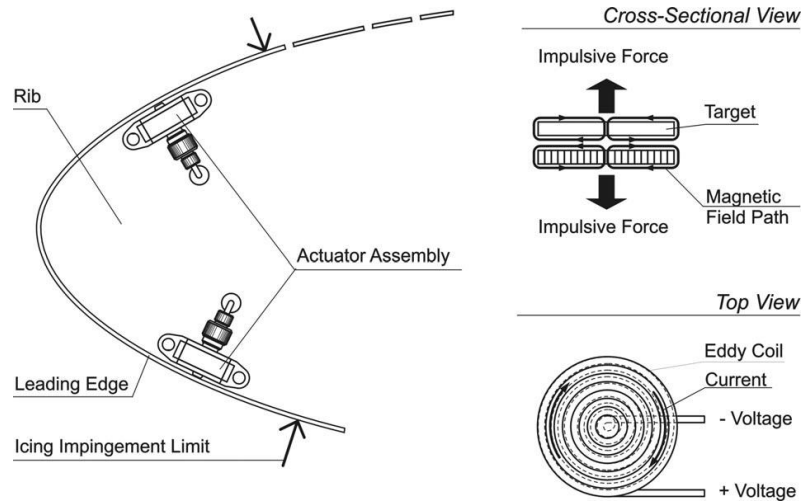


Figure 4 Diagram of an electro-impulsive de-icing system (Source: Goraj [5]).

Electro-Vibratory De-Icing Systems

Electro-vibratory systems utilizing low frequency excitation of rotor blades through higher harmonic shaking were investigated by Bell Helicopter in 1978. By sweeping through various natural resonances of the blade between 0 and 47 Hz, de-icing was successfully achieved on all blade sections except for the tip. Such systems were relatively lightweight and required little power to operate. It was determined that induced stresses were not a fatigue concern in metal blades but may have been a problem in composite constructions.

Microwave Anti-Icing/De-Icing Systems

High-frequency microwave de-icing systems utilize microwaves in the 30 GHz range to cause melting of the accreted ice interface. Microwave methods are only applicable in composite constructions. Since glass-fiber (GFRP) materials have a low electrical conductivity, they can be used as transmission lines to deliver millimeter-scale microwave energy to accreted ice, which is then heated and shed. Carbon-fiber (CFRP) materials, on the other hand, have a high electrical conductivity and also have a high absorption of microwave energy in this frequency range. Thus CFRP materials can be utilized as microwave waveguides which induces volumetric heating of the composite. This generates a thermal heat flux to the cold iced surface of the structure, which melts the accreted ice interface. Any composite component utilizing this technology would need

to be coated with a metallic layer to avoid electromagnetic interference issues with other aircraft systems [20, 21].

Shape Memory Alloy De-Icing Systems

Shape memory alloys (SMA) are materials that undergo a martensitic phase transformation and subsequent deformation when a sufficient amount of energy is applied to the material. A common shape memory alloy is nickel-titanium, but the specific alloy composition can be used to tailor the properties of the material. Shape memory alloys can be used in various configurations to de-ice an airfoil. One such configuration uses a SMA sheet over the leading edge with a SMA actuator on the upper side. When heated the SMA actuator stretches the SMA sheet over an array of structural ribs to create a complex strain field that facilitates de-icing. Cooling of the alloy then allows the SMA to relax to its previous state. Such systems would require on the order of 2.7 kW/m^2 and has been shown to de-ice both rime and glaze ice as thin as 3.175 mm [5, 22, 23].

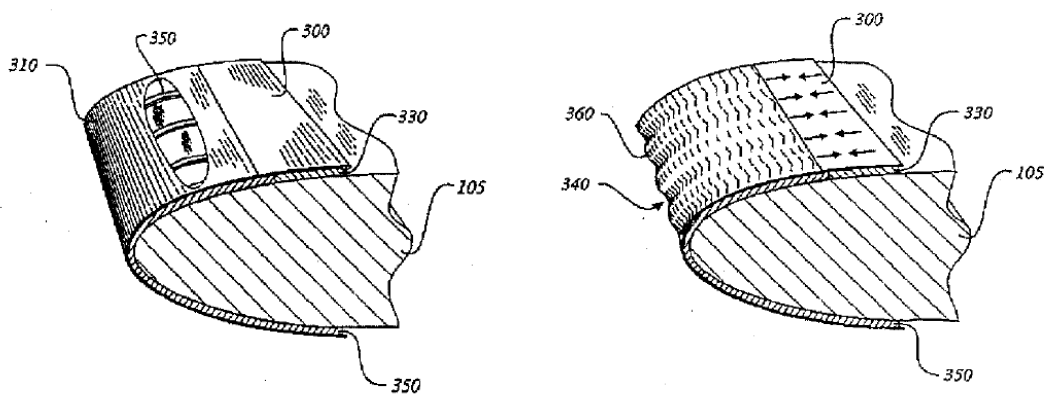


Figure 5 Concept of shape memory alloy de-icing system (Source: Ingram, et al. [22]).

Hot Bleed Air Anti-Icing/De-Icing Systems

Hot bleed air systems provide sufficient thermal energy to de-ice or anti-ice airframe components by redirecting hot exhaust gases from the aircraft engines. These hot exhaust gases often exceed 200°C and are distributed through pipes along the inner regions of metallic fixed-wing aircraft structures. The gases are delivered to the leading edges through small holes. Some drawbacks of such systems are the fact that military guidelines require this to be done with a heat exchanger, that fuel consumption penalties caused by hot bleed air systems arise when coupled

with modern engines, that such systems are incompatible with some components, and that the potential for thermal damage is high when used with composites [5, 7].

Summary of Anti-Icing and De-Icing Systems

A summary from [1] of various anti-icing and de-icing systems for a Bell 412 model helicopter is provided in Table 1. Each of these methods has unique advantages and disadvantages for rotorcraft applications. Weight is of primary concern, as is power consumption. The most common de-icing system currently in use for fixed-wing aircraft is fluid de-icing, which present great environmental concerns and only provides temporary ice protection. For rotor blades, fluid de-icing and electro-thermal systems are the most common, which consumes enormous amounts of power and thus causes unacceptable demands on the helicopter power generation systems and must be operated on a duty cycle. Note that some of the data in this table was compiled in the late 1980s and that advances in some of these systems have likely improved their performance and decreased their weight and power demands to some extent.

Table 1 Comparison of blade anti-icing & de-icing systems for a Bell 412 [15].

	Electro-Thermal	Fluid	Pneumatic	Electro-Impulsive	Electro-Vibratory	Microwave	Ultrasonic (potential)
Weight (lbs)	162	194	54	120	120	TBD	90
Ice accretion	Yes	No	Yes	Yes	Yes	No	Yes
Power Required (kW)	26	negligible	negligible	3.0	1.3	15	4.0
Performance Effects	10% torque rise	none	10% torque rise	10% torque rise	10% torque rise	TBD	none
Runback Potential	Yes	No	No	No	No	No	No
Detached Ice Impacts	Yes	No	Yes	Yes	Yes	No	Yes
Interference with Avionics	No	No	No	No	No	Yes	No

1.4 Literature Survey - Ultrasonic De-Icing Research

Since the early 2000s, research into a low-power high-frequency ultrasonic de-icing/anti-icing system for rotorcraft blades has been ongoing at Penn State University. An extensive amount of work has been carried out and can be reviewed in the dissertations of Ramanathan, Palacios, and Zhu [1, 24, 25]. The work presented herein is intended to build upon the research of these previous investigators, but a complete review of their findings would be impractical for the purposes of this document. Therefore, a brief summary of the accomplishments and conclusions of these researchers, as well as several others, is provided below.

Ramanathan [25] proposed a novel ultrasonic de-icing method of utilizing shear horizontal (SH) guided wave modes to debond ice by exceeding the interfacial shear strength of the accreted ice. A piezoelectric shear actuator was utilized to introduce shear stresses to an ice patch. An equivalent circuit analysis was performed to estimate the interfacial shear stress as a function of input voltage to the actuator and it was predicted that sufficient stress could be generated to debond ice. Experimental results showed that instantaneous delamination was not achievable with this configuration, and melting was eventually observed after 145 seconds. According to the author's analysis, the electrical energy converted to thermal energy in the piezoelectric actuator would generate insufficient thermal energy to melt the ice patch, however, this analysis does not take internal damping losses of the substrate into account, and thermal melting of the ice is apparent. The particular mode and frequency of SH wave excitation was not taken into consideration and the actuator was driven near 1MHz [25].

Venna et al. [26] performed piezoelectric excitation experiments on freezer ice bonded to airfoils at frequencies ranging from 1 to 1000 Hz in an attempt to utilize both shear and normal impulse forces to de-ice the structure. Although this method does not operate in the ultrasonic regime, the similarities in the system setup and the proposed de-icing mechanism are relevant to the current ultrasonic de-icing research. The authors' finite element models predicted shear stresses and forces on the ice sufficient to facilitate complete de-icing in this frequency range. However during experiments, instantaneous de-icing was not achieved and debonding or cracking of the ice was not observed. Melting of the interface between the ice and substrate occurred after 60 seconds at -7°C and after 220 seconds at -15°C [26].

Palacios [1] sought to develop an ultrasonic de-icing system for helicopter blades that could instantaneously debond accreted ice by exceeding the ultimate adhesive shear stress of the ice layer. Palacios calculated the regions on the SH guided wave dispersion curves at which maximum interfacial shear stress was predicted for a transient propagating guided wave. The predicted frequency range at which this occurred was near 200 kHz as well as 1 MHz, but experiments using this configuration were unsuccessful at debonding freezer ice.

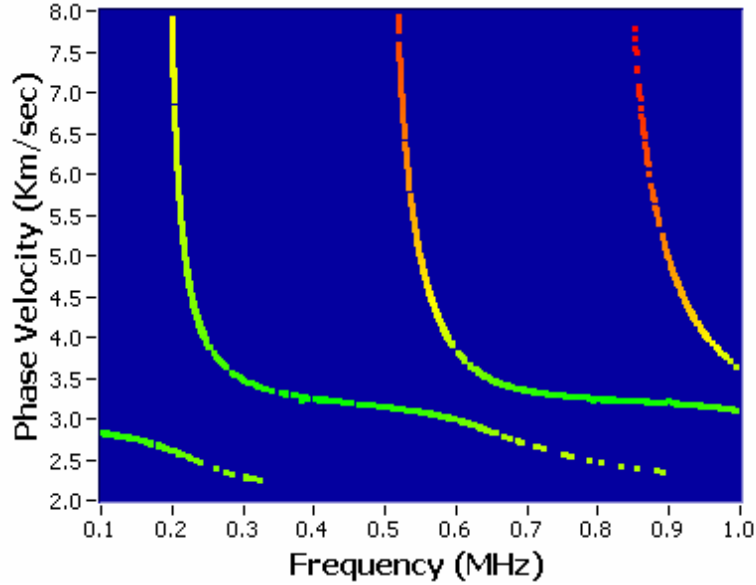


Figure 6 SH wave dispersion curves showing regions of high interfacial shear stress coefficient (ISSC) values (Source: Palacios [15]).

Palacios also investigated the use of lower-frequency ultrasonic actuators including a piezoelectric disk actuator with a radial resonance near 29 kHz and driving the actuator at the impedance minimum of the system. Utilizing this actuator, Palacios was able to instantaneously debond freezer ice as thin as 1-3 mm on a 0.711 mm thick, 30.48 x 30.48 cm steel plate at a power requirement of 0.05 W/cm^2 . The prevention of freezer ice formation was also observed at an input power of 0.1 W/cm^2 . The temperature of the substrate did not exceed -3°C during the experiment. Impact ice de-icing was also studied, in which accreted ice was shed once it exceeded 1.2 mm in thickness at an input power of 0.18 W/cm^2 , but only in regions of maximum stresses. Anti-icing was achieved in the near vicinity of the actuator [15].

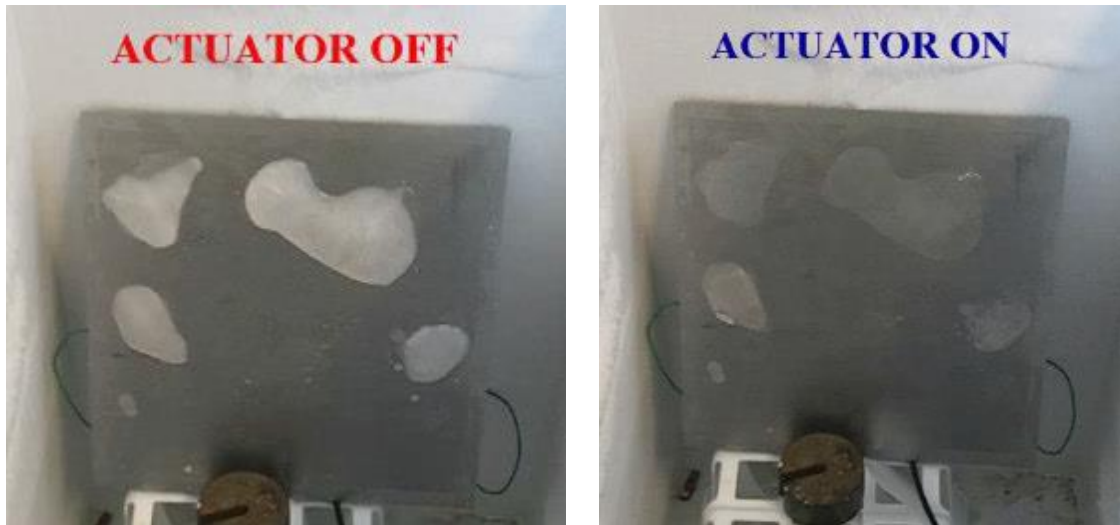


Figure 7 An iced plate before (left) and after (right) ultrasonic excitation (Source: Palacios [15]).



Figure 8 Ultrasonic ice protection results from Goodrich's wind tunnel (Source: Palacios [15]).

Zhu [24] expanded on the work of Palacios by further investigating ultrasonic vibration as the potential de-icing mechanism to achieve instantaneous ice delamination. Some initial work was performed to investigate the relationship between transient ultrasonic waves and the eventual steady-state vibration field driven by a piezoelectric actuator. Zhu also attempted to use d_{15} actuators instead of d_{31} actuators due to the theoretically superior actuation capabilities of these shear piezoelectric devices. However, experiments showed that de-icing was not achieved when such shear actuators were used; a potential reason for this failure was that the impedance of the bonded actuators was well above the impedance-matching capabilities of the amplifier.

The concept of tailored waveguides (TWG) was also introduced, in which periodic material discontinuities are machined into the back side of the substrate to be de-iced. These discontinuities lead to localized interfacial shear stress concentrations that can locally improve de-icing potential. It was predicted that the use of TWGs could potentially increase interfacial shear stresses by as much as 300% as compared to a uniform plate with equivalent mass. Experiments showed that the use of TWGs was effective in reducing the necessary input power to de-ice an isotropic plate [24]. However, the improvements in de-icing performance may be due to the removal of material from the structure, which would be an unacceptable modification in most cases.

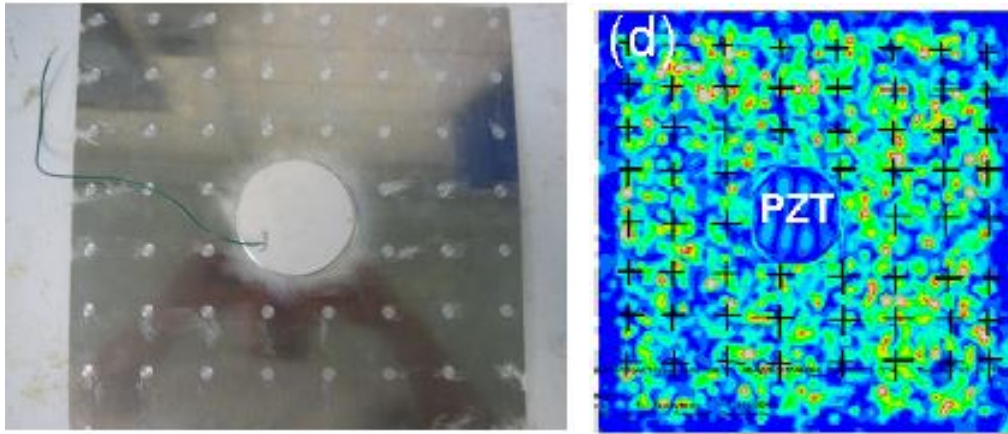


Figure 9 (Left) Tailored waveguide (TWG) and (right) predicted stress field with (Source: Zhu [24]).

1.5 Research Objectives

Although a wide variety of anti-icing/de-icing methods exist in use and in development, many of these systems have serious drawbacks that hamper their usefulness or applicability to particular structures. Many of these issues involve substantial weight and power consumption and are limited by the damping of composite materials and the susceptibility of such materials to high temperatures. The predominant de-icing systems currently in use are fluid de-icing and the electro-thermal blanket systems for rotorcraft. Fluid de-icing carries along with it a substantial

amount of environmental concern and only provides temporary ice protection. Unfortunately electro-thermal systems require power in excess of 3.8 W/cm^2 . Due to this high power consumption, these systems can only be used on a duty cycle, which allows for significant accretion of ice between operations of the system, causing potential aerodynamic and control issues as well as the concern for damage when the ice is shed.

A number of researchers including Palacios and Zhu have successfully utilized steady-state ultrasonic vibration by piezoelectric actuators to de-ice plates and airfoils in both freezer and impact icing scenarios at total power requirements that are lower than the current electro-thermal systems [15, 27, 28, 24]. However, the difficulties of consistently and completely de-icing thin layers of accreted ice on stiffer structures or structures with greater damping, while utilizing limited power, are yet to be overcome. DiPlacido [29] also provided evidence that a multi-frequency tone-burst actuation can provide improved performance over the long-pulse frequency sweeping approach. The previous work has proven that ultrasonic vibration has the potential to provide de-icing capabilities in some circumstances, and further improvement and optimization of such a method may lead to the development of a low-power non-thermal ultrasonic de-icing system capable of fulfilling the role of the primary ice protection system on a range of aircraft including fixed-wing and rotorcraft platforms for metallic and composite components.

The proposed goal of this research is to examine methods to improve the efficiency and effectiveness of an ultrasonic de-icing system by exploring a number of new techniques and to expand its application to fixed-wing aircraft, including those with composite components. The specific objectives of the research are to:

1. Improve the method by which de-icing system operating frequency optimization is achieved. This is currently done by sweeping the electromechanical impedance of the system, selecting the frequency associated with the minimum impedance, and then applying high power while incrementally sweeping frequency within a small bandwidth around that resonance.
2. Improve the methods by which the piezoelectric actuators are fabricated and integrated into various structures.

3. Develop a novel system and method that utilizes electronic phasing between de-icing actuators to improve the efficiency and effectiveness of the system and to ensure full de-icing/anti-icing coverage over the entire surface.
4. Pioneer the application of the ultrasonic de-icing technology to fixed-wing composite aircraft structures.
5. Improve the design and operation of the ultrasonic de-icing system as a whole, which may include revisions to the operational procedure, system hardware, and system software.

The research carried out and the contributions made with respect to each of these tasks will be described in detail in the following chapters.

1.6 Overview of Chapters

A brief description of the content of each subsequent chapter is provided below, including the topics discussed and the conclusions made from the research.

Chapter 1: Introduction

In Chapter 1, an introduction to the importance of developing aircraft icing solutions is provided along with a literature review of current aircraft de-icing technologies and past research into ultrasonic de-icing. The fundamental goals of the research are also outlined.

Chapter 2: Foundational Principles

In Chapter 2, an overview of basic aircraft ice accretion, ice adhesion, and forced structural vibration principles are presented and discussed. These concepts provide a foundation for the ultrasonic de-icing research presented in the following chapters.

Chapter 3: Actuator Design

In Chapter 3, the piezoelectric actuators utilized in the ultrasonic de-icing system are described in detail. This chapter includes a description of the piezoelectric effect, the radial electromechanical vibration modes of a piezoelectric disk actuator, the theoretical optimization

of actuator positioning on a structure, and the improved methods by which piezoelectric actuators were fabricated and installed in composite sandwich panel structures.

Chapter 4: Impedance Analysis

In Chapter 4, the concepts of electrical and electromechanical impedance, as they relate to the ultrasonic de-icing system, are presented. The importance of electrical impedance matching is discussed. A method is developed by which the electromechanical impedance of a multi-actuator structure with actuator phasing can be determined from a combination of the individual complex impedances of each actuator, including finite element verification of this method. The concept of automatic frequency tuning, in which the forward and reflected power between an amplifier and actuator set are monitored through the use of a bi-directional coupler to optimize frequency selection, is introduced and applied to the ultrasonic de-icing system.

Chapter 5: Actuator Phasing Method

In Chapter 5, an actuator phasing method is developed for ultrasonic de-icing. Through a series of finite element models, 3D scanning laser Doppler vibrometer tests, and de-icing experiments, it is demonstrated that actuator phasing provides a substantial improvement in the efficiency and effectiveness of the ultrasonic de-icing system for both non-attenuative and attenuative structures. The details of implementing this actuator phasing method are also explored.

Chapter 6: Ultrasonic De-Icing System Design

In Chapter 6, the hardware used for the ultrasonic de-icing system is presented and discussed in the context of its role in the de-icing system, particularly for the purposes of frequency selection and actuator phasing. The primary components include a custom-designed printed relay control circuit board, an amplifier, an impedance matching network, a phase splitter, an analog/digital I/O device, and a DC power converter. The control software for operating the system is also briefly discussed.

Chapter 7: Concluding Remarks

In Chapter 7, the major findings of the research are summarized and a list of contributions is presented. A series of recommendations for further research and development are also provided.

Chapter 2

FOUNDATIONAL PRINCIPLES

2.1 Ice Adhesion

Aircraft icing occurs during flight through clouds of supercooled water droplets, at temperatures below freezing, in which the droplets impact the aircraft and subsequently freeze [2]. The severity of the ice accretion and the properties of the accreted ice depend on a number of aircraft and environmental characteristics including outside air temperature (OAT), liquid water concentration (LWC), droplet size, airspeed, aircraft component size, and surface roughness [2].

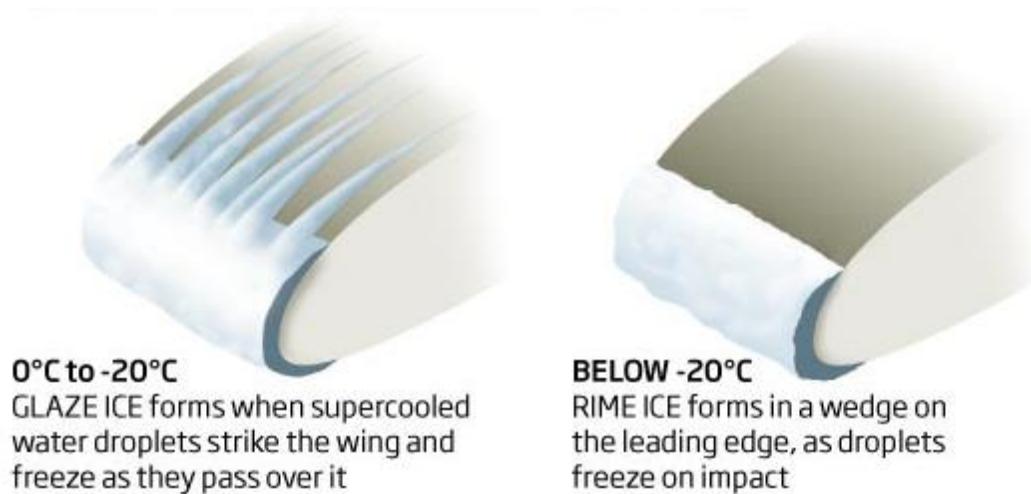


Figure 10 Two types of icing common on airfoil structures are (right) rime ice, which is more granular, rough, and opaque, and (left) glaze ice, which is translucent, smooth, and dense (Source: New Scientist [31]).

Aircraft impact icing can be categorized into three distinct categories: rime, glaze, and beak ice. Rime ice typically develops in low temperatures (roughly -40°C to -10°C [7]) and at low speeds and/or at low LWC conditions, in which droplets immediately freeze on impact, resulting in an opaque streamlined accretion [2]. Glaze typically forms at temperatures closer to freezing (roughly -18°C to 0°C [7]) and at higher speeds and/or higher LWC conditions, in which the water does not immediately freeze on impact, but may run and freeze at a secondary location leading to localized thickening of the accreted ice [2]. The third and final form of ice observed to form on rotor blades and wing leading edges is known as beak ice, which is much less common than rime or glaze ice, typically only forms on the upper surface of the blade leading

edge, and is unstable and self-limiting in size [2]. Due to these factors, only rime and glaze ice will be discussed further.

Physical Mechanisms of Ice Adhesion

In order to effectively understand, design, and model de-icing systems, a thorough understanding of the fundamental physical mechanisms of ice formation is required. This should include an understanding of the physical forces responsible for the adhesion of ice to a surface as well as the elastic properties of the ice and the ice-substrate interface under various conditions. The physical mechanisms responsible for ice adhesion can be categorized into four categories [32, 33]:

1. Covalent or chemical bonding
2. Van der Waals forces
3. Electrostatic interactions
4. Mechanical bonding

The first three forces play a role in ice adhesion on all surfaces, and mechanical bonding can be significant for substrates that have any appreciable surface roughness. The scale of interaction for each of these forces is different, and thus so are the relative adhesion energies associated with them.

Covalent bonding is a form of chemical bonding that occurs between materials with similar electronegativities in which the atoms of the two materials share electrons to form an interfacial compound. These bonds are effective only over a range of 0.1 to 0.2 nm and are highly-dependent on the chemical makeup of the two materials [32]. Some theories state that the ice adhesion bond is primarily due to the interaction of the oxygen atoms in the ice lattice with the atomic structure of the substrate, and that the alignment of these two lattices plays a large role in bond strength [34]. Another form of chemical bonding that is important in ice is hydrogen bonding. Hydrogen bonding is the interaction of an electronegative atom with a hydrogen atom, as illustrated in Figure 11. This type of bonding is responsible for the hexagonal crystalline nature of ice [35], as illustrated in Figure 12. Hydrogen bonding is responsible for the cohesive bonding in ice, meaning the strength of the bulk crystalline structure, but is not responsible for the adhesive bonding of ice, which is the bonding of ice to a substrate.

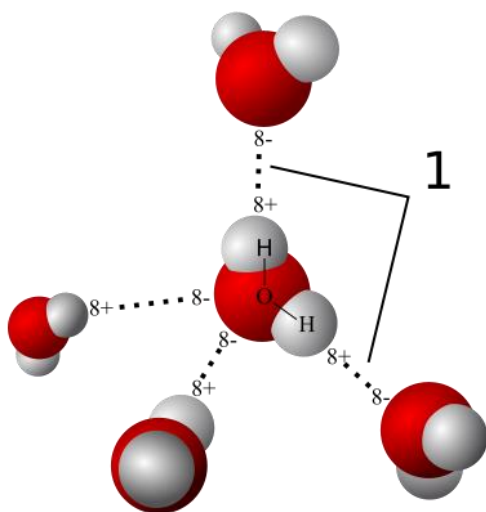


Figure 11 Illustration of five water molecules and the hydrogen bonds between them (Source: Wikimedia Commons [36]).

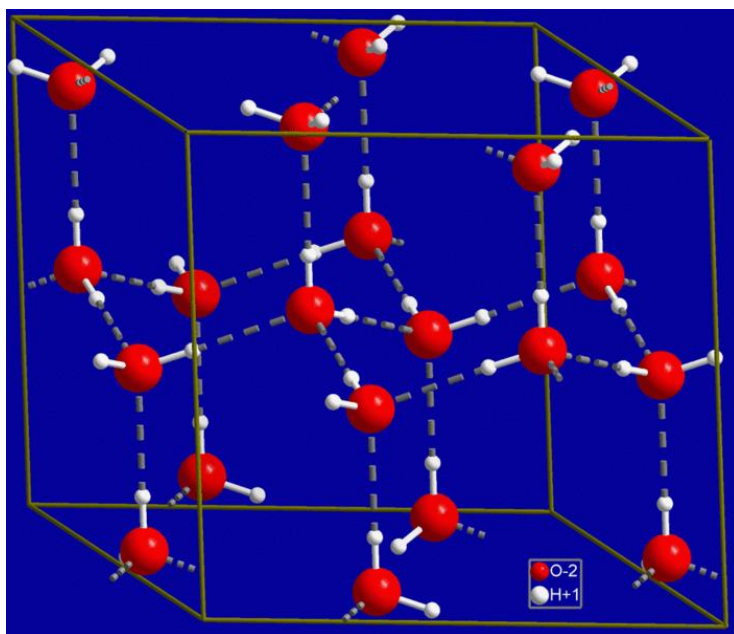


Figure 12 Illustration of hydrogen bonding between water molecules that forms a hexagonal crystal lattice of ice (Source: Wikimedia Commons [37]).

Van der Waals forces are intermolecular forces between permanent molecular dipoles, permanent and induced dipoles, and instantaneously induced dipoles. While a symmetric molecule such as water has no net charge, fluctuations in the electron field of the molecules can

lead to temporary dipoles, which can subsequently induce a dipole in a nearby molecule, as is illustrated in Figure 13. This interaction can lead to a stable force between the two molecules even as the dipoles fluctuate, since they are now coupled. Van der Waals forces operate over a longer range than the chemical bonding forces [32, 38].

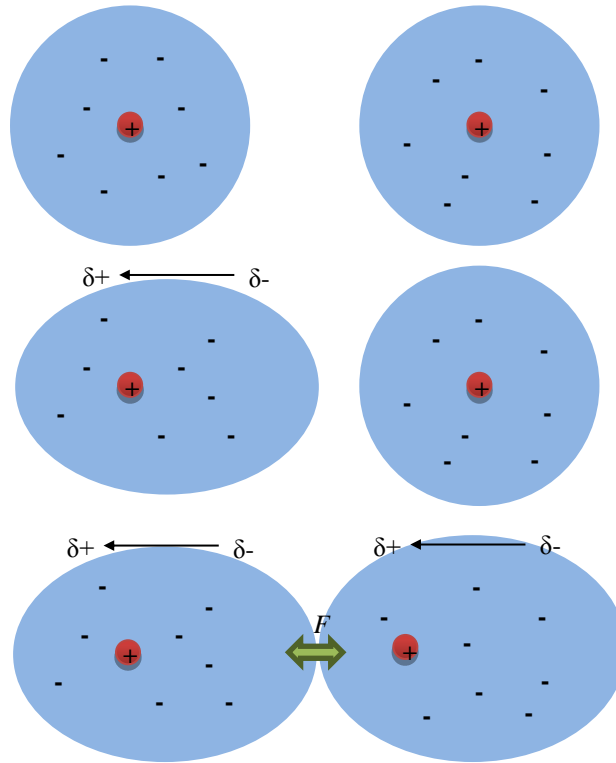


Figure 13 An illustration of Van der Waals forces; (Top) two unpolarized atoms generally have balanced charge distributions; (center) one atom may become an instantaneous dipole due to probabilistic electron field distributions; (bottom) the instantaneous dipole may induce a nearby atom to become a dipole, which creates an interaction force between the two dipoles.

The third ice adhesion mechanism, electrostatic interaction, is due to the attractive electrostatic forces generated between separated charges. It has been shown that at distances greater than 0.276 mm, the electrostatic adhesion mechanism is significantly more important than chemical bonding and that the adhesion energy of the electrostatic forces at this distance is greater than that of the van der Waals interaction. Therefore electrostatic adhesion is the predominant non-mechanical ice adhesion mechanism of the three listed above [32]. Table 2 provides some typical properties of various types of adhesive bonds for comparison [39].

Table 2 Typical properties of various types of adhesive forces.

Chemical Bonds	Bond Length (nm)	Bond Energy (kJ/mol)
Covalent bonds	0.1-0.2	150-950
Metallic bonds	0.3-0.5	100-400
Ionic bonds	0.2-0.3	400-800
Intermolecular Interactions	Bond Length (nm)	Bond Energy (kJ/mol)
Van der Waal's forces	0.4-0.5	2-15
Hydrogen bonds	0.2	20-30

The final adhesion mechanism is mechanical bonding, which is simply the mechanical interlocking of the ice as it forms in the surface features of the substrate. This bonding mechanism is responsible for the dependence of interfacial properties on surface roughness of the substrate. Some studies show that the adhesive strength of ice is proportional to the extent of mechanical interlocking [34], and therefore rougher surfaces offer the potential for much greater bond strength.

Interfacial Strength of Ice

In order to model the effectiveness of various de-icing methods that rely on fracturing the ice from the leading edge, an understanding of the failure strength of ice must first be attained. Several potential failure modes for the ice exist, including adhesive debonding, cohesive debonding, and tensile failure of the ice.

Tests have been conducted to measure the tensile strength of ice as a function of temperature. These experiments showed that the mean ultimate tensile strength of ice may range from 0.827 to 1.172 MPa over a range of -4°C to -23°C, respectively [40]. The tensile adhesion strength of ice to aluminum has been measured to range from 179 to 274 MPa depending on temperature and substrate properties [41].

A large number of studies have been performed over the past 60 years to measure the adhesive strength of ice to various substrates [42-55]. The results of some of these works have been summarized and are presented in Table 3 and Table 4 in terms of the type of ice used (i.e. impact or freezer ice).

Table 3 Comparison of measured shear adhesion strengths for impact ice.

Reference	Substrate	Adhesion Shear Strength (MPa)
Stallabrass and Price (1962) [49]	Al	0.026-0.127
Itagaki (1983) [51]	Al	0.027-0.157
Chu & Scavuzzo (1991) [45]	Al	0.12-0.4
Javan-Mashmool (2006) [42]	Al	0.21-0.35
Kraj & Bibeau (2010) [43]	GFRP	0.023-0.061

Table 4 Comparison of measured shear adhesion strengths for freezer ice.

Reference	Substrate	Adhesion Shear Strength (MPa)
Loughborough & Hass (1946) [46]	Al	1.52
Loughborough & Hass (1946) [46]	Cu	0.85
Raraty & Tabor (1958) [47]	Al	1.66
Ford & Nichols (1961) [53]	SS	0.24
Bascom (1969) [48]	SS	1.63
Reich (1994) [54]	Al	0.896
Brouwers & Palacios (2010) [55]	Al	0.526

A significant scatter is observed in the data amongst the papers referenced and even within any given paper itself. This is due to the variations in ice formation conditions, substrate, and test method [55, 45]. It is important to note that according to the results tabulated above, freezer ice has substantially higher shear adhesion strength than impact ice. According to the literature review in [54], the maximum observed shear strength of freezer ice was 1.7 MPa and the maximum observed impact ice shear strength was 1 MPa. It should be noted that the ultimate tensile strength of ice is greater than the shear adhesion strength, thus it will generally be easier to disbond the accreted ice using shear stress than by inducing tensile stress. The great difference in these adhesion strengths is attributed to a liquid-like layer, only several hundred molecules thick, that exists between the ice and the structure until below -30°C [41].

The most significant variations in impact ice tests included the type of ice (i.e. glaze or rime) and the substrate temperature, particularly between -4°C and 0°C . The shear adhesion strength showed a weak linear decrease with decreasing substrate temperatures below -4°C and a strong linear decrease with increasing substrate temperatures above this threshold. It was also shown

that glaze ice tends to have a significantly higher shear adhesion (0.4 MPa) than rime ice (0.12 MPa), and that rime ice often failed cohesively before it would fail adhesively at the interface [45]. The differences in the adhesion strengths of these two ice types is due to the fact that glaze ice is a solid continuum, while rime ice is typically aerated and powdery.

The factors that did not seem to have an appreciable impact on the shear adhesion strength of ice included tunnel temperature, ice thickness, and substrate material [45]. However, the surface roughness of the substrate played a substantial role in the adhesion shear strength of both freezer and impact ice [55, 44, 45]. Increased surface roughness can cause an extreme increase in adhesion strength due to the mechanical bonding mechanism described above. Additionally, specially-engineered icephobic coatings exist that are designed to reduce the shear adhesion strength of ice.

Interfacial Shear Stress

Piezoelectric transducers applied to the surface of a thin structure, such as an ice-covered plate or airfoil, and actuated with a continuous wave cycle of sufficient duration, will produce a steady-state forced vibration field in that structure. Associated with this field will be a shear stress distribution at the interface of the ice and the substrate structure. If the magnitude of the shear component of the traction on the interfacial plane exceeds the ultimate shear adhesion strength of the ice to the substrate, the ice will be instantaneously debonded. Additionally, fatigue failure of the ice can occur even if the shear stresses are less than the ultimate strength of the interface. Due to the high-frequency nature of the ultrasonic de-icing system, tens of thousands of fatigue cycles can be induced on the interface within just a few seconds. Based on the coordinate system in Figure 14, the magnitude of the shear stress on the interfacial plane can be calculated from the stress tensor at any point on the interface.

Based on the stress tensor in equation (2.1) as defined by Figure 15 [56], the traction force on a small area with a unit normal vector \mathbf{n} is given by $T^{(n)}$, as defined in Figure 15 [57]. This traction can be decomposed into a normal stress $N^{(n)}$ and a shear stress $\tau^{(n)}$ on the plane, as described in equations (2.2) through (2.4).

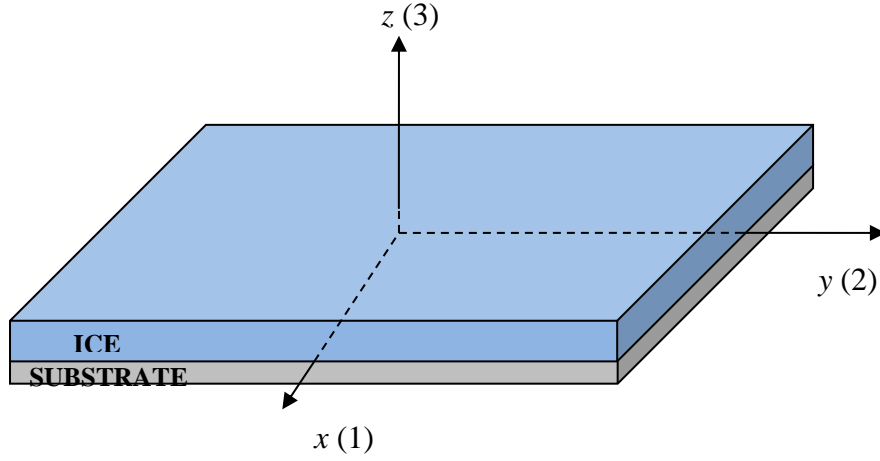


Figure 14 Coordinate system for ice-substrate structure.

$$\sigma = \begin{bmatrix} \sigma_1 & \sigma_{12} & \sigma_{13} \\ \sigma_{21} & \sigma_2 & \sigma_{23} \\ \sigma_{31} & \sigma_{32} & \sigma_3 \end{bmatrix} \quad (2.1)$$

$$\tau^{(n)} = \sqrt{|T^{(n)}|^2 - N^2} \quad (2.2)$$

$$N^{(n)} = \sigma_{ij} n_i n_j \quad (2.3)$$

$$|T^{(n)}|^2 = \sigma_{ji} n_j \sigma_{ki} n_k \quad (2.4)$$

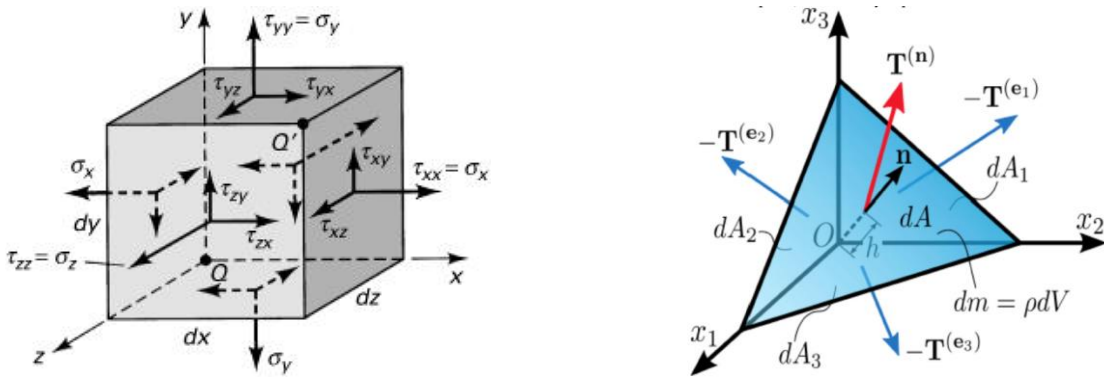


Figure 15 (Left) Stress tensor component definitions (Source: Cook, et al. [56]); (right) traction on a plane (Source: Wikimedia Commons [57]).

Therefore the expression for the magnitude of the shear stress of the plane described by unit normal vector \mathbf{n} is given in equation (2.5).

$$\tau^{(n)} = \sqrt{(\sigma_1 n_1 + \sigma_{12} n_2 + \sigma_{13} n_3)^2 + (\sigma_{12} n_1 + \sigma_2 n_2 + \sigma_{23} n_3)^2 + (\sigma_{13} n_1 + \sigma_{23} n_2 + \sigma_3 n_3)^2 \dots} \quad (2.5)$$

$$\dots - [\sigma_1 n_1^2 + \sigma_2 n_2^2 + \sigma_3 n_3^2 + 2(\sigma_{12} n_1 n_2 + \sigma_{23} n_2 n_3 + \sigma_{13} n_1 n_3)]^2$$

Since we are concerned with shear stress on the ice-substrate interface, the unit normal vector for our analysis is $\mathbf{n} = (0,0,1)$, which allows us to simplify equation (2.5) to the final expression for shear stress magnitude on the interface in equation (2.6).

$$\tau^{(n)} = \sqrt{\sigma_{13}^2 + \sigma_{23}^2} \quad (2.6)$$

Therefore any de-icing analysis will require the measurement of only the two shear stresses σ_{13} and σ_{23} on the ice-substrate interface, and the magnitude of the net shear stress will be calculated with equation (2.6). If this value exceeds the ultimate shear adhesion strength of the ice, instantaneous debonding should occur. These expressions of shear stress magnitude, $\tau^{(n)}$ relative to some surface described by normal vector n , will be used to calculate the shear stresses induced on plate and airfoil surfaces. Utilizing the local shear stress definition relative to the surface normal vector is a critical step in accurately characterizing the shear stress field on non-planar surfaces such as airfoils.

2.2 Forced Structural Vibration

Structures such as an ice-loaded plate or airfoil have inherent mass, stiffness and damping properties associated with their constituent materials and their geometric assembly. Any loads exerted on such structures will result in a deformation response. When these loads are harmonic, a transient response will initially occur, followed by a steady-state harmonic response of the structure, i.e. vibration. For the purposes of this research, the steady-state portion of the response is of the most interest. To understand the dynamics of the steady-state response of complex structures such as those in question, finite element methods are primarily utilized. However, to properly interpret the finite element results and to be able to apply a sufficient level of reasoning

to the problem of ultrasonic vibration of plate and airfoil structures, a more fundamental understanding of structural dynamics is a prerequisite. The basic principles of structural vibrations that will be utilized as a foundation for this research are briefly outlined in this section, particularly the concept of structural resonances, normal modes of vibration, and modal decomposition.

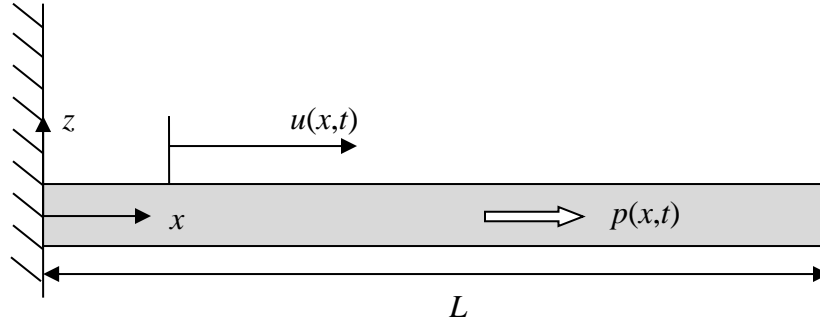


Figure 16 Diagram of a uniform rod.

To present a simplified analysis of structural vibrations, a uniform rod, as shown in Figure 16, will be examined, since it is a continuous elastic system, yet it requires only a succinct one-dimensional analysis.

Assume that the Young's modulus of the rod is E , the length is L , the mass density is ρ , and the cross-sectional area is A . The displacement is defined by $u(x,t)$ and the forcing is defined by $p(x,t)$. Assume that the rod is fixed at one end ($x = 0$) and free at the other ($x = L$). Several methods can be utilized to develop the governing equations for the rod, specifically a classical Newtonian approach or an energy method approach such as Hamilton's Principle [58, 59]. The specific method of arriving at the governing equations is of little consequence for the purposes of this review, so the governing equation is given in equations (2.7) and the boundary conditions are given in equations (2.8) and (2.9).

$$\rho A \frac{\partial^2 u}{\partial t^2} - EA \frac{\partial^2 u}{\partial x^2} = p \quad (2.7)$$

$$u(0, t) = 0 \quad (2.8)$$

$$\frac{\partial u}{\partial x}(L, t) = 0 \quad (2.9)$$

By applying a simple separation of variables approach to the governing equation, assuming a harmonic response, and applying the boundary conditions, the characteristic equation of this system can be determined. The solutions to the characteristic equation then allow us to describe the solutions in terms of the deformation of the structure as in equations (2.10) and (2.11).

$$U_n(x) = \sin(\omega_n x) \quad (2.10)$$

$$\omega_n = \sqrt{\frac{E}{\rho}} \left(\frac{2n+1}{2L} \right) \pi = \frac{\pi}{cL} \left(\frac{2n+1}{2} \right) \quad (2.11)$$

The solutions $U_n(x)$ are the mode shapes of the system and ω_n are the natural frequencies of the system, in which c is the longitudinal wave velocity in the material and $n = 0, 1, 2$, etc. It can be shown that these natural mode shapes are orthogonal with respect to the mass (and stiffness) of the system according to equation (2.12).

$$\int_0^L \rho A U_i U_j dx = \begin{cases} 0, & \text{if } i \neq j \\ m_{ii}, & \text{if } i = j \end{cases} \quad (2.12)$$

Based on this orthogonality, a normal mode expansion theorem can be developed in accordance with equations (2.13) through (2.15). The key principle of this expansion is that a deformation of the structure can be decomposed into a superposition of the normal modes of the structure, which act together with some relative amplitude and phase. Therefore the harmonic response of the structure due to any forcing function, regardless of how complex it may be, can be described in terms of the normal modes of the system.

$$u(x, t) = \sum_{n=1}^{\infty} c_n(t) U_n(x) \quad (2.13)$$

in which $c_n(t)$ is the solution to

$$\ddot{c}_n(t) + \omega_n^2 c_n(t) = N_n(t) \quad (2.14)$$

and $N_n(t)$ is the modal force described by

$$N_n(t) = \int_0^L p(x, t) U_n(x) dx \quad (2.15)$$

The fundamental principles and conclusions of the modal analysis technique described here are directly applicable to more complex structures including three-dimensional structures such as the plates and airfoils that are the focus of this research [58] and [59]. This expansion to more complex structures requires applying the equilibrium equations to the geometry of the structure under consideration, applying the appropriate boundary conditions, and solving the equations in three dimensions instead of two. For all but the simplest of geometries, these equations cannot be practically solved analytically, in which case numerical methods must be used. One of the most powerful and popular numerical approaches for solving complex vibration problems is the finite element method (FEM), which will be explored in greater detail in Chapter 5. An additional variable that was not considered in this simplified example is material damping. Material damping during structural vibration is generally attributable to hysteretic damping, but modeling this phenomenon as velocity-dependent viscous damping is generally considered to be a good representation of reality [58, 59]. Damping can be modeled in various ways, but mass-proportional and stiffness-proportional viscous damping is the most common, in which the damping operator is taken to be a linear combination of the mass and stiffness operators with two scalar coefficients that describe the mass and stiffness dependencies of the damping in the model [58, 59]. Damping will become especially important in terms of the piezoelectric actuators, because their damping properties will dramatically affect the efficiency by which they can convert electrical energy into mechanical energy at resonance.

The key point to take away from this review, in the context of the de-icing work presented herein, is that the structural response is a superposition of the natural modes of the structure, with each natural mode having a greater or lesser influence on the overall vibration depending on its compatibility with the loading function; see equations (2.15). These concepts will be important when discussing the concept of actuator phasing and its influence on the electromechanical impedance of the system as a function of frequency and the induced vibration field. It is also critical to recognize the fact that altering the loading distribution, which will be achieved through actuator phasing within the de-icing system, will also alter the forced vibration state and the frequency response of the structure.

Chapter 3

ACTUATOR DESIGN

Actuator design, which includes the transduction mechanism, actuator geometry, actuator poling, size, fabrication, and configuration on the structure, is critical to developing an efficient and effective ultrasonic de-icing system. The actuator design also plays a large role, in conjunction with the design of the system electronics, in determining the efficiency of the system. There exists a great range of options available for an engineer developing such a system, but past research, a general understanding of various transduction mechanisms, and an understanding of transducer theory can substantially narrow the range of choices.

3.1 Transduction Mechanisms – Piezoelectric versus Magnetostrictive

The basic premise of a de-icing system is to convert electrical energy to mechanical energy in order to remove ice from a structure. This conversion, or transduction, can be achieved via several mechanisms. The most common transducers for high-power applications, such as ultrasonic cleaning and welding, are piezoelectric and magnetostrictive transducers. Piezoelectric and magnetostrictive materials are similar in that they deform in the presence of electric and magnetic fields, respectively. Coupling such materials to a host structure transmits the generated strain from the transducer material into the host structure.

Transducers that rely on either one of these principles may have significant benefits and disadvantages over the other depending on the specific application in which they are intended to be used, so the system designer must examine the details of each to identify the best candidate for the application at hand. Piezoelectric materials stand out as a preferred candidate for ultrasonic de-icing due to the fact that they do not rely on large external magnets or magnetic coils to generate large strain values as high-power magnetostrictive transducers do. Such magnets would be impractical for de-icing applications due to the added weight and bulk.

Piezoelectric transducers have another advantage over magnetostrictive transducers in terms of efficiency. While piezoelectric materials directly convert electrical energy into mechanical energy, magnetostrictive materials must convert electrical energy into magnetic energy before converting magnetic energy into mechanical energy. This double energy conversion can produce

more inefficiency in the system in the form of heat loss. For high-power ultrasonic cleaning applications, for example, piezoelectric systems generally provide an efficiency of up to 70%, while similar magnetostrictive systems only deliver efficiency in the range of 35-40% [60]. In addition to superior energy conversion efficiency, piezoelectric actuators often provide greater efficiency in terms of output energy per unit mass, sometimes as high as ten to twenty times greater than similar magnetostrictive actuators [61]. Additionally, the most efficient magnetostrictive materials, such Terfenol-D are also much less readily available than comparable piezoelectric materials such as PZT [62].

In fact, Palacios et al. [15, 27, 28, 63] have shown that ultrasonic de-icing can be successfully performed using piezoelectric actuators with system efficiency exceeding that of other electromechanical de-icing technologies. Based on past research and the advantages discussed herein, it was determined that piezoelectric actuators are the best transduction choice in light of current materials and technology.

Piezoelectric Materials

Piezoelectric materials can come in many forms, including piezoelectric ceramics (such as PZT), piezoelectric polymers (such as PVDF), and natural piezoelectric crystals (such as quartz). Piezoelectric ceramics, which are made from metal oxides, are the most commonly utilized piezoelectric materials due to their much greater sensitivity than most other materials and the fact that the powder metal oxide sintering process allows for an almost unlimited freedom in element design [64].

Piezoelectric ceramics are generally of the Perovskite class of crystals which are comprised of a rectangular close-packed lattice of divalent metal ions such as Pb^{2+} or Ba^{2+} with smaller anions, such as O^{2-} in the octahedral interstices, and a tetravalent metal ion, such as Ti^{4+} or Zr^{4+} [64, 65]. A generalized Perovskite crystal is illustrated in Figure 17.

Note in Figure 17 that when a piezoelectric crystal exists at temperatures above its Curie point, it is cubically symmetric and thus there is no net charge polarization, but when the crystal is at a temperature below its Curie point, a tetragonal symmetry is assumed that yields a net polarization. The Curie point for most piezoelectric ceramics is between 150 and 400°C, so that at normal environmental temperatures, piezoelectric ceramic crystals exhibit a net polarization in

one direction. In an unpoled piezoelectric ceramic, these domains are randomly aligned, and thus no net polarization of the material exists [61]; see Figure 18.

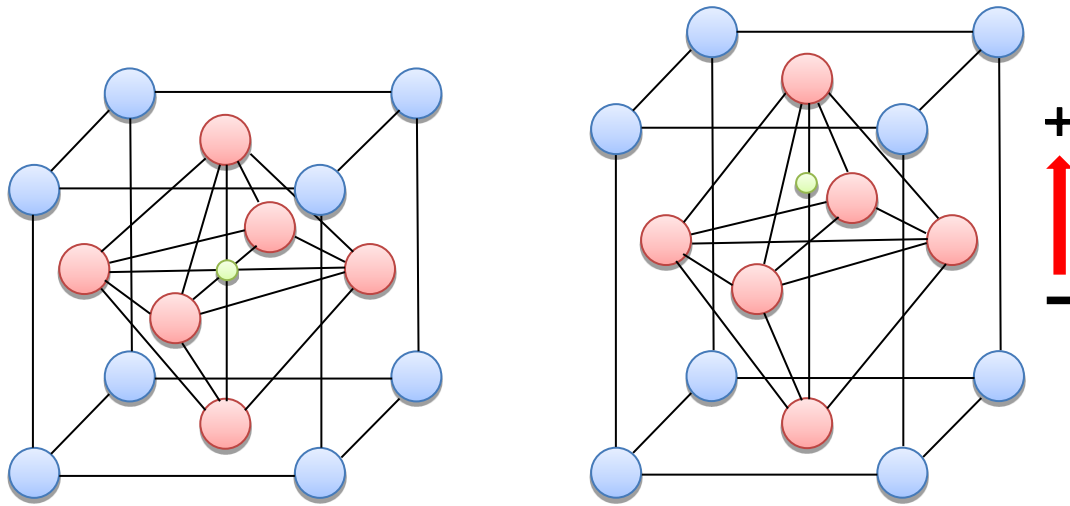


Figure 17 (Left) Piezoelectric crystal ceramic above the Curie temperature and (right) below the Curie temperature; the blue spheres represent large divalent metals, the red spheres represent the smaller anions, and the green spheres represent the small tetravalent metals. The arrow indicates the direction of polarization that occurs in the state below the Curie temperatures.

The typical manufacturing process for piezoelectric ceramics is [64]:

1. The constituent metal oxides, in powder form, are mixed and heated to yield a uniform powder.
2. The powder is mixed with a binder and pressed or molded into the desired shape, which can later be diced.
3. These “green” powder parts are sintered according to a specific heating schedule to solidify the crystal structure of the material.
4. Electrodes are applied to the crystallized ceramic with conductive paint, sputtered silver, or other methods and materials.
5. The material is poled with a large DC voltage to align the polarized domains within the material, usually near the Curie temperature; see Figure 18.

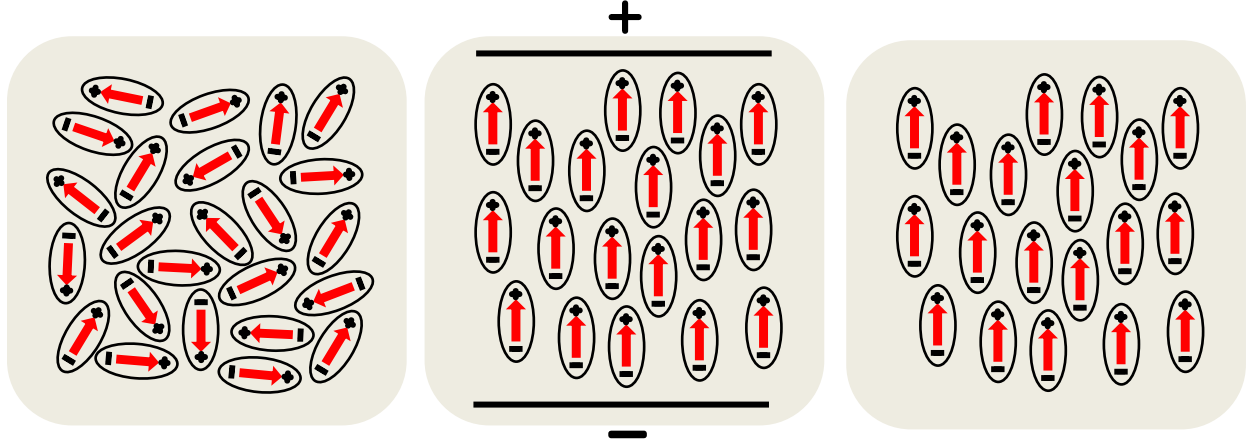


Figure 18 (Left) Unpoled piezoelectric ceramic with randomly aligned domains, (center) polarization of the ceramic under large DC voltage near Curie temperature, and (right) residual polarization after the DC current is removed and the ceramic returns to cooler temperatures.

The polarization of the actuator also determines its modes of vibration, resonant frequencies, and efficiency. Several actuator polarization and geometric configurations are illustrated in Figure 19. Each of these actuator geometries and poling configurations relies primarily on a single component of the piezoelectric coupling coefficient tensor d [64, 65]. These dominant piezoelectric coupling coefficients are indicated next to each actuator configuration, respectively, in Figure 19.

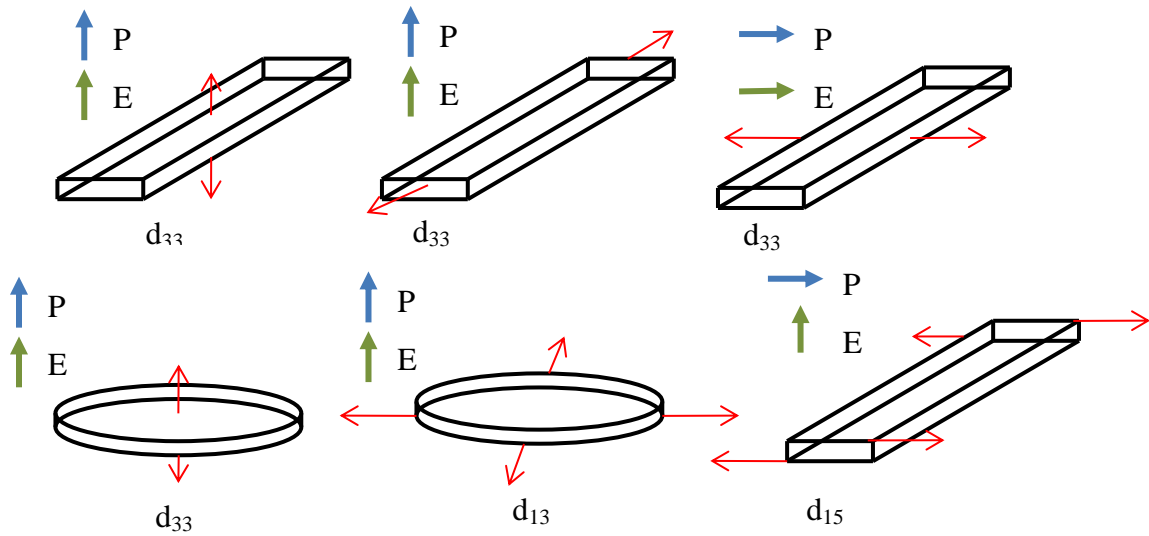


Figure 19 Various piezoelectric actuator geometries, poling configurations, and actuation configurations, as well as the piezoelectric coupling coefficient that each mode of operation depends on.

The electric displacement D , material polarization vector P , and electric field E are related in terms of the dielectric permittivity of a vacuum ϵ_0 by

$$D_i = \epsilon_0 E_i + P_i \quad (4.1)$$

Palacios [1] and Zhu [24] showed that, theoretically, d_{15} type shear actuators are expected to perform more efficiently than d_{13} or d_{33} type actuators for ultrasonic de-icing purposes, but that experimentally this could not be realized due to complications with such shear elements. These complications included difficult fabrication processes for large shear bars, insufficient durability, and high impedance values that could not be effectively matched to the 50Ω amplification electronics. Based on these results and others [27, 28, 63], it was determined that piezoelectric disk actuators operated in the radial d_{13} mode performed best for ultrasonic de-icing.

3.2 Disk Actuator Axial Resonances

Piezoelectric actuators operate as electromechanical resonators, meaning that the electrical properties, mechanical properties, and geometry are all intertwined to dictate the resonate behavior of the actuator. This coupling of the electrical and mechanical resonant characteristics of a piezoelectric actuator occurs through the tensorial piezoelectric constitutive equations [65]

$$S_{ij} = s_{ijkl}^E T_{kl} + d_{kij} E_k, \quad (4.2)$$

$$D_{ij} = d_{jkl} T_{kl} + \epsilon_{jk}^T E_k \quad (4.3)$$

in which S and T are the mechanical strain and stress, D and E are the electrical displacement and field, s is the material elasticity tensor (at zero electric field), ϵ is the material dielectric permittivity (at zero stress), and d is the piezoelectric coupling coefficient. We can analyze the resonant behavior of such a material by applying these equations to the specific case of a thin disk with uncoupled thickness and radial resonances, poled and excited through the thickness.

Piezoelectric Disk Actuator Axial Resonances

The second geometry we will analyze is that of a free axisymmetric disk actuator poled through its thickness, such as that shown in Figure 20, in which h is the actuator thickness, a is the

actuator radius, and E_3 is the magnitude of the applied electric field component in the poling direction. The thickness resonance of such a disk would be nearly identical to that described for the wafer element in the previous case. This derivation can be found with more detail in Giurgiutiu [62].

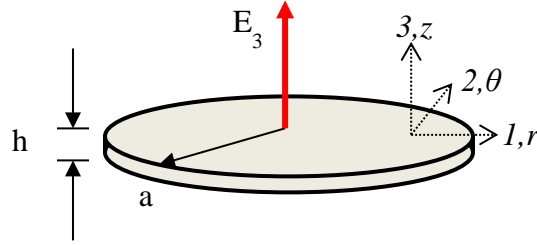


Figure 20 Illustration of a piezoelectric disk actuator.

The piezoelectric constitutive strain equation (3.1), can be simplified for the axisymmetric geometry as

$$S_{rr} = s_{11}^E T_{rr} + s_{12}^E T_{\theta\theta} + d_{31} E_3, \quad (4.4)$$

$$S_{\theta\theta} = s_{12}^E T_{rr} + s_{11}^E T_{\theta\theta} + d_{31} E_3, \quad (4.5)$$

which can be inverted to express stress in terms of strain as

$$T_{rr} = \frac{1}{s_{11}^E (1 - \nu^2)} [(S_{rr} + \nu S_{\theta\theta}) - (1 + \nu) d_{31} E_3] \quad (4.6)$$

$$T_{\theta\theta} = \frac{1}{s_{11}^E (1 - \nu^2)} [(\nu S_{rr} + S_{\theta\theta}) - (1 + \nu) d_{31} E_3], \quad (4.7)$$

in which ν is Poisson's ratio. The strain-displacement equations

$$S_{rr} = \frac{du_r}{dr}, \quad (4.8)$$

$$S_{\theta\theta} = \frac{u_r}{r}, \quad (4.9)$$

in which u denotes displacement, may be substituted into the stress-strain equations to yield the stress-displacement equations

$$T_{rr} = \frac{1}{s_{11}^E(1-\nu^2)} \left[\left(\frac{du_r}{dr} + \nu \frac{u_r}{r} \right) - (1+\nu)d_{31}E_3 \right], \quad (4.10)$$

$$T_{\theta\theta} = \frac{1}{s_{11}^E(1-\nu^2)} \left[\left(\nu \frac{du_r}{dr} + \frac{u_r}{r} \right) - (1+\nu)d_{31}E_3 \right]. \quad (4.11)$$

The dynamic equilibrium equation can be expressed as

$$\frac{dT_{rr}}{dr} + \frac{T_{rr} - T_{\theta\theta}}{r} = -\omega^2 \rho u_r, \quad (4.12)$$

in which ω is the angular frequency of vibration and ρ is the material mass density. Substituting equations (3.9) and (3.10) into (3.11) yields

$$\frac{1}{s_{11}^E(1-\nu^2)} \left[\frac{d^2 u_r}{dr^2} + \frac{1}{r} \frac{du_r}{dr} - \frac{u_r}{r^2} \right] = -\omega^2 \rho u_r. \quad (4.13)$$

Rearranging the terms in (3.12) and introducing the wave speed and wavenumber parameters

$$c = \sqrt{\frac{1}{\rho s_{11}^E(1-\nu^2)}}, \quad (4.14)$$

$$\gamma = \sqrt{\frac{\omega}{c}}, \quad (4.15)$$

the equilibrium equation becomes

$$r^2 \frac{d^2 u_r}{dr^2} + r \frac{du_r}{dr} + (r^2 \gamma^2 - 1) u_r = 0, \quad (4.16)$$

which has first-order Bessel function solutions

$$u_r = A \cdot J_1(\gamma r). \quad (4.17)$$

Applying the traction-free boundary conditions on the radius of the free actuator yields a displacement solution in terms of radius in the form of

$$u_r(r) = d_{31}E_3a \frac{(1+\nu)J_1(\gamma r)}{\gamma a J_0(\gamma a) - (1-\nu)J_1(\gamma a)} \quad (4.18)$$

The electric displacement equation (3.2) for the axisymmetric case is

$$D_3 = d_{31}(T_{rr} + T_{\theta\theta}) + \varepsilon_{33}^T E_3, \quad (4.19)$$

Applying the known stress-displacement equations (3.9) and (3.10) yields

$$D_3 = \varepsilon_{33}^T E_3 \left[(1 - k_p^2) + k_p^2 \left(\frac{1}{2d_{31}E_3} \frac{1}{r} \frac{d}{dr} (ru_r) \right) \right], \quad (4.20)$$

in which

$$k_p^2 = \frac{2}{(1-\nu)} \frac{d_{31}^2}{s_{11}^E \varepsilon_{33}^T} \quad (4.21)$$

is the electromechanical coupling coefficient. Integrating over the actuator area to calculate the charge

$$Q = 2\pi \int_0^a D_3 r \, dr = CV \left[(1 - k_p^2) + \frac{k_p^2}{d_{31}E_3a} u_r(a) \right], \quad (4.22)$$

and using the substitutions

$$C = \varepsilon_{33}^T \frac{\pi a^2}{h}, \quad (4.23)$$

$$V = \frac{E_3}{h}, \quad (4.24)$$

in which C is the capacitance and V is the potential difference between the two faces, yields the admittance and impedance equations

$$Y = \frac{I}{V} = \frac{i\omega Q}{V} = i\omega C \left[(1 - k_p^2) + k_p^2 \frac{(1+\nu) \cdot J_1(\gamma r)}{\gamma a \cdot J_0(\gamma a) - (1-\nu) \cdot J_1(\gamma a)} \right], \quad (4.25)$$

$$Z = \frac{1}{Y} = \frac{1}{i\omega C} \left[(1 - k_p^2) + k_p^2 \frac{(1 + \nu) \cdot J_1(\gamma r)}{\gamma a \cdot J_0(\gamma a) - (1 - \nu) \cdot J_1(\gamma a)} \right]^{-1}. \quad (4.26)$$

The electromechanical impedance Z describes the ratio of the applied voltage to the current generated in the system. As the impedance approaches 0, the induced current approaches ∞ , which represents an electromechanical state of resonance. Since the piezoelectric material converts this large electrical energy into large mechanical energy, this resonance state corresponds to a highly-efficient mechanical response of the actuator to a small electrical input. Note that these resonant frequencies depend on the geometric properties of the actuator (thickness, radius, and shape) as well as the piezoelectric material properties. Thus the efficiency of the actuators, as well as the stress configuration that they apply to a structure, are heavily dependent on the shape of the actuator.

3.3 Actuator Configuration

Once an actuator design is selected, the location of the actuators on the host structure will also play a very significant role in the electromechanical efficiency of the system. Recall that the electromechanical impedance equations for d_{13} disk actuators derived in equation (3.25) was for a free disk. Once such an actuator is coupled to a host structure, it is no longer free, but is rather constrained by the host structure itself. The degree to which the host structure constrains the actuator depends on the vibration characteristics of the host structure, and this relationship can be calculated by taking the general solution (3.16) and considering the case of time-varying harmonic vibration, in which the solution becomes

$$u_r(r, t) = A \cdot J_1(\gamma r) e^{i\omega t}. \quad (4.27)$$

The boundary conditions for a radially-constrained actuator, as shown in Figure 21, which represents a disk actuator bonded to a host structure and vibrating in a radial mode, can be expressed as

$$T_{rr}(a) = \frac{1}{h} k_{str}(\omega) u_r(a), \quad (4.28)$$

in which $k_{str}(\omega)$ represents the frequency-dependent stiffness of the radial constraints of the host structure, as shown in Figure 21, in which the structural stiffness is represented by radial springs.

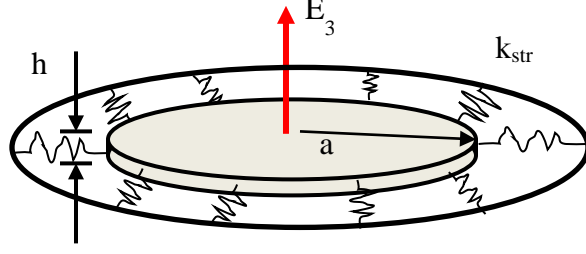


Figure 21 Illustration of a radially-constrained disk actuator operating in the radial mode, in which the constraint stiffness of the boundary, k_{str} , is frequency-dependent.

Applying the boundary conditions (3.27) to the impedance equation (3.25) yields, after some manipulation [65],

$$Z = \frac{1}{i\omega C(1 - k_p^2)} \left[1 + \frac{k_p^2}{1 - k_p^2} \frac{(1 + \nu)J_1(\gamma r)}{\gamma a J_0(\gamma a) - (1 - \nu)J_1(\gamma a) - \frac{k_{str}(\omega)}{k_{PZT}}(1 + \nu)J_1(\gamma a)} \right]^{-1}, \quad (4.29)$$

in which

$$k_{PZT} = \frac{h}{as_{11}^E(1 - \nu)} \quad (4.30)$$

describes the static stiffness of the piezoelectric disk. Since k_{str} is the frequency-dependent stiffness of the host structure at a particular point, it can also be defined as

$$k_{str} = \frac{F_{PZT}(a)}{u_{PZT}(a)}, \quad (4.31)$$

in which $F_{PZT}(a)$ is the force applied by the actuator at its radius and $u_{PZT}(a)$ is the displacement generated by the actuator at its radius, considering the stiffness of the constraints. This is the inverse of the definition of the vibration frequency response function (FRF) of the structure at the points along the radius of the actuator. Therefore the structural constraint stiffness felt by the actuator when it is coupled to a structure is directly dependent on the vibrational resonances and mode shapes of the structure. Therefore the boundary conditions associated with the radial constraints are frequency dependent; this is the source of the “frequency-dependent” stiffness experienced by the actuator. Therefore, placing the actuators in a location in which their radial

mode of vibration is especially compatible with a particular mode shape will beneficially alter the resonant characteristics of the actuators.

Unfortunately, the vibration characteristics of an iced structure will vary dramatically (in the ultrasonic regime) with small perturbations in material properties, shape, and thickness of accreted ice. Additionally, the mode shapes at ultrasonic frequencies have a small scale structure and thus there is little room for error in terms of locating the actuators at an “optimal” position based on this premise. Therefore even if a set of piezoelectric actuators could be optimally configured to resonate with a particular structural vibration mode, the assumptions under which that optimization was developed would almost never be valid as the structure, and thus its resonant characteristics, constantly change during real ice accretion. It will be shown in Chapter 5 that some more generalized configuration modeling can be performed using finite element methods for a particular structure.

3.4 Actuator Wiring and Bonding Methods

While past research has shown that piezoelectric disk actuators operated in the d_{13} radial mode provide the best performance for ultrasonic de-icing, the details of fabricating and integrating such actuators into a structure has been lacking. The method of actuator wiring and bonding employed during early research was to solder wires directly to the electrodes of the actuator and bond the actuators to the host structure using various forms of two-part epoxy. Palacios [1] and Overmeyer [63, 66] discuss the issues of actuator debonding and fracture, shown in Figure 22, that plagued early efforts using these wiring and bonding methods.

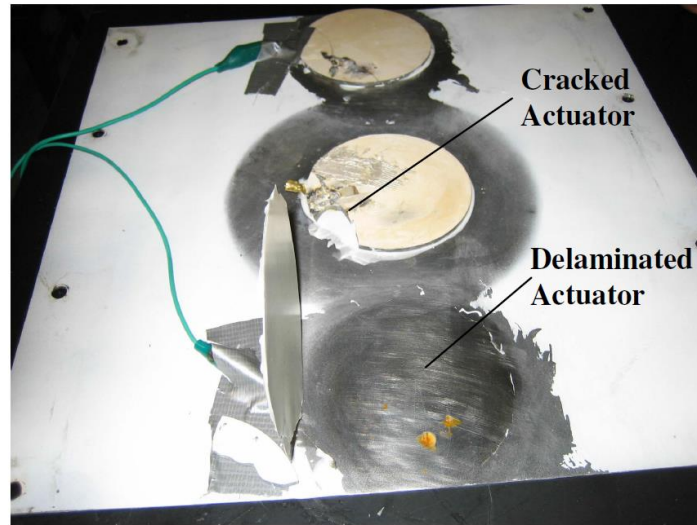
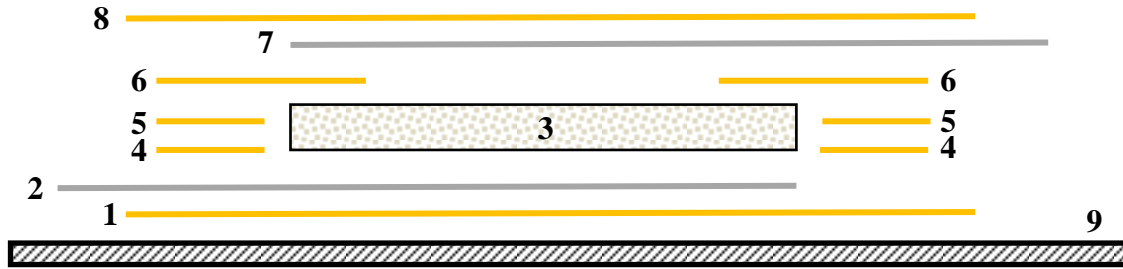


**Figure 22 Photograph of fractured and debonded piezoelectric actuators after an ultrasonic de-icing test
(Source: Palacios [15]).**

To address these problems, Overmeyer [63, 66] developed an improved method, detailed in Figure 23, of wiring and bonding actuators using aluminum mesh and film epoxy. In this method, a series of Cytec FM-73 film epoxy layers were utilized to insulate and bond the actuator and two aluminum mesh tabs were used to wire the electrodes on the surfaces of the disk.



- 1 – Bottom film epoxy layer bonds actuator to the substrate (9) and connects bottom mesh electrode (2) to PZT (3).
- 2 – Bottom aluminum mesh electrode.
- 3 – PZT actuator.
- 4 - Filler epoxy ring 1 helps insulate the top (7) and bottom (2) electrodes and prevent gaps.
- 5 – Filler epoxy ring 2 helps insulate the top (7) and bottom (2) electrodes and prevent gaps.
- 6 – Insulating epoxy ring prevents top electrode (7) from folding over edges of PZT (3).
- 7 – Top aluminum mesh electrode.
- 8 – Top film epoxy layer connects top mesh electrode (7) to the PZT (3) and insulates the actuator.

Figure 23 Actuator wiring and bonding method developed by Overmeyer.

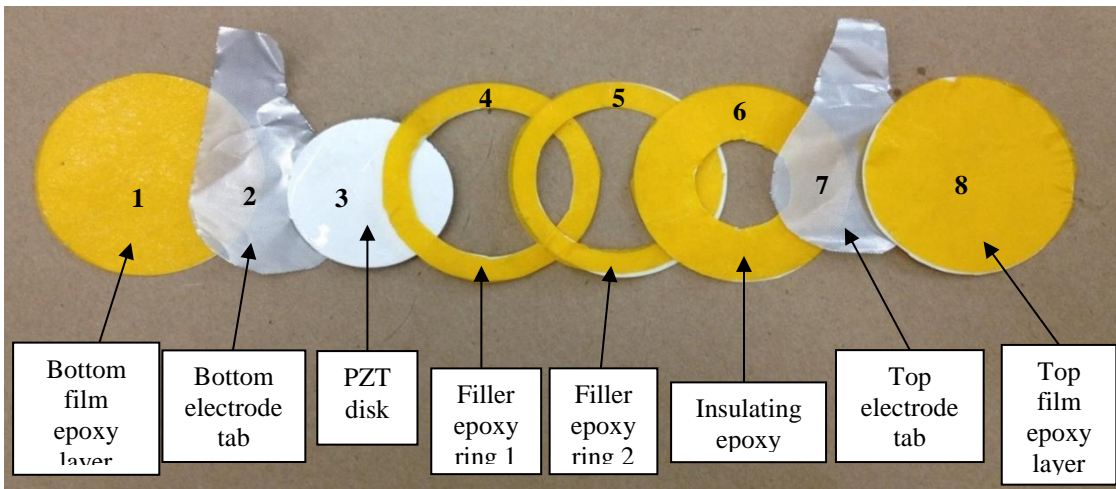


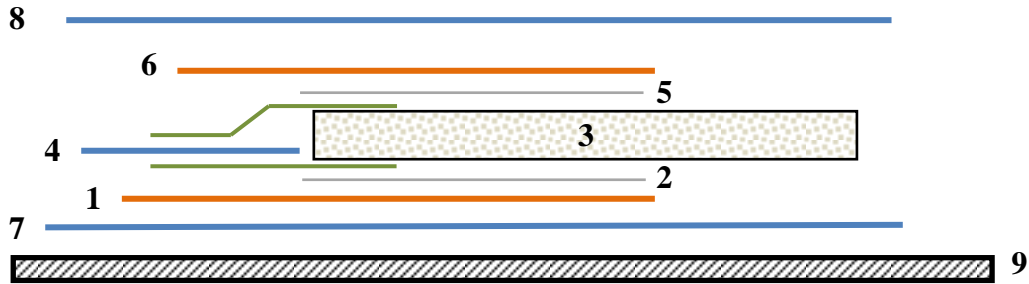
Figure 24 Layout of materials used to wire and bond a single actuator using the method developed by Overmeyer.

This method did provide some improvements in actuator bonding. In particular, the film epoxy proved to be much more consistent and reliable in bonding the actuators to various structures and effectively addressed the problem of actuator de-bonding during intense actuation. Additionally, the use of aluminum mesh tabs to connect wires to the silver electrode faces of the actuator

eliminated the stress concentrations caused by solder connections, which would often lead to actuator cracking and failure under large deformations.

However, in addition to these benefits, this method has some drawbacks. One problem associated with this method is the sheer amount of epoxy that encases the actuator, which in turn restrains the actuator during operation; this manifests itself as a significant increase in the minimum impedance of the bonded actuator. Additionally, the connection between the aluminum mesh electrode tabs and the silver electrodes of the PZT were inconsistent and often failed altogether. For instance, in bonding 12 actuators to one specimen using this method, 5 out of 12 of the actuators had failed electrical connections in which either the electrodes were shorted to one another or one electrode failed to make electrical contact with the silver electrode of the actuator. Due to the nature of the film epoxy, if such a failure occurs, the entire disk must be scrapped, which sometimes involves the need to remove the bonded actuator from the structure, potentially damaging the structure. Finally, this method requires three cures to complete: one to bond the disk and layers 1 and 2, a second to bond layers 3-5, and a third to bond layers 6 and 7. This adds up to a substantial amount of time and work to fabricate a specimen and leads to more opportunities for error.

Therefore an effort was made to develop an improved actuator wiring and bonding method that built upon the contributions of Overmeyer. The new method retains the bottom layer of film epoxy because it provides strong, well-controlled, and consistent bonding to the substrate. The concept of distributed electrodes was also retained in order to avoid stress concentrations that occur with soldering, but the aluminum mesh was replaced with copper foil tabs. These tabs are bonded to the actuator using a low-viscosity two-part epoxy (Epo-Tek 301-2). This epoxy provides sufficient bond strength and although it is non-conductive, when bonded properly the bond line is sufficiently thin to create excellent electrical conductivity through small porosities in the bondline. This method of electrode bonding is employed in the commercial manufacturing of some types of piezoelectric transducers. The two copper tabs are applied simultaneously and are oriented in the same direction, which is not done in Overmeyer's method, but which simplifies wiring. The filler and insulating rings of epoxy are removed and a single piece of Mylar film is used to insulate the two electrodes from one another. A top piece of film epoxy is also applied to insulate the entire disk. This method is diagramed in Figure 25.



- 1 – Bottom copper foil tab.
- 2 – Thin Epo-Tek epoxy layer bonds the bottom copper tab (1) to the PZT (3).
- 3 – PZT actuator.
- 4 – Mylar film and film epoxy tabs insulates between the bottom (1) and top (6) copper tabs.
- 5 – Thin Epo-Tek epoxy layer bonds the top copper tab (1) to the PZT (3).
- 6 – Top copper foil tab.
- 7 – Bottom film epoxy layer bonds actuator to the substrate (9).
- 8 – Top film epoxy layer insulates the actuator.
- 9 – Substrate to which the actuator is bonded.

Figure 25 Diagram of the improved actuator bonding method.

The impedance plots in Figure 26 compare the impedance curves for two disk actuators before and after bonding them to a composite specimen with Overmeyer's bonding method and the improved bonding method. Note that the reduction in epoxy reduces the degree to which the actuator is damped. Higher impedance translates into decreased efficiency and makes it increasingly difficult to match the electromechanical impedance of the actuators to the electrical impedance of the amplifiers. Figure 27 and Figure 28 compare actuators bonded with the old method and the improved method.

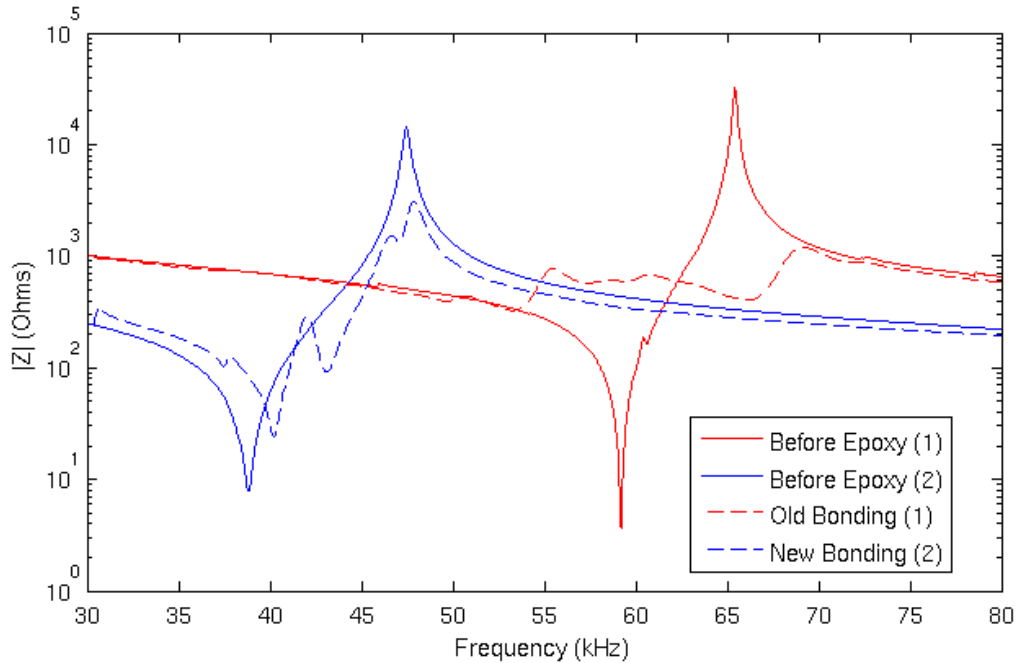


Figure 26 Comparison of the shifts caused by previous and new bonding method; note that the differences in the initial curves are due to the fact that two different size discs were compared here, but that does not significantly influence the effect of the bonding.

At the time of writing, more than 85 actuators have been bonded to titanium, aluminum, and carbon fiber plate and airfoil specimens using this method with only six instances of failed wiring connections during the bonding process, four of which were in a single batch and thus were likely due to improper mixing of the Epo-Tek 301-2 epoxy. Additionally, no actuators have debonded or fractured during ultrasonic de-icing tests using this method at the time of writing. These observations support the conclusion that the described method of actuator fabrication is more reliable than previous methods, but further controlled evaluations would be required to fully quantify this effect. However, as the improved method is simpler, neater, and appears to be more reliable, it was adopted throughout the remainder of this work.

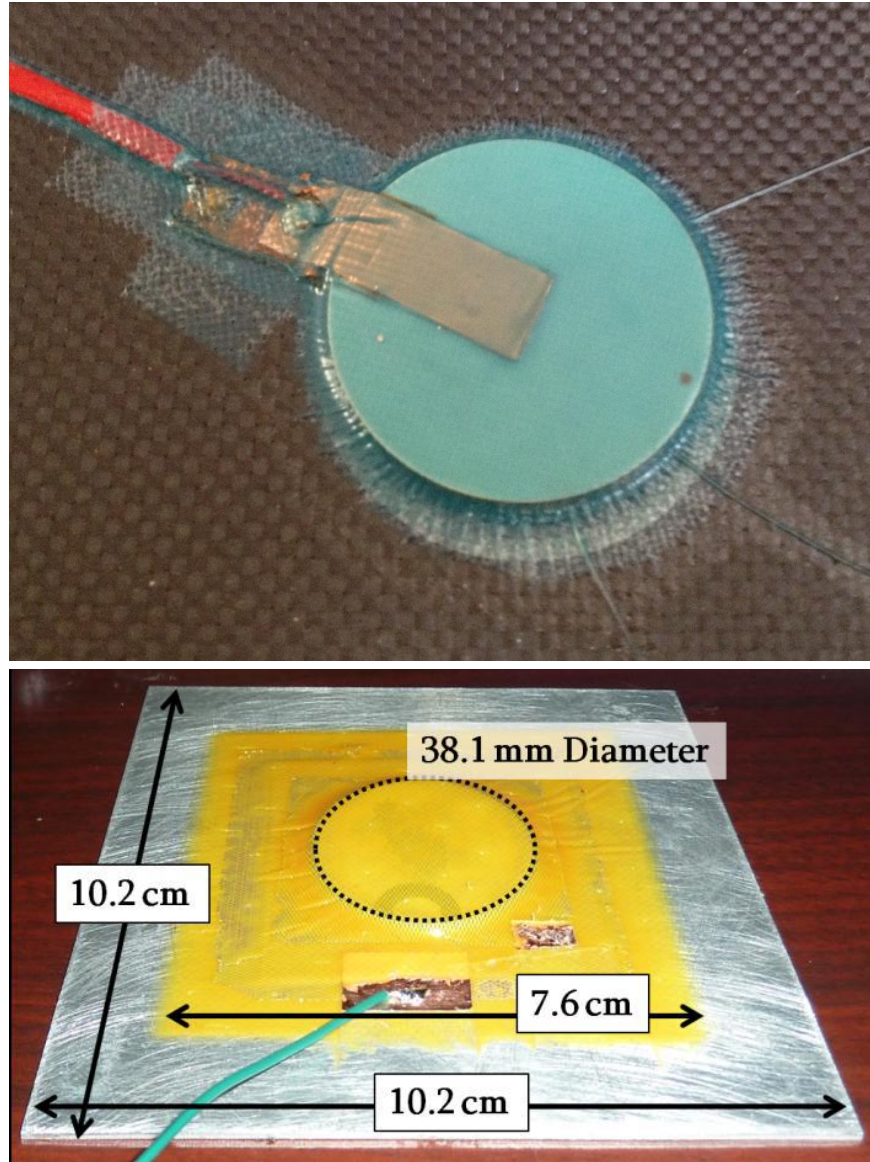


Figure 27 Comparison of a single actuator wired and bonded using the improved method (top) and a single actuator wired and bonded with the method developed by Overmeyer (bottom); bottom image from (Source: Overmeyer [66]).

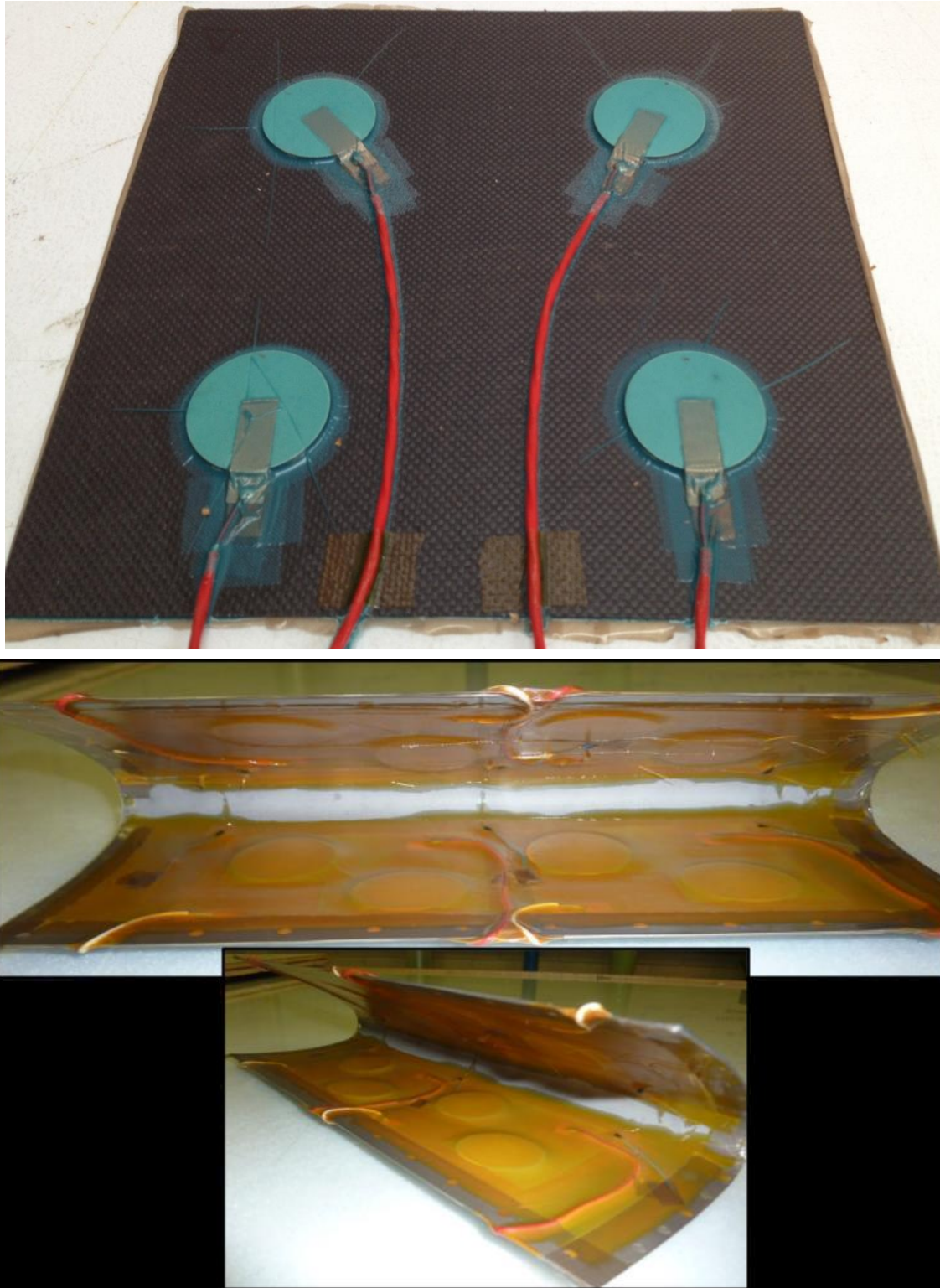


Figure 28 Comparison of multiple actuators wired and bonded using the improved method (top) and actuators wired and bonded with the method developed by Overmeyer (bottom); bottom image from (Source: Overmeyer [66]).

3.5 Integrating Actuators into Composite Sandwich Panel Structures

While certain aircraft surfaces are composed of a single layer of material, such as an aluminum or titanium wing leading edge, many modern aircraft are constructed using more advanced composite layups. One composite fabrication method uses a carbon fiber and Nomex honeycomb sandwich construction for certain structures such as wing leading edges and engine inlets that may experience in-flight icing. An example of this type of structure is shown in Figure 29. Incorporating ultrasonic de-icing actuators into such sandwich panel constructions is a new challenge for the ultrasonic de-icing system. In fact, no work has been reported on ultrasonic de-icing of composite leading edges prior to this research.

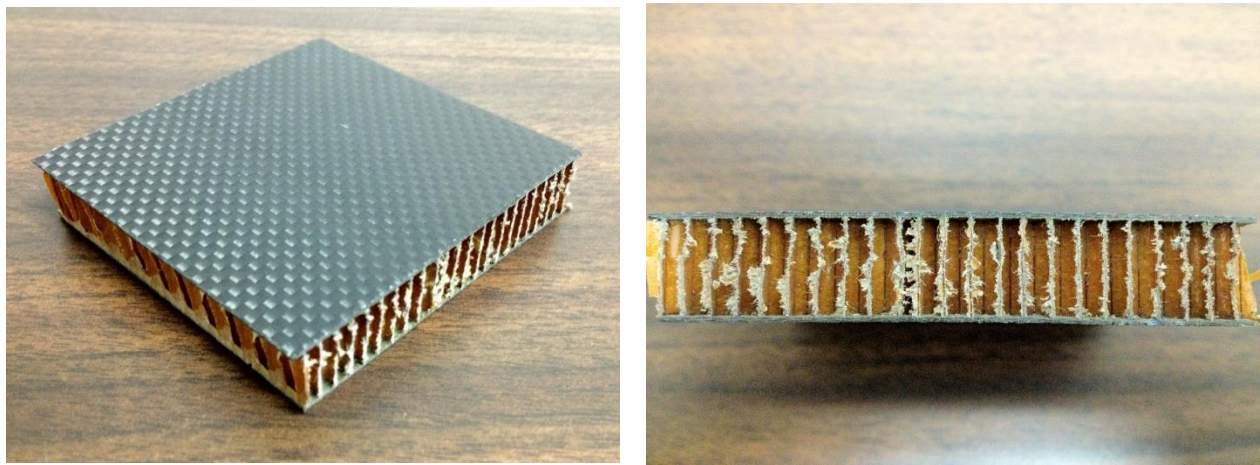


Figure 29 A carbon fiber and Nomex honeycomb sandwich panel structure.

In order to de-ice one carbon fiber surface, the de-icing actuators must be bonded directly to the reverse side of that panel, since the ultrasonic energy is very poorly transmitted through the honeycomb structure. A method was developed to incorporate the actuators and wiring into the sandwich panel during fabrication. The process is detailed below:

1. Actuators and copper tabs are prepared and bonded together using Epo-Tek 301-2 two-part epoxy under pressure from a rat trap. This pressure guarantees that a consistent thin bond line will be achieved that allows for electrical conductivity between the copper tab and the silver electrode of the actuator (Figure 30).

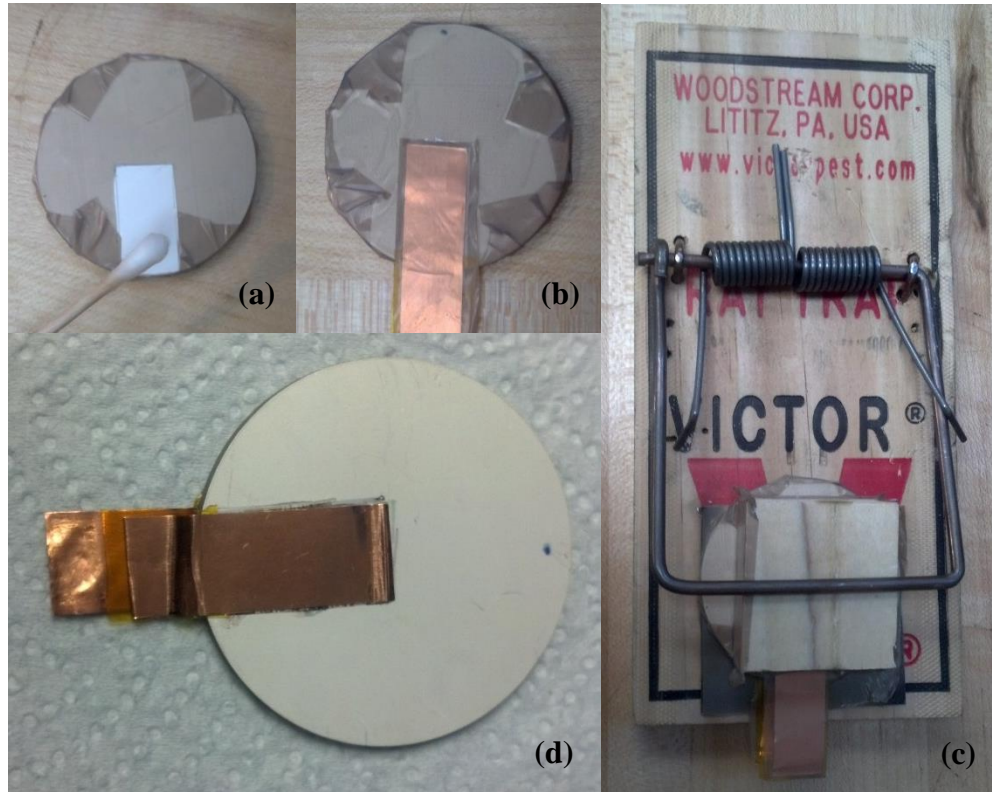


Figure 30 Bonding the copper tabs to the electrodes (a) and (b), curing the tabs under pressure in a rat trap (c), and an actuator with attached electrode tabs (d).

2. The actuators are then wired using shielded twisted pair cabling and are prepared for bonding with Cytec FM-94 film epoxy on the inner surface of the exterior carbon fiber panel (the panel exposed to icing conditions) (Figure 31).

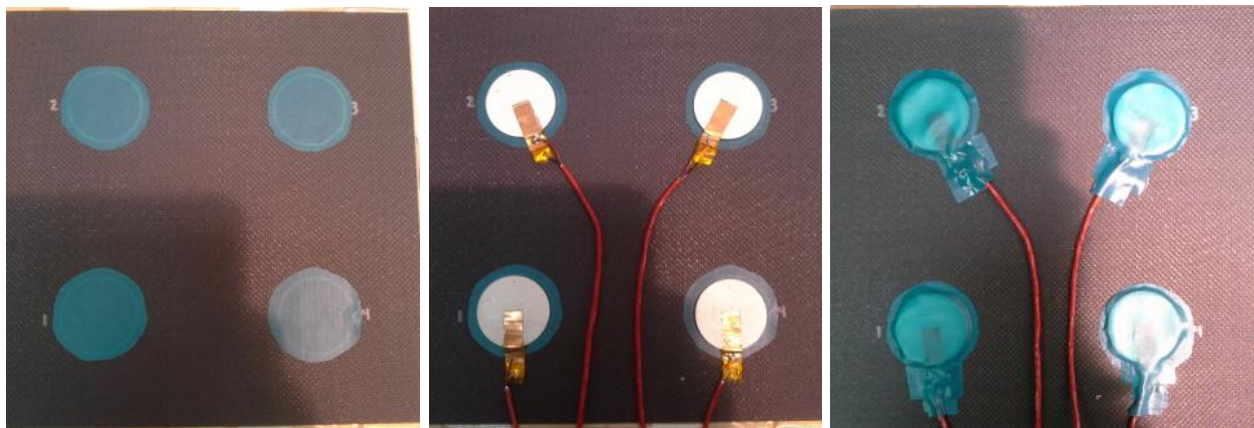


Figure 31 Laying up the actuators for bonding to the exterior carbon fiber panel.

3. The panel and actuators are then vacuum bagged and cured according to the film epoxy manufacturer's recommendations (Figure 32).

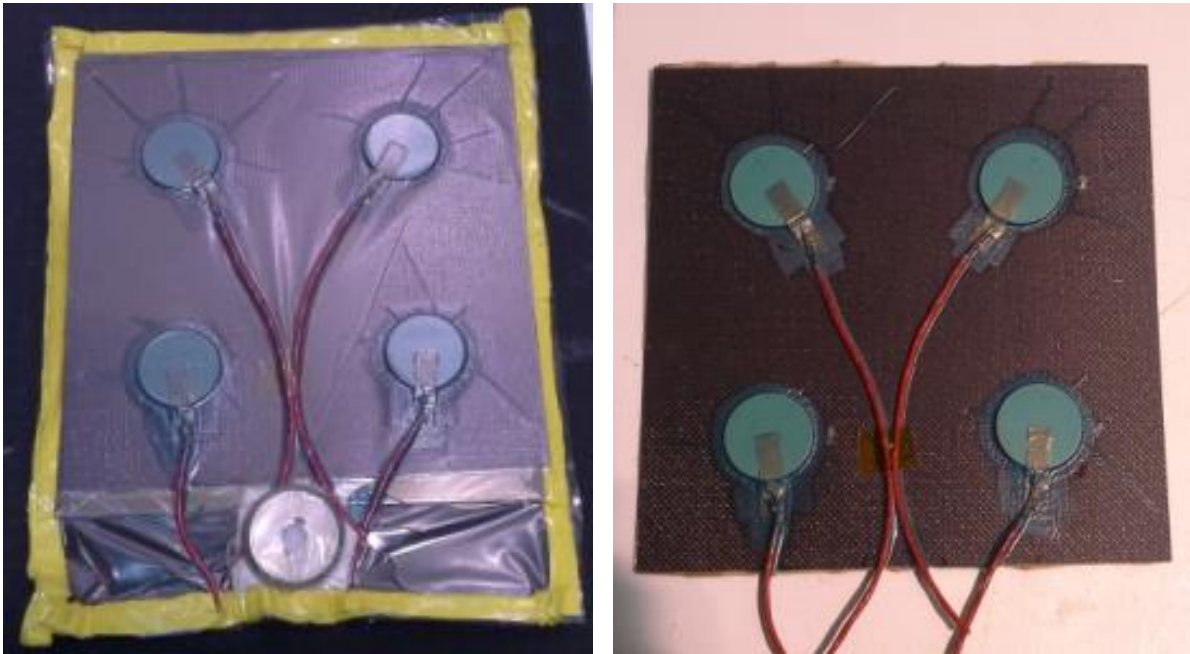


Figure 32 Vacuum bagged and cured carbon fiber panel with four actuators.

4. The actuator and wire pattern is then transferred to a transparent sheet, which is then used to reverse and transfer the pattern to a piece of Nomex honeycomb (Figure 33).

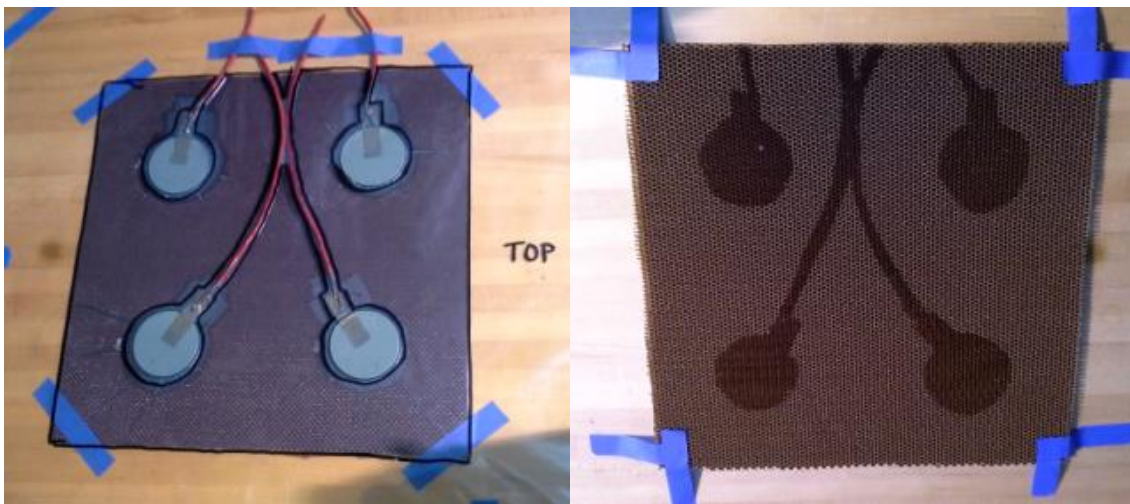


Figure 33 Transferring the pattern from to a transparent sheet and then to reverse the pattern and transfer it to a honeycomb panel.

5. The honeycomb material is then manually removed to accommodate the thickness of the actuators and wiring (Figure 34).



Figure 34 Removing honeycomb material to accommodate the thickness of the actuators and wiring.

6. Finally, a square sheet of film epoxy is placed between the actuators and the honeycomb as well as the honeycomb and the interior carbon fiber sheet. This layup is vacuum bagged and cured (Figure 35). Figure 36 shows an exploded view of a similar panel.

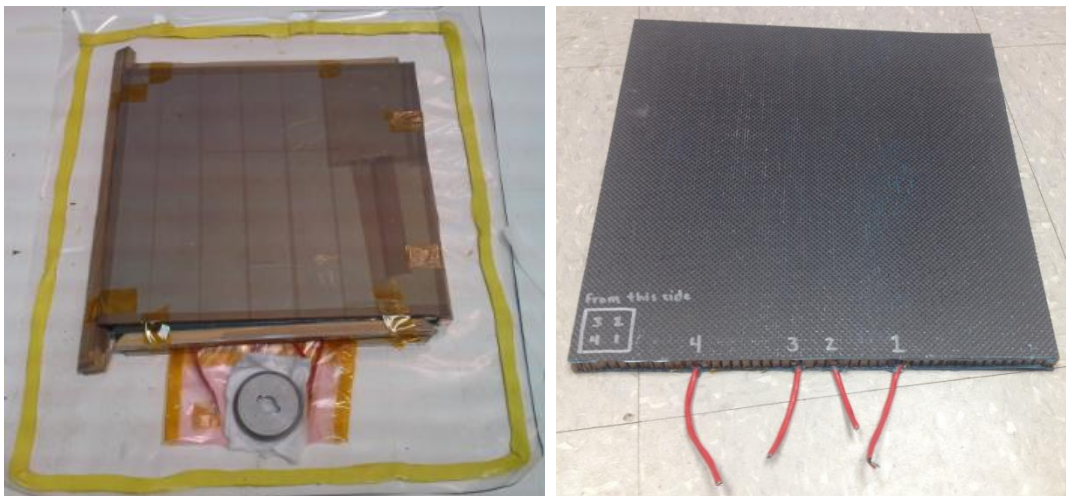


Figure 35 Vacuum bagged and completed sandwich panel with integrated actuators.

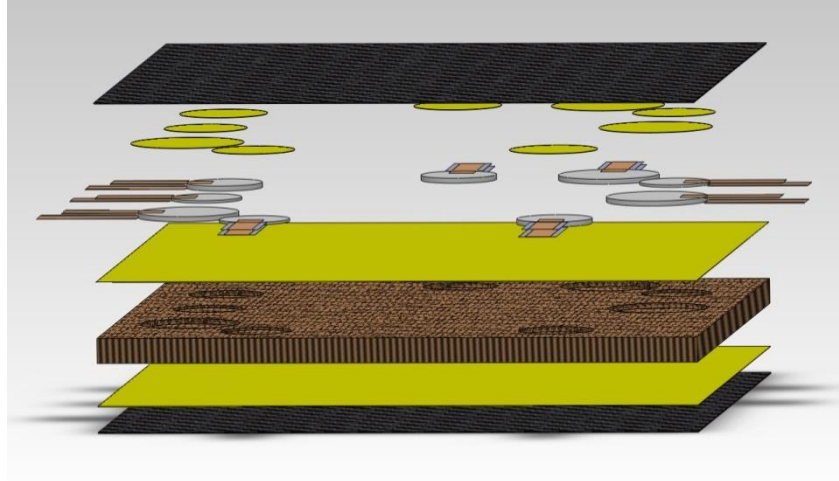


Figure 36 Exploded model of a carbon fiber sandwich panel with various imbedded actuators.

3.6 Summary

In this chapter, past research into ultrasonic de-icing actuator design was reviewed, including the selection of piezoelectric disk actuators operated in the radial d_{13} mode [15, 24, 27, 28, 63, 66]. The relationship between actuator geometry, polarization, and location with the electromechanical impedance of the bonded actuators was discussed, and an improved actuator wiring and bonding method was presented. The improved method removes much of the film epoxy utilized by the method introduced by Overmeyer [63, 66] and improves upon the reliability of the method by replacing the aluminum mesh electrodes with copper electrodes that are connected to the actuator with an ultra-thin layer of non-conductive epoxy. This method was also expanded to include a procedure for bonding ultrasonic de-icing actuators into carbon fiber and Nomex honeycomb sandwich panels for advanced composite aircraft structures.

Chapter 4

IMPEDANCE ANALYSIS

In the fields of mechanics, acoustics, and electrical engineering, “impedance” can be generally defined as a measure of resistance to some impetus that is applied to various physical parameters of systems undergoing some form of harmonic oscillation. Impedance analysis is important in the design of an ultrasonic de-icing system for the purposes of impedance matching for maximum power transfer and electromechanical resonance analysis for optimum frequency selection. In this chapter the definition of impedance, in its various forms, will be discussed, as will the manner in which impedance measurements are employed in the design and operation of the ultrasonic de-icing system.

4.1 Mechanical, Electrical, and Electromechanical Impedance

For the purposes of the work described here, impedance may take on several meanings. The first type of impedance is mechanical impedance, which is a complex value defined as [67, 68]

$$Z(\omega) = \frac{F(\omega)}{v(\omega)}, \quad (4.1)$$

in which F is an applied force, v is the velocity resulting from the applied force, and ω is the angular frequency at which the system is oscillating. Mechanical impedance is typically described at a single point on the structure, as the structural response varies on a point-by-point basis, although some measures of generalized mechanical impedance for certain structures have been introduced by Thomas [69]. Mechanical impedance is not a commonly-used measure of structural dynamics, although some work has been done in using it as a non-destructive inspection method in the Soviet Union and later in the western world [67, 68]. Mechanical impedance is closely related to the structural frequency response $H(\omega)$, which is very common in vibration analysis:

$$H(\omega) = \frac{u(\omega)}{F(\omega)} = \frac{1}{i\omega} \frac{1}{Z(\omega)}. \quad (4.2)$$

The second type of impedance is electrical impedance, which is a complex value defined as

$$Z(\omega) = \frac{V(\omega)}{I(\omega)}, \quad (4.3)$$

in which V is the voltage and I is the current measured between two points in a circuit. While mechanical impedance is rarely used in structural analysis, electrical impedance is an extremely important parameter in the design of electrical circuits. This becomes especially important in RF power-transmission applications including amplification and broadcasting [70, 71, 72]. Each component of an electrical system has associated with it some characteristic electrical impedance, and the transmission efficiency for any power between any two components will be affected by any mismatch of their electrical impedances; the topic of impedance matching will be discussed later in this chapter.

The third type of impedance is electromechanical impedance, which is a measure of the coupled electrical and mechanical response of a structure, and may be defined as the electrical impedance in equation (4.3) measured across the electrodes of a device that has coupled electrical and mechanical properties. In the case of ultrasonic de-icing, this coupling occurs due to the electromechanical coupling in the piezoelectric element. This measurement is important for optimizing power transfer between the amplifier system and the actuators and for determining the optimum frequency for driving a set of actuators bonded to a host structure. These topics will be discussed later in this chapter.

4.2 Electrical Impedance Matching

Impedance matching is the practice of optimizing power transfer between components in an electrical circuit by designing the circuit components to minimize the impedance mismatch between them. In general, the two components being matched are considered the source and the load, although a component may be a source in reference to one component and a load in reference to another, since impedance matching between components in series can be considered a sequence of independent impedance matching problems. For the de-icing system, the most important impedance matching is between the amplifiers and the actuators, although additional small-signal impedance matching is also important to achieve stable de-icing system performance. This is particularly true between the signal generator and the amplifier and between

the bi-directional coupler in the amplifier and the data collection circuits in the digital I/O device used to monitor the power transfer from the amplifiers.

Impedance Matching Theory

In DC (direct current) circuit analysis, maximum power transfer is achieved by matching the resistance of the source and the resistance of the load [70]. For systems operating at non-zero frequencies, impedance replaces resistance as the key value. Note that impedance is a complex quantity for which the real part is resistance R and the imaginary part is reactance X :

$$Z(\omega) = R(\omega) + iX(\omega), \quad (4.4)$$

The reflection coefficient, Γ , is defined as the ratio of the amplitude of the voltage reflected from a load, V_R , to the voltage provided by the source, V_S and is related to impedance by:

$$\Gamma = \frac{V_S}{V_R} = \frac{Z_S - Z_L}{Z_S + Z_L}, \quad (4.5)$$

in which the subscript S denotes source and L denotes load. The impedance relation between the source and the load required to achieve maximum power transfer can be derived by considering the time-averaged power through the load

$$P_L = \frac{1}{2} \text{Re}\{V_L I_L^*\} \quad (4.6)$$

and substituting in equations (4.3) and (4.5) to express this in terms of impedance as

$$P_L = \frac{1}{2} \frac{|V_S|^2}{\text{Re}\{Z_L^*\}} \left| \frac{Z_L}{Z_S + Z_L} \right|^2. \quad (4.7)$$

Assuming the source impedance Z_S to be fixed and differentiating the power with respect to the real and imaginary parts of the load impedance yields two homogeneous equations:

$$\frac{\partial P_L}{\partial R_L} = 0 \rightarrow R_S^2 - R_L^2 + (X_S^2 + 2X_S X_L + X_L^2) = 0 \quad (4.8)$$

$$\frac{\partial P_L}{\partial X_L} = 0 \rightarrow X_L(X_S + X_L) = 0 \quad (4.9)$$

Solving these equations yields

$$Z_L = Z_S^* \quad (4.10)$$

Therefore, for optimum power transfer, the impedance of the source must be the complex conjugate of the impedance of the load. This means that they must have an identical resistance but an opposite reactance [70].

The primary need for impedance matching in the ultrasonic de-icing system is between the amplifiers and the actuators. The amplifier outputs have a constant impedance of 50Ω , so the ideal actuator system would also have an impedance of 50Ω . Unfortunately, the electromechanical impedance of the actuators varies greatly depending on the actuator design, the number of actuators in the system, the temperature of the actuators, the structure to which they are mounted, and the locations at which they are mounted to the structure. The impedance of a well-designed set of de-icing actuators can vary between just a few ohms and several hundred ohms, and in some cases it can be even higher. In order to match this impedance, an additional electrical component, known as an impedance matching network, is required between the amplifiers and the actuators.

There exists a great range of impedance matching network designs for various applications. These networks are generally comprised of inductors and capacitors, which have positive and negative reactances, respectively. Utilizing resistors to match impedance would introduce new losses to the system, which should be avoided at all costs when attempting to maximize power transmission. By configuring inductors and capacitors with appropriate values in various parallel and series configurations, such as those shown in Figure 37, lossless impedance matching can be achieved between an unmatched source and an unmatched load, regardless of the magnitude and phase mismatch between the two [70].

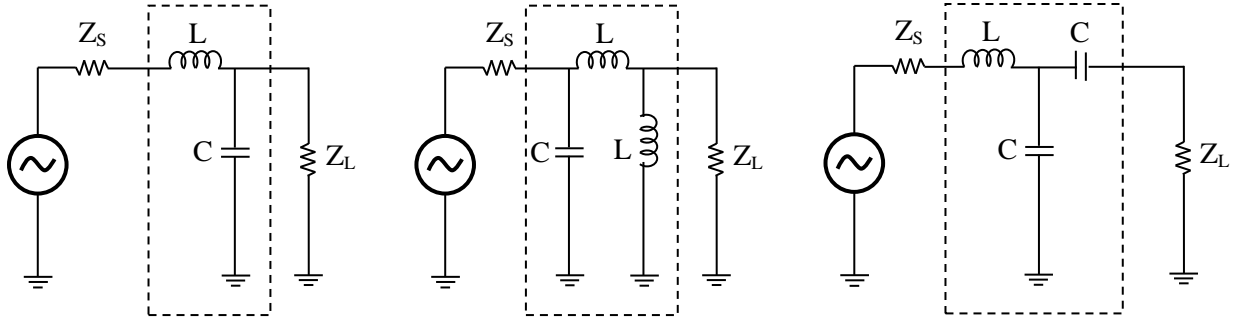


Figure 37 (Left) L-network, (center) pi-network, and (right) T-network impedance matching circuits are highlighted in the dashed boxes; capacitors and inductors may be interchanged depending on matching requirements.

Impedance Matching with a Single-Winding Autotransformer

For the case of piezoelectric actuators in the de-icing system, the impedance matching needs are somewhat simplified due to the nature of the impedance near resonance. For frequencies at which the actuator-structure system experiences a resonance, the magnitude of the impedance is minimized and the phase goes to approximately zero [65], as shown in Figure 38 and Figure 39. This is similar to the behavior of frequency response spectrum of mechanical systems at resonance [68] as studied in modal analysis.

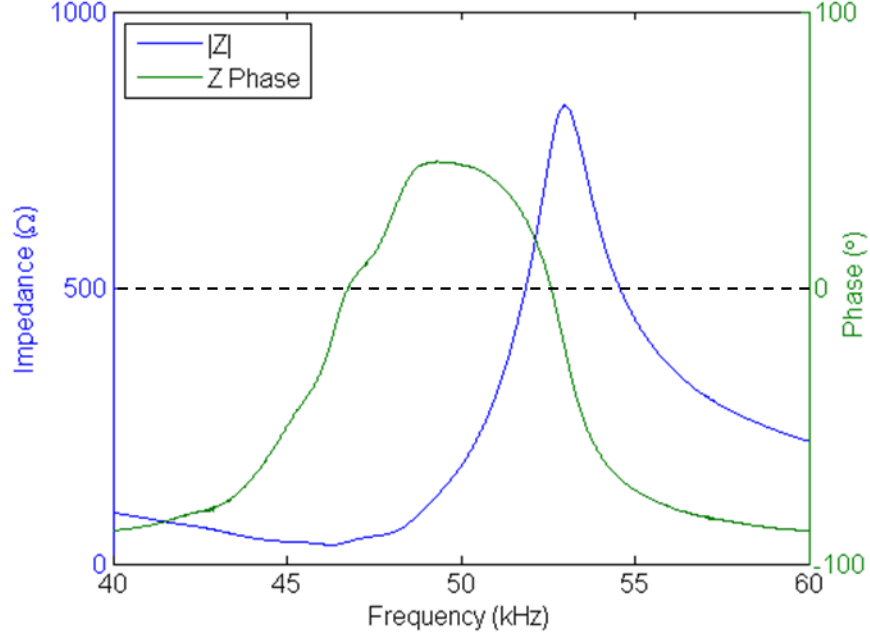


Figure 38 Impedance magnitude and phase of a set of four 2"-diameter PZT actuators bonded in a carbon fiber sandwich panel.

This effect holds for simple impedance curves like the highly-damped carbon fiber sandwich panel specimen in Figure 38 as well as the complicated impedance curve of the mildly-damped titanium specimen in Figure 39. The fact that the phase of the impedance goes to zero (which is equivalent to the reactance going to zero) at resonance means that we only need to match two unequal impedance magnitudes without considering a phase mismatch. One type of lossless network for matching two such systems is a simple transformer, such as the one shown in Figure 40, which achieves impedance matching according to equation (4.11), in which N_1 and N_2 represent the number of primary and secondary windings on the transformer [70].

$$\frac{Z_S}{Z_L} = \left(\frac{N_2}{N_1} \right)^2, \quad (4.11)$$

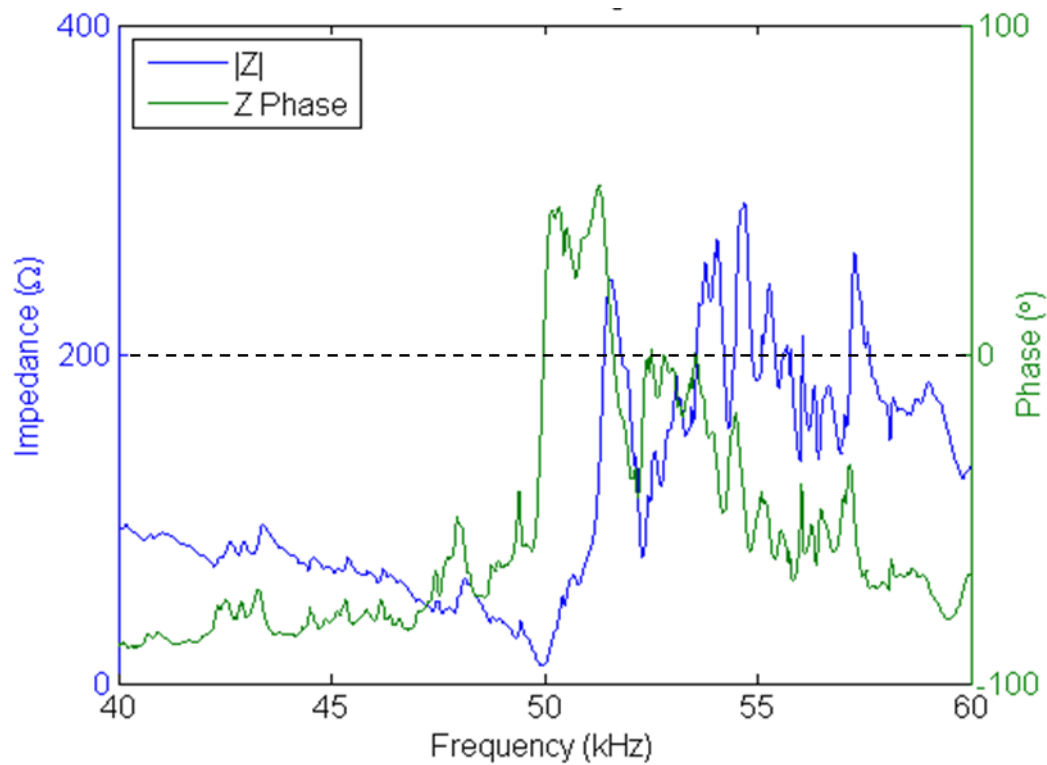


Figure 39 Impedance magnitude and phase of a set of four 2"-diameter PZT actuators bonded on a titanium panel.

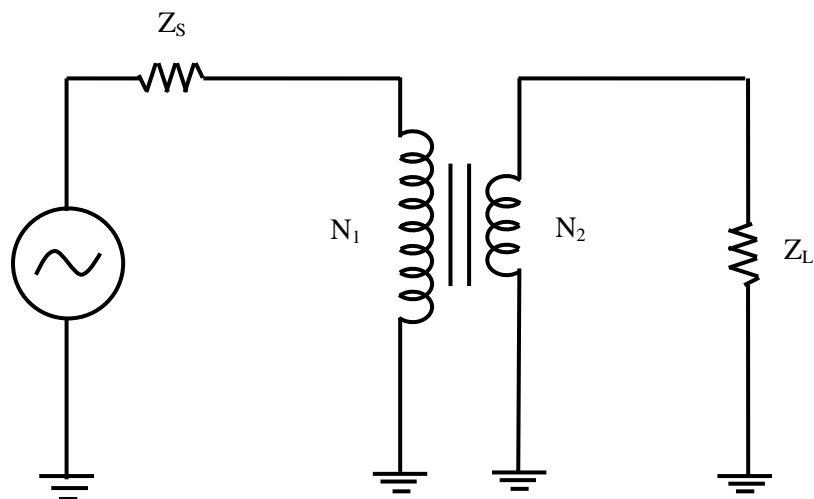


Figure 40 Circuit diagram of a source and load impedance matched with a transformer; here the load impedance must be larger than the source impedance because a step-down transformer is used.

The impedance matching network used in the de-icing system is a special type of transformer known as a single-winding autotransformer [73], such as the one shown in Figure 41. In the single-winding autotransformer circuit, a variable connection is used to tap into a single toroidal transformer, which allows for simple adjustment of the turn ratios to accommodate a range of load impedances. Further details of the impedance matching network incorporated in the de-icing system are provided in Chapter 6.

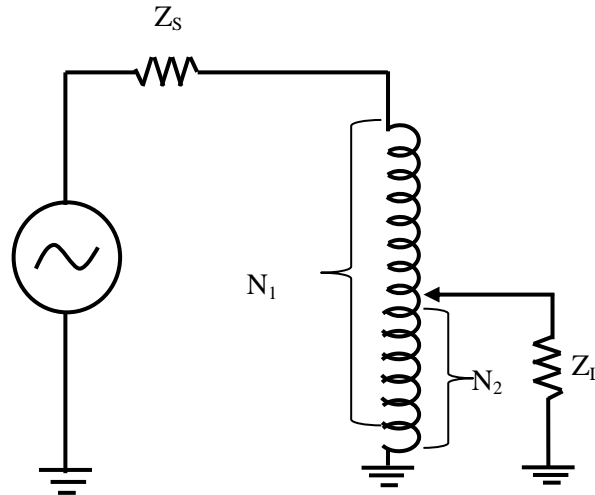


Figure 41 A single-winding autotransformer circuit similar to the ones used for matching the amplifier impedance to the actuator impedance in the ultrasonic de-icing system.

Figure 42 shows the effect of the autotransformer impedance matching network on the impedance magnitude and phase of a four-actuator carbon fiber sandwich panel. Here the minimum impedance of the system is $24\ \Omega$ at $46.1\ \text{kHz}$, and thus the matching network was switch to the $25\ \Omega$ setting. The effect of the matching network was to increase the impedance in a non-linear manner that attempts to bring the impedance minimum up to $50\ \Omega$. In this case the impedance at $46.1\ \text{kHz}$ was adjusted upward from $24\ \Omega$ to $47\ \Omega$, which will provide much better transmission efficiency than the unmatched system. The phase of the impedance near the frequency of interest was minimally affected.

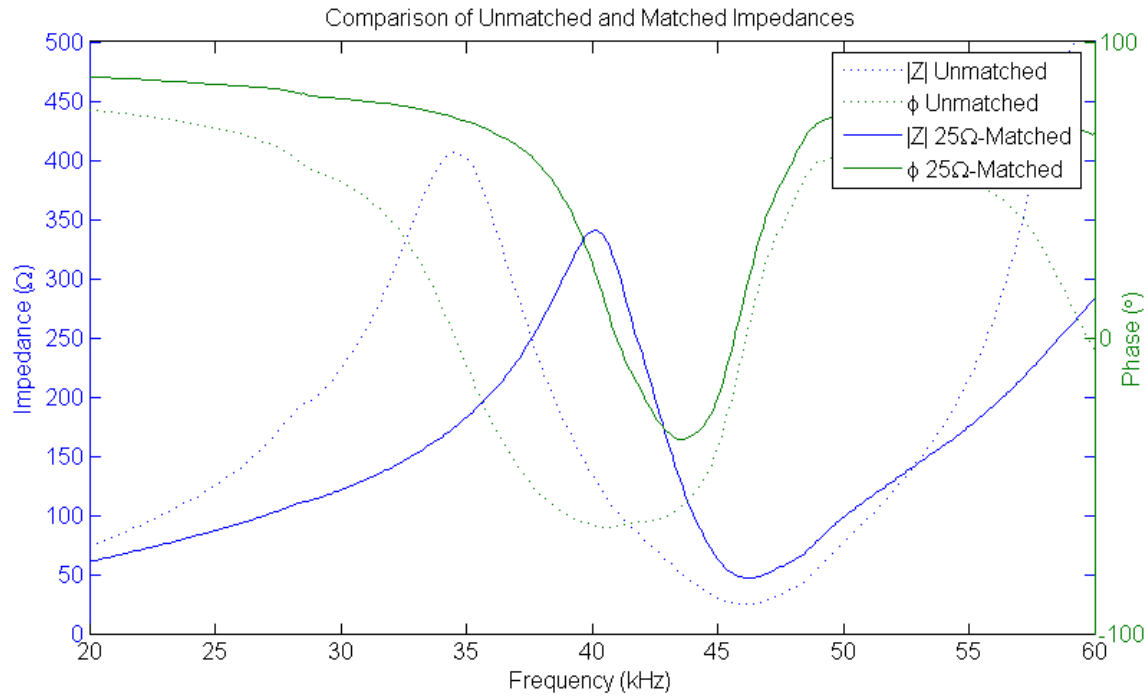


Figure 42 Comparison of system impedance of four actuators in a carbon fiber sandwich panel without and with appropriate 25Ω impedance matching via an autotransformer.

Figure 43 compares the forward, reflected, and net load power measured as a function of frequency for this same specimen, both with and without impedance matching. The forward power is the power generated by the amplifier and sent to the actuators, the reflected power is the power that was reflected from the actuators back to the amplifier, and the net load power is the power that was effectively transmitted into the actuators. Note that the forward and net power was higher for the unmatched system. This is due to the fact that the amplifier gain changes with the load impedance. However, the reflected power was also higher, and in the end, the efficiency of the system is greater with the impedance matching network than without it, as is shown in Figure 44. The details of how these power measurements were obtained are provided later in this chapter.

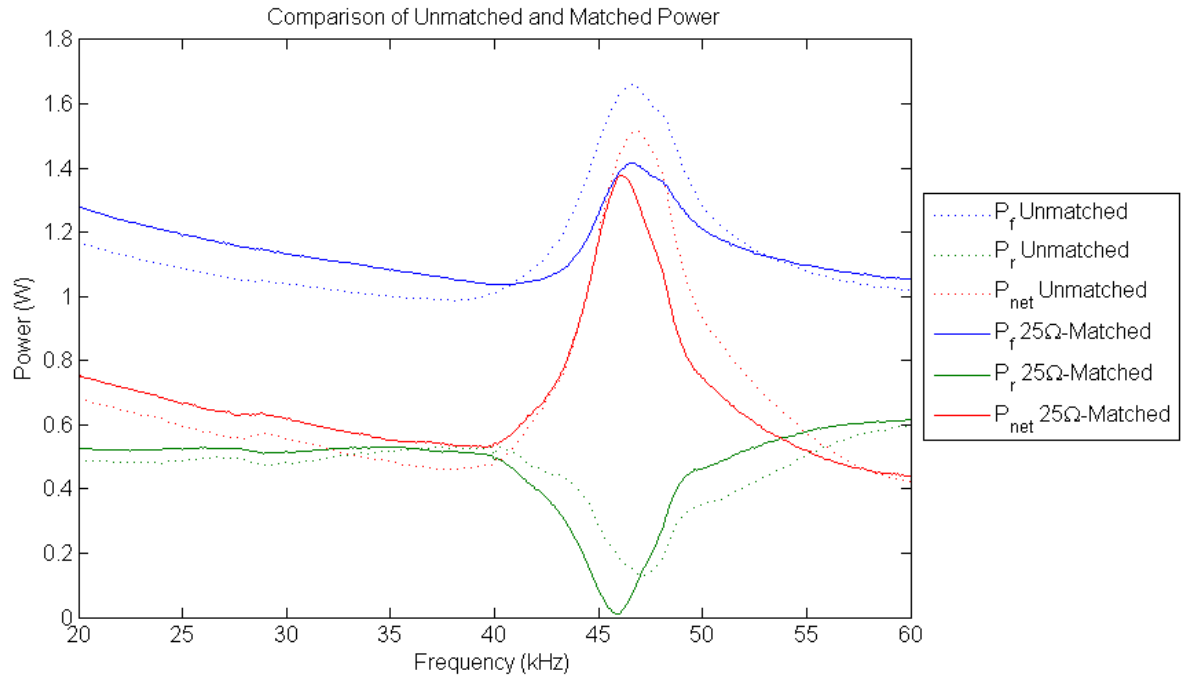


Figure 43 Comparison of forward, reflected, and net load power with and without the appropriate 25Ω impedance matching network.

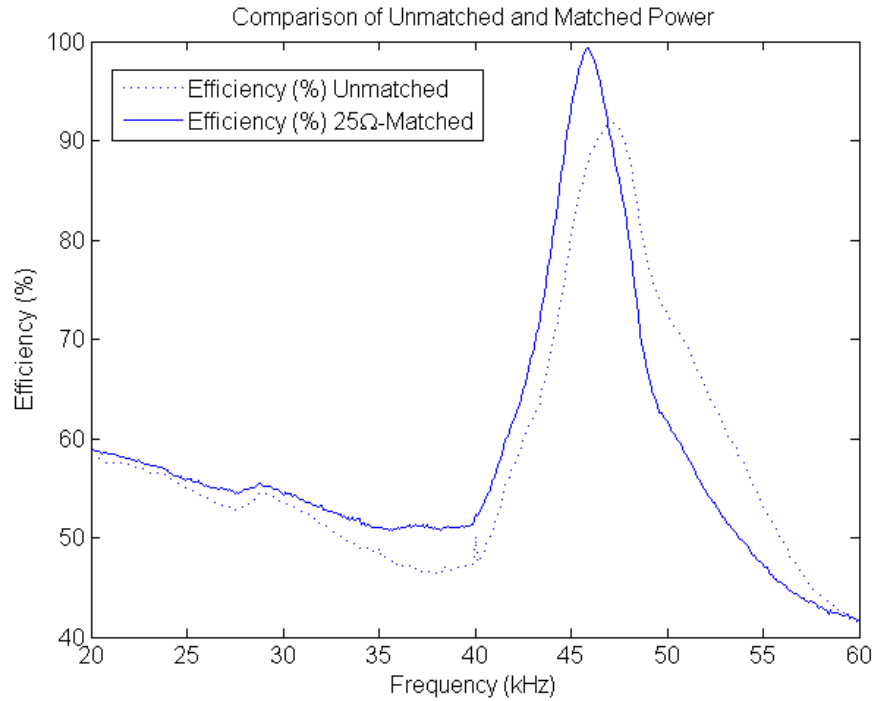


Figure 44 Comparison of efficiency with and without the appropriate 25Ω impedance matching network.

4.3 Electromechanical Impedance Analysis of a Coupled-Actuator System

In Chapter 3: Actuator Design, the electromechanical impedances of a free piezoelectric disk and a constrained piezoelectric disk were calculated in terms of the actuator geometry and the local frequency response function of the structure at the actuator bonding location. Recall that the expression of the electromechanical impedance of a constrained piezoelectric disk was described by

$$Z = \frac{1}{i\omega C(1 - k_p^2)} \left[1 + \frac{k_p^2}{1 - k_p^2} \frac{(1 + \nu)J_1(\gamma r)}{\gamma a J_0(\gamma a) - (1 - \nu)J_1(\gamma a) - \frac{k_{str}(\omega)}{k_{PZT}}(1 + \nu)J_1(\gamma a)} \right]^{-1} \quad (4.12)$$

$$k_{PZT} = \frac{h}{as_{11}^E(1 - \nu)}, \quad (4.13)$$

$$k_{str} = \frac{F_{PZT}(a)}{u_{PZT}(a)} \quad (4.14)$$

in which k_{PZT} describes the static stiffness of the piezoelectric disk and k_{str} describes the dynamic stiffness of the structure, which is defined as the ratio of the applied radial force at a to the radial displacement response at a [65, 74]. Equation (4.12) provides the solution for a single piezoelectric actuator bonded to a structure, but multiple actuators are used in the ultrasonic de-icing system. Therefore it should be determined how the impedances of multiple actuators bonded to a single structure combine to form the net electromechanical impedance that will be seen by the amplifiers.

Simple Independent Impedance Combinations

Calculating the net impedance of a circuit comprised of a set of independent impedances connected in parallel, such as the components in Figure 45, is a simple matter of applying equation (4.15).

$$Z_{eq} = \left[\frac{1}{Z_1} + \frac{1}{Z_2} + \cdots + \frac{1}{Z_N} \right]^{-1}, \quad (4.15)$$

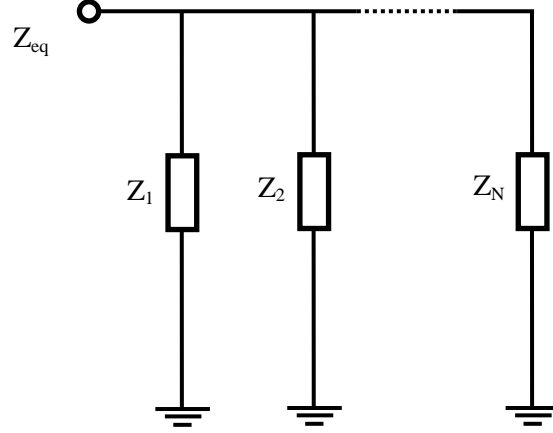


Figure 45 Circuit diagram of N impedances in parallel.

However, this equation cannot be applied to the case of several piezoelectric actuators attached to a single structure, because each of the components of the circuit in Figure 45 is independent of one another. This is not true for a multi-actuator de-icing system, and therefore a new formula for calculating the equivalent system impedance must be derived.

Equivalent Impedance of a Complex Coupled-Component System

In the case of actuators attached to a structure, each actuator is electromechanically coupled to each other actuator through the structural dynamics of the host structure. For instance, consider the panel with two piezoelectric actuators shown in Figure 46. If a voltage is applied to actuator 1, a current will be induced not only across actuator 1, but also across actuator 2 due to the deformation of the structure induced by actuator 1. This coupled impedance dramatically complicates the matter of calculating the combined impedance of multiple actuators. To develop a method of combining the impedances of multiple actuators, we may consider the case of Figure 47, which is the representative circuit of the plate and actuators shown in Figure 46.

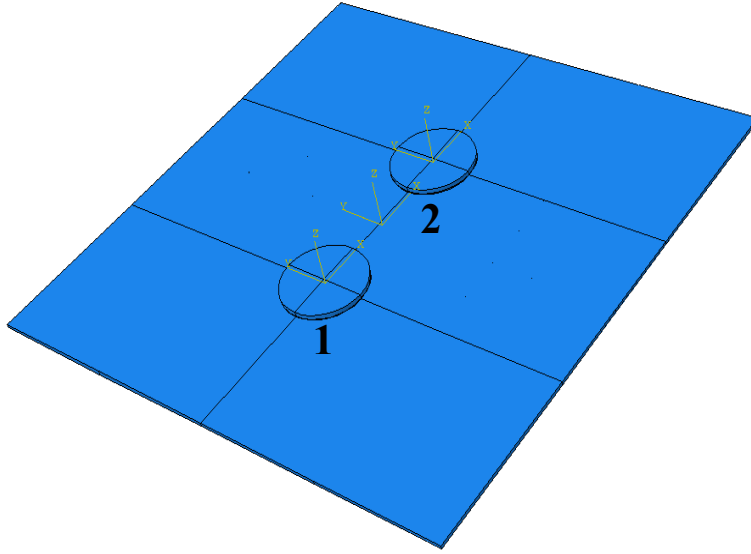


Figure 46 Drawing of a plate with two piezoelectric actuators bonded to its surface.

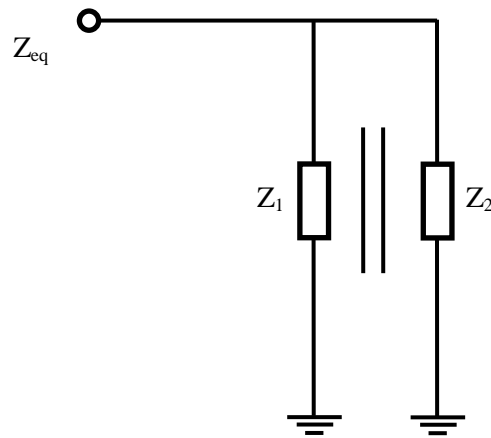


Figure 47 Representative circuit of the two-actuator system in Figure 46, in which the actuators have coupled electromechanical impedances.

Consider the case in which a voltage V is applied across the circuit shown in Figure 47. This voltage will induce a current across component 1 and component 2, so that the impedance can be described as

$$Z = \frac{V}{I} = \frac{V}{I_1 + I_2}. \quad (4.16)$$

The current I_I induced across actuator 1 will be comprised of a direct current I_{11} , induced due to the voltage across component 1 as well as an indirect current I_{12} induced by the voltage across component 2, due to the impedance coupling between the two components. Therefore equation (4.16) can be rewritten as

$$\begin{aligned} Z_{eq} = \frac{V}{I} = \frac{V}{I_1 + I_2} = \frac{V}{I_{11} + I_{22} + I_{12} + I_{21}} = \frac{V}{\frac{V}{Z_{11}} + \frac{V}{Z_{22}} + \frac{V}{Z_{12}} + \frac{V}{Z_{21}}} \\ = \left[\frac{1}{Z_{11} + Z_{22} + 2Z_{12}} \right]^{-1} \end{aligned} \quad (4.17)$$

in which impedance values Z_{11} and Z_{22} are the direct impedances Z_1 and Z_2 of the two actuators, while Z_{12} is the cross-coupled impedance between the two actuators defined by

$$Z_{12} = \frac{V}{I_{12}} = \frac{V}{I_{21}}. \quad (4.18)$$

The relationship between the currents and voltages measured across any actuator combination may be written in terms of the impedances as

$$\begin{bmatrix} V_1 \\ V_2 \\ V_3 \\ \vdots \\ V_N \end{bmatrix} = \begin{bmatrix} Z_{11} & Z_{12} & Z_{13} & \dots & Z_{1N} \\ Z_{21} & Z_{22} & Z_{23} & \dots & Z_{2N} \\ Z_{31} & Z_{32} & Z_{33} & \dots & Z_{3N} \\ \vdots & \vdots & \vdots & \ddots & \vdots \\ Z_{N1} & Z_{N2} & Z_{N3} & \dots & Z_{NN} \end{bmatrix} \begin{bmatrix} I_1 \\ I_2 \\ I_3 \\ \vdots \\ I_N \end{bmatrix} \quad (4.19)$$

This assumes that the interaction between actuators 1 and 2 is linear, and thus that the structure undergoes linear vibration. This can be expanded to any number of actuators N , and by the equation

$$Z_{eq} = \left[\sum_{m=1}^N \sum_{n=1}^N \frac{1}{Z_{nm}} \right]^{-1}. \quad (4.20)$$

Note that this equation could be applied to equation (4.12) in the form of

$$Z_{eq} = \frac{N}{i\omega C(1 - k_p^2)} \left\{ \sum_{m=1}^N \sum_{n=1}^N \left[1 + \frac{k_p^2}{1 - k_p^2} \frac{(1 + \nu)J_1(\gamma r)}{\gamma a J_0(\gamma a) - (1 - \nu)J_1(\gamma a) - \frac{k_{str}^{nm}(\omega)}{k_{PZT}}(1 + \nu)J_1(\gamma a)} \right] \right\}^{-1}, \quad (4.21)$$

in which it is assumed that all actuators are identical and the term

$$k_{str}^{nm} = k_{str}^{mn} = \frac{F_{PZT}(a_n)}{u_{PZT}(a_m)} = \frac{F_{PZT}(a_m)}{u_{PZT}(a_n)}. \quad (4.22)$$

Here $u_{PZT}(a_m)$ is the displacement at radius a_m of actuator m induced by a radial force $F_{PZT}(a_n)$ applied at radius a_n of actuator n , and therefore this term represents the structural response between the locations of the two actuators on the structure.

This type of calculation does not need to be directly applied to experimentally determine the net impedance of a set of actuators, because the voltage and current measured across the set of actuators provides an equivalent value, with one exception. This exception occurs when the actuators will not be driven with equivalent signals, for instance, if the signals are out of phase. In such a case, equation (4.20) could be applied in a modified form that separates the impedance magnitude and phase values

$$Z_{eq} = \left[\sum_{m=1}^N \sum_{n=1}^N \frac{1}{|Z_{nm}|} e^{-i(\varphi_n + \varphi_m)} \right]^{-1}, \quad (4.23)$$

in which φ_n and φ_m are the phase shifts of the signals applied to actuators n and m , respectively. To measure each of the direct and cross-coupled impedance terms required to carry out such a calculation, $\frac{1}{2}N(N+1)$ calculations would be required. Table 5 details the number of impedance measurements that would be required for a given number of actuators in a single de-icing actuator set.

Table 5 Minimum number of impedance measurements required to calculate the net impedance of a given number of actuators in a single set.

Number of Actuators	Impedance Measurements Required
2	3
4	10
6	21
8	36
10	55
12	78
14	105
16	136

Implementation of Coupled-Impedance Calculations

Carrying out such measurements would be problematic in several ways.

1. The sheer number of measurements required for even a relatively small number of actuators would take up a considerable amount of time during operation of the de-icing system. Since impedance measurements cannot be acquired while the system is actively driving, this down time would render the system ineffective.
2. Measuring the direct impedance of a single actuator would require short-circuiting all of the other actuators, which would require additional relays to short-circuit each actuator.
3. Measuring the cross-coupled impedance between two actuators would require shorting all other actuators, applying a voltage across one actuator, and recording the induced current across the other, which would require a complex array of relays to short-circuit each actuator and to independently measure voltage and current across individual actuators.
4. The impedance analyzer is not designed to measure voltage and current separately, so a new measurement system, including hardware and software, would be required to carry out these measurements.

Without measuring the impedance of the actuator set under the phasing conditions that the system will be operated under, there will be no way of determining the optimum driving

frequency or the impedance of the actuator set for impedance matching purposes. This is problematic and seems to exclude the potential for actuator phasing. Fortunately, two methods were developed to utilize phasing while overcoming these limitations; these will be detailed later in this chapter and in Chapter 5: Actuator Phasing.

The method of equivalent impedance calculation for phased actuators described by equation (4.23), while impractical for direct implementation in the de-icing system, is, in fact, very useful for finite element analysis of phased actuator configurations. The details of the actuator phasing process, the finite element modeling techniques employed for this research, and the manner in which equation (4.23) is applied to the finite element modeling process will be provided in Chapter 5: Actuator Phasing. These will be skipped for the current section as the focus here is simply on the result of one such analysis.

Finite Element Verification of Coupled-Impedance Calculations

Consider the four-actuator system coupled to a plate with a layer of ice in Figure 48. The actuators in this model 2"-diameter PZT-4 piezoelectric actuators, the plate is a 0.0787" thick 12" by 12" titanium panel, and the ice is a uniform 0.118" thick layer. To fully populate equation (4.23), a total of 10 individual impedance terms are required for this case, in which $N = 4$. These 10 individual impedance measurements, as well as the net impedance value predicted using equation (4.23), and the impedance directly measured across all the actuators driven together are shown in Figure 49. Again, the details of the impedance calculation from the finite element modeling process will be provided in Chapter 5, only the results are provided here.

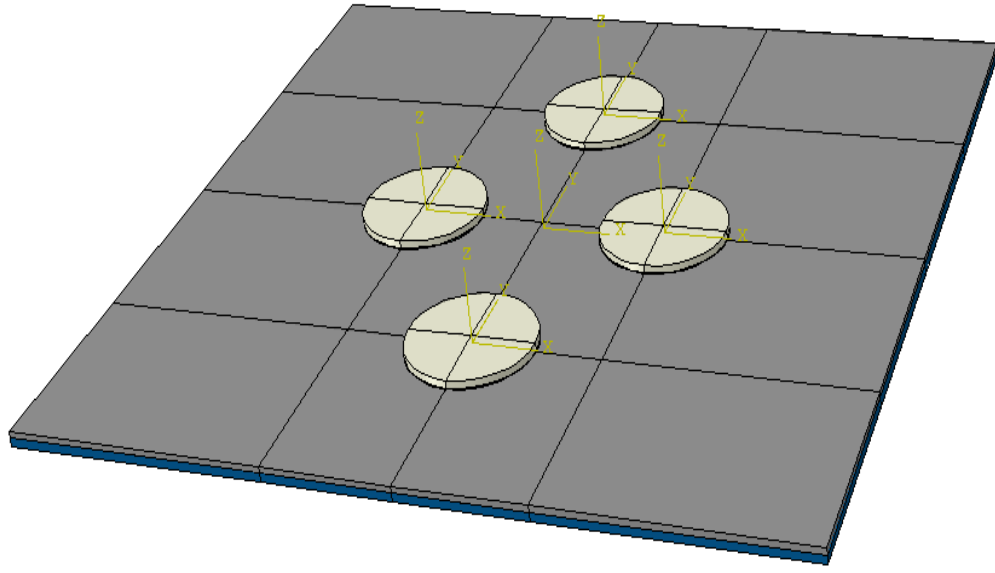


Figure 48 Drawing of a finite element model of a four-actuator de-icing system used to evaluate the accuracy of the indirect impedance calculation method detailed by equation (4.21).

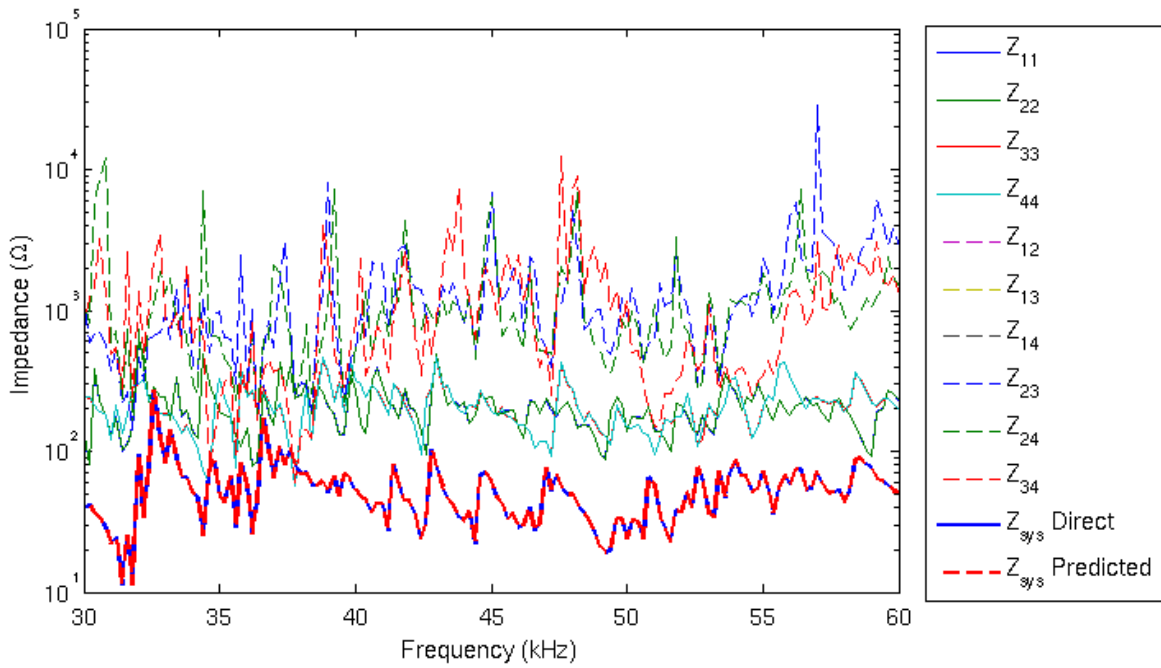


Figure 49 The ten individual impedance curves calculated from the finite element model illustrated in Figure 48, as well as the directly-calculated system impedance from this model and the system impedance predicted using equation (4.21). Figure 50 is a version of this plot with only the system impedance curves.

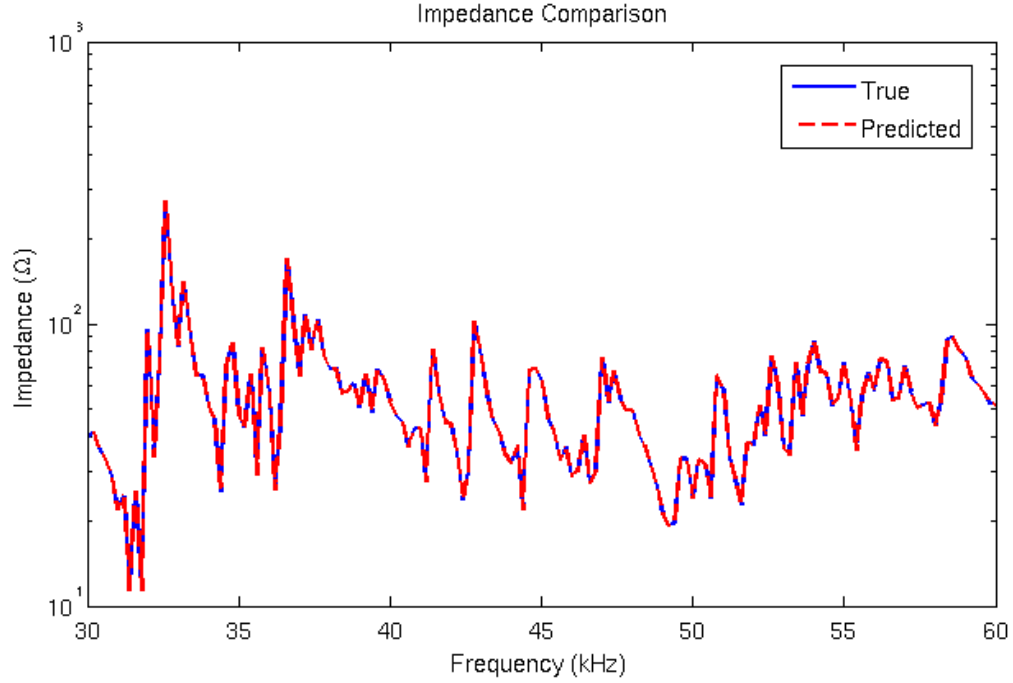


Figure 50 A comparison of the directly-calculated system impedance from the model illustrated in Figure 48 and the system impedance predicted using equation (4.21) and ten individually calculated impedance curves from the same model.

The data in Figure 49 shows that the directly-calculated system impedance is identical to the impedance calculated indirectly using the ten individual impedance curves and equation (4.23). This verifies the derivation of equation (4.23) for finite element modeling purposes. Figure 50 provides a less-cluttered comparison of these two curves.

Multi-Port Electrical Network Impedance Matrix

It should be noted that these calculations are similar to those for calculating the equivalent impedance of a multiport electrical network [72], such as the one diagrammed in Figure 51. This represents an electrical circuit with multiple inputs and/or outputs in which the current and voltage measurements at each terminal have some relationship with the current and voltage measurements at each other terminal. The voltage at terminal 1, for instance, can be described by

$$V_1 = Z_{11}I_1 + Z_{12}I_2 + \cdots + Z_{1N}I_N. \quad (4.24)$$

This expression can be expanded for each terminal into matrix format as in equation (4.25), in which the $N \times N$ matrix is known as the “impedance matrix” for the multi-port network [72]. Note that this equation is identical to the one derived for the voltage and current relations between N electromechanically-coupled piezoelectric actuators attached to a common structure earlier in this chapter.

$$\begin{bmatrix} V_1 \\ V_2 \\ V_3 \\ \vdots \\ V_N \end{bmatrix} = \begin{bmatrix} Z_{11} & Z_{12} & Z_{13} & \dots & Z_{1N} \\ Z_{21} & Z_{22} & Z_{23} & \dots & Z_{2N} \\ Z_{31} & Z_{32} & Z_{33} & \dots & Z_{3N} \\ \vdots & \vdots & \vdots & \ddots & \vdots \\ Z_{N1} & Z_{N2} & Z_{N3} & \dots & Z_{NN} \end{bmatrix} \begin{bmatrix} I_1 \\ I_2 \\ I_3 \\ \vdots \\ I_N \end{bmatrix} \quad (4.25)$$

This is further validation that the method developed herein for calculating the equivalent impedance of such a system is accurate. Also note that equation (4.25) and the multi-port network impedance theory in general does not provide an explicit solution for obtaining the net impedance across a set of actuator, because such a value will be entirely dependent on the relationships between individual elements.

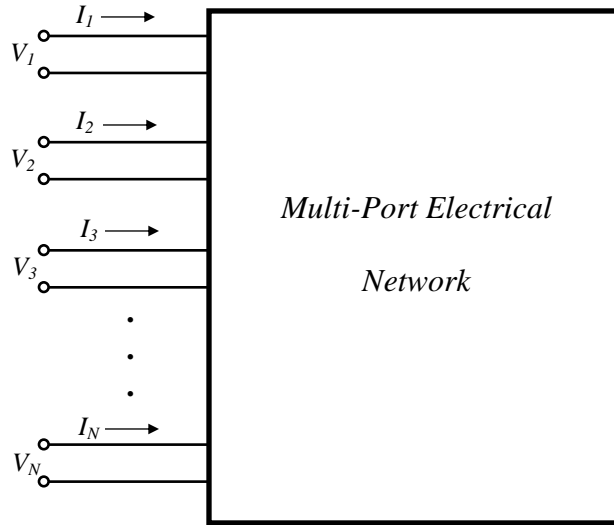


Figure 51 Diagram of a multi-port network, for which the equivalent impedance calculations are very similar to those of an electromechanical system with multiple coupled elements.

4.4 Automatic Frequency Tuning (AFT) Method

As was explained in this chapter, the electromechanical impedance of the piezoelectric actuators attached to a host structure will vary as a function of frequency. The impedance curve, which describes this trend, will not be constant for a given set of actuators due to external factors such as environmental temperature, and structural changes. These structural changes may be associated with the piezoelectric actuators, such as actuator and bondline wear, and they may be associated with the host structure, such as boundary condition changes and the accretion of ice, which can manifest itself with various shapes, thicknesses, and material properties. Since driving the actuator-structure system at resonance is very important for achieving maximum vibration amplitude and system efficiency, a method of tracking this optimum frequency must be employed to determine the optimum driving frequency at any given time. The method used for driving frequency optimization in ultrasonic de-icing research to date has consisted of the following [15, 24, 27, 28, 63]:

1. Attaching an impedance analyzer to the piezoelectric actuators, connected in parallel.
2. Performing an impedance sweep over a pre-specified bandwidth.
3. Determining the frequency at which the impedance was minimized.
4. Setting the impedance matching network to match the minimum impedance as closely as possible using a discrete number of impedance matching network configurations.
5. Driving the actuators at the frequency for which the impedance was minimized.

This method is effective in monitoring the impedance minimum and selecting an appropriate driving frequency, but it has some significant drawbacks. These drawbacks include the need for an impedance analyzer built into the system, switching relays to transfer the actuator connection between the amplifiers (for actuation) and the impedance analyzer (for impedance monitoring), and down time for reading the impedance in which the actuators cannot be driven. Therefore a technique that can determine the optimum driving frequency for the system, but does not require explicit impedance analysis, would be advantageous.

A technique known as “automatic frequency tuning” has been employed for RF amplifier tuning optimization, particularly in broadcasting applications, for several decades [75, 76]. This technique utilizes transmitted and reflected power measurements from the amplifier to determine the optimum frequency for operation.

The measurement of transmitted and reflected power at the output of an amplifier is achieved through a bi-directional coupler device, such as the one diagrammed in Figure 52. In general, ports 1 through 4 in the figure are known as the input port, the transmitted port, the coupled port, and the isolated port, respectively. For the case of sampling forward and reverse power signals from an amplifier, ports 1 through 4 labeled in this figure would represent the amplifier output, the load, the forward power reading, and the reverse power reading, respectively. The concept of such a coupler is to sample the signal in the main line (port 1 to port 2) via induction to the secondary line (port 3 to port 4), and to do so in a way that the signals propagating in a particular direction are then transmitted in the secondary line in that same direction with minimal coupling to the other secondary line port. This is achieved, in one manifestation, using a cross-connected transformer such as the one shown in Figure 52 [77].

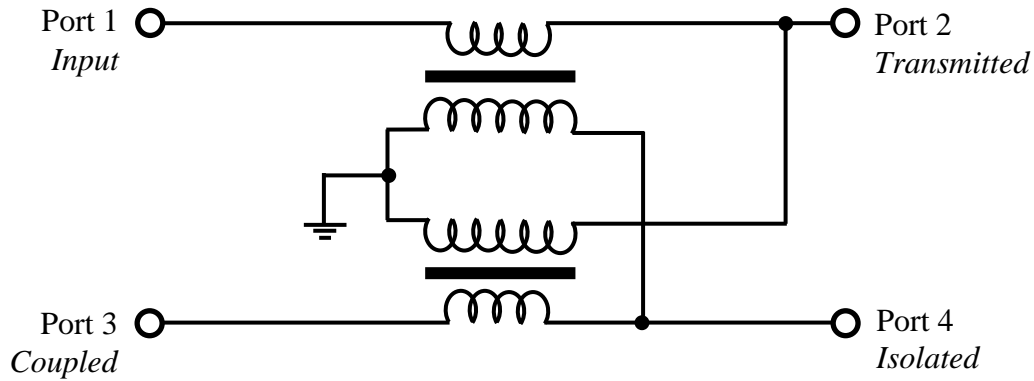


Figure 52 Diagram of a bi-directional coupler circuit in the form of cross-connected transformers.

The effectiveness of such a coupler is described by several parameters including the coupling factor $C_{3,1}$, the insertion loss $L_{2,1}$, the isolation $I_{4,1}$, and the directivity $D_{3,4}$. Each of these measures describes the amplitude relationship of the signal power between the four ports of the bi-directional coupler. These parameters are defined below [78].

$$C_{3,1} = -10 \log_{10} \left(\frac{P_3}{P_1} \right) = 20 \log_{10}(n) \quad (4.26)$$

$$L_{3,1} = -10 \log_{10} \left(\frac{P_2}{P_1} \right) \quad (4.27)$$

$$I_{3,1} = -10 \log_{10} \left(\frac{P_4}{P_1} \right) \quad (4.28)$$

$$D_{3,4} = -10 \log_{10} \left(\frac{P_3}{P_4} \right) \quad (4.29)$$

In an ideal coupler, the directivity should be as high as possible and the isolation should be as low as possible to achieve full directionality. The coupling factor, which is dependent on the turn ratio, n , between the primary and secondary transformer coils, determines what portion of the main line power is siphoned off to the secondary line. The insertion loss measures the loss on the main line due to the coupler, which is a combination of coupling losses and system inefficiencies.

A coupler similar to the one illustrated in Figure 52 is used in the de-icing amplifiers to sample the forward and reverse power readings. The forward power is the power generated by the amplifier and directed outward through the amplifier output port, and the reverse power is the power reflected from the load back into the amplifier output port. Subtracting these two values yields

$$P_{net} = P_f - P_r \quad (4.30)$$

in which P_f is the forward power, P_r is the reverse power, and P_{net} is the net power delivered to the load, the power transmitted into the load can be determined in real time. This real-time net load power reading can be used to determine the optimal system operating frequency.

In order to utilize this power reading method for frequency optimization, one of two methods can be employed.

1. The forward and reverse power can be monitored during continuous operation and the frequency can be automatically oscillated to track the impedance minimum based on the local slope of the net power reading [75].
2. The forward and reverse power data can be periodically collected over a pre-set frequency bandwidth using a rapid frequency sweep and analyzed for the optimum excitation frequency.

Due to the fact that the de-icing system is run on a duty cycle to minimize actuator overheating, there is nothing lost in periodically sweeping a frequency range at low power to measure an impedance curve, particularly since this process is very fast (usually just a few seconds). As compared to the impedance analysis method previously used [15, 24, 27, 28, 63], this method eliminates the need for the impedance analyzer and any associated switching hardware. This represents a weight savings of more than 5 lbs from the laboratory version of the de-icing system and also reduces its cost and complexity.

This direct power data is also more valuable than an impedance analysis because it provides direct information regarding the power transmission efficiency into the actuators, while the impedance analysis is an indirect analysis. In some cases the frequency associated with the impedance minimum may not be the optimal frequency for maximizing net load power for several reasons. First, the forward power generated by the amplifier is not constant, but rather a function of the impedance into which it is operating, as lower impedances will generally draw greater voltage from the power supply. Second, the reflected power is greater for loads not equal to 50Ω , even after impedance matching, which is rarely perfect. The automatic frequency tuning (AFT) method inherently accounts for all of these variables and any others that may arise. Figure 53 compares the impedance amplitude with the power readings for a carbon fiber sandwich panel fitted with four integrated actuators.

Note that the impedance minimum (measured without impedance matching) for this specimen is 24Ω at 46.1 kHz. The frequency that achieves maximum net load power to the actuators is also 46.1 kHz in this case. This excellent agreement testifies to the validity of the AFT method, but it should be noted that if the actual impedance minimum is not so close to a pre-set impedance matching network setting (in this case 25Ω), the impedance matching may not be as good as was observed here, and thus the maximum net power may not occur at the frequency of the impedance minimum.

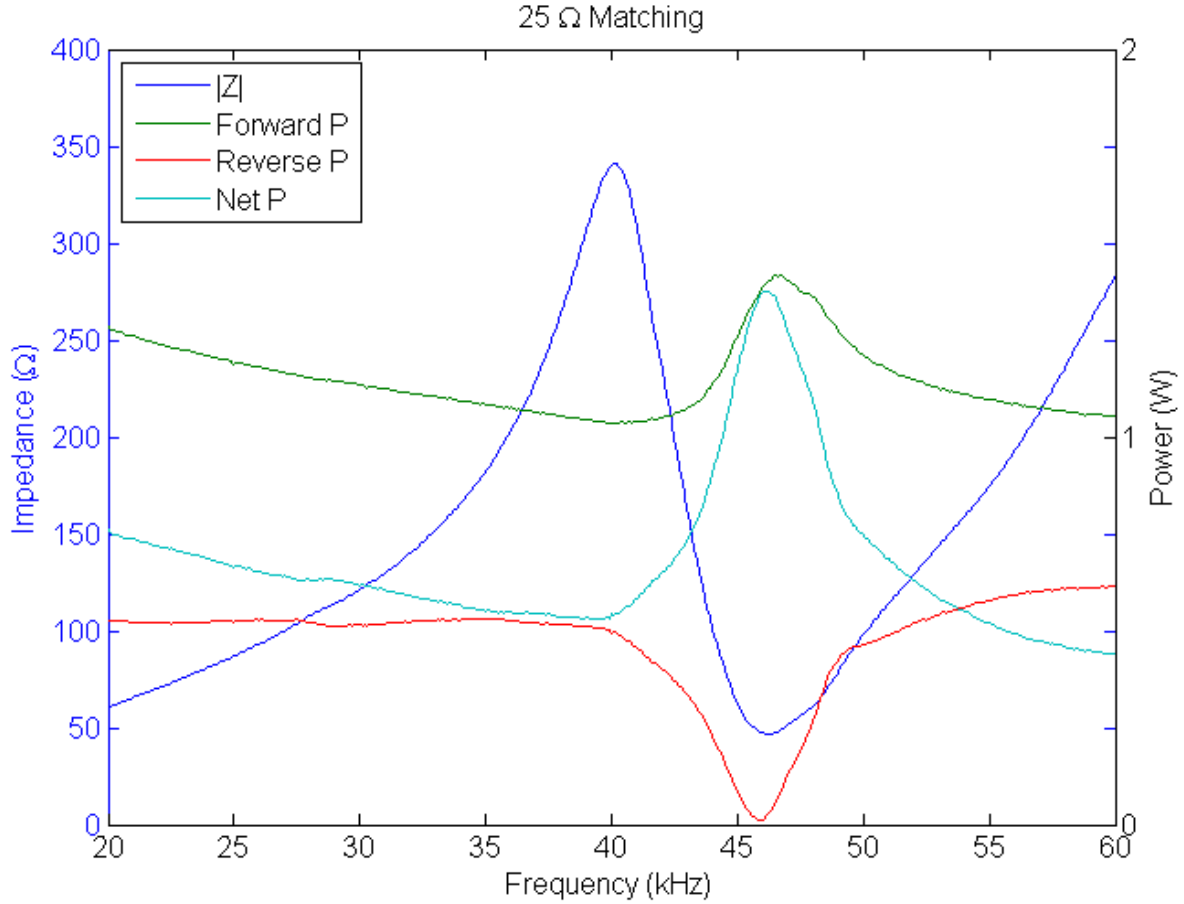


Figure 53 Comparison of the impedance and power data as a function of frequency for a four-actuator carbon fiber sandwich panel specimen with 25Ω impedance matching.

The forward power data can also be used to monitor system power consumption. In reality, the amplitudes measured from the coupler are simply voltages, but if the coupling factor is known, this can be used to calculate true power. In the case of the de-icing amplifiers, which are Electronics & Innovation, Ltd. 1040L amplifiers, the coupling factor is -30dB, therefore the main line voltages are 31.62 times the measured voltages from the coupler. Since the impedance of all the lines in the coupler and the data cables is a constant 50Ω, Ohm's Law can be used to determine the main line power.

$$P = \frac{V}{I} = \frac{V^2}{Z} \quad (4.31)$$

Any other measures of power taken from the actuators or the transmission line between the actuators and amplifiers will be highly inaccurate due to interference of the forward and reflected signals in the transmission line, which may have an arbitrary phase relative to one another [71]. Additionally, both the impedance of the actuators and the measured voltage (which would be incorrect anyway) would be required to calculate power since the impedance of the actuators is not constant. On the other hand, reading the power directly from the bi-directional coupler provides accurate power readings. Several of the parameters that may be used to measure transmission efficiency are

$$RL = 10 \log_{10} \left(\frac{P_r}{P_f} \right), \quad (4.32)$$

$$\Gamma = \left(\frac{V_r}{V_f} \right) = 10^{RL/20}, \quad (4.33)$$

$$VSWR = \frac{1 + \Gamma}{1 - \Gamma}, \quad (4.34)$$

in which RL is the return loss, Γ is the reflection coefficient, and $VSWR$ is the voltage standing wave ratio of the system [70, 71, 72]. For our purposes, return loss is the most meaningful measure for power transmission efficiency. A return loss of -20 dB would indicate 99% power transmission efficiency, a return loss of -3dB would indicate 50% power, and a return loss of 0 dB would indicate 0% efficiency.

The forward and reflected power readings from an E&I 1040L amplifier were measured and compared to the calibrated front-panel display information from the amplifier. In order to ensure accuracy of the front-panel display, the system must be operated in steady-state, as the front-panel output is inaccurate over short periods of time due to the processing of the power signals that is employed by the manufacturer. A sine dwell test was conducted in which the amplifier was attached to a composite de-icing specimen and the frequency of excitation was incrementally shifted from one frequency to another while the forward and reflected power data from both the retrofitted data ports and the front panel display were simultaneously recorded. After applying a calibration factor of 1.27 to the raw output voltages (recall that the front panel display is calibrated by the manufacturer), a comparison of the two power measurement methods

is provided in Figure 54. These values generally agree with the exception of the higher frequencies, at which they diverge. However, notice that the net power reading is accurate over all frequencies, because any offset in the forward power is accompanied by an equivalent offset in the reflected power as well. The accuracy of the power data measured from the retrofitted data ports could be improved further by directly calibrating it using the manufacturer-recommended calibration procedure. However, it was not practical to purchase the specialized equipment required to carry out such a calibration.

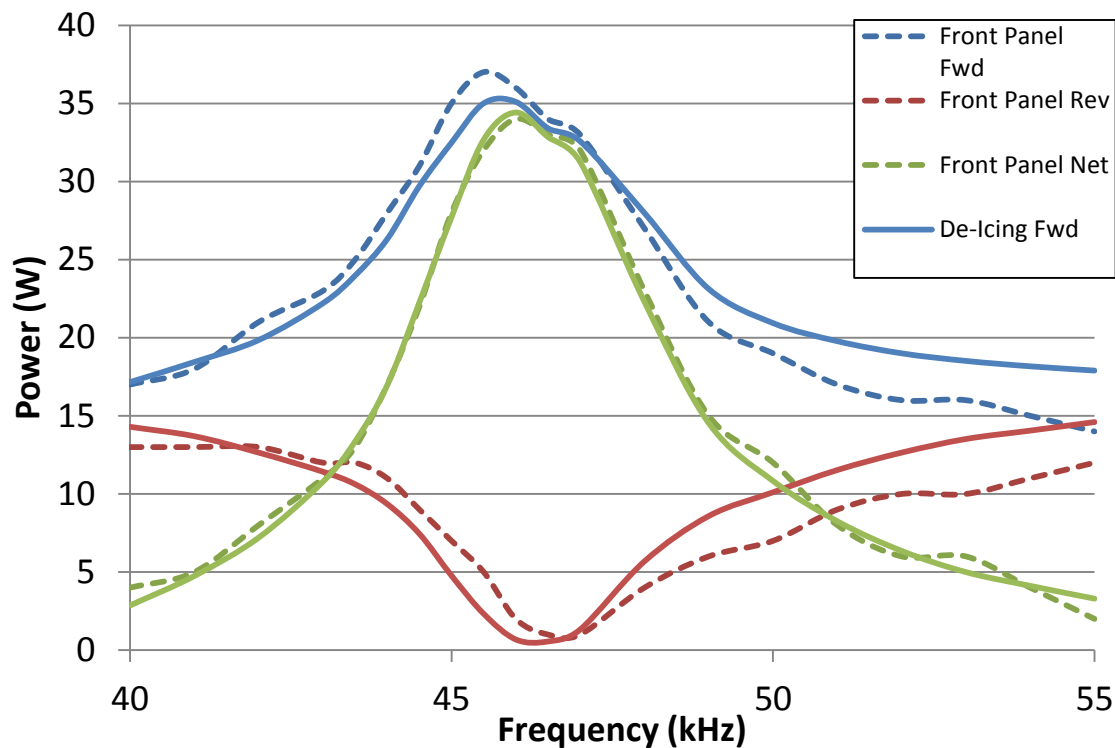


Figure 54 Comparison of measured forward and reflected power using the manufacturer-calibrated front panel display and the retrofitted data ports.

Therefore, selecting the impedance minimum, attempting to match it, and driving at the impedance minimum frequency does not guarantee maximum power transmission to the amplifiers or maximum efficiency, while the AFT method does. This method also reduces the amount of equipment required to operate the de-icing system and can provide real-time direct forward and net power readings that can be used to determine the true system power consumption and efficiency.

Chapter 5

ACTUATOR PHASING METHOD

5.1 The Role of Phasing

The fundamental concept behind the ultrasonic de-icing approach is to generate shear stresses in a host structure that exceed the ultimate shear adhesion strength of a layer of accreted ice. However, generating isolated regions of high shear stresses does not assure successful de-icing of a structure. As ice generally forms in large sheets, debonding a small, or even a large percentage of that ice, the sheet as a whole may remain attached to the airfoil due to small regions of well-bonded ice [63, 66]; this is sometimes referred to as “bridging”. Additionally, even if ice is generally removed from the airfoil, the remaining patches may still cause unacceptable changes in the aerodynamics and operation of the aircraft. To avoid the bridging and remnant ice issues mentioned, it is necessary to achieve some threshold level of shear stress coverage over a very large proportion of the airfoil to ensure reliable and effective de-icing. Overmeyer predicted that, based on a theoretical study of a generic rotor system, less than 9% of the surface can experience very low shear stress levels and still be effectively de-iced [66]. This value will likely vary greatly for different ice formations, ice material properties, and between rotor blades, fixed-wing airfoils, and other structures of interest, but it is an initial value for consideration.

In past ultrasonic de-icing research, the method of achieving this shear stress coverage was to employ frequency sweeping. This was done by locating the resonance of the actuators with an impedance analyzer and subsequently driving the actuators at several frequency increments over a small bandwidth around the resonance [63, 66]. The theory was that by driving the system at several frequencies, various forced vibration patterns could be induced in the structure with varying stress distributions. However, the primary limitation of this method is that it could only be applied to a small frequency bandwidth centered around the resonance of the actuators, generally only 500 to 1500 Hz. Operating the actuators too far off resonance leads to deleterious effects on the efficiency of the system and thus its ability to generate high levels of shear stress. This method was tested on rotating test specimens by Overmeyer [66] and deemed to be

sufficient, although no detailed analyses were performed to characterize the stress distributions induced by such a frequency sweep.

The goal of this research is to develop a better method for achieving full shear stress coverage that can allow for a much wider range of stress distribution possibilities while simultaneously retaining or improving the efficiency of the system. The method proposed herein is a novel method of actuator phasing, in which phase-shifted signals are applied to some actuators relative to the others. This out-of-phase excitation of some subset of actuators will induce a different forced vibration pattern in the structure by predominantly exciting different ultrasonic vibration modes. The details of how such an approach might be implemented, as well as the effectiveness of the approach, will be discussed in this chapter.

The primary questions regarding the introduction, development, and evaluation of an actuator phasing method are:

1. What type of phase shifts should be applied, to what actuators, and in how many combinations?
2. Should the frequency of activation be static (based on the unphased actuator impedance minimum) or adaptive (based on the vibration state induced by phasing the actuators)?
3. How effective is this approach at improving shear stress coverage?
4. What is the effect of this approach on system efficiency?
5. How can this approach be implemented with hardware and software in a real-world de-icing system?

Questions 1-4 will be evaluated and answered in this chapter using a combination of finite element modeling and experimental testing, and question 5 will be addressed in Chapter 6. Finite element models of plate and airfoil structures will be considered and the results of experimental de-icing tests and laser vibrometer measurements on plate specimens will be presented.

5.2 Finite Element Modeling Details

The fundamental physical principles at work in an ultrasonic de-icing system are the coupled electrical and mechanical responses of a piezoelectric material to an applied electrical potential and the response of an elastic structure to an applied steady-state harmonic loading function.

These phenomena are governed by several sets of partial differential equations, and solving these equations for complex geometries and configurations would be, in all practicality, impossible. The finite element method, which involves discretizing a structure into a number of small constituent elements with discrete nodes at which these equations are applied and solved, fulfills this need [79, 80]. Therefore finite element modeling methods were applied to simulate the response of complex plate and airfoil structures with accreted layers of ice to excitation by bonded piezoelectric actuators. The commercial finite element method (FEM) package ABAQUS/STANDARD version 6.10-2, referred to simply as ABAQUS from this point, was utilized for the analyses described in this chapter.

Direct-Solution Steady-State Dynamic Analysis

The ABAQUS finite element (FE) software has the ability to perform many different types of analyses. Since the phenomenon of interest is steady-state ultrasonic vibration, and since the transient effects will not be considered, only two analysis procedures offered by ABAQUS are worth serious consideration; these analysis methods are the mode-based steady-state harmonic response analysis and the direct-solution steady-state harmonic response analysis. The mode-based method extracts the eigenmodes of the system in an initial step and then solves the dynamic equations in terms of the eigenvector solutions. The direct-solution method, on the other hand, directly solves the dynamic equations in terms of the physical degrees of freedom of the model. For linear systems with material properties that are independent of frequency, the subspace-based method is generally more computationally efficient [81]; however, due to the need for coupled electromechanical piezoelectric elements in the model, the direct solver must be used [82]. Fortunately, the direct method, although more computationally expensive, is generally more accurate than the mode-based method [81]. Additionally, for the high frequencies (up to 60 kHz) at which the de-icing analyses are performed, the mode-based methods would have required a very large number of natural mode solutions to accurately characterize the vibration response of the structure and may have thus been much more computationally expensive than for traditional lower-frequency analyses.

The formulation for the steady-state dynamic direct (SSDD) method is based on the dynamic virtual work equation [82]

$$\int_V \rho \delta \mathbf{u} \cdot \ddot{\mathbf{u}} dV + \int_V \rho \alpha_c \delta \mathbf{u} \cdot \dot{\mathbf{u}} dV + \int_V \delta \varepsilon : \boldsymbol{\sigma} dV - \int_{S_t} \delta \mathbf{u} \cdot \mathbf{t} dS = 0, \quad (5.1)$$

in which \mathbf{u} is the displacement vector, \mathbf{t} is the applied traction over surface S_t , V is the volume of the body, ρ is the mass density, α_c and β_c are the mass- and stiffness-proportional Rayleigh damping coefficients, ε is the strain, $\boldsymbol{\sigma}$ is the stress, dot notation is used for partial differentiating with respect to time, and δ is used in the variational sense. This equation can be discretized using FE theory to form

$$\delta \mathbf{u}^N \{ \mathbf{M}^{NM} \ddot{\mathbf{u}}^M + \mathbf{C}_{(m)}^{NM} \dot{\mathbf{u}}^M + \mathbf{I}^N - \mathbf{P}^N \} = 0, \quad (5.2)$$

in which

$$\mathbf{M}^{NM} = \int_V \rho \mathbf{N}^N \cdot \mathbf{N}^M dV, \quad (5.3)$$

$$\mathbf{C}_{(m)}^{NM} = \int_V \rho \alpha_c \mathbf{N}^N \cdot \mathbf{N}^M dV, \quad (5.4)$$

$$\mathbf{I}^N = \int_V \beta^N : \boldsymbol{\sigma} dV, \quad (5.5)$$

$$\mathbf{P}^N = \int_{S_t} \mathbf{N}^N \cdot \mathbf{t} dS, \quad (5.6)$$

represent the mass matrix, damping matrix, internal load vector, and external load vector, respectively. For the SSDD procedure, small linear perturbations are assumed and applied, yielding equation (5.2) in a new form

$$\delta \mathbf{u}^N \{ \mathbf{M}^{NM} \ddot{\mathbf{u}}^M + (\mathbf{C}_{(m)}^{NM} + \mathbf{C}_{(k)}^{NM}) \dot{\mathbf{u}}^M + \mathbf{K}^{NM} \mathbf{u}^M - \mathbf{P}^N \} = 0, \quad (5.7)$$

in which the stiffness matrix \mathbf{K}^{NM} and the stiffness damping matrix $\mathbf{C}_{(k)}^{NM}$ are defined as

$$\mathbf{K}^{NM} = \int_V \left[\frac{\partial \beta^N}{\partial \mathbf{u}^M} : \boldsymbol{\sigma}_0 + \beta^N : \mathbf{D}^{el} : \beta^M \right] dV, \quad (5.8)$$

$$\mathbf{C}_{(k)}^{NM} = \int_V [\beta_c \beta^N : \mathbf{D}^{el} : \beta^M] dV. \quad (5.9)$$

The perturbation changes in displacement and external force can be written, assuming harmonic excitation at frequency ω , in the format

$$\Delta \mathbf{u}^M = [\Re(\mathbf{u}^M) + i \Im(\mathbf{u}^M)] e^{i\omega t}, \quad (5.10)$$

$$\Delta \mathbf{P}^N = [\Re(\mathbf{P}^N) + i \Im(\mathbf{P}^N)] e^{i\omega t}. \quad (5.11)$$

Substitution of these expressions into equation (5.7) and converting into matrix form yields

$$\begin{bmatrix} \Re(A^{NM}) & \Im(A^{NM}) \\ \Im(A^{NM}) & -\Re(A^{NM}) \end{bmatrix} \begin{Bmatrix} \Re(u^M) \\ \Im(u^M) \end{Bmatrix} = \begin{Bmatrix} \Re(P^N) \\ -\Im(P^N) \end{Bmatrix}, \quad (5.12)$$

in which the symmetric real and imaginary parts of the matrix A^{NM} are defined as

$$\Re(A^{NM}) = K^{NM} - \omega^2 M^{NM}, \quad (5.13)$$

$$\Im(A^{NM}) = -\omega (C_{(m)}^{NM} + C_{(k)}^{NM}). \quad (5.14)$$

ABAQUS solves matrix equation (5.12) independently for each frequency requested during the steady-state dynamic analysis procedure.

Airfoil Model Overview

The airfoil, illustrated in Figure 55 and Figure 56, modeled for this analysis is a 32” half airfoil section modeled with a symmetric boundary condition on one end and based on an engine inlet design by a leading aircraft manufacturer. The specifics of the airfoil design and the manufacturer are withheld as the design is proprietary and these details are not relevant to the results. The thickness of the airfoil is 0.080”. A 0.20”-thick ice layer was accreted around a region of the leading edge dictated as typical by the manufacturer. Eight piezoelectric disks were modeled on the airfoil in three different configurations, which will be compared in a later section. The ¼” strip around the outer edge of the airfoil, with the exception of the symmetric boundary condition edge, was modeled with a “clamped” boundary condition, which sets the translational and rotational degrees of freedom to zero in order to simulate rigid mounting to a frame.

The details of the modeling parameters used for the phasing analyses are provided below; however this is just an overview. The complete modeling and analysis process is quite lengthy and complicated, so a step-by-step walk through of the model creation, submission, and post-processing methodology is provided in Appendix A and several MATLAB codes required for the analysis are provided in Appendix B. These materials should allow others, with a reasonable degree of effort, to replicate the methods employed here.

It should be noted that some of these methods, specifically the piezoelectric actuator modeling, was first developed and verified by Soltis, Palacios, and Overmeyer at Penn State University. The work in this thesis expands upon those efforts.

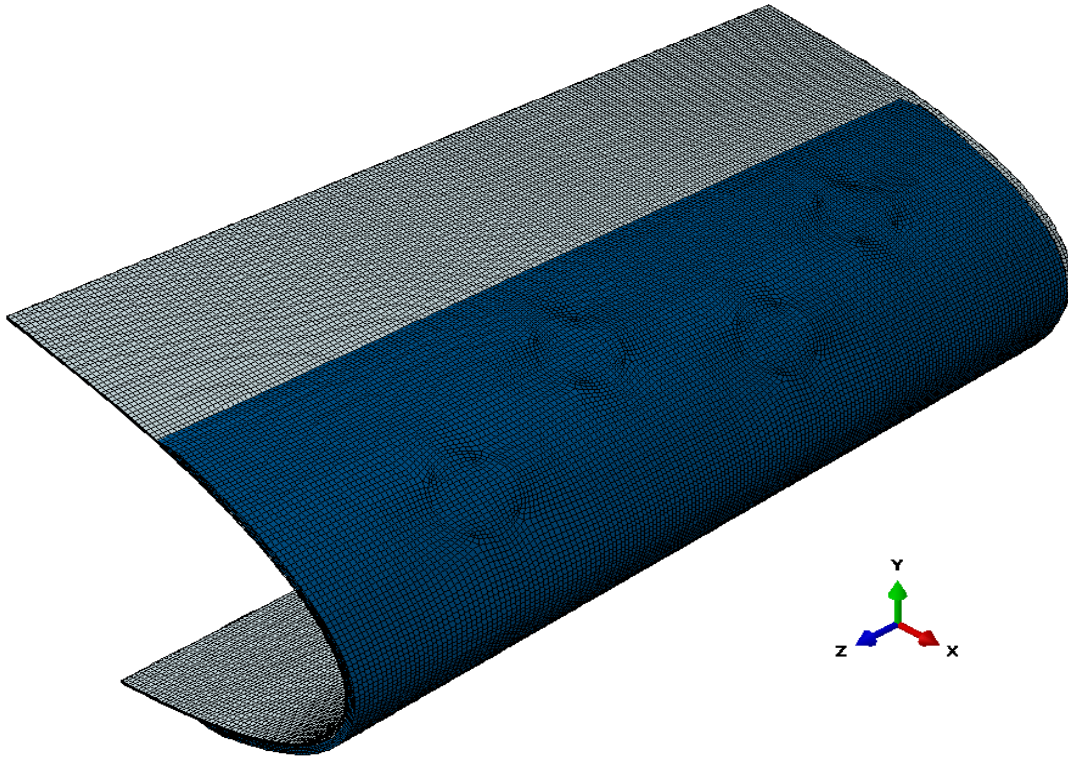


Figure 55 Meshed airfoil model, isometric view.

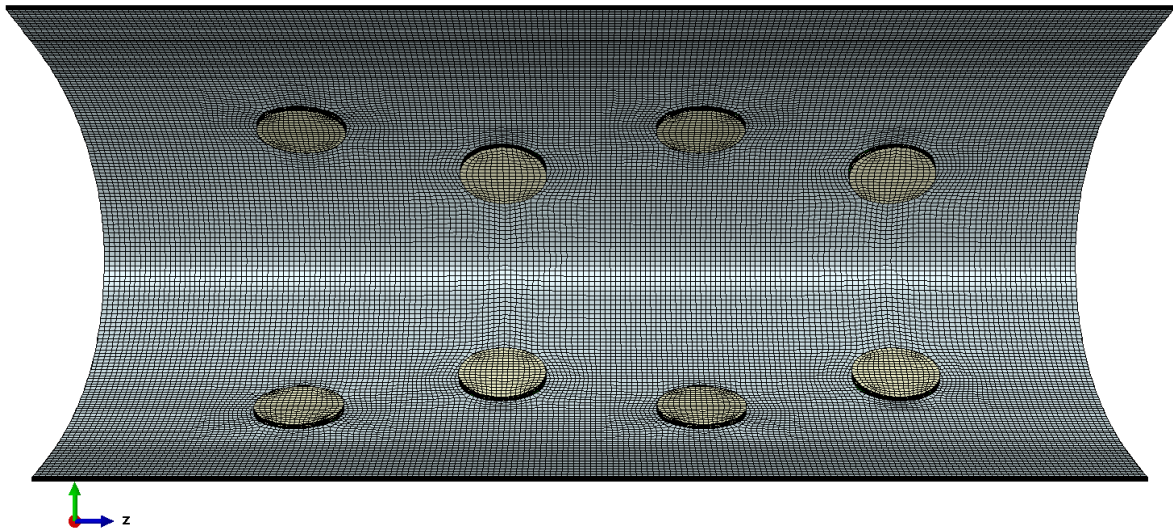


Figure 56 Meshed airfoil model, back view; note that this image shows 2" actuators, while 2.5" actuators were used for the final analysis.

Material Properties

The materials included in the modeling of the de-icing system were aluminum, ice, epoxy, and PZT-4. The material properties used are nearly identical to those used during prior Penn State de-icing research by Palacios [15, 27, 28], Zhu [24], and Overmeyer [63, 66]. The aluminum, ice, and epoxy were all modeled as isotropic materials according to the material properties in Table 6.

Table 6 Summary of the isotropic material properties used in the finite element analyses [28, 66].

Material	E (GPa)	ν	ρ (kg/m ³)	β
Aluminum (6061-T6)	70.0	0.33	2700	0.005/ ω
Ice	9.10	0.28	915	0.005/ ω
Epoxy (FM94-1)	2.24	0.36	915	4.00 x 10 ⁻⁷

Here E is Young's modulus, ν is Poisson's ratio, ρ is mass density, and β is the stiffness-proportional damping coefficient, which is modeled as a function of ω , the angular frequency of activation. The material properties used for aluminum were those of 6061-T6. The properties of ice can vary dramatically. The epoxy material properties were those of FM94-1, which is the film epoxy used for the actuator fabrication and integration method detailed in Chapter 3. Since the purpose of this modeling was not to directly model a particular specimen or case, but rather to identify trends and patterns based on a realistic representative specimen, the specific ice and material properties are not critical, as long as they are realistic and consistent between models.

The piezoelectric material properties are more complex than those of the isotropic materials detailed in Table 6. APC-841 is a proprietary version of PZT-4 produced by APC International and selected for experimental use during this research due to its slightly improved material properties over APC-840, which is the traditional version of PZT-4 available through APC International [64]. PZT-4 was selected for modeling because it is the variety of lead-zirconate-titanate (PZT) that was shown to perform best in prior de-icing research [15, 24, 27, 28, 63, 66]. PZT-4, also known as Navy Type I, is typically used for high-power applications in which large amounts of ultrasonic energy and strong resonance are required, including ultrasonic cleaning, sonar applications, high power actuators, and vibratory ultrasonic motors [64]. PZT-4 is

characterized by a high piezoelectric voltage constant, a high mechanical quality factor, and a high stiffness compared to other common varieties of PZT [64]. The material properties in Table 7 were used for the purposes of modeling the APC-840 piezoelectric material [64].

Table 7 Orthotropic elastic and piezoelectric material properties used for modeling APC-841

Properties	Format	Values
Elasticity Matrix	$\begin{bmatrix} C_{11} & C_{12} & C_{13} & 0 & 0 & 0 \\ C_{12} & C_{22} & C_{23} & 0 & 0 & 0 \\ C_{13} & C_{23} & C_{33} & 0 & 0 & 0 \\ 0 & 0 & 0 & C_{44} & 0 & 0 \\ 0 & 0 & 0 & 0 & C_{55} & 0 \\ 0 & 0 & 0 & 0 & 0 & C_{66} \end{bmatrix}$	$\begin{bmatrix} 134.8 & 74.9 & 74.9 & 0 & 0 & 0 \\ 74.9 & 76.7 & 116.4 & 0 & 0 & 0 \\ 74.9 & 116.4 & 134.8 & 0 & 0 & 0 \\ 0 & 0 & 0 & 29.1 & 0 & 0 \\ 0 & 0 & 0 & 0 & 24.4 & 0 \\ 0 & 0 & 0 & 0 & 0 & 24.4 \end{bmatrix} \text{ GPa}$
Relative Dielectric Constants	$[\epsilon_{11} \quad \epsilon_{22} \quad \epsilon_{33}]/\epsilon_0$	[1475 1475 1300]
Piezoelectric Charge Constants	$\begin{bmatrix} 0 & 0 & 0 & 0 & d_{15} & 0 \\ 0 & 0 & 0 & d_{15} & 0 & 0 \\ d_{13} & d_{13} & d_{33} & 0 & 0 & 0 \end{bmatrix}$	$\begin{bmatrix} 0 & 0 & 0 & 0 & 450 & 0 \\ 0 & 0 & 0 & 450 & 0 & 0 \\ -109 & -109 & 300 & 0 & 0 & 0 \end{bmatrix} \times 10^{-12} \text{ C/N}$
Density	ρ	7500 kg/m ³
Damping	β	0.005/ ω

Elements and Meshing

The models used a combination of three-dimensional stress/displacement continuum elements and three dimensional piezoelectric continuum elements. The stress/displacement elements used for the aluminum, epoxy, and ice were 8-node linear brick elements with reduced integration (C3D8R) with hourglassing control, such as the one illustrated in Figure 57 [81]. These elements were required to overcome memory limitations for the very large three-dimensional airfoil models, which each required nearly 300,000 elements, 50 GB of memory, and over 25 hours to run for 25 frequency points; a total of 432 of these models were executed for the airfoil phasing analysis (4 successive frequency sweeps for 108 models to cover the entire frequency range of interest). The piezoelectric elements used for the PZT-4 were 8-node linear brick elements (C3D8E), which have the same geometry as the elements illustrated in Figure 57, but with an additional degree of freedom for the electrical displacement.

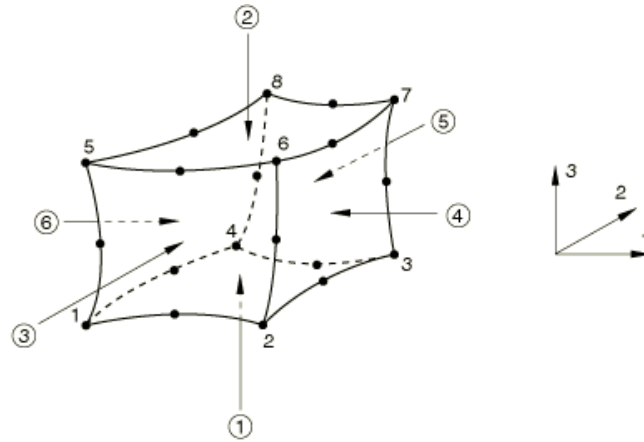


Figure 57 8-node linear brick element [81]

Structured meshing was utilized as often as possible in the model to ensure high-quality meshing. Figure 56 and Figure 55 illustrate the mesh for the large airfoil models. Five elements were utilized through the thickness of the actuators, the airfoils, and the ice, while three layers were utilized through the epoxy, as shown in Figure 58. In the frequency range considered in the model (25-45 kHz), the shortest wavelengths expected would be those of the A_0 guided wave mode in the aluminum airfoil at 45 kHz. The A_0 mode for this structure at this frequency would have a phase velocity of 2218 m/s, which would correspond to a minimum wavelength of 49 mm. The general mesh seeding size was 4.25 mm, more than a factor of 10 smaller than the smallest expected wavelengths.

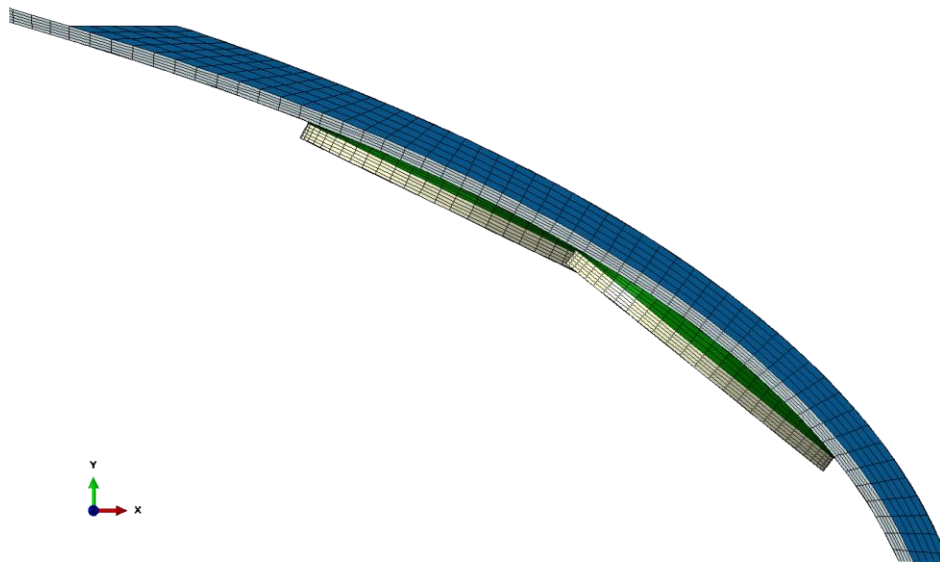


Figure 58 Meshed airfoil model, edge view.

Constraints between Materials at Interface Layers

Since multiple entities and materials were included in the finite element models, it was necessary to dictate the interactions between these entities to fully define the problem in ABAQUS. A commonly-employed method, and one that was used in prior ultrasonic de-icing research, was to utilize the “mesh tie” constraints provided by ABAQUS. The mesh tie constraint is a surface-based constraint that allows two nearby surfaces with non-coincident nodes to be coupled together during a simulation. This requires the user to define master and slave surfaces. ABAQUS then utilizes the translational and rotational degrees of freedom of the nodes on the master surface to dictate the degrees of freedom on the slave surface, while allowing some position tolerance (usually 5-10% by default). However, this approach can be problematic and in order to minimize such problems and to maximize the accuracy of the models at the interfaces, a different approach was used. Instead of creating multiple independent parts and assembling them, the airfoil was constructed and the epoxy, actuators, and ice were extruded from it, then partitioned. This approach, paired with careful assembly partitioning prior to meshing, ensures that the interfaces between the actuators and epoxy, the epoxy and airfoil, and the airfoil and ice all have shared nodes so that no additional tie constraints are required. For the details of this method, see the procedure in Appendix A.

Piezoelectric Modeling Conditions

The modeling method applied to the piezoelectric actuators is identical to the method adopted by Overmeyer [66]. This approach involved applying an equation constraint to ensure uniform voltage across the top and bottom surfaces of the actuators, respectively. These equations are

$$q_S^n - q_P^n = 0, \quad (5.15)$$

in which q represents charge, the subscripts S and P denote the surface and point sets (defined in Figure 59), and the superscript n represents any individual actuator top or bottom surface. The bottom surface of each actuator was selected as the “ground” and held at zero voltage with an electric boundary condition, while a harmonic voltage was applied to the top electrode during simulation. For the details of this method, see the procedure in Appendix A.

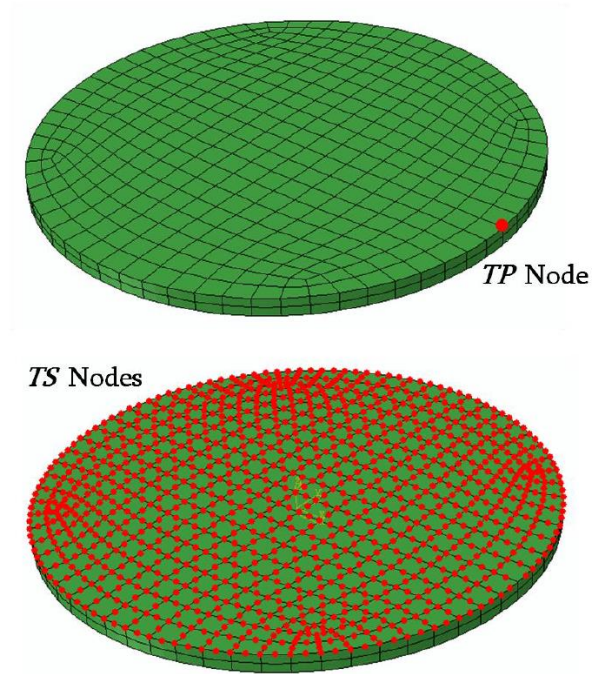


Figure 59 Surface and point node sets upon which the equation constraints are applied to ensure common voltage across the entire electrode surface [66].

Model Output Variables

The output information desired from the models included the impedance of the actuators and the shear stresses on the interface of the airfoil. In order to collect this data, the following variables were requested for output:

1. “PHCHG” for all nodes in the node sets defined on the top surface of each actuator.
2. “PHS13” for all the elements in the element set defined on the ice interface
3. “PHS23” for all the elements in the element set defined on the ice interface

Output variable PHCHG outputs the magnitude and phase of the charge in the node set on the top of each actuator. It is critical that this variable be used and not “RCHG”, which only outputs the real component of the charge from a SSDD analysis step. Erroneously collecting this output variable would lead to underestimation of the charge and inaccuracies in almost all cases since the charge is generally not in phase with the excitation.

The impedance was calculated from the measured charge variable using the definition of impedance and charge

$$|Z| = \left| \frac{V}{I} \right| = \left| \frac{V}{\dot{q}} \right| = \left| \frac{V}{\omega q} \right|, \quad (5.16)$$

in which V is the voltage applied by the electric boundary condition in the FE model, q is the charge calculated from the model, and ω is the angular frequency at which the analysis was performed.

Output variables PHS13 and PHS23 output the σ_{13} and σ_{23} shear stresses in the element set on the interface between the ice and the airfoil. Just as with the charge output variable, it is critical that these specific outputs be utilized during a SSDD analysis and not the standard S13 and S23 outputs, which only provide the real parts of the stresses. Therefore, once again, if the magnitude and phase are not known, the stresses will be underestimated and inaccurate since the stresses are, in general, out of phase with the excitation.

The downside of requiring the magnitude and phase variables is that ABAQUS cannot print these to the output database (.odb), but rather only to the data file (.dat). Since ABAQUS cannot load and analyze data from the .dat file, a MATLAB script had to be written to read the .dat files line-by-line and extract the information for each node and element. The manner in which this is done is outlined in the “Finite Element Post-Processing” section below, and the complete MATLAB scripts are provided in Appendix B.

In addition to outputting the correct variables, it is also crucial that the local coordinate system of each element in the airfoil is appropriately defined so that the “3-direction” is consistently oriented parallel to the surface normal vector. This can be achieved with relative ease in ABAQUS by defining discrete material orientations to the ice and airfoil elements such that the “normal” vector is defined according to the airfoil surface and the “primary” vector is defined according to the edge of the airfoil, as is illustrated in Figure 60. Failure to account for this coordinate system rotation in the model or in the post-processing will lead to completely erroneous shear stress values for the interface. Again, see the step-by-step procedure outlined in Appendix A for more details of this method.

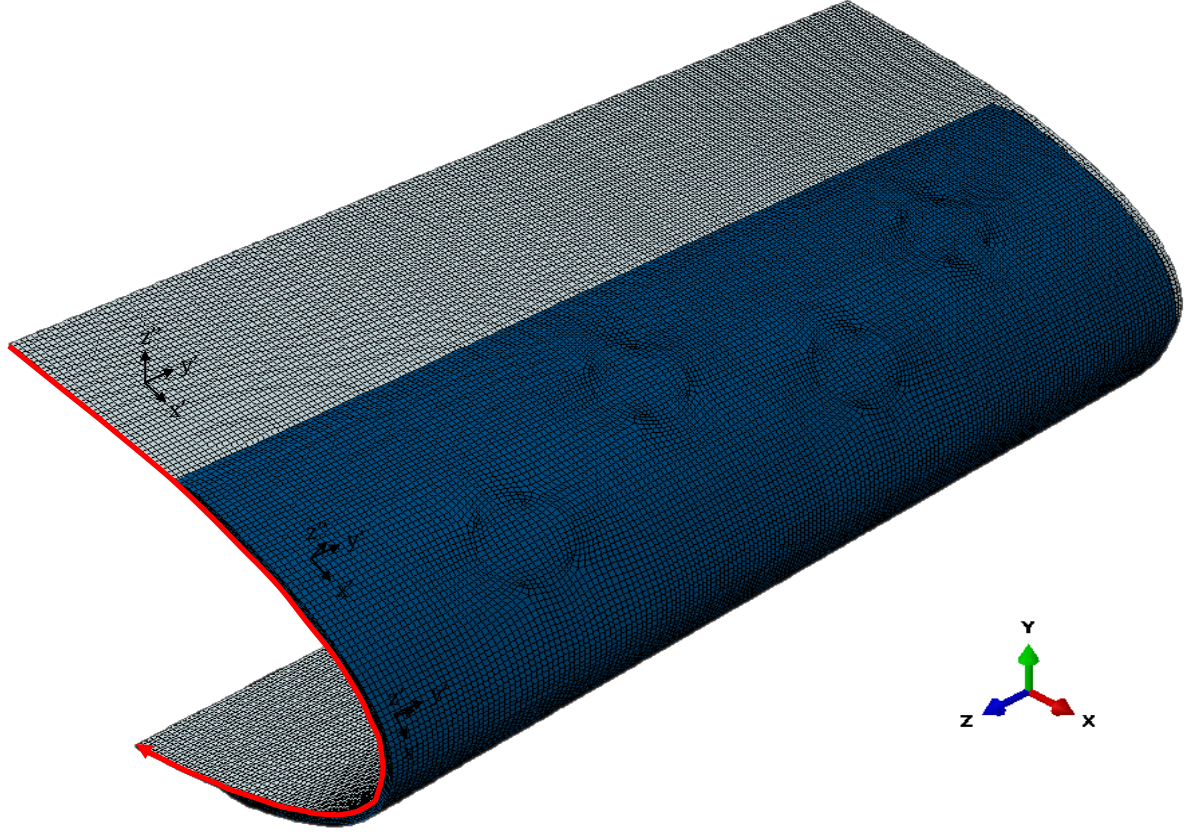


Figure 60 Illustration of the “normal surface” (green) and “primary vector” (red) used to define the local coordinate systems (black) for each element in the designated set; the global coordinate system is shown in the lower right corner for reference.

The FE models were each set up with constant voltage across the actuators, but in reality this does not ensure constant power, since the impedance is a function of frequency. In order to compare one model to another or one frequency or phase to another, some type of power normalization based on the calculated impedance curve is required. This must, of course, be performed in post processing since the impedance curve is calculated from the FE results themselves. The formula for power as a function of voltage and impedance is

$$P = IV = \frac{V^2}{|Z|}. \quad (5.17)$$

Therefore power normalization can be achieved by calculating the voltage required to maintain a constant power level relative to the constant voltage applied to the actuators. The ratio of the required voltage for power normalization to the applied voltage can be used to scale the results at

each frequency [15, 24, 66]. This is acceptable in theory, but in reality the output power from an amplifier is not constant. The forward power the amplifier produces is dependent on the impedance of the load that it is driving, and the amount of transmitted (non-reflected) power depends on how well the load is impedance matched to the amplifier. This power normalization method is especially problematic for high impedance values, at which it theoretically predicts the response of the system to be incredibly large, even at anti-resonances. However, these responses could never be achieved due to the impedance mismatch of the amplifier and the inability of the amplifier to produce sufficient forward power into such loads. These limitations must be considered when analyzing any data for which this type of power normalization is applied.

Independent Actuator Analysis Method

A novel method of independent actuator analysis was used to efficiently investigate the actuator phasing phenomena of interest. Since a large number of unique phasing and frequency combinations are possible for a multi-actuator de-icing system, it would be greatly advantageous to develop a method of combining the influence of individual actuators in post-processing calculations, which would allow the impedance and shear stress results to be calculated for any arbitrary phasing scheme from a subset of finite element model results. To accomplish this, a method had to be developed to recombine the shear stress results and the impedance results.

Assuming a linear vibration response, the stress field induced by a single actuator is independent of the stress field induced by any other actuators. Therefore if the magnitude and phase of the shear stress fields, σ_{13} and σ_{23} , induced at the interface by each individual actuator driven at frequency f , then the resultant shear stress fields, σ_{13}^{net} and σ_{23}^{net} , induced by N actuators with individual driving voltages, having amplitudes V_n and phases φ_n , is a superposition of the individual fields calculated by

$$\sigma_{13}^{net} = \sum_{n=1}^N V_n \sigma_{13}^n e^{i\varphi_n}, \quad (5.18)$$

$$\sigma_{23}^{net} = \sum_{n=1}^N V_n \sigma_{23}^n e^{i\varphi_n} \quad (5.19)$$

These can be combined to calculate the net shear stress of the phased system

$$\tau^{net} = \sqrt{\left(\sum_{n=1}^N V_n \sigma_{13}^n e^{i\varphi_n}\right)^2 + \left(\sum_{n=1}^N V_n \sigma_{23}^n e^{i\varphi_n}\right)^2} \quad (5.20)$$

Note that the calculation of the net shear stress τ^{net} can only be made from the net shear stress components σ_{13}^{net} and σ_{23}^{net} . Attempting to calculate the net shear stress from each independent model and recombine them using equation (5.21) is incorrect.

$$\tau^{net} \neq \sum_{n=1}^N V_n \tau_n e^{i\varphi_n} \quad (5.21)$$

This is incorrect based on the following reasoning. Consider two stress fields, A and B, which are superimposed to form a stress field, A+B:

$$\sigma_{13}^{A+B} = \sigma_{13}^A + \sigma_{13}^B, \quad (5.22)$$

$$\sigma_{23}^{A+B} = \sigma_{23}^A + \sigma_{23}^B, \quad (5.23)$$

$$\tau^{A+B} = \sqrt{(\sigma_{13}^{A+B})^2 + (\sigma_{23}^{A+B})^2} = \sqrt{(\sigma_{13}^A + \sigma_{13}^B)^2 + (\sigma_{23}^A + \sigma_{23}^B)^2}. \quad (5.24)$$

Equation (5.24) correctly calculates the net shear stress field from the superimposed shear stress components. Prematurely calculating the net shear stress and adding these values yields:

$$\tau^A = \sqrt{(\sigma_{13}^A)^2 + (\sigma_{23}^A)^2}, \quad (5.25)$$

$$\tau^B = \sqrt{(\sigma_{13}^B)^2 + (\sigma_{23}^B)^2}, \quad (5.26)$$

$$\tau^A + \tau^B = \sqrt{(\sigma_{13}^A)^2 + (\sigma_{23}^A)^2 + (\sigma_{13}^B)^2 + (\sigma_{23}^B)^2}. \quad (5.27)$$

Clearly equation (5.27) is not equivalent to equation (5.24). These stress field recombination calculations were verified using a four-actuator plate model, shown in Figure 48 and Figure 62, and comparing the predicted shear stress fields σ_{13} and σ_{23} calculated from the independent actuator analysis results and equation (5.20) to those calculated directly from a finite element model in which the phasing was explicitly applied during excitation. The results of this comparison are provided for a single frequency in Figure 63; other frequencies showed similar agreement.

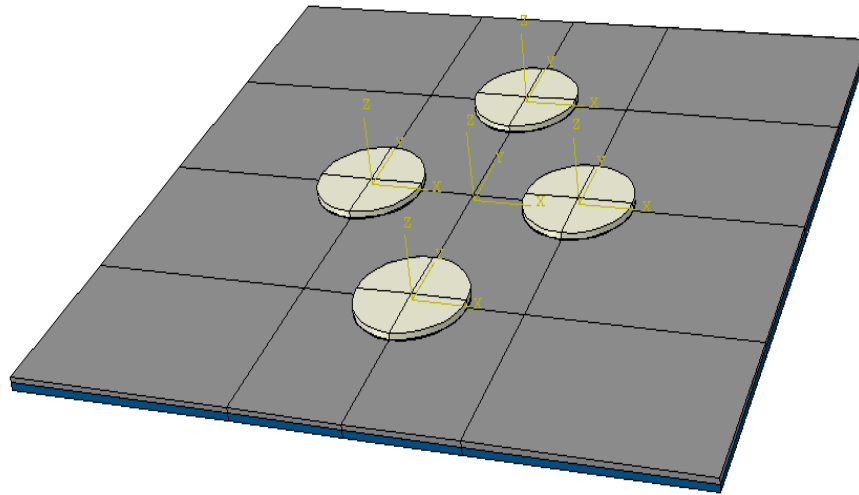


Figure 61 Drawing of the finite element model of a four-actuator de-icing system on a 2-mm aluminum plate with a 3-mm layer of accreted ice used to evaluate the accuracy of the independent actuator analysis method.

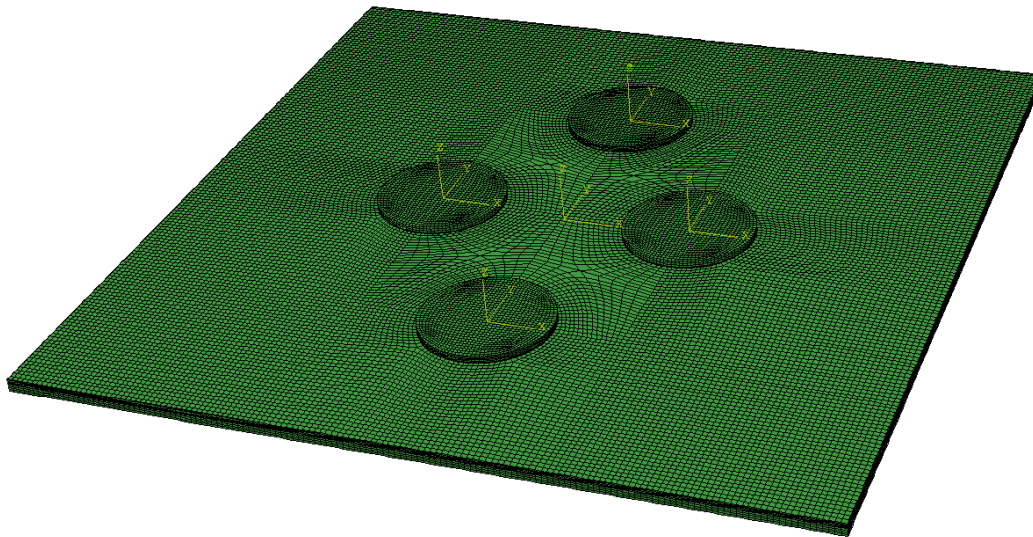


Figure 62 Image of the meshed model shown in the previous figure.

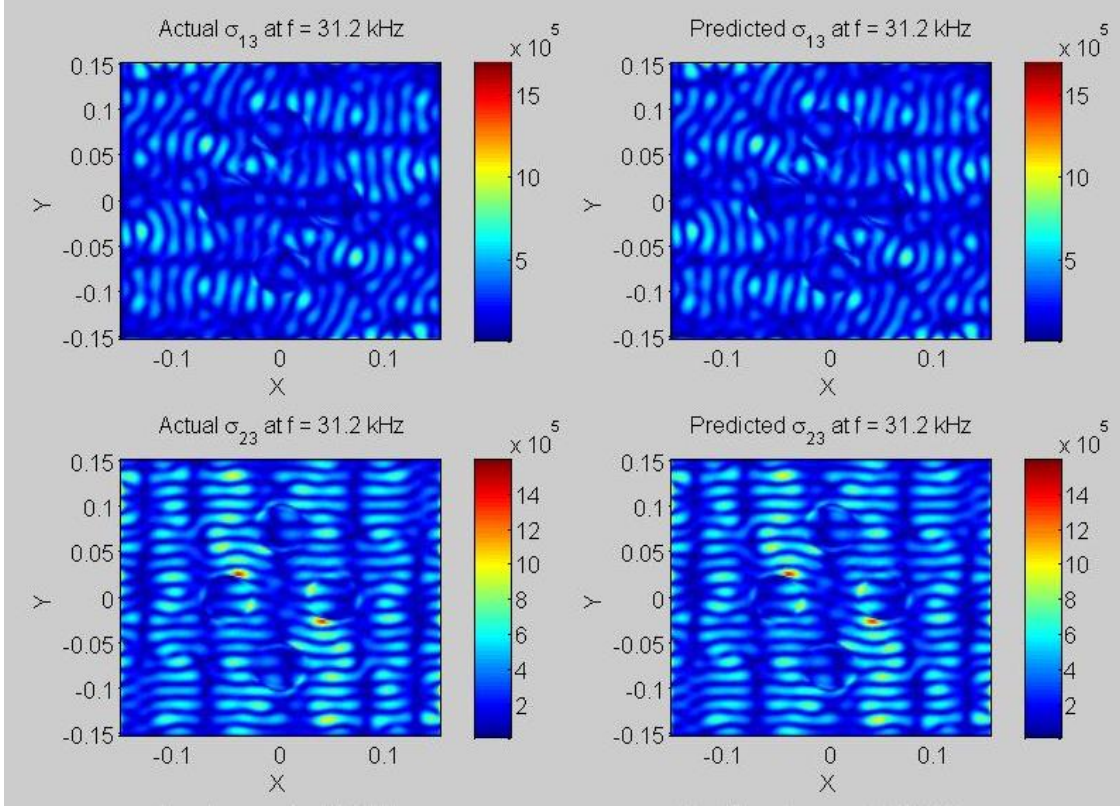


Figure 63 Comparison of the stress fields calculated from (left) a finite element model with direct phasing applied and (right) the independent actuator analysis predictions.

In order to gather the data required for this calculation, N models had to be executed, each with a voltage load applied to only one actuator while the other actuators are “short-circuited” by applying an additional equation constraint

$$q_P^T - q_P^B = 0, \quad (5.28)$$

in which P indicates that the constraints were applied to a single node on each actuator face and T and B indicate the top and bottom faces of the short-circuited actuator(s). For the eight-actuator airfoil, for instance, eight models would be required.

However, as was discussed in Chapter 4: Impedance Analysis, the calculation of the impedance curves cannot be performed from just the impedance data of each actuator individually due to the cross-coupled impedances between actuators. To account for this, additional models had to be executed in accordance with the cross-coupled impedances Z_{nm} . Each cross-coupled impedance term Z_{nm} was calculated by applying a voltage load to actuator n and short-circuiting all other actuators with the exception of actuator m , which was left as an open circuit so that the charge

output data could be calculated and recorded. This approach to calculating Z_{nm} is based on the derivation of the cross-coupled impedances in Chapter 4: Impedance Analysis and corroborated by the multi-port network impedance matrix theory [72]

$$Z_{nm} = \left. \frac{V_n}{I_m} \right|_{V_k=0}, \quad (5.29)$$

in which the voltage is held at zero for all actuators $k \neq n, m$. The method of combining these impedance elements to calculate the phased impedance of an actuator set was derived and verified in Chapter 4 and is repeated here

$$Z_{eq} = \left[\sum_{m=1}^N \sum_{n=1}^N \frac{1}{|Z_{nm}|} e^{-i(\varphi_n + \varphi_m)} \right]^{-1}. \quad (5.30)$$

This requires an additional $\frac{1}{2}(N^2 - N)$ in addition to the N models run for the shear stress fields and direct impedances for a total of $\frac{1}{2}(N^2 + N)$ models. An example of the number of models required to fully characterize the system is provided for several actuator counts in Table 5. However, once the calculations are completed, they can be recombined in a much greater number of possible phasing combinations.

Table 8 Number of impedance measurements required to calculate the net impedance of a given number of actuators in a single set.

Number of Actuators	Finite Element Models Required
2	3
4	10
6	21
8	36
10	55
12	78
14	105
16	136

The number of phasing combinations possible for a system depends on the number of actuators and the phasing increment that is to be used. The phasing increment is the increment of the phase delays applied between actuators, which can be any phasing value that can be multiplied by an

integer to equal 360° . The number of unique phase delay combinations n_φ for an N actuator system with $\Delta\varphi$ phase delays is described by

$$n_\varphi = \left(\frac{360^\circ}{\Delta\varphi} \right)^{1-N}, \quad (5.31)$$

and examples are provided in Table 9, which does not account for the reduction in unique phasing combinations after the effects of geometric symmetry are considered.

Table 9 Phasing increments and the number of unique phasing combinations that could be utilized in a four-actuator system

Phasing Increment	2 Actuators	4 Actuators	6 Actuators	8 Actuators	10 Actuators
360°	1	1	1	1	1
180°	2	8	32	128	512
120°	3	27	243	2187	19683
90°	4	64	1024	16384	262144
60°	6	216	7776	279936	10077696
30°	12	1728	248832	35831808	5.16E+09
15°	24	13824	7962624	4.59E+09	2.64E+12
5°	72	373248	1.93E+09	1E+13	5.2E+16
1°	360	46656000	6.05E+12	7.84E+17	1.02E+23

It can be easily determined whether it is more efficient to simply run a finite element model for each actuator phasing configuration or to utilize the independent actuator analysis detailed above using the inequality

$$\frac{360^\circ}{\Delta\varphi} \leq \sqrt[1-N]{\frac{1}{2}(N^2 + N)}. \quad (5.32)$$

The independent actuator analysis method was used to calculate the phased impedances and phased stress fields for the analyses that follow in order to make these analyses more efficient and practical.

Validation of the Quality of the Airfoil Finite Element

The quality of the finite element model of the airfoil, as detailed in the preceding sections, can be verified based on the following merits:

- At least 5 elements were utilized through the thickness of the airfoil, ice, and actuators
- At least 3 elements were utilized through the thickness of the epoxy
- The element size in the other dimensions was seeded at 4.25 mm, which is less than 1/10 the smallest expected wavelength in the model
- All layers were fully connected; no tie constraints were utilized
- The impedance minima generally agree between model and experiment, despite some differences in bonding layer and configuration

The airfoil that was eventually fabricated based on these models had some slight differences in terms of actuator configuration and bonding method. Specifically, aluminum mediator wedges were used to replace much of the thick epoxy layer between the actuators and the airfoil. This will be discussed in a later section. However, despite these differences, the impedance minima generally agree between the model and the experimental measurements from the actual airfoil, as shown in Table 10 and Figure 64.

Table 10 Comparison of the measured and predicted impedance minima for the airfoil actuators.

Measured			FEM		
	$Z_{\min} (\Omega)$	$f_{\min} (\text{kHz})$		$Z_{\min} (\Omega)$	$f_{\min} (\text{kHz})$
Actuator 1	175.9	37.9	Actuator 1	131.6	34.8
Actuator 2	126.6	37.3	Actuator 2	120.3	37.6
Actuator 3	125.8	37.5	Actuator 3	109.6	37.6
Actuator 4	149.9	37.7	Actuator 4	123.2	37.8
Actuator 5	178.1	37.2	Actuator 5	119.2	38
Actuator 6	118.9	37.2	Actuator 6	112.7	38.4
Actuator 7	132.4	37.1	Actuator 7	116.6	36.8
Actuator 8	135.2	37.1	Actuator 8	120.3	36.6

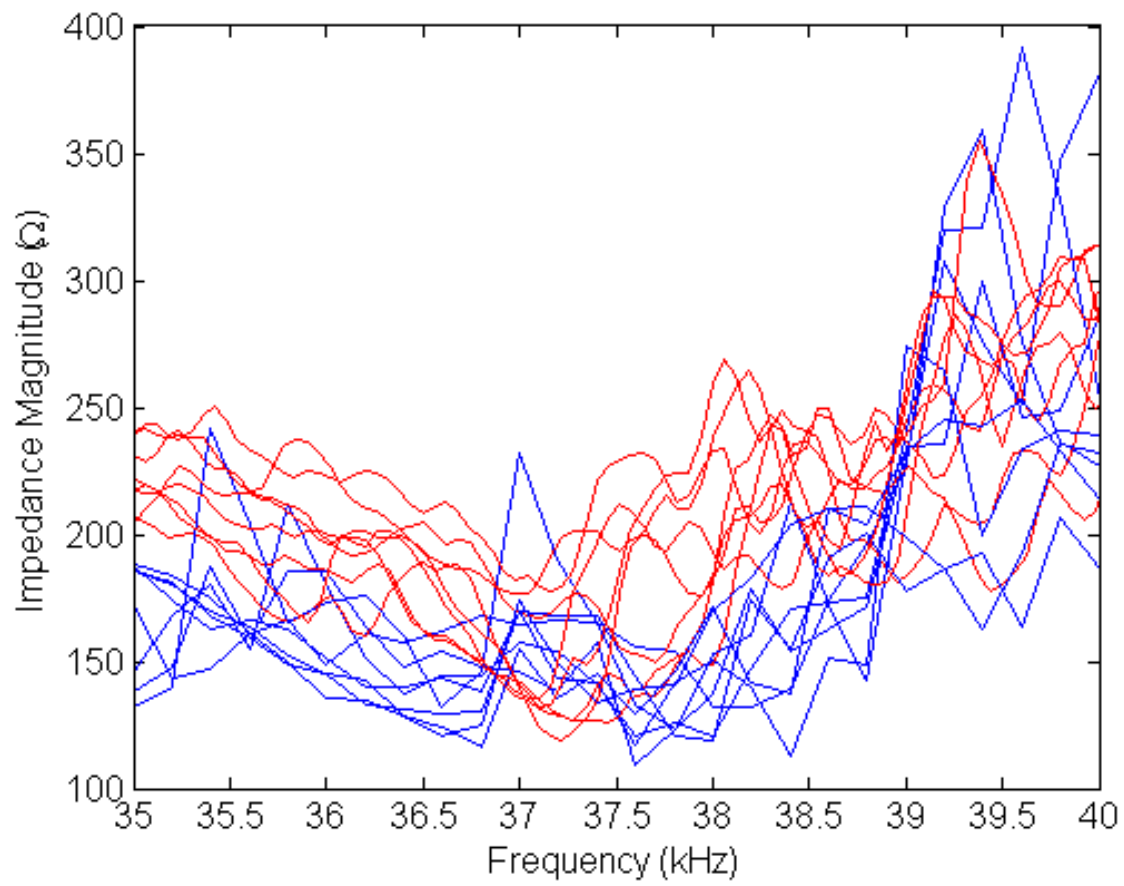


Figure 64 Comparison of the experimentally measured impedance minima (red) for each actuator on the airfoil and the values predicted from the finite element model (blue).

5.3 Phasing Optimization with a Genetic Algorithm

A series of FE models were executed using the four-actuator titanium-ice plate model shown in Figure 48 to investigate the answers to the first question from Section 5.1 of this chapter: “What type of phase shifts should be applied, to what actuators, and in how many combinations?”. This question is partially addressed in terms of practicality by Table 6. If we chose to sweep the majority of unique phase delays to achieve the most shear stress coverage possible, this would quickly become impractical with phase delay increments any smaller than 180° , even for systems with as little as 5 or 6 actuators. The goal of the FE analysis described in this section is to address the need for sweeping a large number of phase delays and to begin to determine if a small number of phase delays, such as those available with only a 180° phasing increment, are sufficient.

In order to determine the relationship between stress coverage and phasing combinations, the 8 independent actuator models required for a complete characterization of the four-actuator system were executed. This data was saved and a genetic algorithm code was developed to attempt to optimize a set of phasing combinations in a way that maximizes the shear stress coverage of the system. This optimization was conducted under several combinations of phasing increment value and total number of allowable phasing combinations. Phasing increments of 30° , 60° , 90° , and 180° were considered, and anywhere from 1 to 8 phasing combinations were allowed for optimization. The final stress coverage, after all phasing combinations for that set of criteria were considered, was then plotted and compared.

Genetic Algorithm

Genetic algorithms belong to a class of adaptive stochastic optimization algorithms [83] that were first used by Holland in 1975 [84]. These algorithms attempt to optimize a solution based on the biological principles of natural selection. Just as in natural evolution, a genetic algorithm selects individuals from a population to act as parents for subsequent generations. Parent solutions that correspond with a higher value of the fitness function will be favored over weaker parents, and children share a mixed set of characteristics based on those of the parents. After a series of generations, the genetic algorithm trends toward an optimized solution. Genetic algorithms (GAs) have several characteristics that make them well suited for the phasing

combination optimization task described in this section, which is why they were selected over other optimization methods.

1. GAs work well for optimizing discrete or integer-based solutions. The solutions for the phasing optimization problem are vectors of unique phasing permutations, neither of which can be represented as continuous functions [85].
2. The phasing vectors are comprised of several unique phasing combinations that are superimposed to improve full structural coverage, which means that each phasing vector solution is comprised of a series of characteristic traits (each phasing combination). Therefore traits (phasing combinations) that yield excellent stress coverage and/or high levels of stress will be favorably weighted and thus will be likely to be passed on to subsequent solution generations. Therefore the concept of phasing vector optimization follows very closely to the logic of the GA, in which the quality of a solution is based on its constituent characteristics.
3. GAs utilize large random populations of solutions so that high-dimensionality problems (such as the optimization of an 8-component series of phasing combinations from a possible set of 1728 unique candidates yielding 1.94×10^{21} unique combinations) are more likely to be well-optimized than if single-point solutions are considered.

GAs require a set or domain of possible solutions with constraints within which it can operate, a set of initial conditions, a set of reproduction rules, and a fitness function to evaluate the quality of each solution in each generation. Each of these factors is discussed in the following paragraphs.

The domain of possible solutions for the phasing optimization problem are all unique non-repeating series of M_ϕ phasing combinations selected from the set of n_ϕ unique phasing combinations that exist for the actuator system and phasing parameters selected. For the phasing optimization analyses detailed here, the number of phasing combinations, M_ϕ , that were considered ranged from 1 (no phasing applied during de-icing) to 8 (eight phasing combinations successively applied during de-icing). The phasing parameter that determined the number of unique phasing combinations for the four-actuator system modeled here is simply the phasing increment, $\Delta\phi$, which determines the number of unique phasing combinations using equation

(5.31). Table 9 shows that for a four-actuator system, the number of unique phasing combinations, n_ϕ , using 180° , 90° , 60° , and 30° increments will be 8, 64, 216, and 1728, respectively. The complete possible population set size, P_{max} , for all M_ϕ unique non-repeating combinations of these n_ϕ phases is given by

$$P_{max} = \frac{n_\phi!}{(n_\phi - M_\phi)!(M_\phi!)} \quad (5.33)$$

Table 11 summarizes the complete population set size based on the variables considered in this analysis. Here it is apparent that the optimization of the 180° phasing increment case is much simpler than the optimization of cases with smaller phasing increments, particularly for more than a few possible phasing combinations.

Table 11 Summary of total population set sizes for the various parameters considered during the genetic algorithm optimization of the phasing combination problem for the four-actuator de-icing panel model.

	$M_\phi = 1$	$M_\phi = 2$	$M_\phi = 3$	$M_\phi = 4$	$M_\phi = 5$	$M_\phi = 6$	$M_\phi = 7$	$M_\phi = 8$
$n_\phi = 180^\circ$	8	28	56	70	56	28	8	1
$n_\phi = 90^\circ$	64	2016	41664	6.4×10^5	7.6×10^6	7.5×10^7	6.2×10^8	4.4×10^9
$n_\phi = 60^\circ$	216	23220	1.7×10^6	8.8×10^7	3.7×10^9	1.3×10^{11}	4.0×10^{12}	1.0×10^{14}
$n_\phi = 30^\circ$	1728	1.5×10^6	8.6×10^8	3.7×10^{11}	1.3×10^{14}	3.7×10^{16}	9.0×10^{18}	1.9×10^{21}

The initial population must be at least as large as the total number of variables, which in this case is M_ϕ . Since the size of each subsequent generation grows exponentially, a larger initial population size will dramatically increase the computational time of the algorithm. A balance between consistency and run time was found with a starting population of 50, which required nearly 24 hours to complete for the larger values of M_ϕ , which required more iterations to converge and thus required more generations to be created and evaluated.

GAs utilize three sets of reproduction rules [85] to alter the population of solutions from generation to generation. These are the:

1. Selection rules – these rules govern the manner in which parent solutions are selected from the current generation

2. Crossover rules – these rules govern the manner in which traits from the parent solutions are combined to determine (some of) the traits in the child solutions
3. Mutation rules – these rules govern the manner in which random new traits are given to child solutions in addition to those inherited by their parent solutions.

The genetic algorithm used for this analysis is built into the Global Optimization Toolbox in MATLAB. There are a large number of options that can be used to tune the performance of the algorithm, including modifications to the complex reproduction rules, but for the most part the default selections [85] were utilized as there are dozens of settings that could be adjusted. The specific settings will not be listed here, but can be found in the MATLAB codes used to carry out the genetic algorithm optimization, which are provided in Appendix C.

The fitness function used to evaluate the quality of each solution was the total percent of the area of the interface that was calculated to experience net shear stresses above a threshold value after each of the M_φ phasing combinations are applied. Therefore each member of the population was a vector of numbers, each of which corresponded to one of the n_φ unique phasing combinations, and the net shear stress field was calculated for each of the phasing combinations in the phasing vector solution and superimposed to yield the effective stress coverage field. The individual stress fields for each phasing combination were calculated by first reconstructing the phased impedance curve with equation (5.30), finding the impedance minimum, and then reconstructing the net shear stress field τ_{net} at that frequency using equation (5.20). This field was evaluated by calculating the net shear stress level that 90% of the field exceeded. For instance, if 90% of the field had values greater than or equal to 0.5 MPa, then the 90% coverage stress level would be 0.5 MPa. This 90% threshold value is somewhat arbitrary (as long as it is within a reasonable range) since the point of the analysis is to compare phasing states to one another, and as long as they are compared using the same criteria, the comparison is meaningful.

Results of the Analysis

The results of this analysis are summarized by Figure 65, in which the 90% percent coverage stress level is compared for each phasing increment case using 1, 2, 3, 4, 5, 6, 7, or 8 different phasing combinations. As was predicted, the coverage level increased as more phasing combinations were utilized. The case of only one phasing increment is the unphased case, which

provided a shear stress coverage level of 0.27 MPa. Utilizing a second phasing combination increased that to nearly 0.34 MPa, a third increased it to around 0.37, and so on with diminishing returns. An interesting fact is that even though the smaller phasing increments offer a much greater set of possible phasing combinations, they yielded returns that were comparable to simply using in-phase or out-of-phase (180°) excitation.

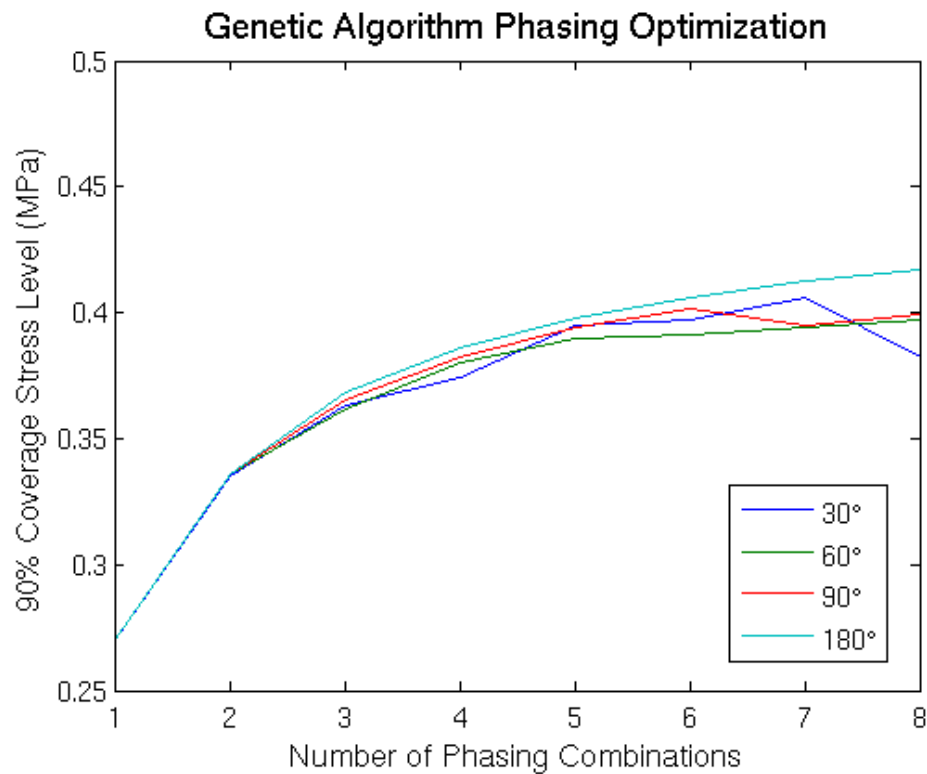


Figure 65 Comparison of the 90% coverage stress level results from the four-actuator finite element model using genetic algorithm optimization for each phasing increment and phasing vector length considered.

The case of 180° phasing increments, referred to from here on as “phase inversion”, is preferred for practical reasons, and the fact that it performed as well as the smaller phasing increments is fortunate, since it could be less practical to intelligently implement such phasing increments. It would be essentially impossible to attempt to truly optimize the phasing combinations for a de-icing system due to the constantly changing nature of accreted ice and the fickle nature of ultrasonic resonances, which are dramatically affected by small perturbations in material properties, geometry, and boundary conditions. In fact, even with the benefit of the genetic algorithm and many hours of computation, the smaller phasing increments were not even

optimized to the level of the phase inversion approach, even though the phase inversion phasing combinations are included in the possible vector solution population of the smaller phasing increment cases. These results also show that even a small number of phasing combinations can provide a substantial benefit in terms of improving the stress field coverage. This is further displayed in Figure 66, which plots the relative improvement in 90% coverage stress level as a function of the number of phase inversion combinations that were applied. In this case the application of all 8 phase inversion combinations yielded a 55% increase in the 90% coverage stress level, which was at 0.27 MPa without phasing and up to 0.42 MPa after phasing.

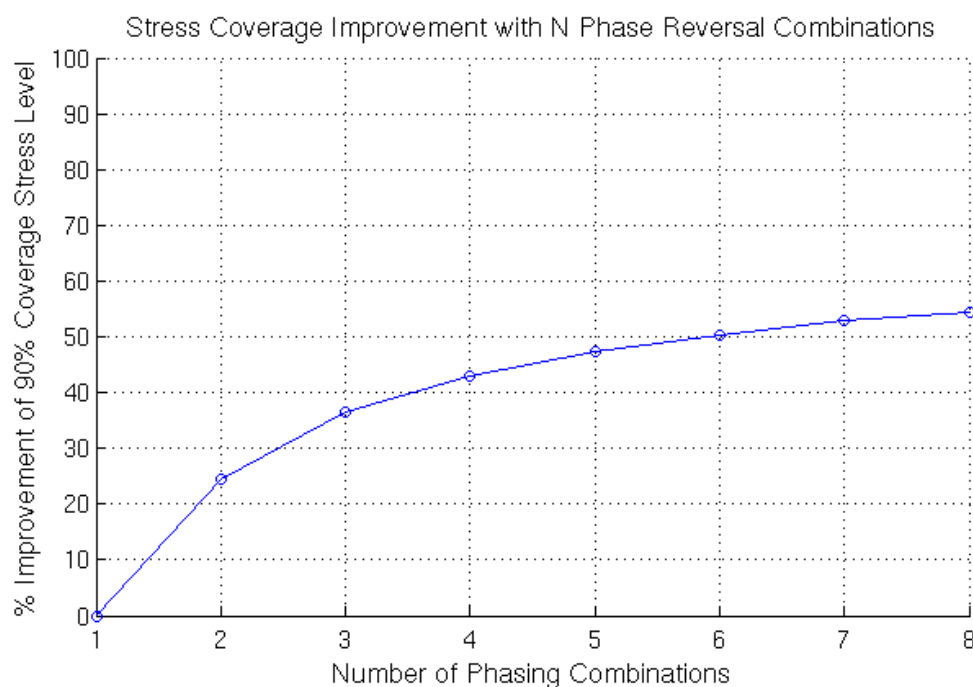


Figure 66 Relative improvement in the 90% coverage stress level for the model considered here using only phase inversion combinations (i.e. 180° phasing increments).

Therefore this analysis shows that even with simple 180° “phase inversion” phasing increments, the stress level can be dramatically improved after only a few phasing combinations. This is a promising result that indicates that actuator phasing is a worthwhile endeavor and that phase inversion, which is practically easier to implement than other forms of phasing, can be just as effective as those other forms without the need for complicated optimization routines or dozens or even hundreds of phasing combinations (both of which are wholly impractical).

5.4 Phasing Evaluation of an Airfoil

Many of the most critical applications for aerospace de-icing technology are those of airfoil-like structures including fixed wing leading edges, rotor blade leading edges, tail leading edges, and engine inlets. Therefore it makes sense to analyze the effectiveness of phasing on a realistic FE model, such as that of an airfoil. An airfoil model with 8 actuators was used to perform a more in-depth analysis of the effects of actuator phasing on a more realistic geometry. Three different actuator configurations were analyzed. The effects of phasing and frequency sweeping were also analyzed and compared, as were different methods of performing phasing with respect to frequency selection.

The details of the airfoil model are provided in Section 5.2 of this chapter, including the geometry, the boundary conditions, and the details of the FE setup and analysis. The airfoil model was analyzed using the independent actuator analysis approach, in which the impedance and stress fields of the model were calculated using 36 actuator excitation and charge measurement configurations to enable a complete phasing analysis with any phasing configuration by superimposing the results of these individual calculations using equations (5.20) and (5.30). In all, 432 models were executed (3 actuator configurations x 36 models required for the independent actuator analysis method x 4 runs to cover the entire frequency range for each model), totaling around 10,800 hours of calculation time.

Actuator Configuration Comparison

The three different actuator configurations that were considered are shown in Figure 67, Figure 68, and Figure 69 below, along with their respective impedance curves. The goal behind analyzing multiple configurations was two-fold. The first objective was to investigate the relative effectiveness of the various configurations so that this information could be applied to future de-icing system designs. The second objective was to add some variation into the model so that the phasing and frequency sweeping analyses were not for a single unique case, but rather several cases. It was hoped that this would aid in identifying real trends and not mistakenly drawing conclusions based on a single model, for which the behavior of phasing and frequency sweeping might be unique.

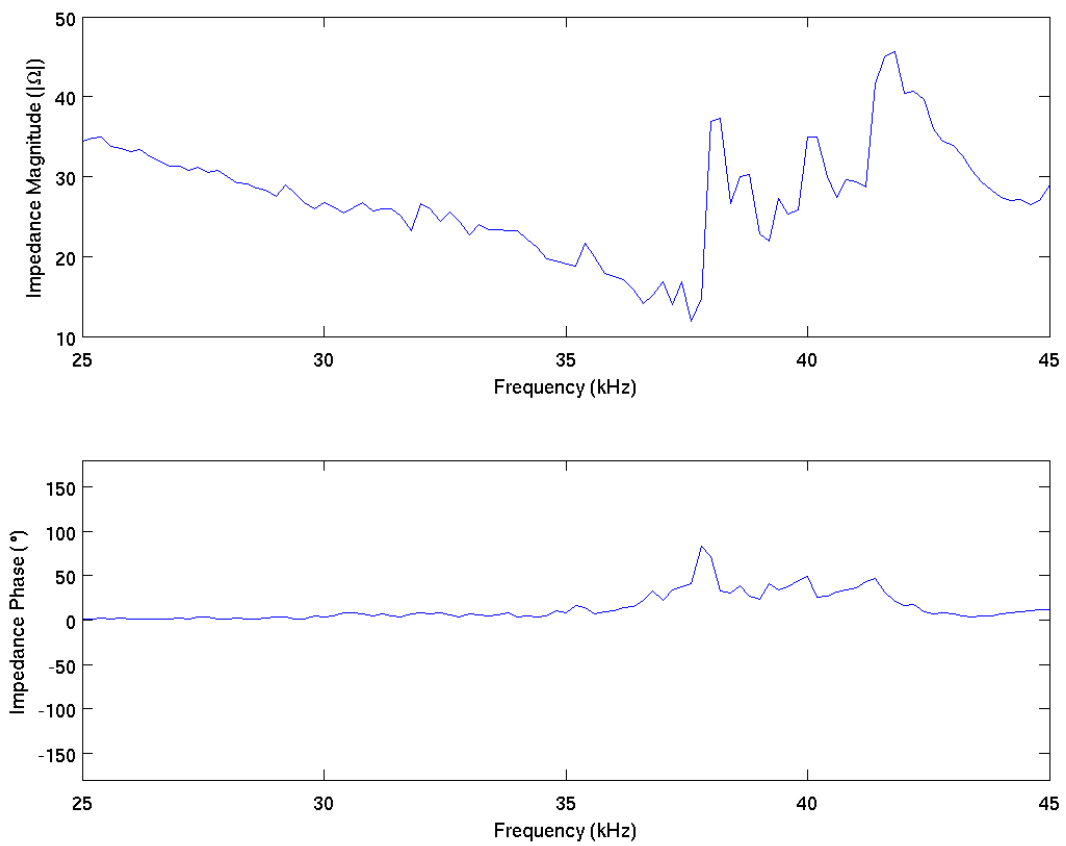
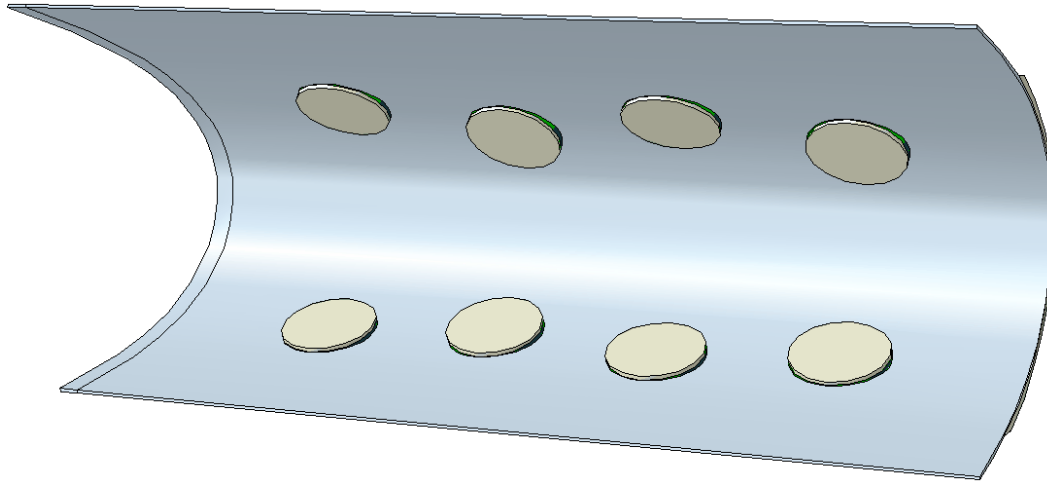


Figure 67 Airfoil actuator configuration 1 and the impedance curve for this configuration.

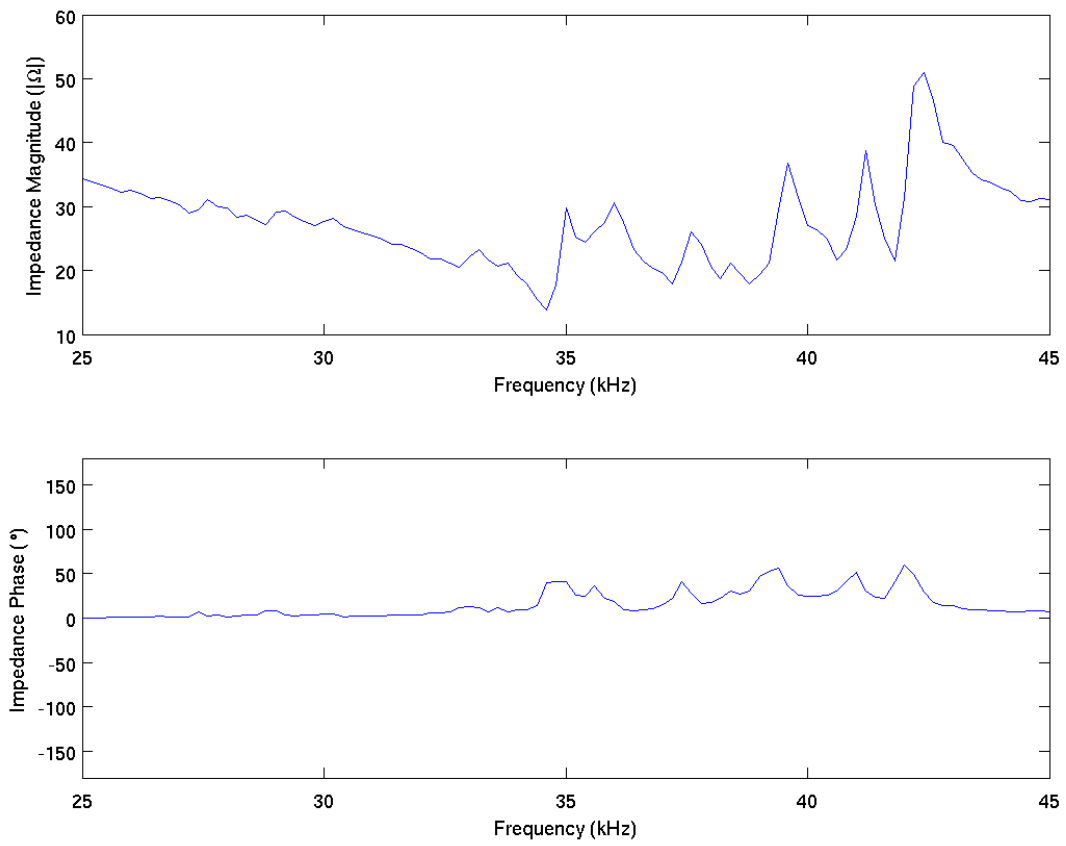
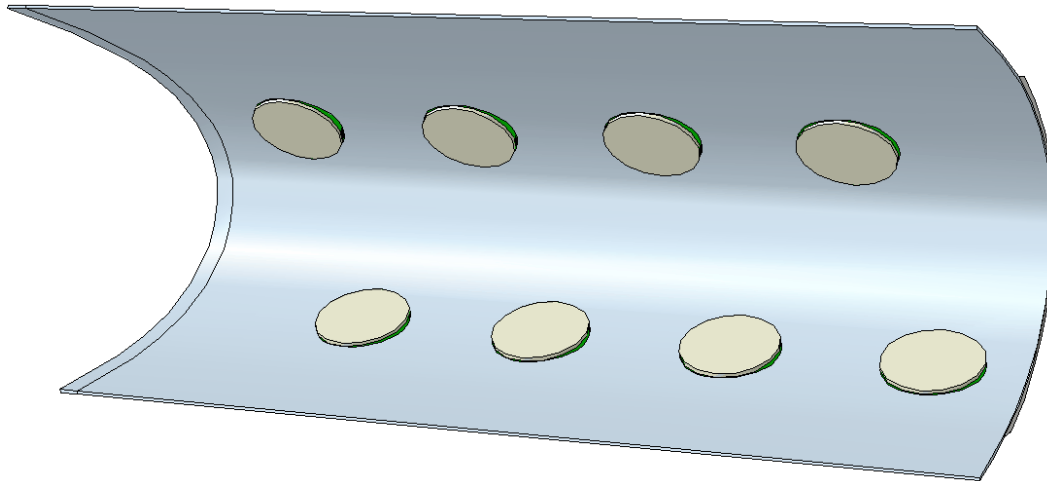


Figure 68 Airfoil actuator configuration 2 and the impedance curve for this configuration.

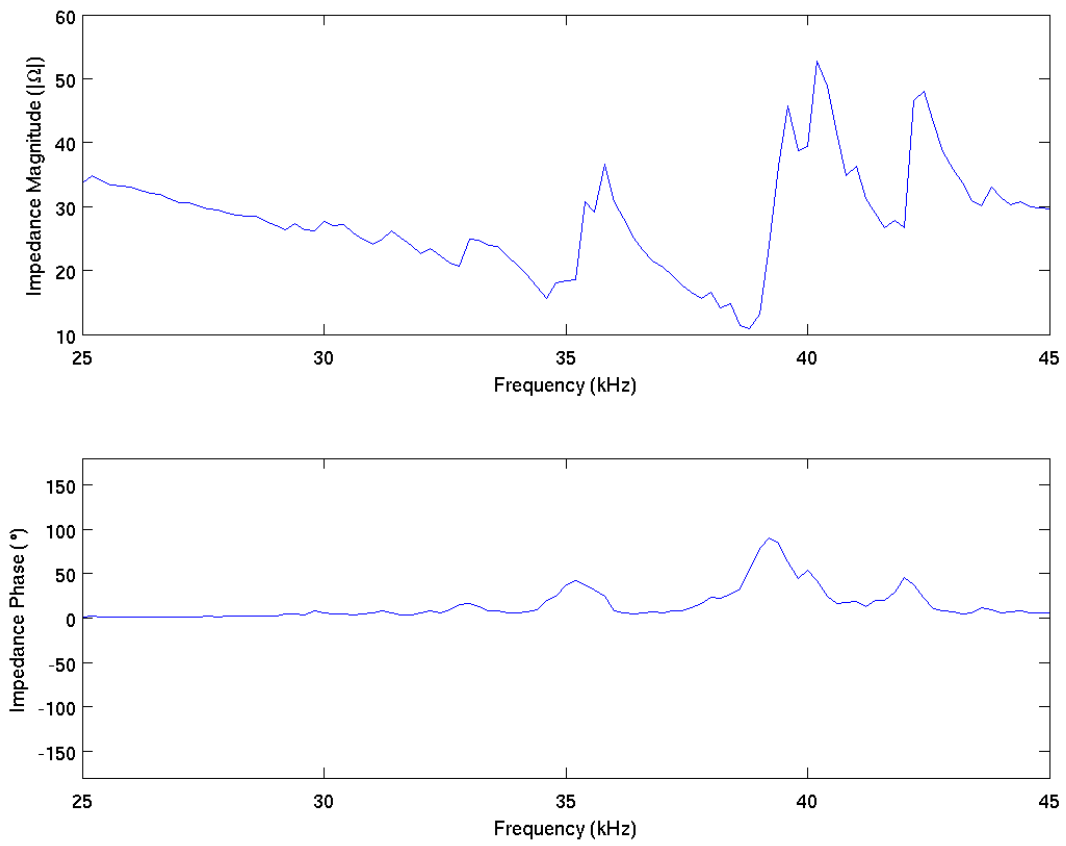
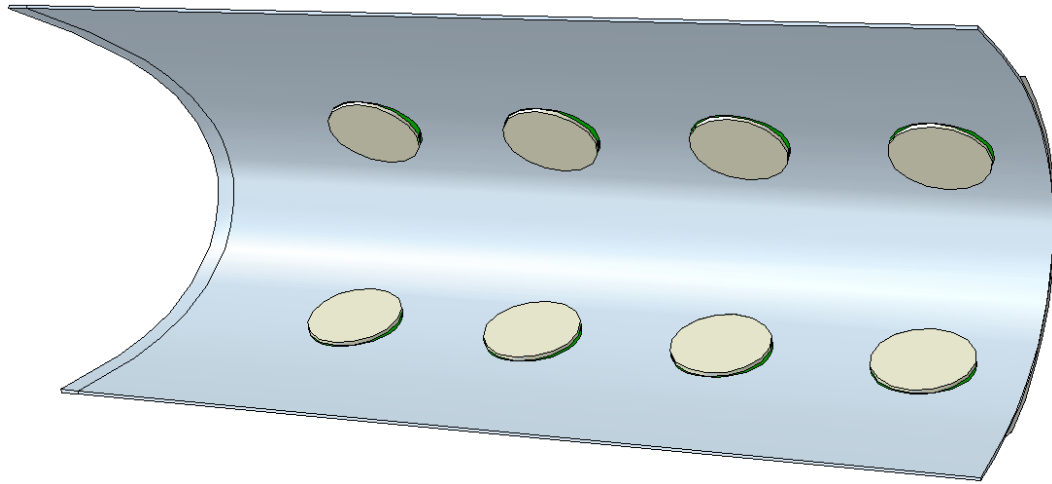


Figure 69 Airfoil actuator configuration 3 and the impedance curve for this configuration.

The average shear stresses across the ice-airfoil interface are shown for each of the three configuration models in Figure 70. No actuator phasing or frequency sweeping is considered for the stress values shown in Figure 70.

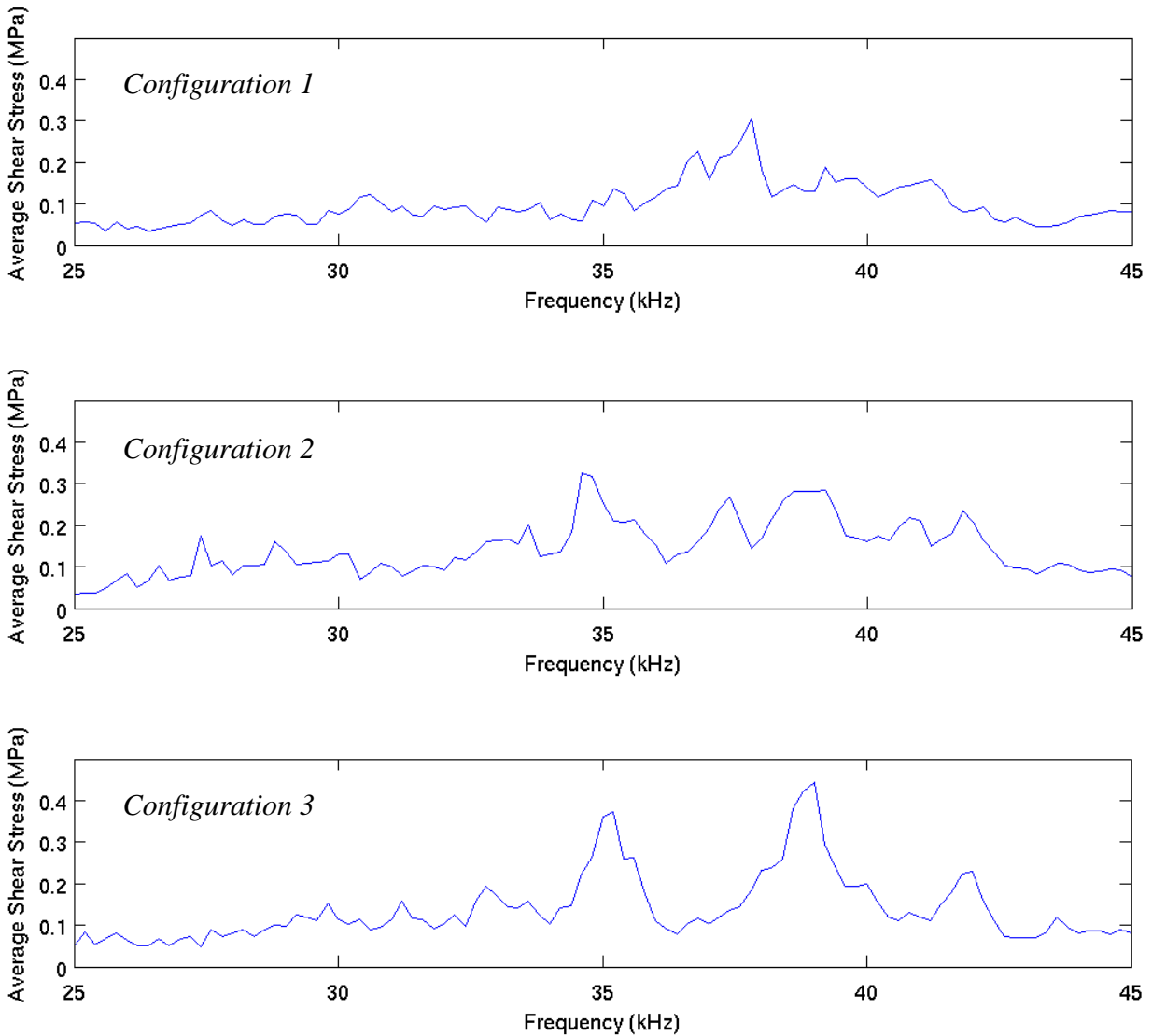


Figure 70 Comparison of the average shear stress, as a function of frequency, for each of the actuator configurations.

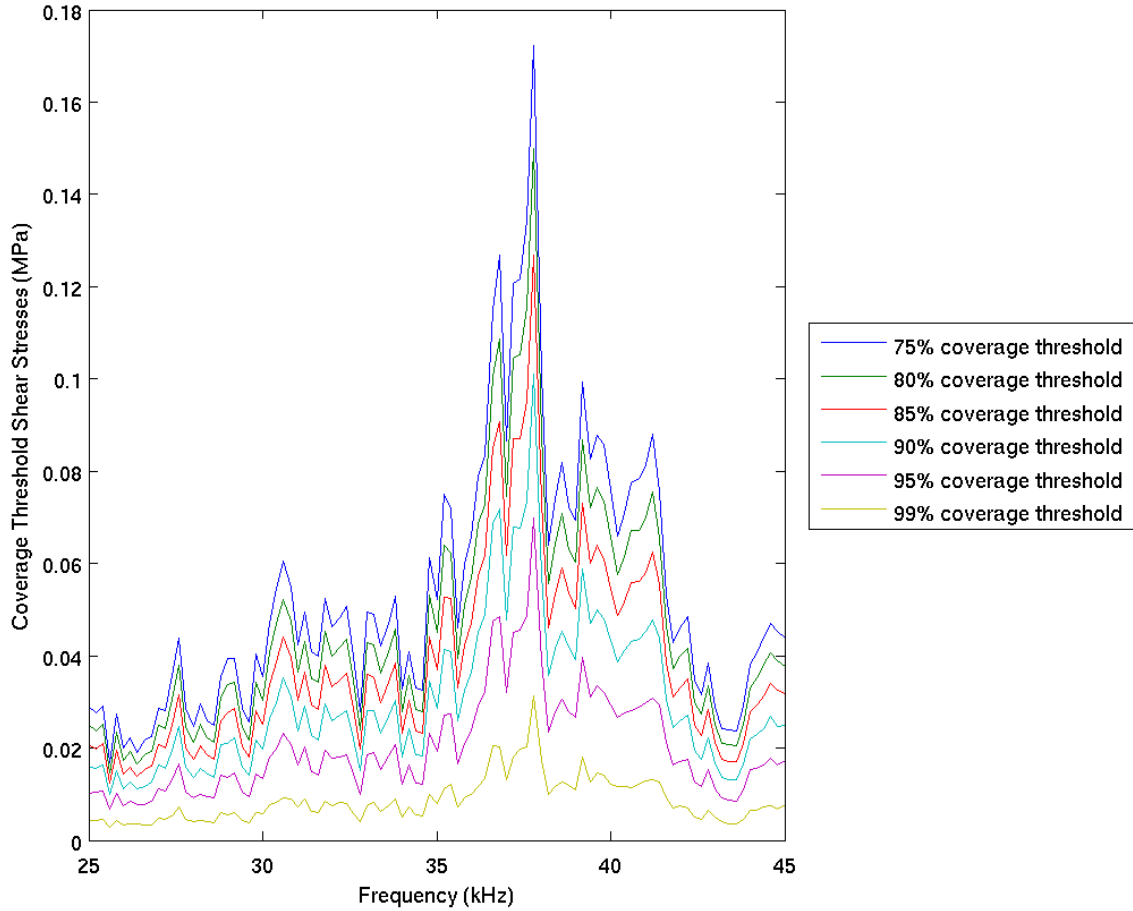


Figure 71 Stress coverage threshold levels, as a function of frequency, with no phasing or frequency sweeping, for actuator configuration 1.

Figure 71, Figure 72, and Figure 73 show the stress coverage threshold levels for (75, 80, 85, 90, 95, and 99% coverage levels), as a function of frequency, for each of the three actuator configurations. The 90% coverage threshold shear stress level of 0.175 MPa near 37 kHz in Figure 71, for instance, indicates that at that frequency, 90% of the surface area of the ice-airfoil interface will experience stresses of at least 0.175 MPa of shear stress. Note that the vertical axis limits are different on each of these three plots. The stress plots in these six figures seem to initially indicate that the second and third configurations are capable of generating greater shear stresses than the first configuration, which is similar to the configuration utilized in much of the prior ultrasonic de-icing research [15, 63, 66]. However, further analysis of the effects of actuator phasing and frequency sweeping will be reviewed before any final comparisons of these configurations are made.

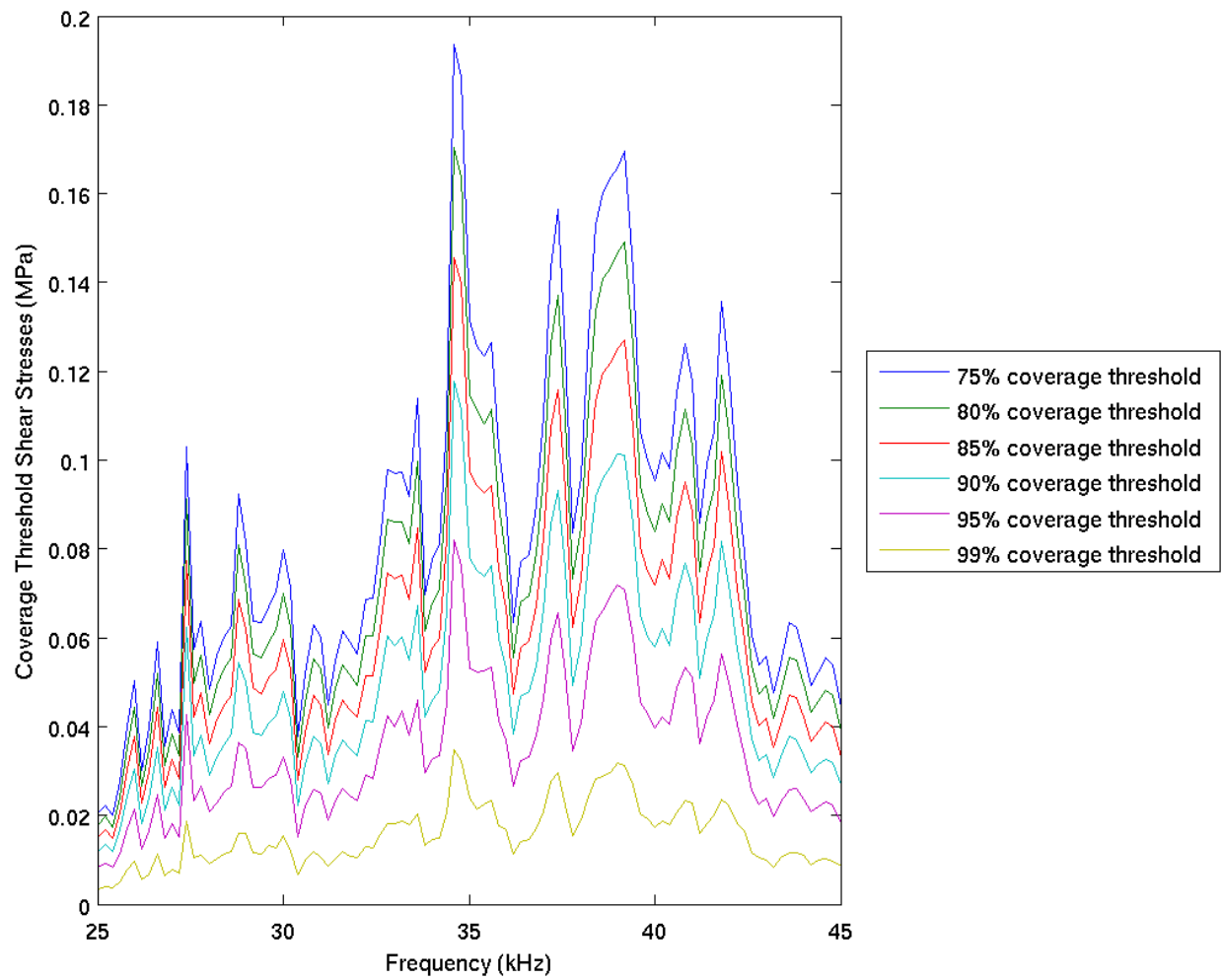


Figure 72 Stress coverage threshold levels, as a function of frequency, with no phasing or frequency sweeping, for actuator configuration 2.

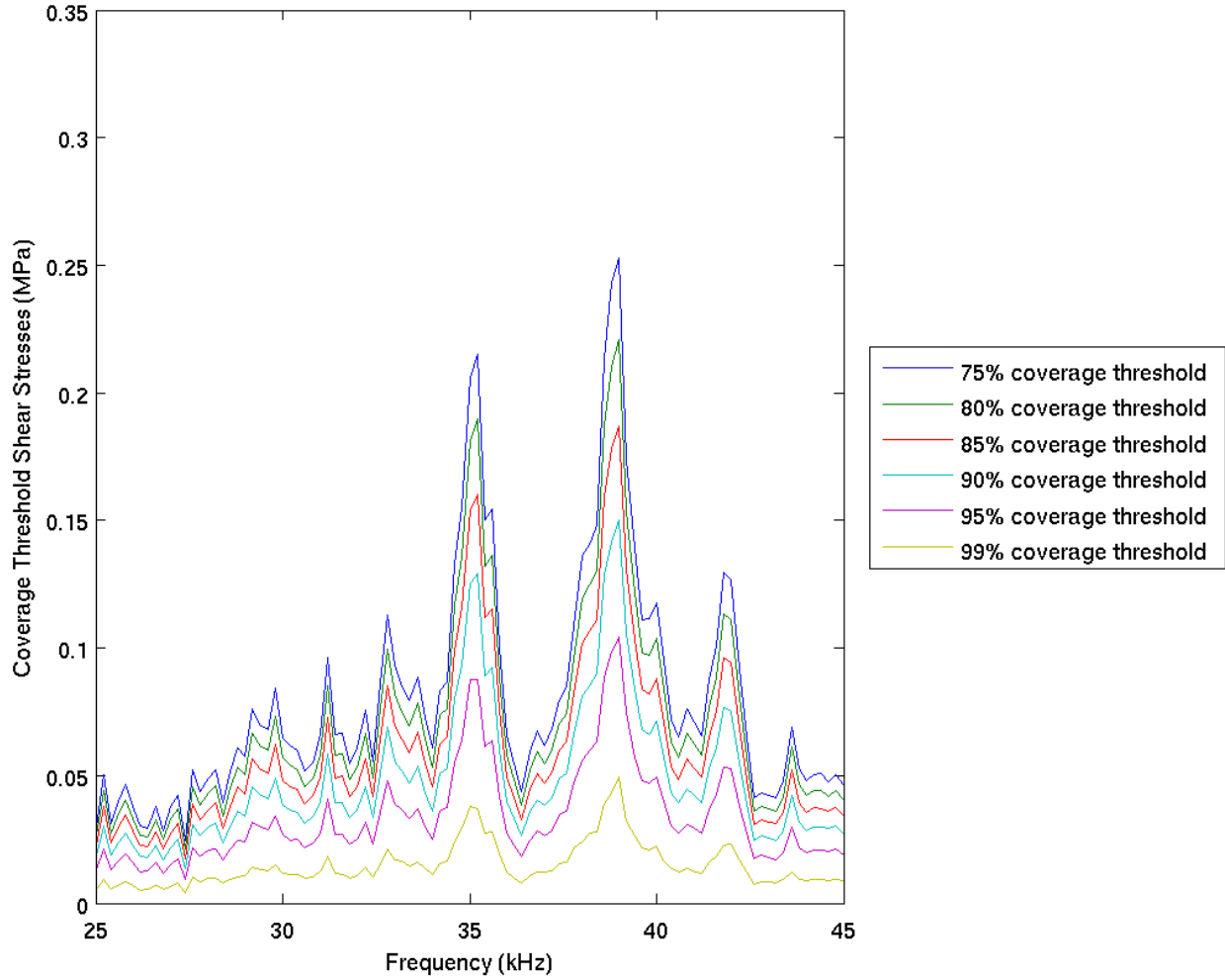


Figure 73 Stress coverage threshold levels, as a function of frequency, with no phasing or frequency sweeping, for actuator configuration 3.

Phase Inversion Effectiveness

In order to evaluate the effectiveness of the phase inversion approach at improving the de-icing coverage of the shear stress field(s) induced by the ultrasonic de-icing system, the stress fields induced by various actuator phasing combinations were calculated. According to Table 9, for an 8-actuator system with 180° phasing increments, there are 128 possible phasing combinations. However, after considering the symmetry of the airfoil and the actuators, many of these would be redundant and can thus be disregarded. Figure 74 illustrates the 30 unique non-redundant phasing

combinations possible for the airfoil model, in which green indicates in-phase operation and red indicates phase inversion. Since the utilization of 30 phasing increments would still be too slow and cumbersome for practical de-icing system operation, a subset of 8 selective phasing combinations was identified. These particular phasing combinations were selected without analyzing the stress fields or impedances resulting from such phasing combinations. They were selected solely on their simple symmetry. The stress coverage from this subset of eight combinations will be compared to that of the full set of 30 phasing combinations to identify the effectiveness of utilizing a small number of combinations to achieve substantial stress coverage improvements. The results from Section 5.3 of this chapter, particularly the results in Figure 66, seem to indicate that just a few phasing increments can yield substantial changes in stress coverage and that diminishing returns are achieved as more phasing increments are utilized.

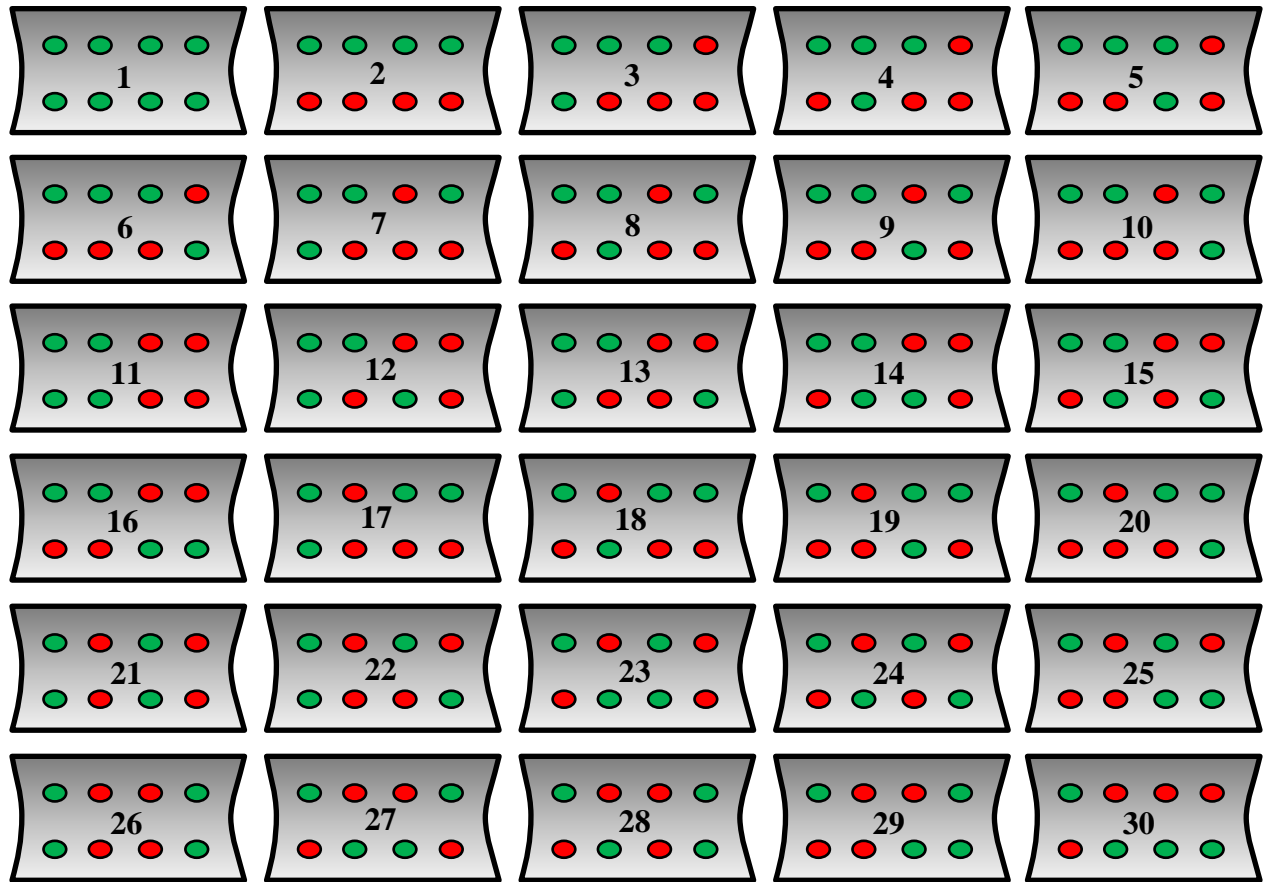


Figure 74 Illustration of all 30 unique non-redundant phasing combinations for the airfoil model, in which green indicates in-phase operation and red indicates phase inversion.

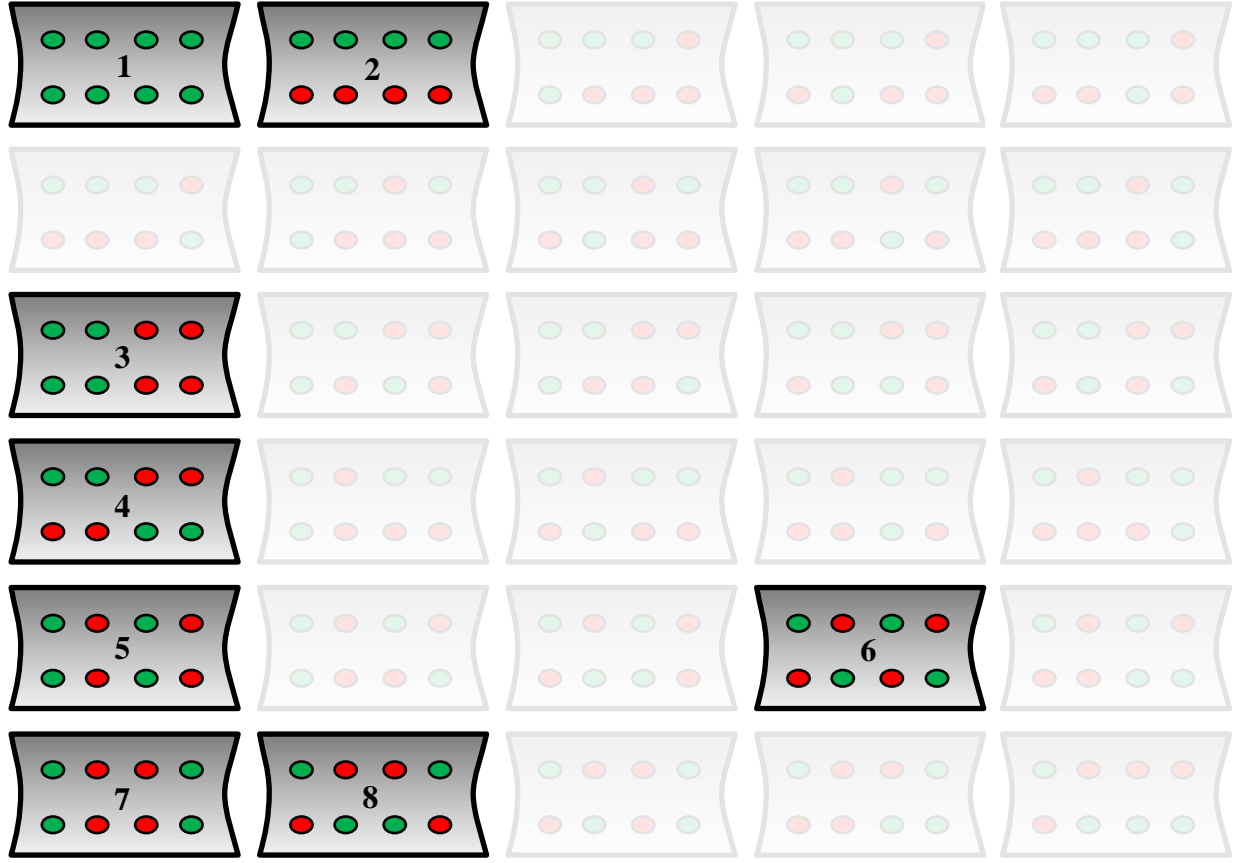


Figure 75 Illustration of the 8 selective phasing combinations out of the 30 unique non-redundant phasing configurations for the airfoil model, in which green indicates in-phase operation and red indicates phase inversion.

The stress calculations in this section were performed in a manner similar to that adopted in Section 5.3, in which the phased impedance curve is first calculated, the minimum impedance is identified, and the phased stress field at the phased impedance minimum is calculated and analyzed. A second method of determining the driving frequency during phasing will be evaluated in a later section. In this section, no frequency sweeping was considered; this will also be evaluated in a later section. Figure 76, Figure 77, and Figure 78 plot the average interface shear stresses for each of the actuator phasing combination when driven at the phased impedance minimum for each of the three actuator configurations, respectively. In these plots the red bars indicate the selective phasing combinations.

Recall that for these plots the unphased state is phasing combination #1. Here it can be observed that the average stresses induced by any one phasing combination can vary by nearly 150%. This value is only comparing the ability of each phasing combination to generate large shear stresses and does not evaluate the variations in the distribution of these stresses across the surface of the airfoil.

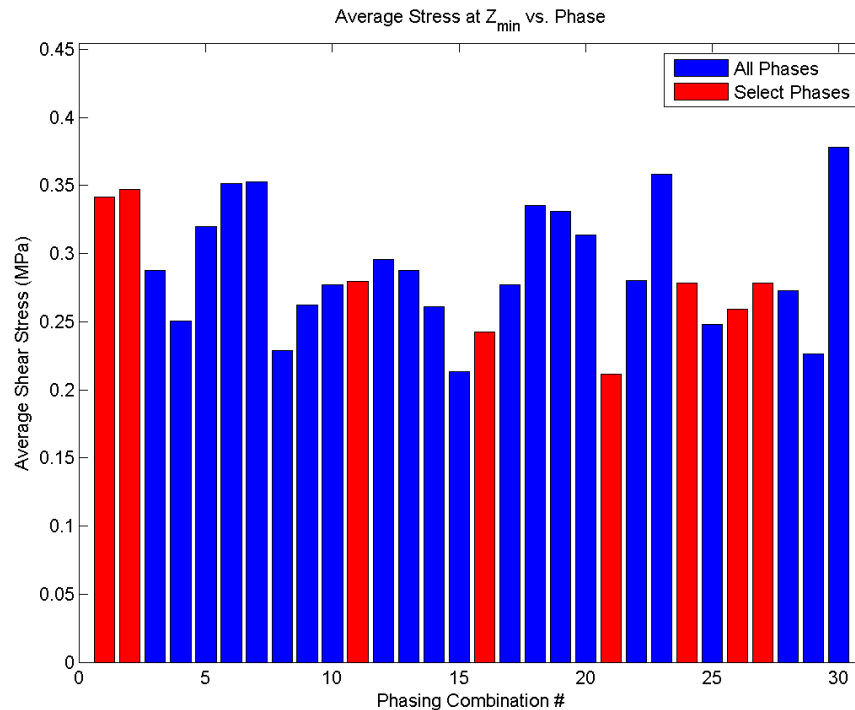


Figure 76 Average interface shear stress at the phased impedance minimum for all 30 phasing combinations for actuator configuration 1.

The coverage of these phasing combinations are compared in Figure 79, Figure 80, and Figure 81, in which three groups of phasing combinations are considered; these groups are “no phasing”, “selective phases”, and “all phases”. The shear stress coverage threshold levels are defined in the same manner as earlier in this section. These plots show that even the application of the eight selective phasing increments yields a dramatic improvement in stress coverage levels for each of the three actuator configuration models. The application of the remaining 22 phasing combinations yields further improvement, but it is less substantial than the gains achieved with

the first eight selective phasing combinations. This is a very promising result and agrees well with Figure 66.

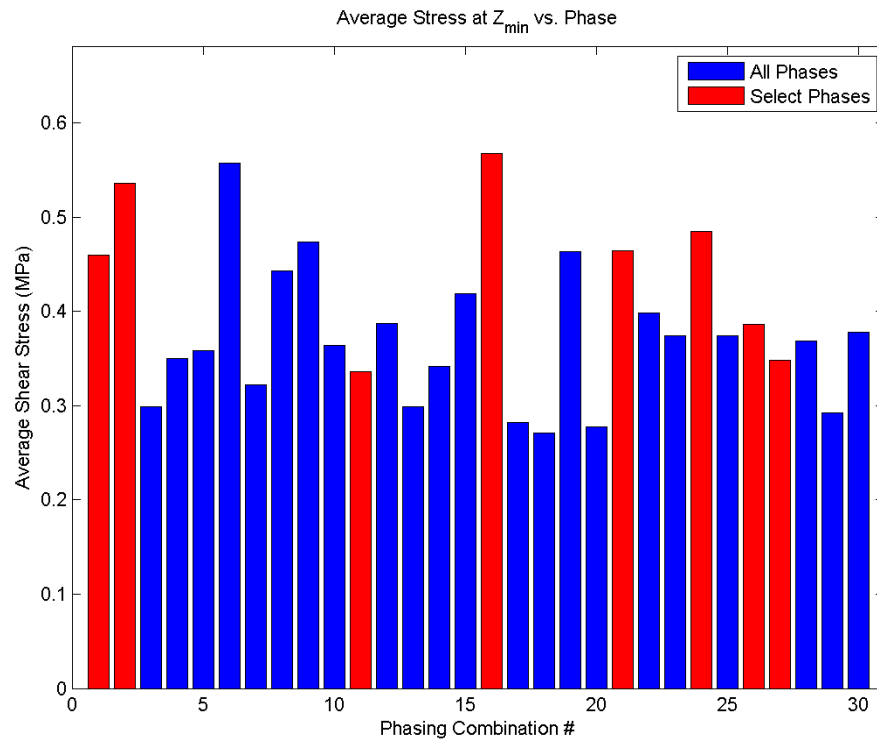


Figure 77 Average interface shear stress at the phased impedance minimum for all 30 phasing combinations for actuator configuration 2.

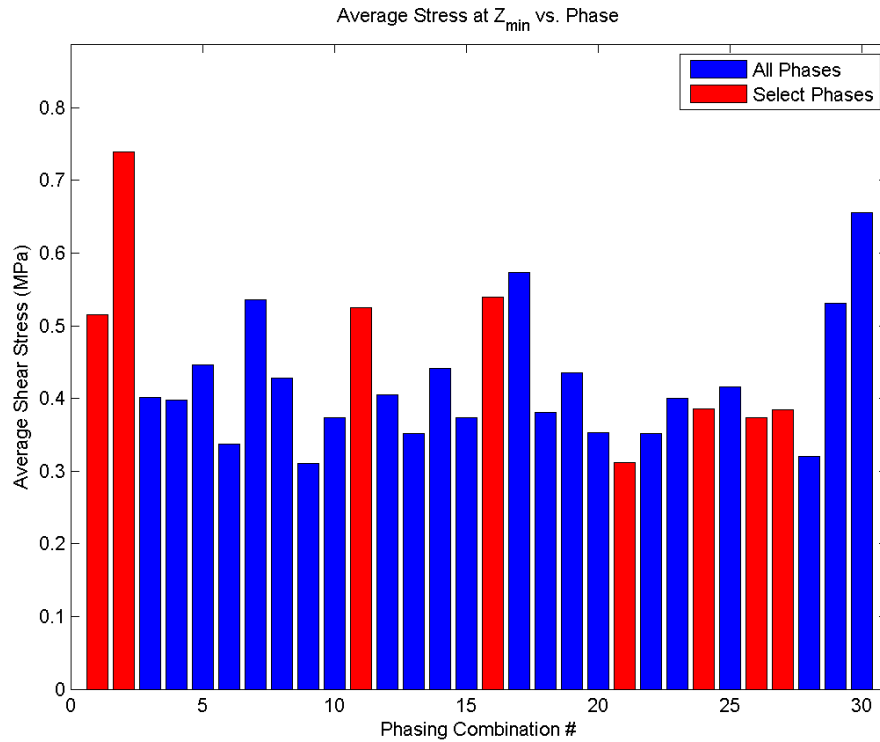


Figure 78 Average interface shear stress at the phased impedance minimum for all 30 phasing combinations for actuator configuration 3.

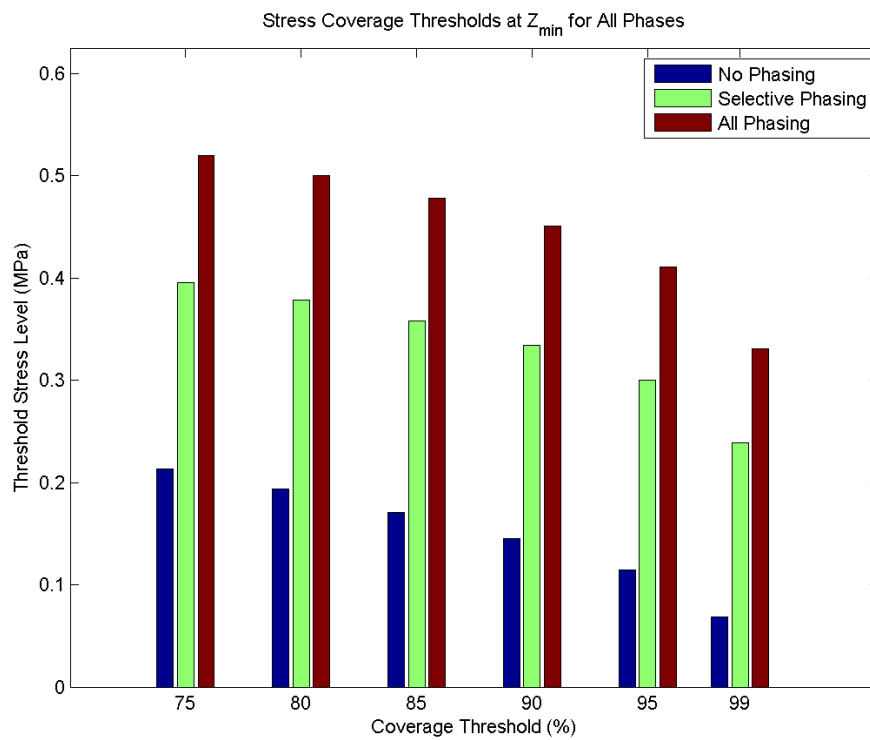


Figure 79 Coverage threshold shear stress levels for various phasing groups, actuator configuration 1.

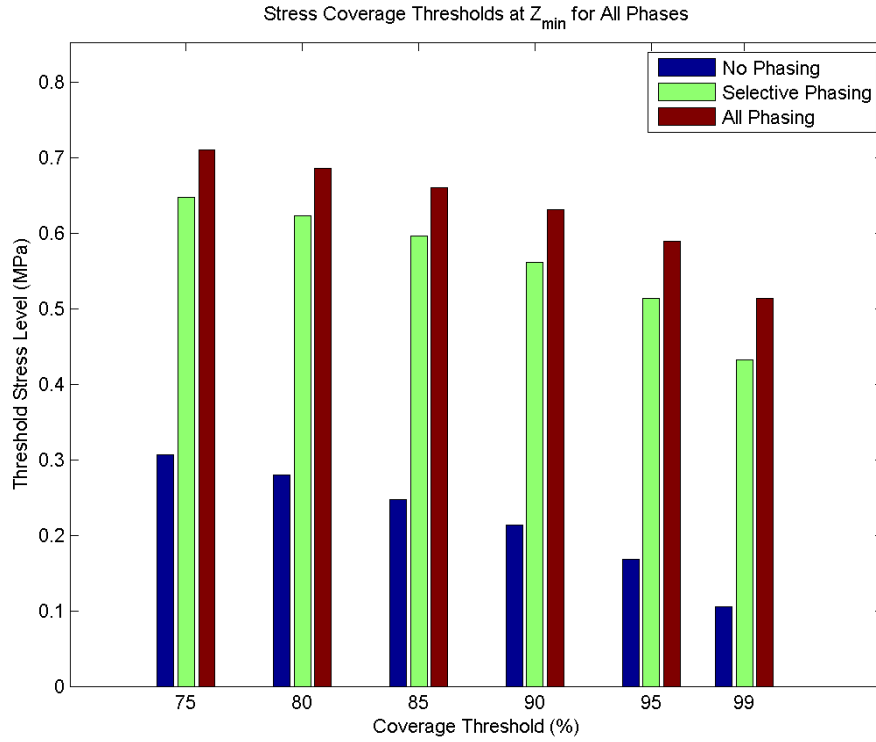


Figure 80 Coverage threshold shear stress levels for various phasing groups, actuator configuration 2.

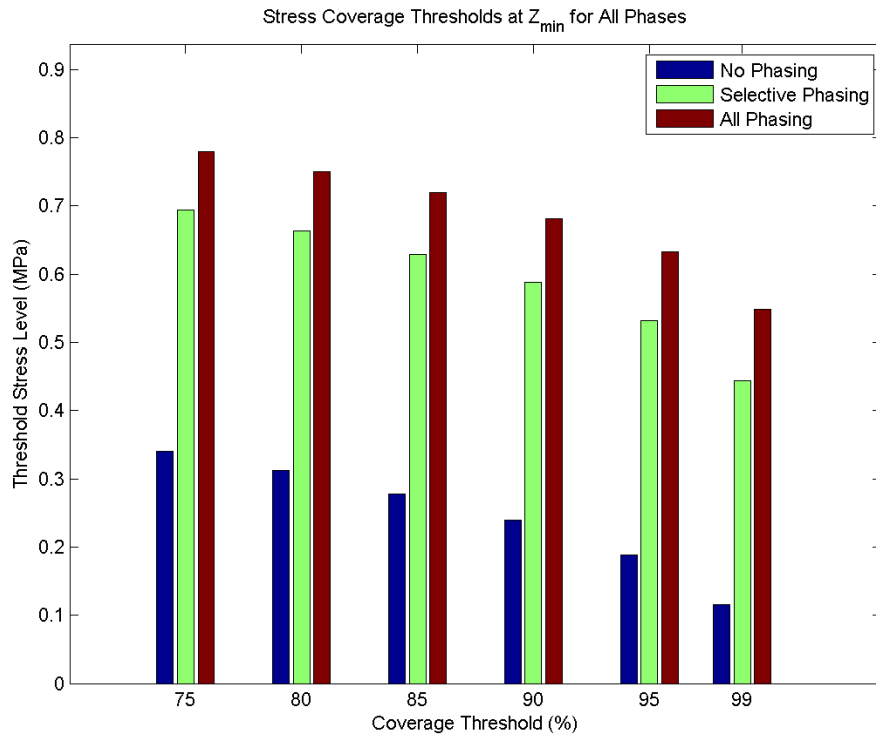


Figure 81 Coverage threshold shear stress levels for various phasing groups, actuator configuration 3.

For actuator configuration 1, the selective phasing improved the shear stress coverage thresholds by more than 90%, and the complete phasing improved the thresholds by nearly 150%. For actuator configuration 2, the selective phasing offered 115% improvement, and complete phasing increased this to 140% improvement. For the third actuator configuration, the selective phasing improved the coverage thresholds by more than 100%, and the complete phasing improved the thresholds by nearly 130%. These are very substantial gains. These improvements will be compared to frequency sweeping and phasing in conjunction with frequency sweeping in a later section.

The effects of phasing may be better visualized by comparing the actuator stress fields on the ice-airfoil interface. The stress fields for individual phasing combinations and the net effective stress fields for groups of phasing combinations were plotted onto the 3-dimensional airfoil surface using MATLAB. The codes developed to carry out this plotting, as well as most of the other calculations in this chapter, are provided in Appendix B. Figure 82, Figure 83, and Figure 84 show the shear stress fields induced for each of the eight selective phasing combinations for each of the three actuator configurations, respectively. The upper left image in each plot is phasing combination #1, which is the unphased system. The plots then proceed from left to right and then along the bottom row from left to right in the same order as the phasing combinations defined in Figure 75.

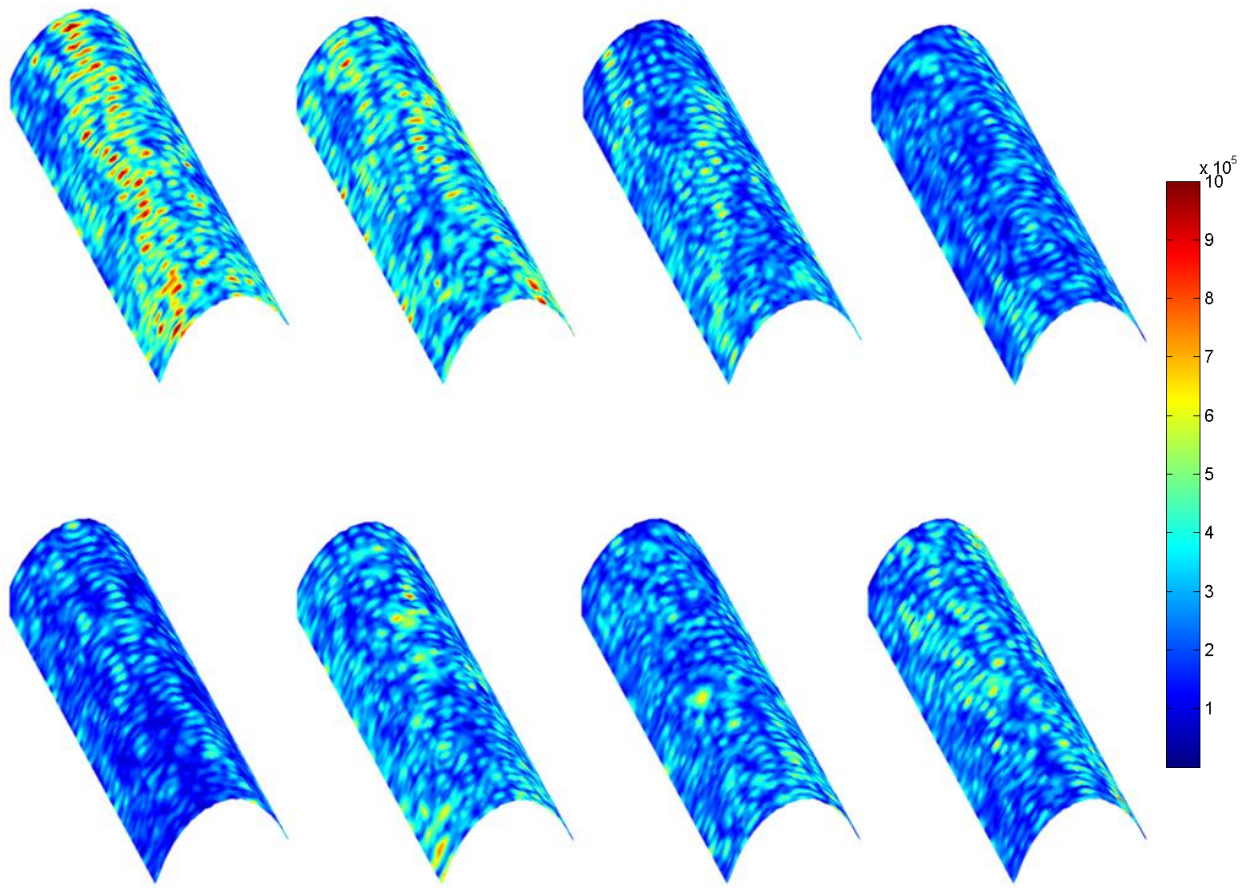


Figure 82 The shear stress fields induced on the ice-airfoil interface by the eight selective phasing combinations while driving the actuators at the phased impedance minimum for actuator configuration 1.

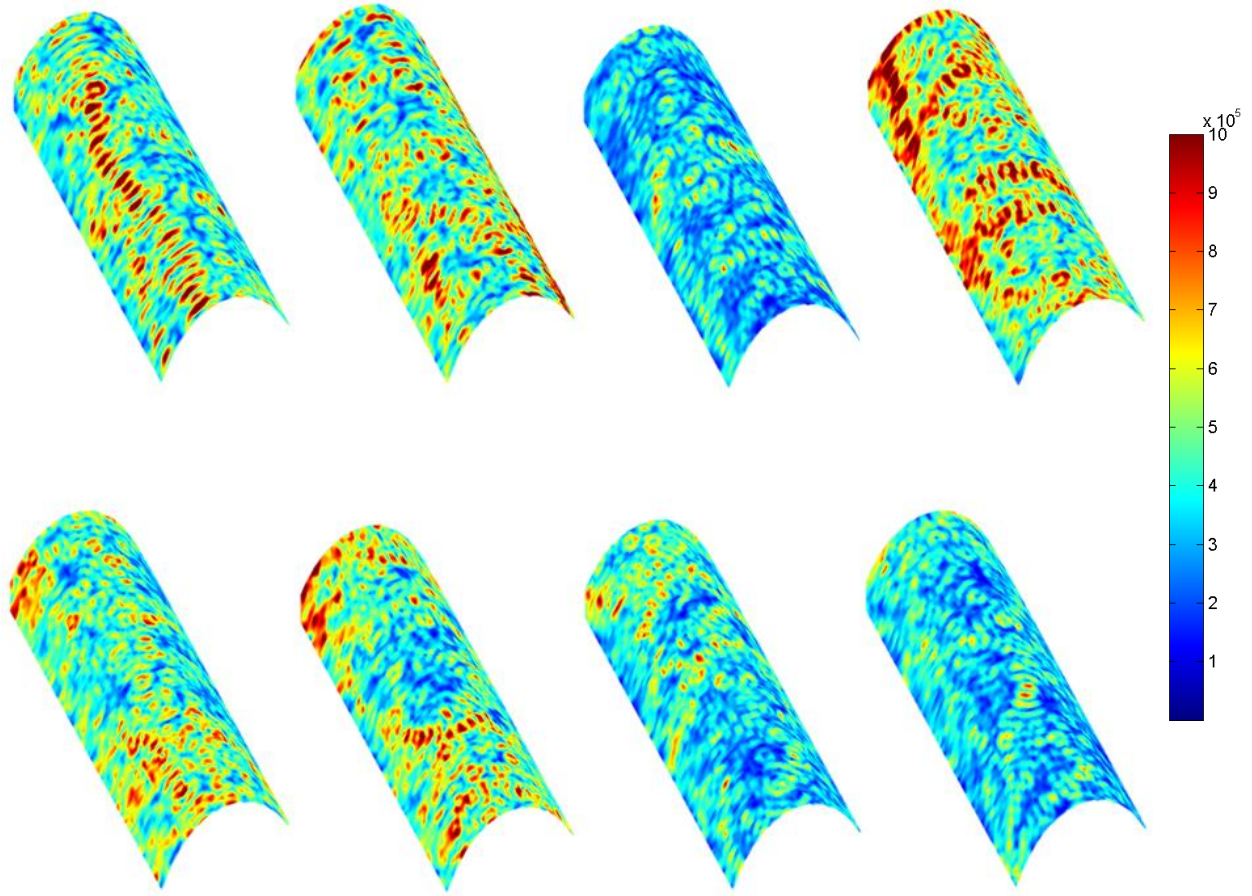


Figure 83 The shear stress fields induced on the ice-airfoil interface by the eight selective phasing combinations while driving the actuators at the phased impedance minimum for actuator configuration 2.

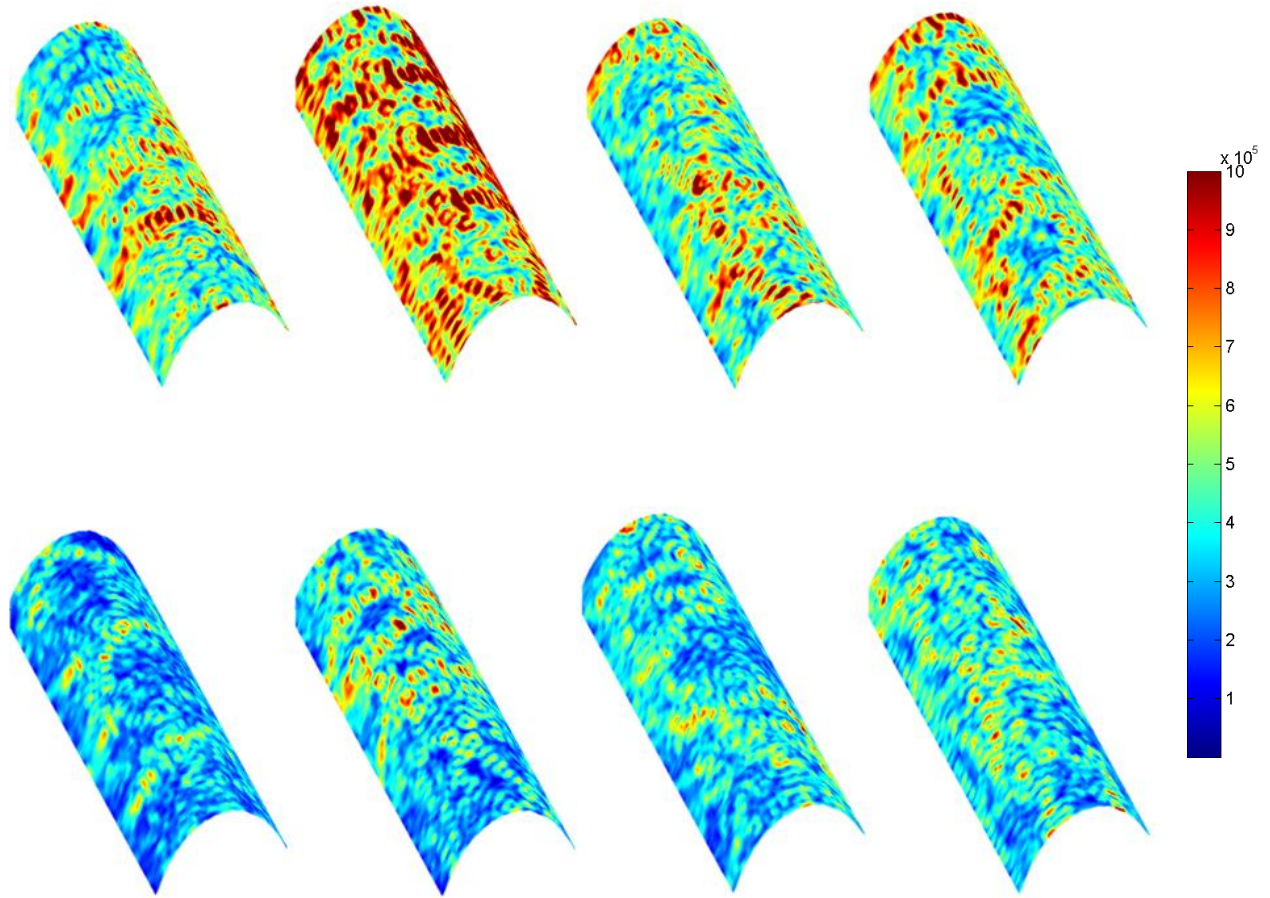


Figure 84 The shear stress fields induced on the ice-airfoil interface by the eight selective phasing combinations while driving the actuators at the phased impedance minimum for actuator configuration 3.

Note that for each actuator configuration, certain phasing combinations yield generally similar stress fields, although variations in these fields are presents. However, certain phasing combinations yield dramatically different stress fields, some of which exhibit generally higher stress values. Here again, it is apparent that the staggered actuator configuration 1, shown in Figure 67, performs poorly compared to the other two configurations, shown in Figure 68 and Figure 69, at least for this particular geometry. To see the net effect of combining these phasing fields, the maximum shear stress across the fields generated by each phasing combination for each point on the interface is plotted in Figure 85, Figure 86, and Figure 87. These plots are compared to the unphased field (phasing combination #1). These plots are all on the same 0 to 1 MPa scale shown in Figure 84.

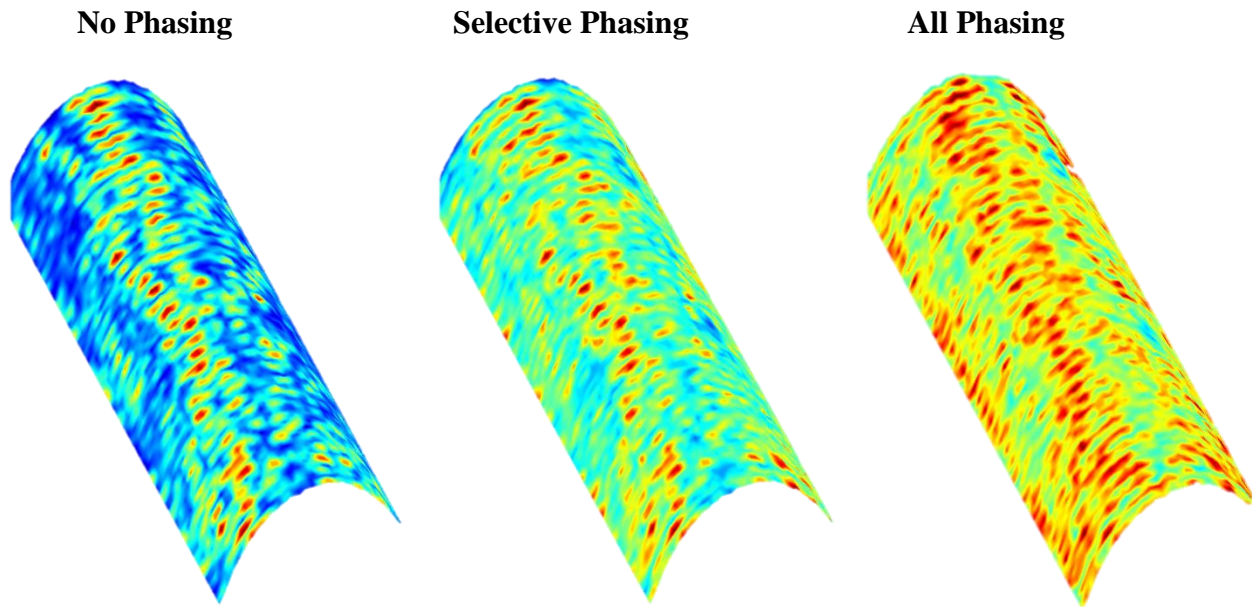


Figure 85 Comparison of the net stress field for the unphased system, selective phasing, and all phasing for actuator configuration 1.

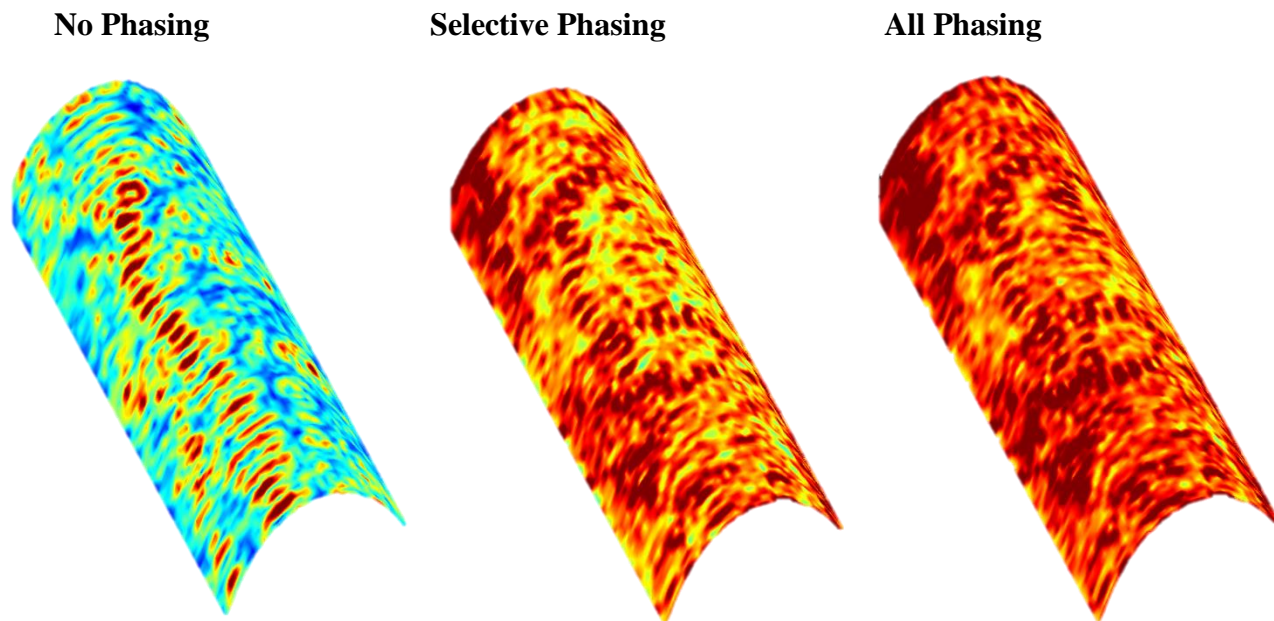


Figure 86 Comparison of the net stress field for the unphased system, selective phasing, and all phasing for actuator configuration 2.

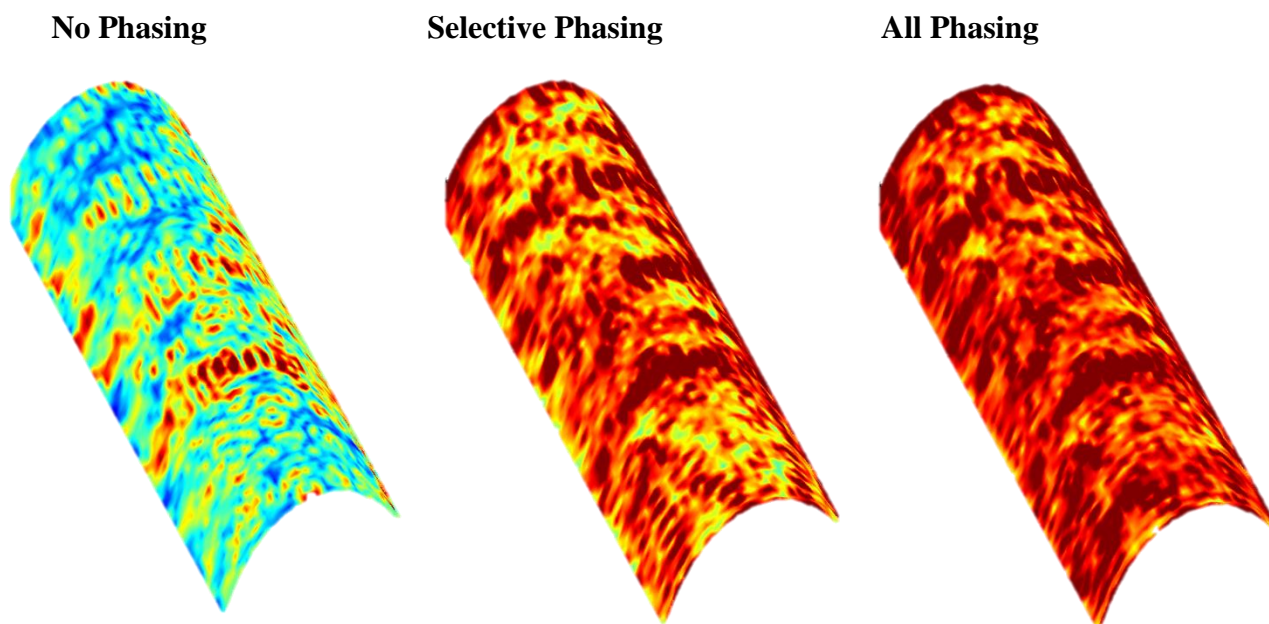


Figure 87 Comparison of the net stress field for the unphased system, selective phasing, and all phasing for actuator configuration 3.

This analysis has shown that phase inversion, in which 180° phasing increments are applied, can be very effective in increasing the coverage threshold shear stress levels on an airfoil. The effect of eight pre-selected phasing combinations was substantial enough to offer improvements in this coverage threshold of around 100% for each of the actuator configurations, and utilizing the complete set of phasing combinations yielded further improvement.

These calculations were repeated with power normalization based on equation (5.17), and the normalized versions of Figure 76 through Figure 81 are provided Appendix D. The limitations of the power normalization technique were discussed in Section 5.2 and must be kept in mind. However, since this analysis is performed solely near the actuator resonances and the phased system impedances are generally in a range that can be well-matched with the de-icing system impedance matching networks and amplifiers, the power normalization results are likely realistic. The power normalization alters the numeric values of the results but it does not significantly alter the trends associated with them.

Excitation Frequency Selection during Phase Inversion

The method by which the excitation frequency is selected for normal unphased de-icing system operation has already been detailed in previous work and in this dissertation. The method of frequency selection during phasing will be investigated here. Two methods will be proposed:

1. *Static frequency method* – In this method the impedance of the unphased actuator system is evaluated, the minimum (Z_0) is identified, and the system is driven at this frequency for all phasing combinations.
2. *Dynamic frequency method* – In this method the impedance is re-evaluated for each phasing combination, the phased minimum (Z_{min}) is identified, and the system is driven at the corresponding frequency for each phasing combination.

It will be shown in this section that the dynamic frequency method yields superior results. Conceptually, this makes sense, since the impedance curve changes for each phasing combination and therefore the resonance of the system, as a function of frequency, changes for each phasing combination. The method by which the phased impedance can be measured is detailed in Chapter 4: Impedance Analysis.

Figure 88, Figure 89, and Figure 90 compare the average stress fields induced by each phasing combination using the dynamic method (blue) and the static method (red) for each actuator configuration. Figure 91, Figure 92, and Figure 93 plot the average of each of the bar plots (over all phasing combinations) for the dynamic (blue) versus the static (red) frequency selection method. Particularly for configurations 2 and 3, utilizing the dynamic method over the static method yields substantially greater average stresses. For configuration 1, the dynamic method yielded an average stress field value approximately 10% greater than the static method. For configurations 2 and 3, these improvements were 115% and 47%, respectively.

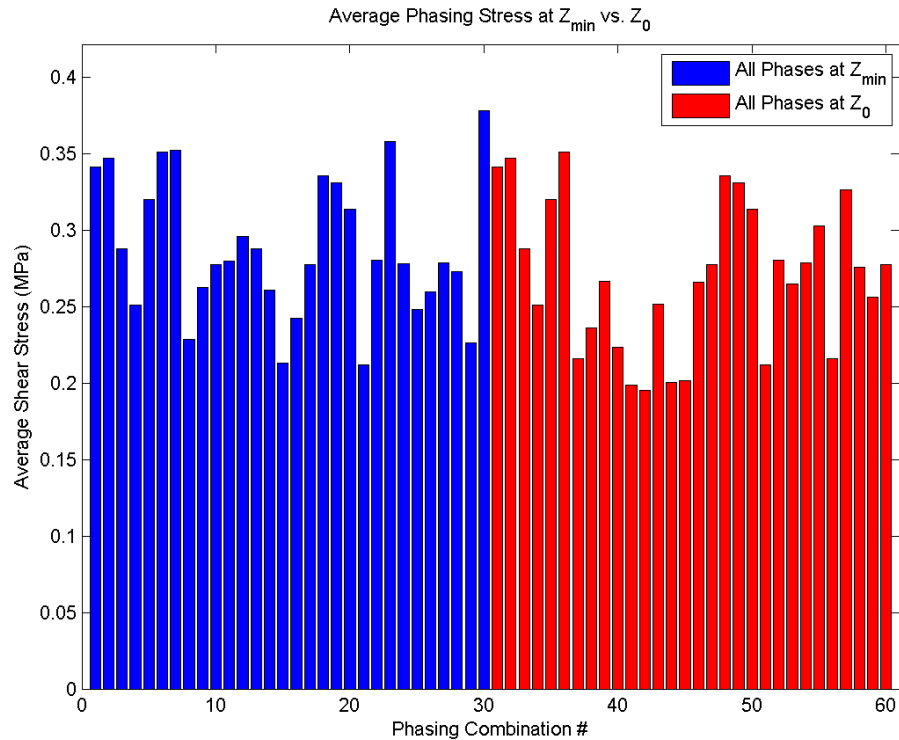


Figure 88 Average shear stress field values for each phasing combination using the dynamic frequency selection approach (blue) and the static frequency selection approach (red) for actuator configuration 1.

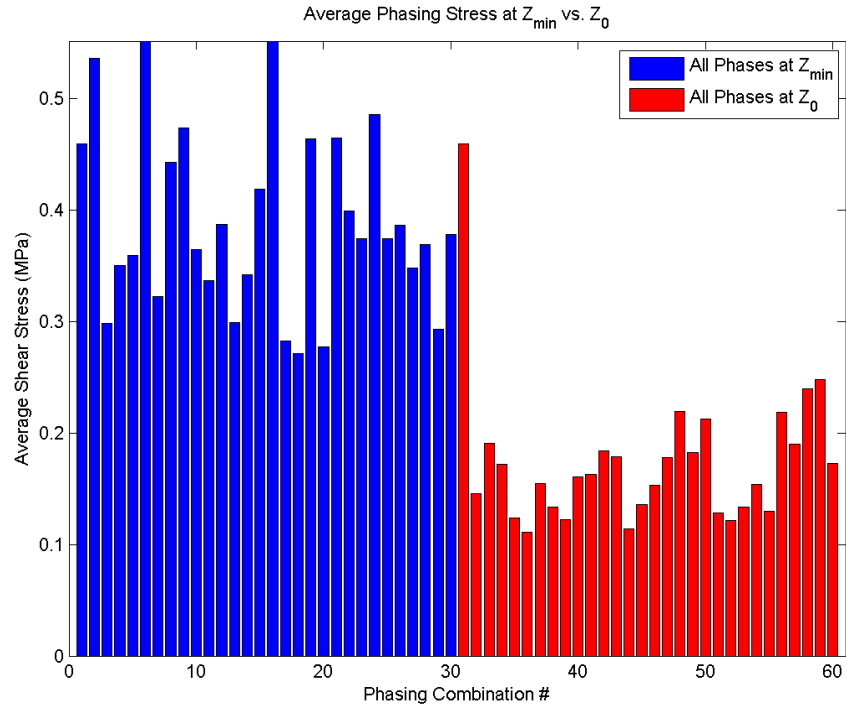


Figure 89 Average shear stress field values for each phasing combination using the dynamic frequency selection approach (blue) and the static frequency selection approach (red) for actuator configuration 2.

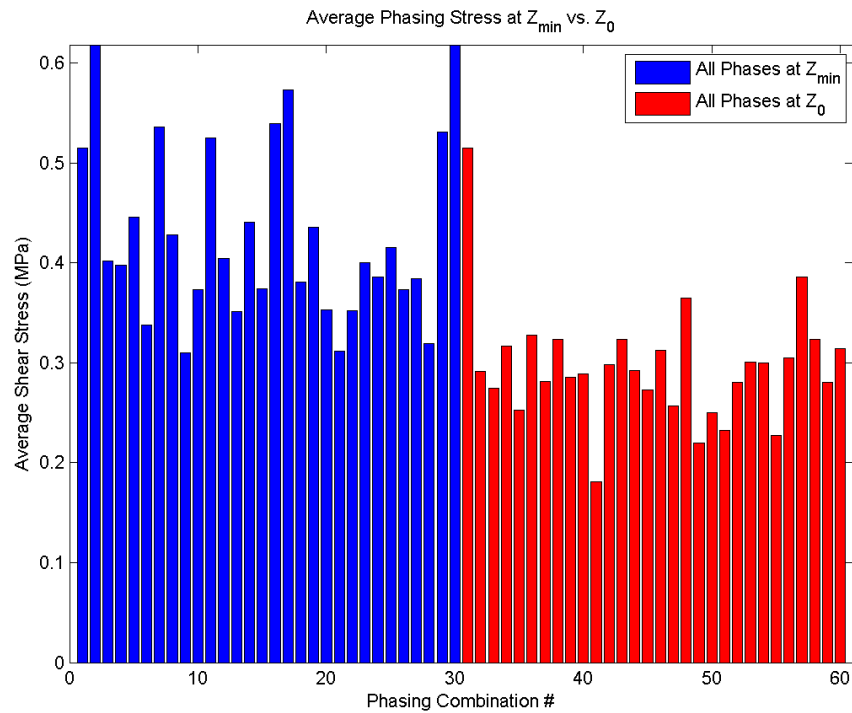


Figure 90 Average shear stress field values for each phasing combination using the dynamic frequency selection approach (blue) and the static frequency selection approach (red) for actuator configuration 3.

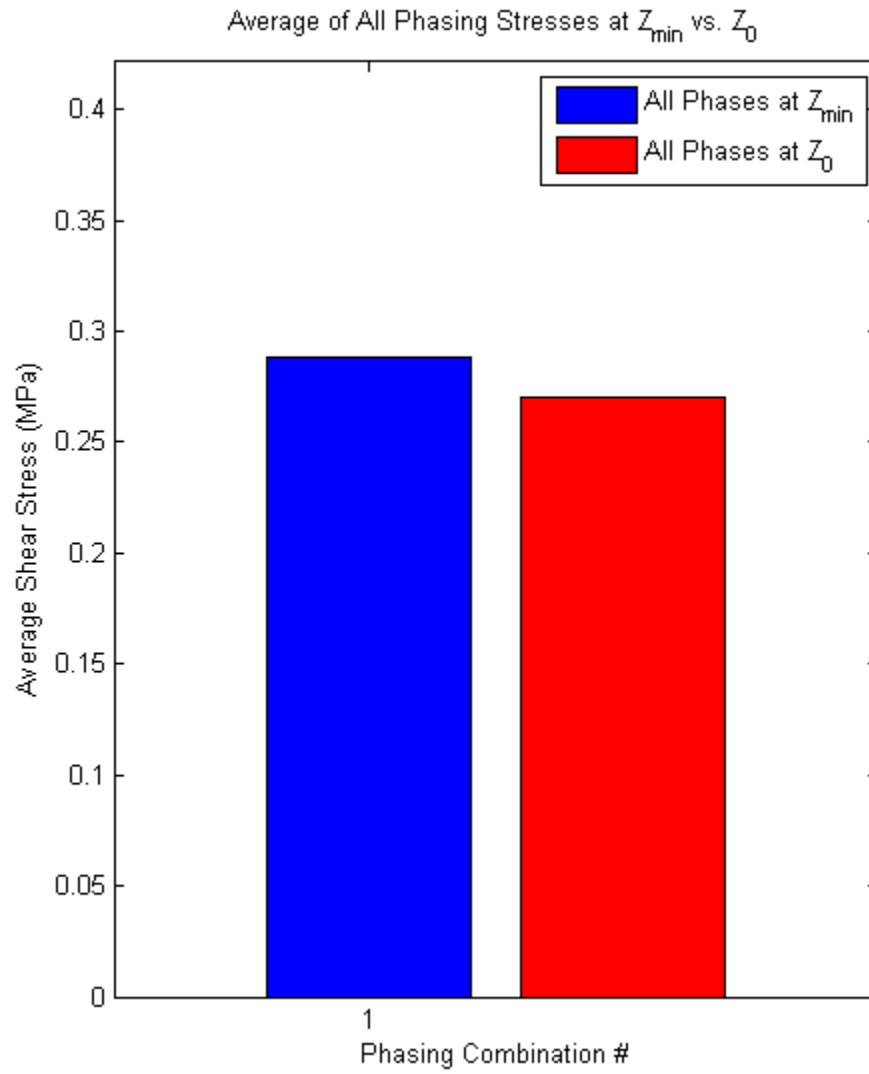


Figure 91 Average of the average shear stress values across all phasing combinations using the dynamic frequency selection approach (blue) and the static frequency selection approach (red) for actuator configuration 1.

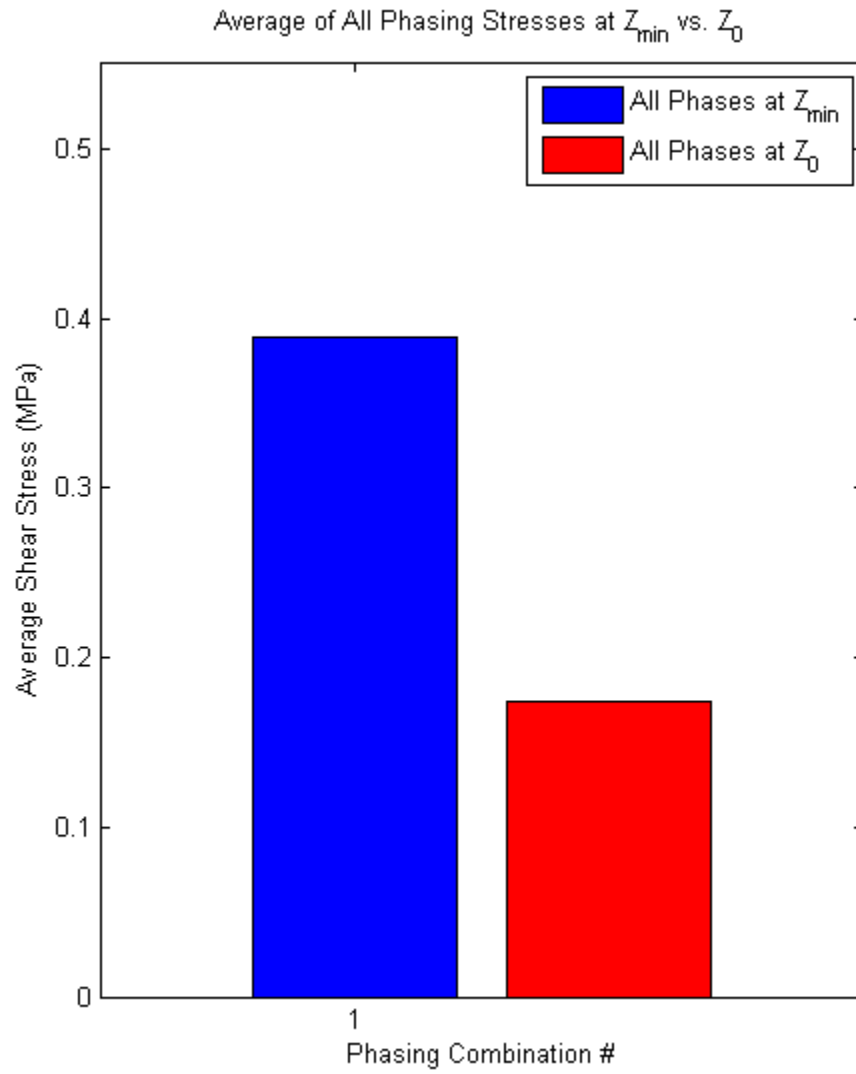


Figure 92 Average of the average shear stress values across all phasing combinations using the dynamic frequency selection approach (blue) and the static frequency selection approach (red) for actuator configuration 2.

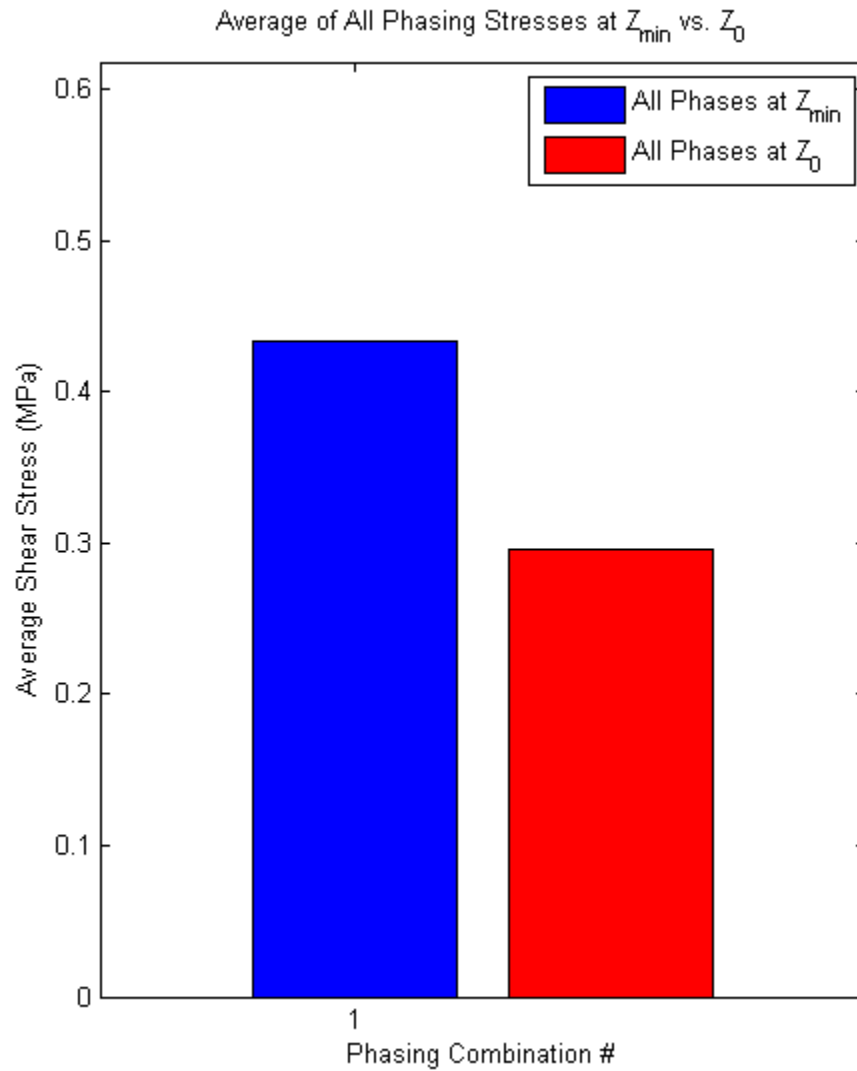


Figure 93 Average of the average shear stress values across all phasing combinations using the dynamic frequency selection approach (blue) and the static frequency selection approach (red) for actuator configuration 3.

Comparison of Phase Inversion and Frequency Sweeping

Prior ultrasonic de-icing research [63, 66] included the notion that a method was required for improving the shear stress coverage of the de-icing system since the nodes and other low-stress regions of any single vibration field will most likely yield regions of the airfoil with insufficient ice protection. The manner of addressing this issue that was adopted by other researchers was the method of frequency sweeping, in which a number of frequencies within a small bandwidth above and below the resonant frequency are sequentially excited [63, 66]. As was mentioned in Section 5.1, the theory was that by driving the system at several frequencies, various forced vibration patterns could be induced in the structure with varying stress distributions. However, the primary limitation of this method is that it could only be applied to a small frequency bandwidth around the resonance of the actuators, generally only 500 to 1500 Hz. Operating the actuators too far off resonance leads to deleterious effects on the efficiency of the system and thus its ability to generate high levels of shear stress. This method was tested on rotating test specimens by Overmeyer [66] and deemed to be sufficient, although no detailed analyses were performed to characterize the stress distributions induced by such a frequency sweep.

The effectiveness of frequency sweeping was evaluated in the airfoil models for each of the three actuator configurations and compared to phasing without frequency sweeping and phasing coupled with frequency sweeping. The frequency interval in the model was 200 Hz; this was also the step size used for the frequency sweeping analysis. The frequency was swept over a range of 1200 Hz (600 Hz below and 600 Hz above the resonance) with 7 total increments. Figure 94, Figure 95, and Figure 96 illustrate the coverage threshold shear stress levels for the cases of no phasing, selective phasing, and all phasing, each with and without frequency sweeping, for the three actuator configurations, respectively. For all of the actuator configurations, both frequency sweeping alone (blue) and selective phasing (cyan) yield substantial gains in shear stress coverage over no phasing and no frequency sweeping (purple). However, selective phasing (cyan) yields greater shear stress coverage than frequency sweeping alone (blue) for each of the three actuator configurations, substantially more in cases 2 and 3. By frequency sweeping at each selective phasing combination (yellow), by utilizing all phasing combinations (orange), or by utilizing all phasing combinations and frequency sweeping (red), even greater improvements can be realized. These plots demonstrate that the utilization of phase inversion with dynamic frequency selection will yield greater shear stress coverage than frequency sweeping alone, and

that coupling the two methods is dramatically more effective still. Note that the most important states to compare are frequency sweeping without phasing (blue) and frequency sweeping with selective phasing (yellow).

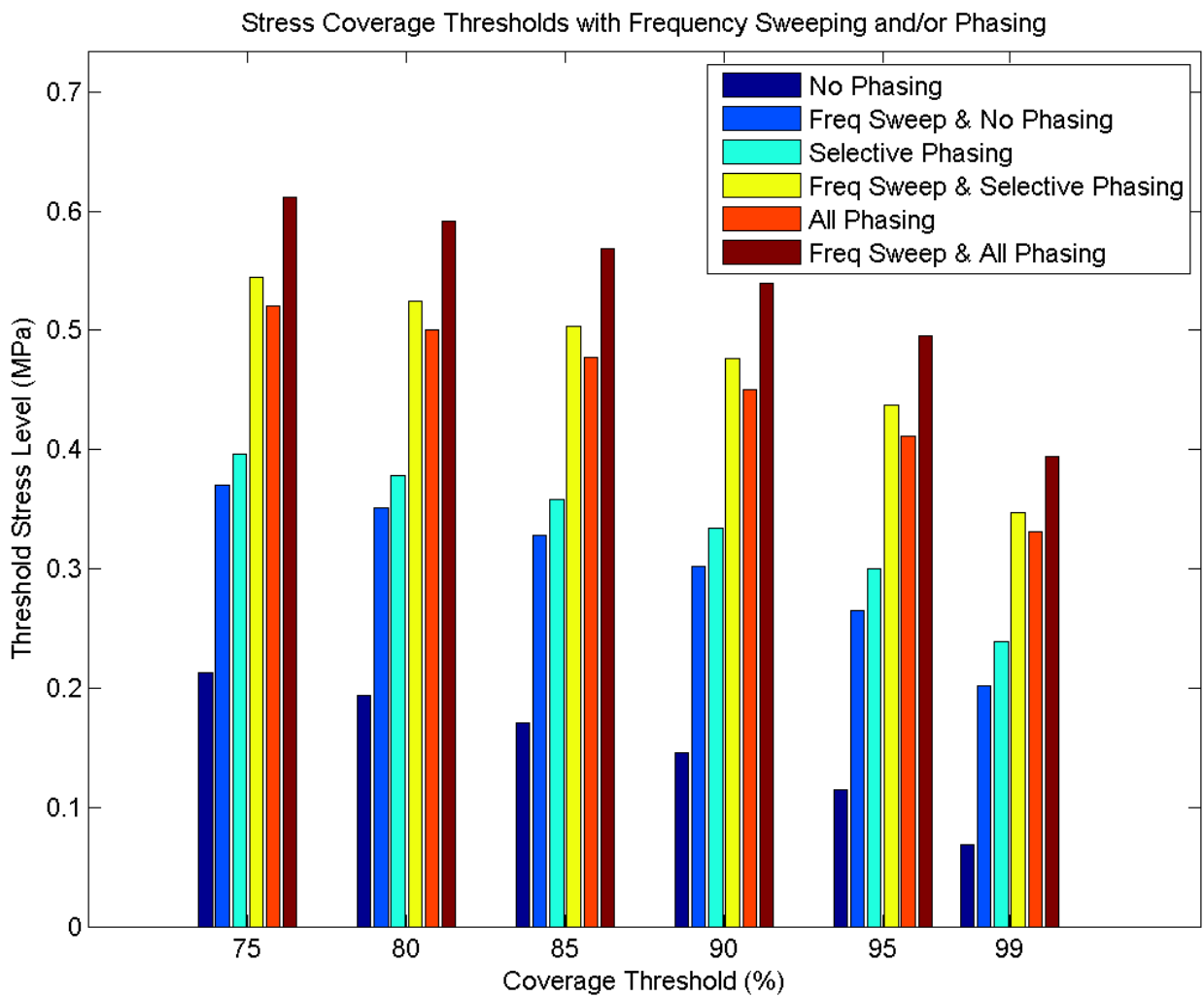


Figure 94 Shear stress coverage threshold levels for six combinations of phasing and frequency sweeping for actuator configuration 1.

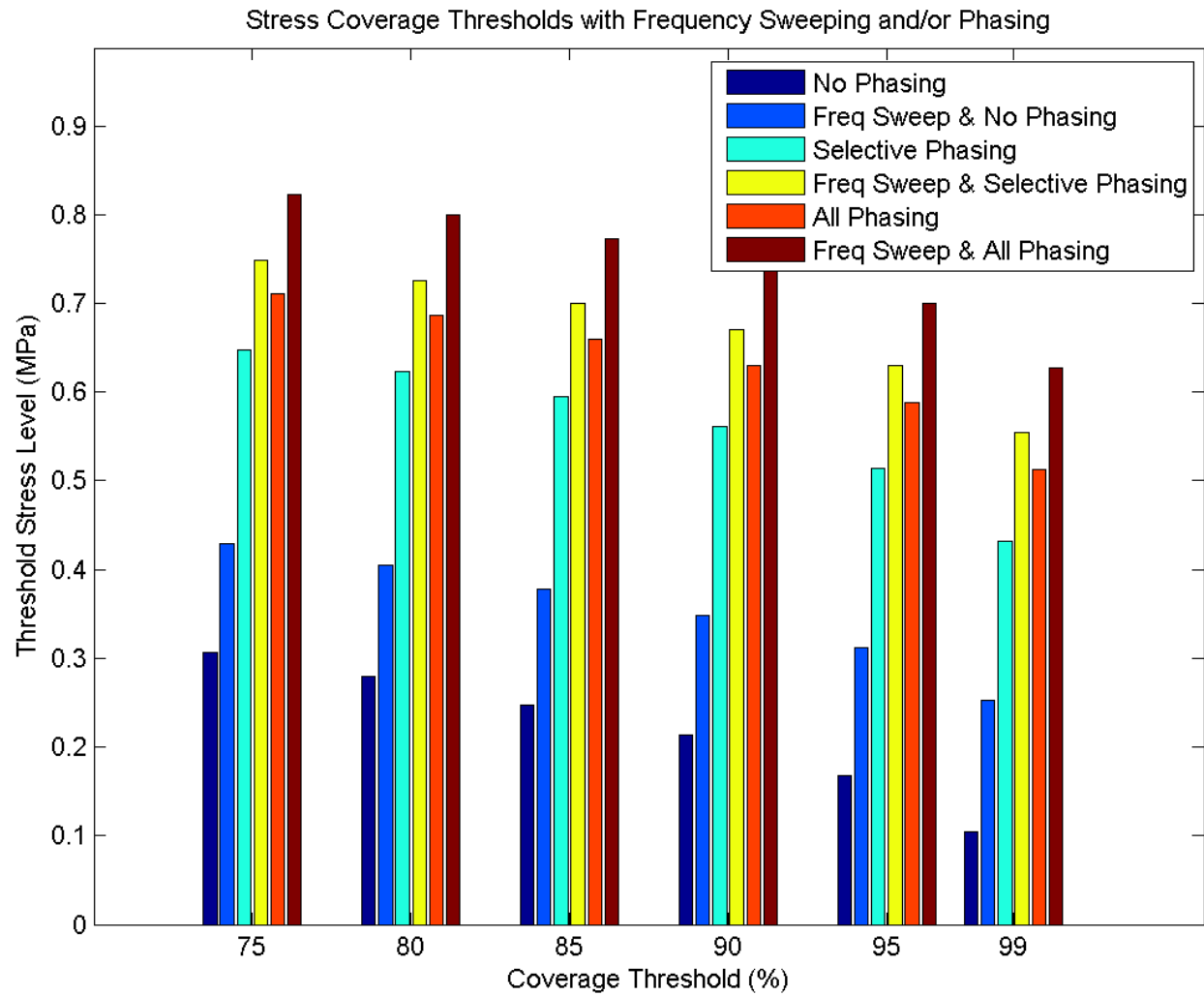


Figure 95 Shear stress coverage threshold levels for six combinations of phasing and frequency sweeping for actuator configuration 2.

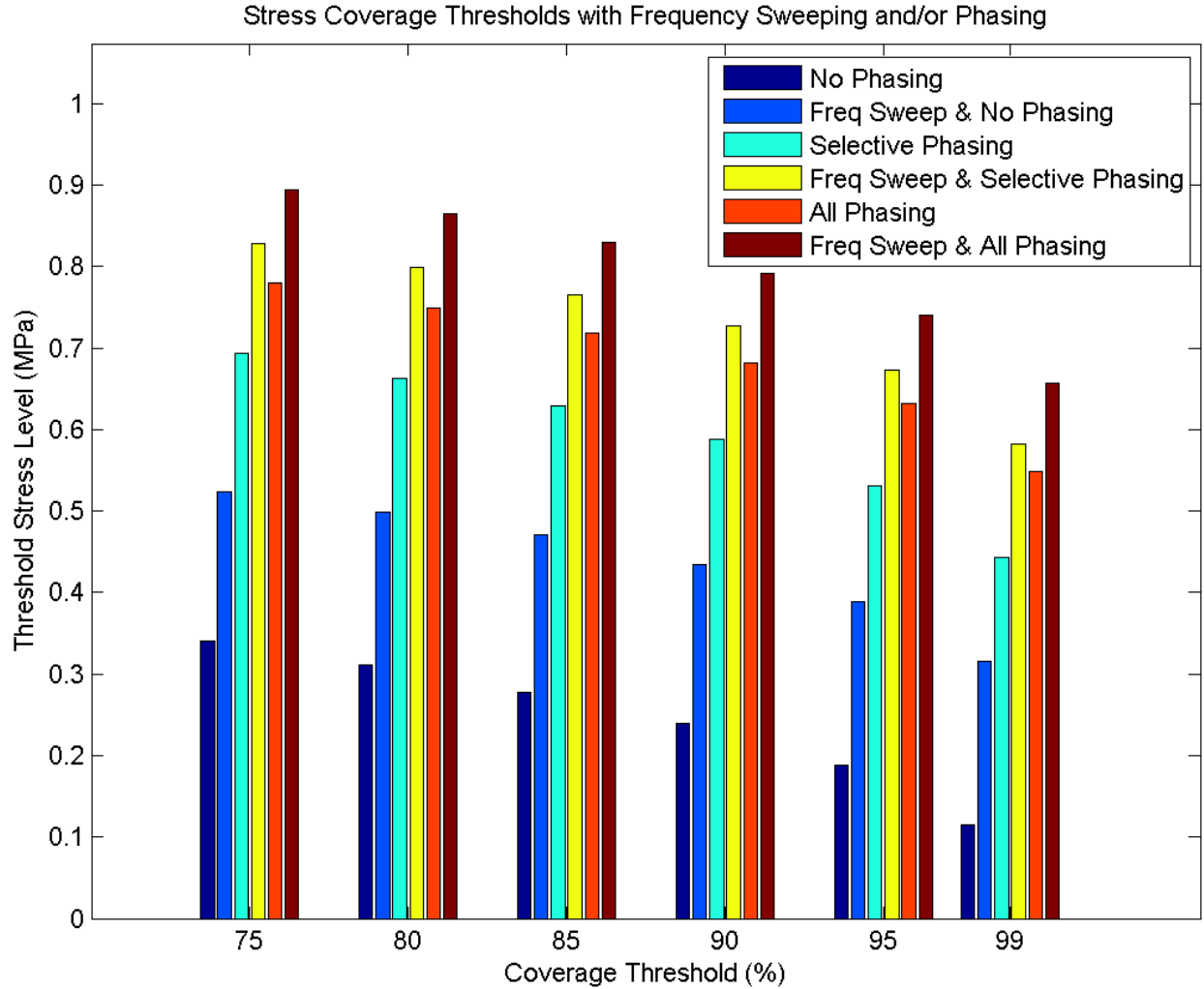


Figure 96 Shear stress coverage threshold levels for six combinations of phasing and frequency sweeping for actuator configuration 3.

The stress fields for frequency sweeping alone and for selective phasing alone are provided in Figure 97, Figure 98, and Figure 99 to demonstrate the differences in the stresses generated by the two methods. The difference between the two is minor for the first actuator configuration, but for the other two it is dramatic, which agrees with the three previous bar graphs. As was also shown in the bar graphs in the previous three figures, adding frequency sweeping to the phasing routines increases the shear stress coverage improvement even more, yielding far superior performance compared to frequency sweeping alone. The power-normalized versions of Figure 94, Figure 95, and Figure 96 are also provided in Appendix D. Again, the results are generally quite similar.

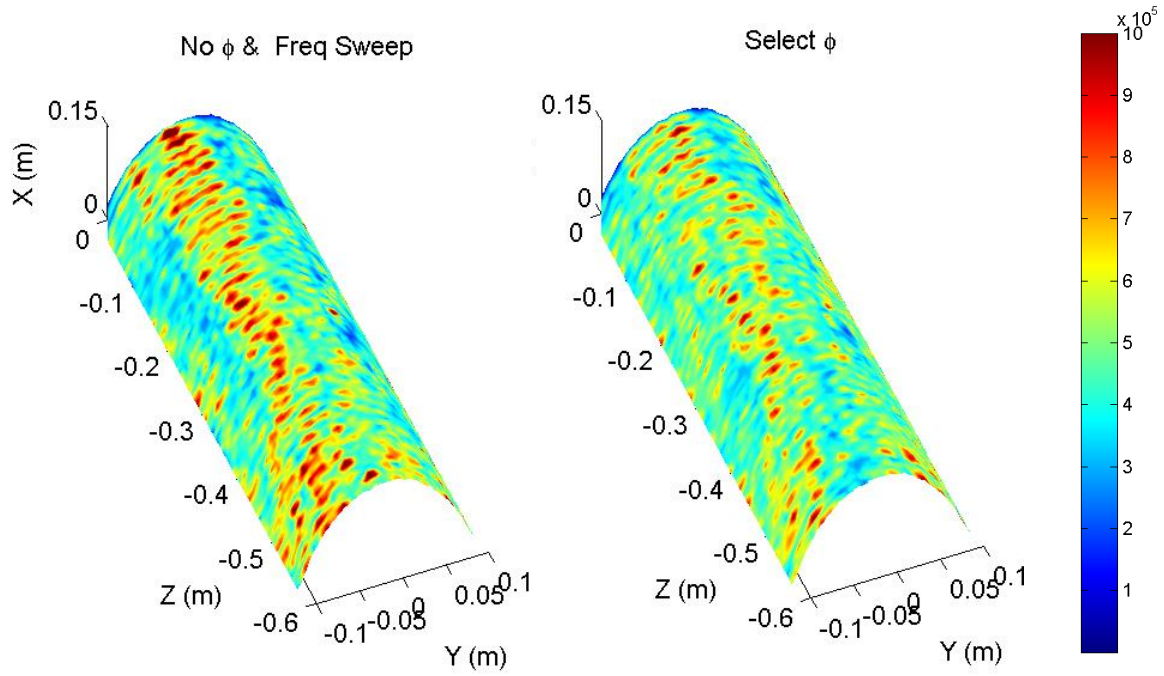


Figure 97 Comparison of the stress fields with only frequency sweeping (left) and only selective phasing (right), for actuator configuration 1.

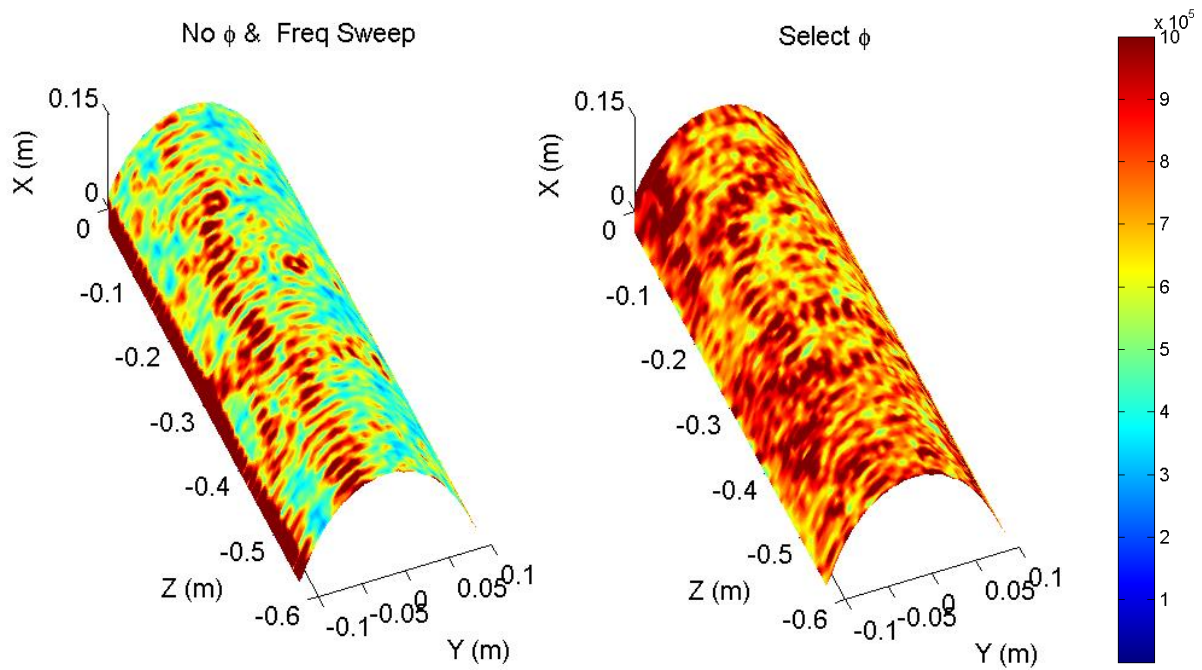


Figure 98 Comparison of the stress fields with only frequency sweeping (left) and only selective phasing (right), for actuator configuration 2.

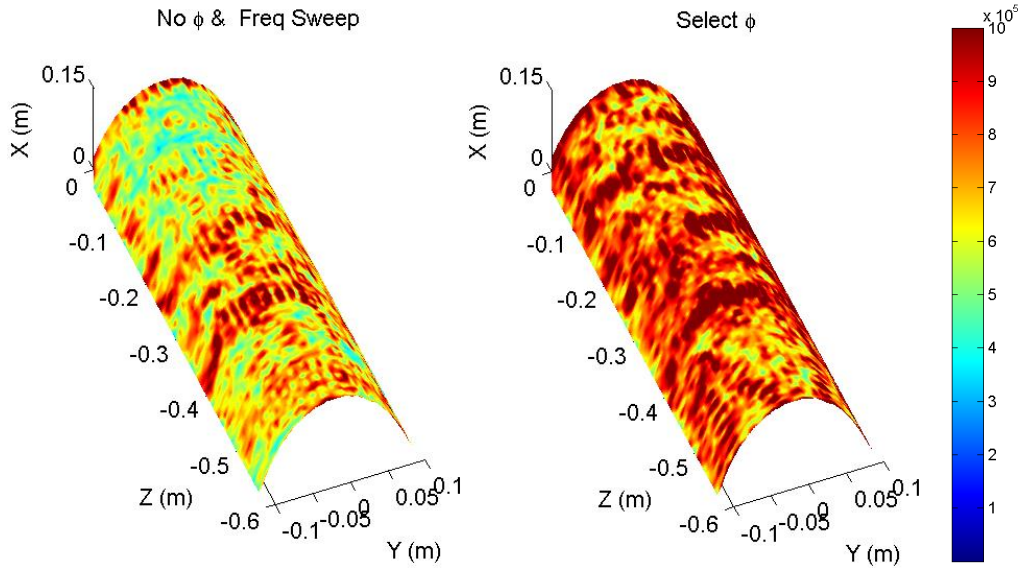


Figure 99 Comparison of the stress fields with only frequency sweeping (left) and only selective phasing (right), for actuator configuration 3.

Summary of Airfoil FE Modeling Results

The section presented the results and analysis of a number of airfoil FE models focused on evaluating the effectiveness of actuator phase inversion, determining the best method of selecting the excitation frequency during phasing, and comparing phasing to frequency sweeping. The results showed that even a small number of pre-selected phasing combinations can improve the shear stress coverage threshold by as much as 115% and that utilizing a complete set of phasing combinations can yield improvements as high as 150%. It was determined that dynamic frequency selection, in which the phased system is always driven at the phased impedance minimum, is superior to the static frequency selection method, in which the minimum impedance frequency of the unphased system is always used. It was also shown that in most cases selective actuator phasing yields better shear stress coverage than frequency sweeping alone, and that frequency sweeping in conjunction with phasing can improve shear stress coverage by as much as 170% compared to a single-frequency unphased system and by as much as 90% for a system utilizing frequency sweeping without phasing, even when the phasing combinations are selected without prior knowledge of the vibration states that they may induce.

5.5 3D Scanning Laser Doppler Vibrometer Phasing Measurements

Three separate sets of experiments were carried out to evaluate the effects of actuator phasing both directly (via de-icing experiments on a plate specimen and a composite sandwich panel airfoil specimen) and indirectly (via laser Doppler vibrometer measurements on another plate specimen). The test methods and results for each of these experiments will be presented in this section.

3D Scanning Laser Doppler Vibrometer Experimental Setup

The first set of phasing experiments utilized a 3D scanning laser Doppler vibrometer (3D SLDV) system at the University of Maryland Baltimore County (UMBC). The 3D SLDV system at UMBC is a Polytec PSV-500-3D system, shown in Figure 100, which is comprised of three laser vibrometer heads and a control system.



Figure 100 Polytec PSV-500-3D scanning laser Doppler vibrometer system [86].

Each laser vibrometer head measures the Doppler shift of a laser beam reflected off of the surface of the test specimen to measure the velocity component parallel to the beam at one point on the specimen. The system measures the Doppler shift in the laser beam using optical interferometry as illustrated in Figure 101. The induced Doppler frequency shift is proportional to the vibration component of the test specimen parallel to the path of the incident laser beam

according to the following equation, in which v is the velocity component parallel to the laser and λ is the wavelength of the laser beam [87]:

$$\Delta f = 2 \frac{v}{\lambda}. \quad (5.34)$$

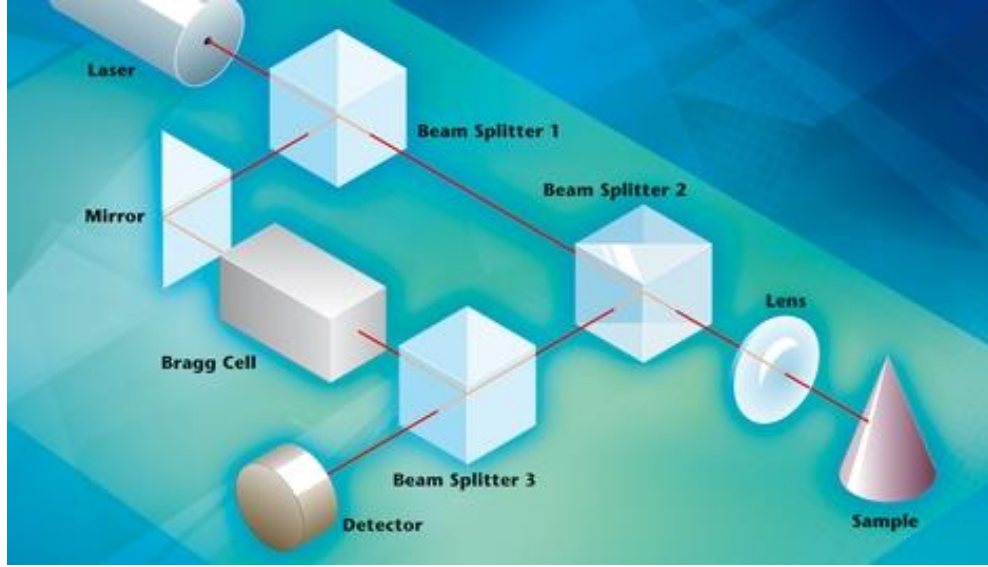


Figure 101 Basic laser Doppler vibrometer mechanism [87].

The intensity of the recombined beam measured at the detector is a combination of the reference beam (splitter 1 \rightarrow Bragg cell \rightarrow splitter 3 \rightarrow detector) and the measurement beam (splitter 1 \rightarrow splitter 2 \rightarrow sample \rightarrow splitter 2 \rightarrow splitter 3 \rightarrow detector), according to the following equation [87]

$$I_{total} = I_1 + I_2 + 2 \sqrt{\frac{I_1 I_2 \cos[2\pi(r_1 - r_2)]}{\lambda}}, \quad (5.35)$$

in which I_1 and r_1 are the intensity and path length of the reference beam, I_2 and r_2 are the intensity and path length of the measurement beam, and λ is the wavelength of the laser beam (632 nm for the helium-neon laser used here). All of these variables are effectively constant except for the path length of the measurement beam r_2 . The detector is insensitive to the laser light frequency, $f_0 = 4.74 \times 10^{14}$ Hz, but is sensitive to the much lower beat frequency between the Doppler-shifted measurement beam and the 40 MHz-shifted reference beam; the 40 MHz shift is induced by the Bragg cell. The signal measured at the detector is a frequency modulated

signal as illustrated in Figure 102. These signals can then be demodulated to extract the velocity component of the test sample parallel to the laser beam.

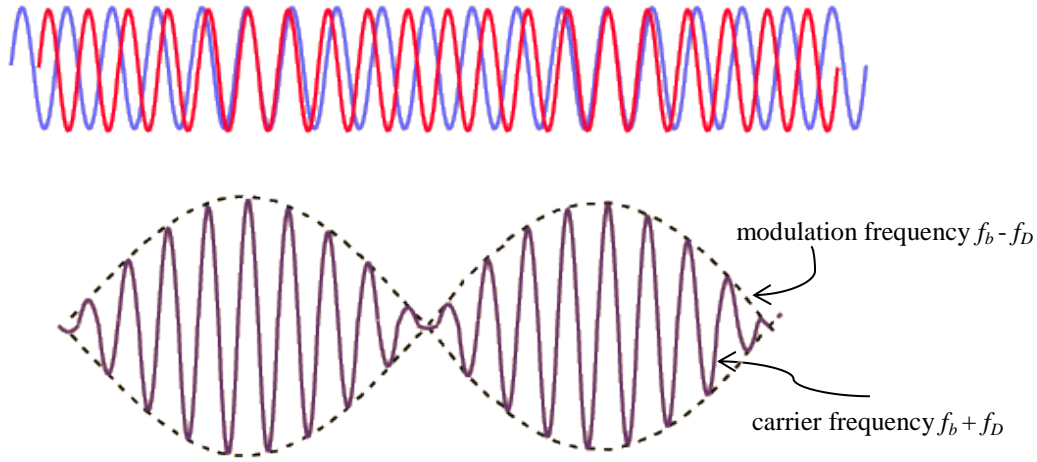


Figure 102 Illustration of two frequencies f_b (red) and f_D (blue) generating a frequency modulated signal (purple) with a carrier frequency $f_b + f_D$ and a modulation frequency $f_b - f_D$.

The 3D system used for these experiments features three laser vibrometer heads that are arranged at three different viewing angles relative to the specimen and calibrated to extract a three-dimensional velocity field by measuring three unique velocity components at each point. Each head also has the capability of automatically scanning its measurement beam over a pre-defined grid of points on the specimen to map the entire velocity field.

These tests were intended to evaluate the effectiveness of the de-icing system in distributing vibration energy across the surface of a plate-like carbon fiber honeycomb sandwich panel specimen, including the frequency sweeping and phasing techniques employed in the de-icing routine. The primary goal of these experiments was to evaluate the effectiveness of actuator phasing at redistributing the surface vibration energy and to compare the technique to frequency sweeping.

The 3D SLDV tests consisted of collecting a 200-ms time series of 3D velocity measurements on a grid of 644 points across the top surface of the carbon fiber sandwich specimen under a number of different de-icing system operating settings. The input voltage was maintained at a constant level, but the frequency and phasing were changed in each subsequent test. To collect the data

associated with frequency sweeping, the system was operated at the resonant frequency of the panel and actuators, then tests were repeated at three frequencies above and 3 frequencies below the resonance over a 1.2 kHz bandwidth. To collect the phasing data, the test at the system resonance was repeated and then three unique phasing combinations were subsequently applied. The system was operated at the resonant frequency associated with each phasing combination during these tests. Due to the limited period of access to the vibrometry equipment and the amount of time required to gather a full set of vibration data for each test, frequency sweeping results for each actuator phasing combination could not be collected. Therefore the results here only compare frequency sweeping without phasing to phasing without frequency sweeping.

Laser Vibrometer In-Plane Surface Vibration Field Results

The in-plane velocity fields from the frequency sweeping tests are shown in Figure 103, and the fields from the phasing tests are shown in Figure 104.

As is apparent in the previous two figures, the vibration fields varied little under frequency sweeping over the 1.2 kHz bandwidth, but they varied substantially during phasing. This supports the theory that phasing is more effective at redistributing the stresses than frequency sweeping and is in general agreement with the finite element modeling results in this regard. Note that even when the system is operated at the same frequency (46.5 kHz) as one of the frequency sweeping tests, the vibration field for the phased case is substantially different from that of the unphased case. Of course, in-plane vibration is not equivalent to shear stress, but it is the most relevant measure of the vibration field that can be collected using a laser vibrometer system. The results from this experiment do not provide explicit information regarding the stress fields that would be induced if an ice layer was applied to the panel, but they do provide an excellent measure of how frequency sweeping and phasing can alter the forced vibration field induced in such a structure.

Without phasing, the vibration field is weak in many regions of the plate, particularly between the actuators. After three different phasing increments are applied, the vibration energy is redistributed. The “effective” vibration field can be considered the maximum vibration achieved at each point on the structure after applying the seven frequencies (for frequency sweeping) or the four phases (for phasing). These effective vibration fields are shown in Figure 105, in which

it is apparent that the overall coverage after phasing is substantially greater than that achieved with frequency sweeping, including in the regions between actuators. Further actuator phasing used in conjunction with frequency sweeping (for each phasing combination) would only be expected to further improve the distribution and coverage of the vibration field in such specimens.

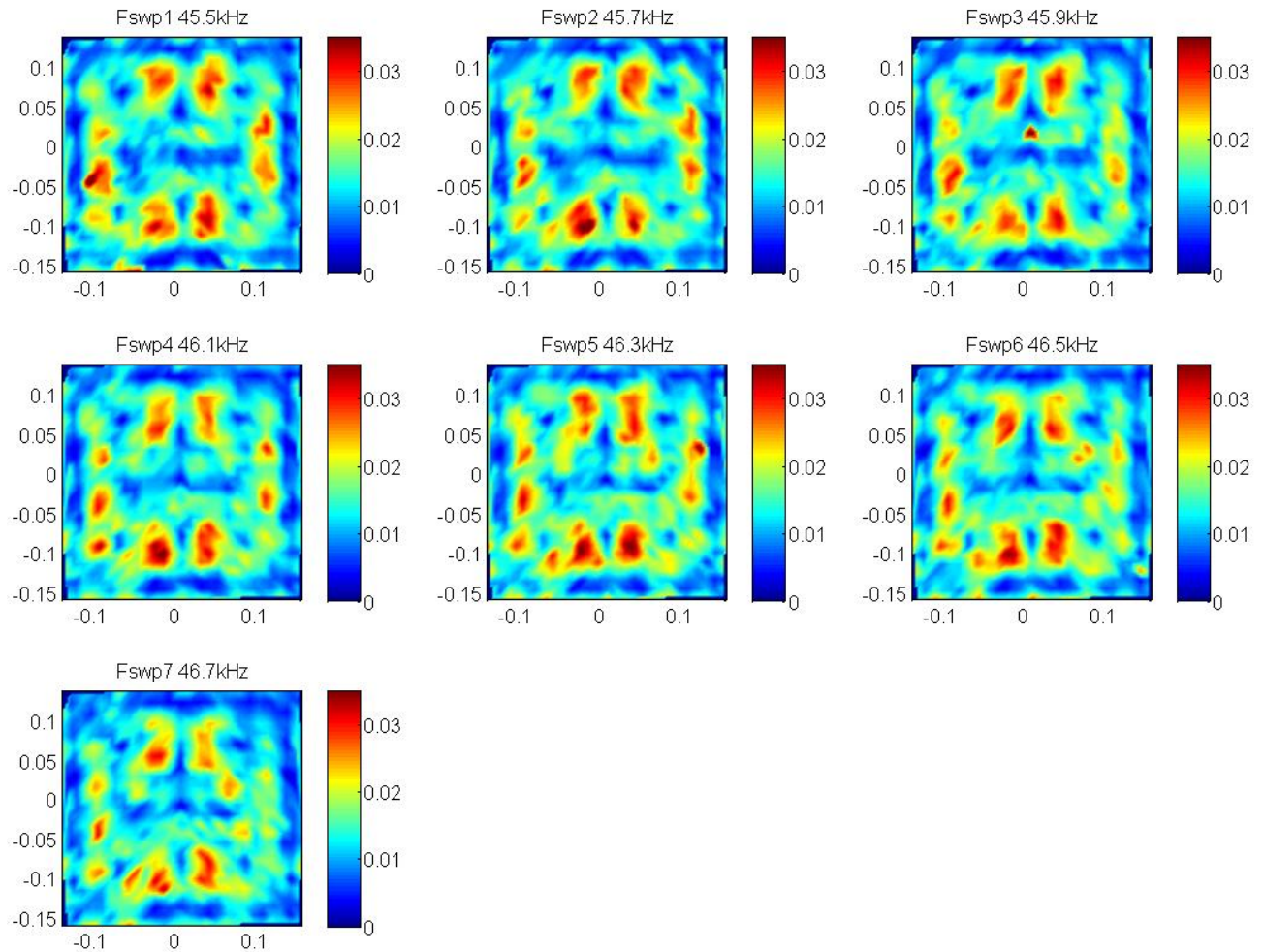


Figure 103 In-plane velocity fields on carbon fiber sandwich panel surface at seven frequencies during ultrasonic de-icing system frequency sweeping.

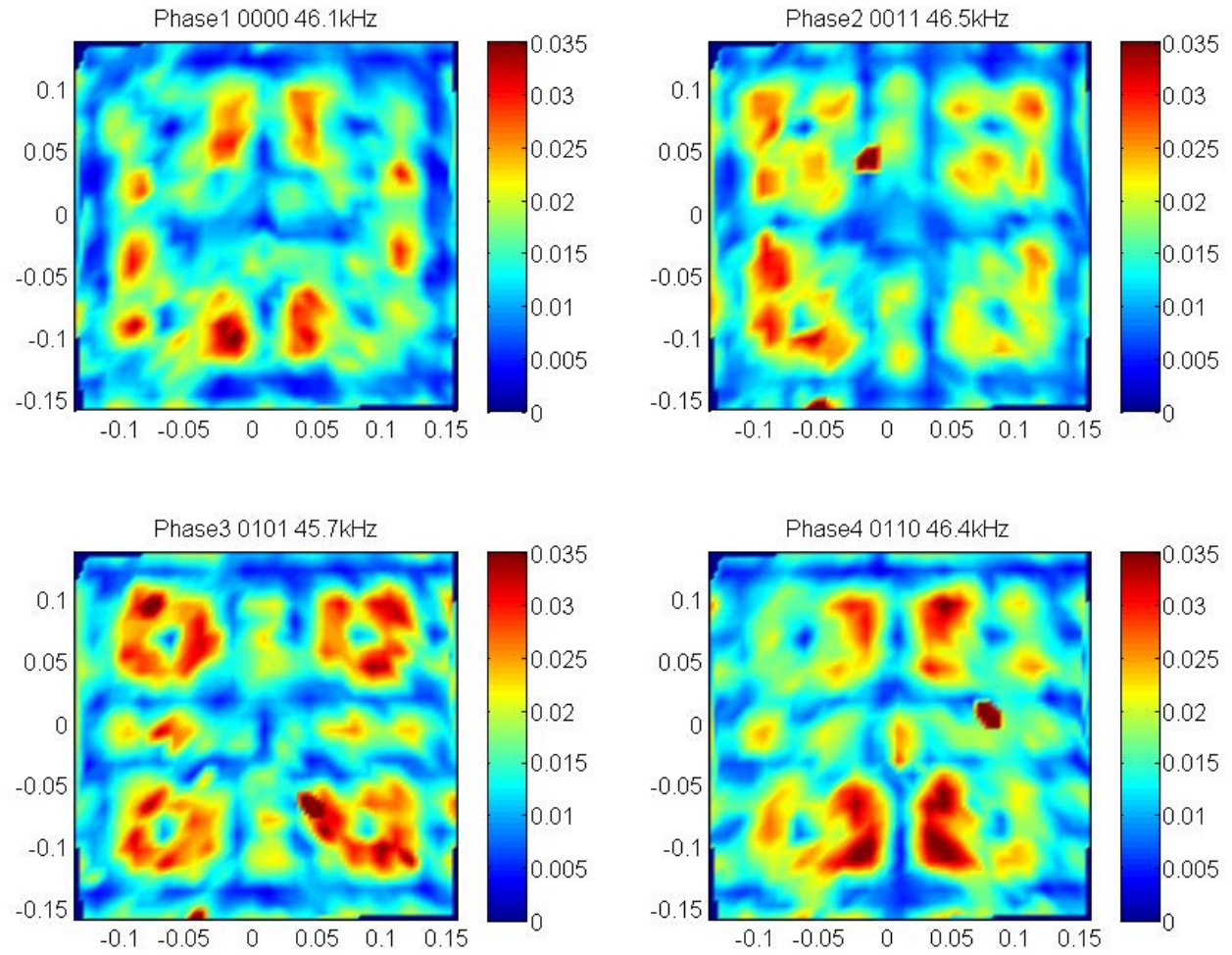


Figure 104 In-plane velocity fields on carbon fiber sandwich panel surface with four phasing combinations during ultrasonic de-icing system phasing.

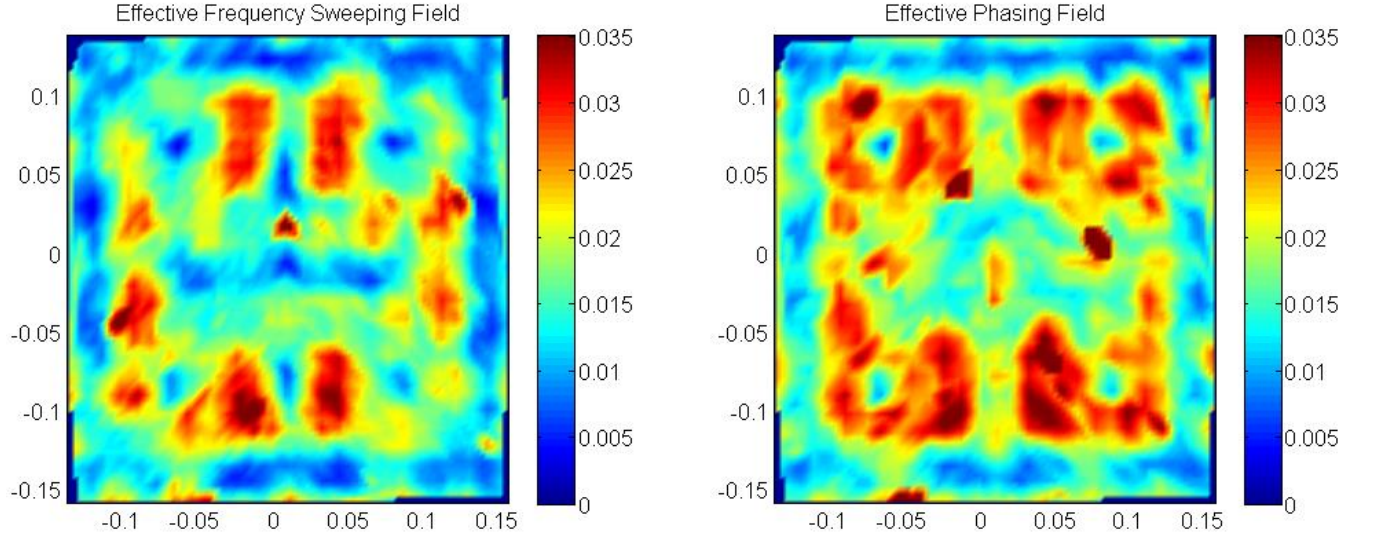


Figure 105 Effective vibration fields after frequency sweeping (left) and phasing (right).

Laser Vibrometer Results Analysis

The amount of change in the vibration fields while applying frequency sweeping or phasing can be measured by calculating the two-dimensional auto-correlation of each field with respect to the baseline field (the field with no phasing, driven at the resonant frequency of 46.1 kHz), which is the zero-shift point of the two-dimensional cross-correlation. The equation for the two-dimensional cross-correlation, c , between two distributions, f and g , is given by

$$c(u, v) = f(x, y) * g(x, y) = \int_{-\infty}^{\infty} \int_{-\infty}^{\infty} f(u, v) \cdot g(x - u, y - v) du dv, \quad (5.36)$$

and the corresponding auto-correlation is $c(0,0)$. In discrete form, this equation becomes

$$c[k, l] = (f * g)[k, l] = \sum_{m=0}^{M-1} \sum_{n=0}^{N-1} f[m, n] \cdot g^*[m - k, n - l], \quad (5.37)$$

in which $*$ denotes complex conjugation, M is the number of discrete points in the x domain, and N is the number of discrete points in the y domain. Here the auto-correlation is again $c[0,0]$.

The two-dimensional auto-correlation calculates the similarity of two fields, and by normalizing these values, one can attain a quantitative measure of the relative change in the distribution of

those two fields in a way that is independent of the overall amplitude of either field. The normalized two-dimensional cross-correlation, c' , is given by

$$\begin{aligned} c' &= \frac{[f(x, y) - \bar{f}(x, y)] * [g(x, y) - \bar{g}(x, y)]}{\sigma_f \sigma_g} = \frac{F(x, y) * G(x, y)}{\sigma_f \sigma_g} \\ &= \frac{1}{\sigma_f \sigma_g} \int_{-\infty}^{\infty} \int_{-\infty}^{\infty} F(u, v) \cdot G(x - u, y - v) du dv. \end{aligned} \quad (5.38)$$

In discrete form, this equation becomes

$$\begin{aligned} c'[k, l] &= \frac{(f - \bar{f}) * (g - \bar{g})[k, l]}{\sigma_f \sigma_g} \\ &= \frac{1}{\sigma_f \sigma_g} \sum_{m=0}^{M-1} \sum_{n=0}^{N-1} F[m, n] \cdot G^*[m - k, n - l], \end{aligned} \quad (5.39)$$

and the normalized auto-correlation is c' [0,0]. Since we are concerned with the change in the distribution *relative* to the unphased center frequency case, each of the auto-correlations can be compared to this value using the calculation of the relative change in normalized auto-correlation

$$\frac{c'[0,0] - c'_0[0,0]}{c'_0[0,0]}, \quad (5.40)$$

in which the subscript 0 refers to the baseline state (unphased center frequency in this case).

These values are plotted in the bar charts in Figure 106. Note that the 4th frequency in the frequency sweeping plot and the 1st phase in the phasing plot are zero, because these are the “baseline” fields to which the others are being compared. The key point to take away from Figure 106 is that phasing creates a substantially greater variation (approximately 4-5 times as much by this measure) in the vibration distribution than frequency sweeping. This is already apparent from the previous figures of the velocity fields, but this provides a quantitative measure of the variation. The variation measured during frequency sweeping was in the range of 10-15%, while the variation due to actuator phasing (without frequency sweeping) was in the range of 50-70%. As may be expected, as frequency sweeping is performed further from the center frequency (either above or below), the variation in the field becomes less and less similar to the baseline center frequency case.

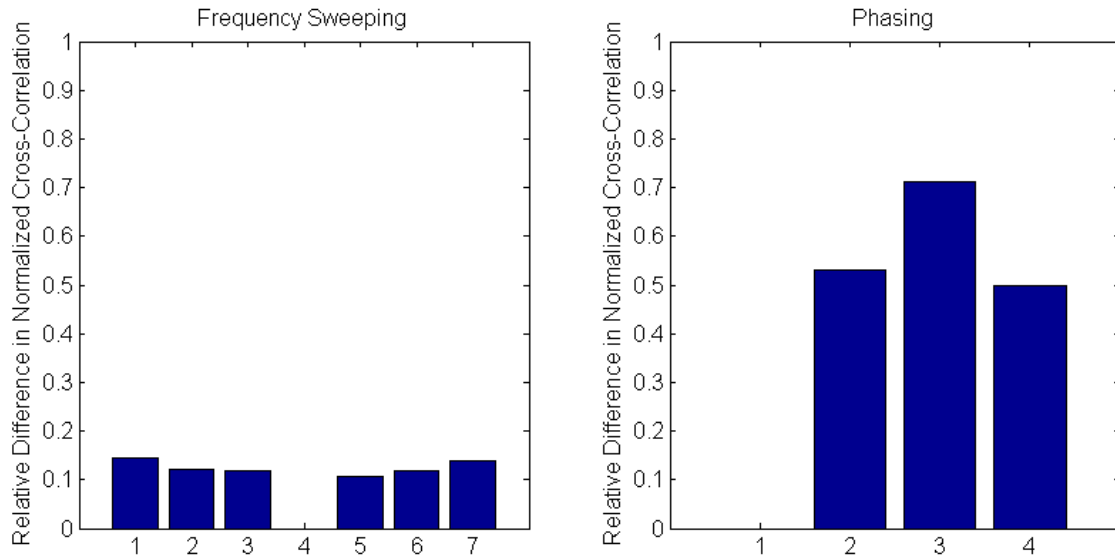


Figure 106 Relative normalized two-dimensional cross-correlations of the velocity fields compared to the baseline field with frequency sweeping (left) and phasing (right).

Another important finding is that phasing achieves these substantial changes in the vibration distribution without losing efficiency or operating off-resonance, as is evidenced by the relative average velocity amplitude plots in Figure 107. This is important, because achieving sufficient de-icing coverage is a matter of both varying the field and maintaining a sufficiently high level of vibration simultaneously. In this case, phasing not only improves the variation in the field, but also increases the average amplitude of vibration across the surface, therefore improving the efficiency of the system. Although the average vibration amplitude will not always increase as different phasing combinations are applied, such increases are quite possible since the system is operated at the new system resonance each time a new phasing combination is applied.

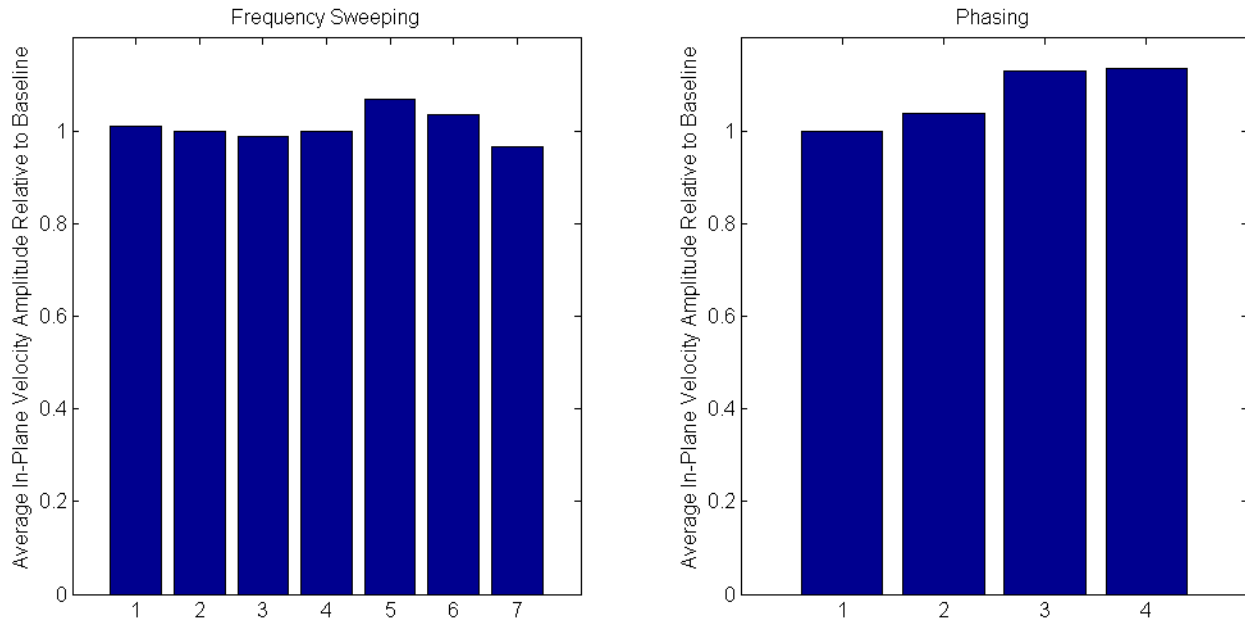


Figure 107 Relative average velocity across the panel surface as a function of frequency sweeping (left) and phasing (right).

One final measure of the effectiveness of the de-icing method at covering the entire structure is to determine the stress (or in this case, velocity) amplitude threshold that is achieved across a certain percentage of the structure. For instance, if after phasing and frequency sweeping is applied, 90% of the surface area of the structure experienced stresses of 1 MPa or greater, then the 90% coverage threshold would be 1 MPa. These values are shown for frequency sweeping and phasing for a number of velocity coverage thresholds in Figure 108. The percent improvement in these values when switching from frequency sweeping to phasing is shown in Figure 109.

Note that these tests were carried out on a carbon fiber honeycomb sandwich panel structure. Due to time restrictions, the tests could not be repeated on a metallic panel to compare the results. However, it can generally be assumed that the damping would be less in the metallic structure and thus the vibration would be less isolated to the regions immediately around the actuators, which is the general trend that has been observed during de-icing experiments between composite sandwich panels and metallic panels.

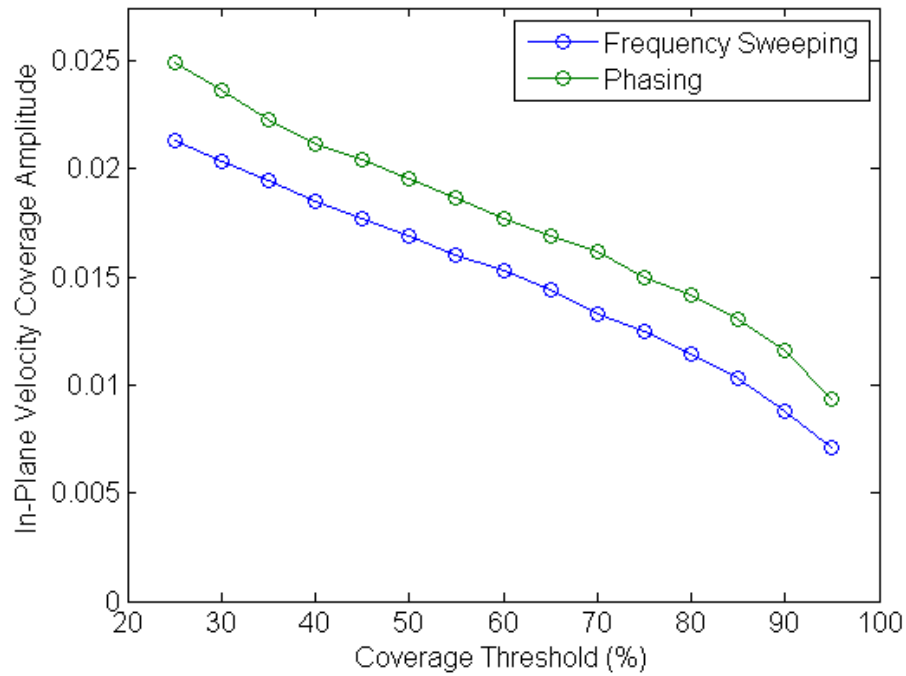


Figure 108 Velocity coverage thresholds for frequency sweeping and phasing.

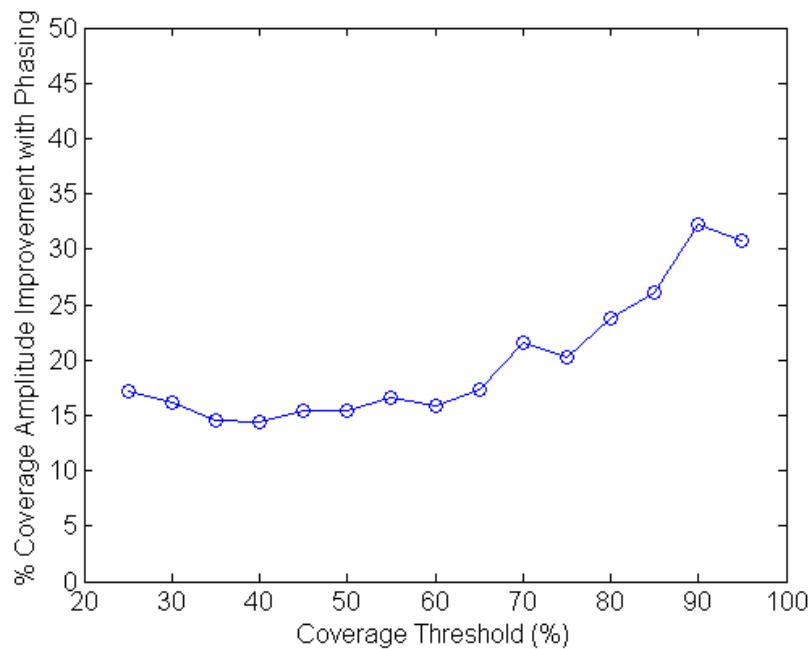


Figure 109 Percent improvement in coverage thresholds when switching from frequency sweeping to phasing.

Overall, these results confirm the theory that actuator phasing is a critical part of the ultrasonic de-icing system and that it provides better structural coverage than frequency sweeping. In

reality, frequency sweeping and phasing can be implemented together in the final de-icing system routine to further improve the coverage and efficiency of the system, which should provide even better system performance than demonstrated by these laser vibrometer tests.

5.6 De-Icing Grid Phasing Experiments

The finite element modeling and laser vibrometry experiments discussed thus far make a strong case for the benefits afforded by actuator phasing in terms of improving de-icing coverage and efficiency. These benefits were also directly evaluated via a series of de-icing experiments on a titanium plate. The primary purpose of the de-icing experiments described in this section is to compare the capabilities of a de-icing system operating under three sets of parameters:

1. No frequency sweeping or phasing
2. Frequency sweeping only
3. Phasing and frequency sweeping

De-Icing Grid Phasing Experiment Setup and Procedure

In order to be able to quantitatively evaluate the de-icing coverage of the system in a repeatable and unambiguous manner, an ice grid approach was used in lieu of a single sheet of ice. In the ice grid approach, a grid of ice dots was applied to the plate. Using this setup, the number of ice dots fully and/or partially delaminated can easily be counted after each de-icing test. The ice dots were consistently created by following the procedure listed below.

- A 10 x 10 grid of 100 points was mapped onto the plate surface on a 1" square grid
- PTFE (Teflon) tape was applied across the surface of the plate and ½"-diameter circles were cut out of the tape, centered on the 100 grid points; see Figure 110.
- 0.2 mL of water was applied in each of the 100 circular cutouts and allowed to freeze; see Figure 111.

The PTFE tape serves to contain the water to each circular cutout on the grid without the water bonding to the template. Other methods were tested, but this approach provided the best and most consistent results for creating a grid of ice dots.

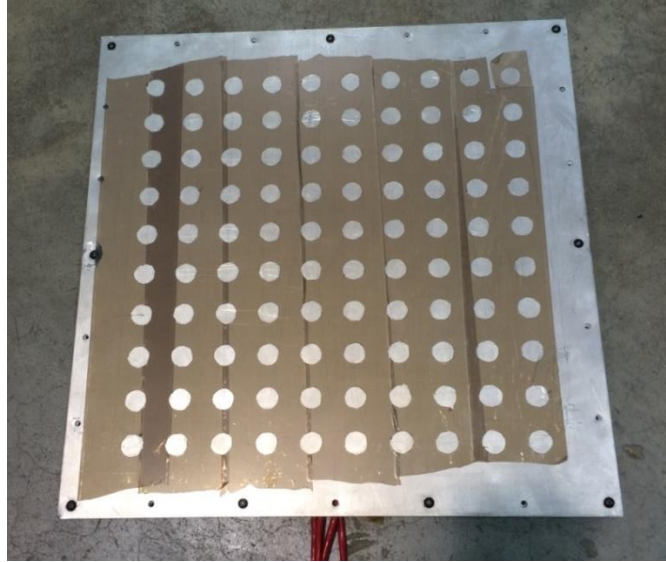


Figure 110 The 12" x 12" titanium plate with a 100-point grid of circular 1/2"-diamter cutouts in a PTFE tape covering.

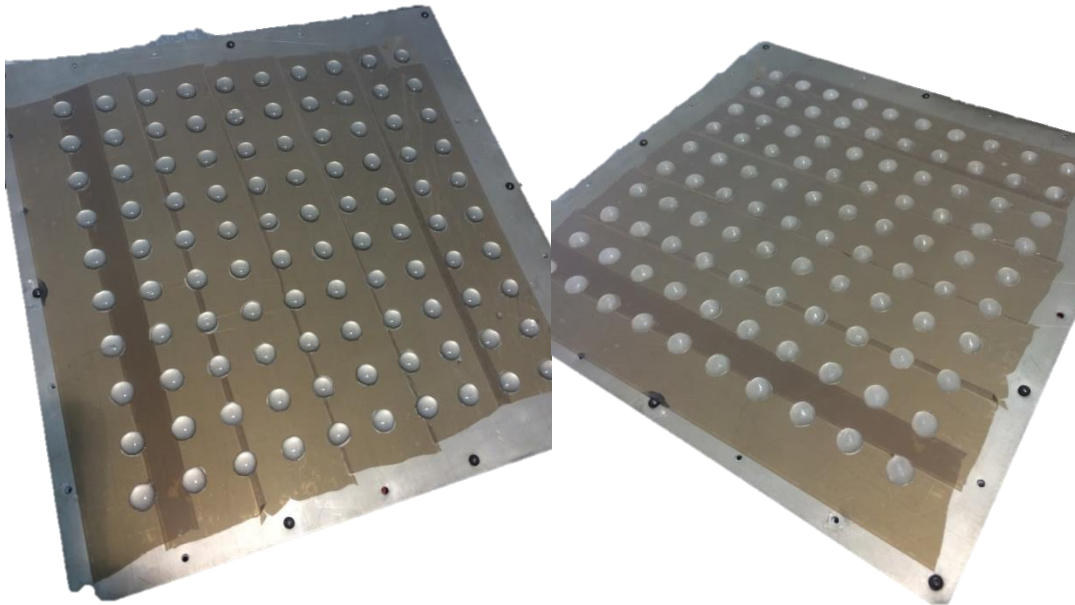


Figure 111 (Left) 0.2 mL of water applied to each grid point and (right) the frozen grid of ice dots.

These tests were carried out on a 12"-square 0.040"-thick titanium plate mounted to an aluminum frame for added stiffness. Four 2"-diameter PZT actuators were mounted to the reverse side of the titanium panel in a square pattern as shown in Figure 112.

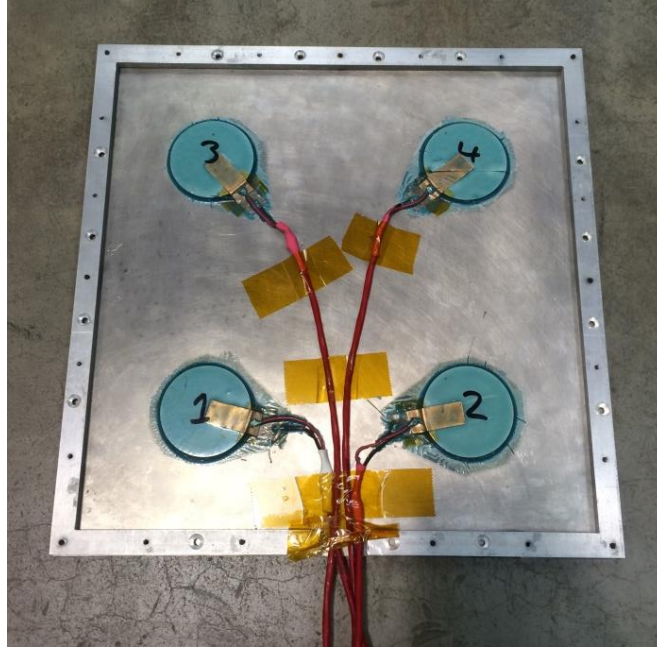


Figure 112 The 12" x 12" titanium plate with four 2"-diameter PZT actuators bonded to the reverse side.

Four tests were carried out under test condition 1 (no phasing or frequency sweeping) and condition 2 (frequency sweeping only) and 3 tests were carried out under condition 3 (phasing and frequency sweeping). Frequency sweeping was performed at 7 frequencies (including the center frequency) over a 1.0 kHz bandwidth. The phasing was performed for the eight unique phasing combinations. Each test scheme was cycled through 3 loops, i.e. for frequency sweeping, the entire frequency range was swept through three times. The test scheme details are shown in

Table 12. The phasing combinations used during actuator phasing are shown in Table 13.

Table 12 De-icing grid phasing test scheme details.

	Freq. Sweep?	Phase?	Procedure
Test Scheme I:	NO	NO	1 frequency, 3 cycles
Test Scheme II:	YES	NO	7 frequencies, 3 cycles
Test Scheme III:	YES	YES	8 phases, 7 frequency, 3 cycles

Table 13 Actuator phasing combinations used during the de-icing grid phasing tests.

	Act 1	Act 2	Act 3	Act 4
Phase 1	0	0	0	0
Phase 2	0	180	180	0
Phase 3	0	180	0	180
Phase 4	0	0	180	180
Phase 5	0	180	0	0
Phase 6	0	0	180	0
Phase 7	0	0	0	180
Phase 8	0	180	180	180

The results under each of these test conditions were averaged across all three iterations. During each test the input power to the system was incrementally increased over 8 steps between 0.3 V and 0.6 V, and the number of fully delaminated and partially delaminated (defined as cracked or partially debonded, but not fully removed) ice dots was recorded after each increment. The temperature of the panel was monitored to ensure that it did not exceed 0°C at any point during the tests. The input power was controlled by increasing the voltage of the signal supplied to the amplifier, which has a fixed gain. Once the total ice removal reached the target of 90%, the tests were stopped.

De-Icing Grid Phasing Experiment Results and Analysis

The results of each test are provided in Table 14 below, in which the total number of fully and fully + partially delaminated dots are provided for each test. The full delamination results from Table 14 are compiled in Figure 113, including the error bars derived from the standard deviation of the results. The results for the full and partial delamination are compiled in Figure 114. These figures clearly show that the phasing scheme dramatically increases the percentage of total ice removed for any given level of input to the system. They also show that the input voltage required to achieve a comparable level of de-icing coverage is far less with phasing than without. The approximate power levels were measured for each voltage input level, and the results as a function of power are shown in Figure 115 and Figure 116. The average ice removal improvement with phasing versus without phasing was 189% (a ratio of 1:2.89). This improvement is larger than that predicted by the finite element models for the airfoil structure (around 90-150% predicted improvement).

Scheme	Test #	Level	Result	Test #	Level	Result
I	I1.1	1	0, 0	I4.1	1	0, 0
	I1.2	2	0, 0	I4.2	2	0, 0
	I1.3	3	0, 0	I4.3	3	0, 1
	I1.4	4	0, 0	I4.4	4	0, 2
	I1.5	5	1, 2	I4.5	5	3, 7
	I1.6	6	7, 13	I4.6	6	6, 10
	I1.7	7	10, 16	I4.7	7	9, 17
	I1.8	8	16, 24	I4.8	8	19, 31

Scheme	Test #	Level	Result	Test #	Level	Result
II	II1.1	1	6, 9	II4.1	1	6, 17
	II1.2	2	14, 15	II4.2	2	15, 34
	II1.3	3	24, 28	II4.3	3	22, 49
	II1.4	4	31, 36	II4.4	4	35, 59
	II1.5	5	35, 41	II4.5	5	45, 69
	II1.6	6	40, 46	II4.6	6	52, 79
	II1.7	7	49, 54	II4.7	7	64, 90
	II1.8	8	60, 66	II4.8	8	72, 90

Scheme	Test #	Level	Result	Test #	Level	Result
III	III1.1	1	10, 16	III3.1	1	34, 35
	III1.2	2	27, 48	III3.2	2	56, 62
	III1.3	3	66, 76	III3.3	3	66, 73
	III1.4	4	84, 87	III3.4	4	82, 85
	III1.5	5	92, 94	III3.5	5	89, 91
	III1.6	6	N/A	III3.6	6	N/A
	III1.7	7	N/A	III3.7	7	N/A
	III1.8	8	N/A	III3.8	8	N/A

Test #	Level	Result	Test #	Level	Result
I2.1	1	0, 0	I3.1	1	1, 1
I2.2	2	0, 0	I3.2	2	1, 1
I2.3	3	1, 2	I3.3	3	1, 2
I2.4	4	1, 2	I3.4	4	1, 2
I2.5	5	1, 2	I3.5	5	2, 3
I2.6	6	2, 4	I3.6	6	2, 3
I2.7	7	6, 9	I3.7	7	12, 16
I2.8	8	11, 16	I3.8	8	18, 23

Test #	Level	Result	Test #	Level	Result
II2.1	1	15, 18	II3.1	1	3, 3
II2.2	2	29, 30	II3.2	2	4, 7
II2.3	3	36, 39	II3.3	3	8, 12
II2.4	4	41, 42	II3.4	4	15, 22
II2.5	5	44, 50	II3.5	5	20, 32
II2.6	6	64, 72	II3.6	6	29, 45
II2.7	7	68, 77	II3.7	7	41, 60
II2.8	8	75, 78	II3.8	8	46, 61

Test #	Level	Result	Test #	Level	Result
III2.1	1	34, 35	III3.1	1	34, 35
III2.2	2	52, 53	III3.2	2	56, 62
III2.3	3	67, 74	III3.3	3	66, 73
III2.4	4	79, 88	III3.4	4	82, 85
III2.5	5	89, 90	III3.5	5	89, 91
III2.6	6	N/A	III3.6	6	N/A
III2.7	7	N/A	III3.7	7	N/A
III2.8	8	N/A	III3.8	8	N/A

Table 14 De-icing grid phasing experiment results.

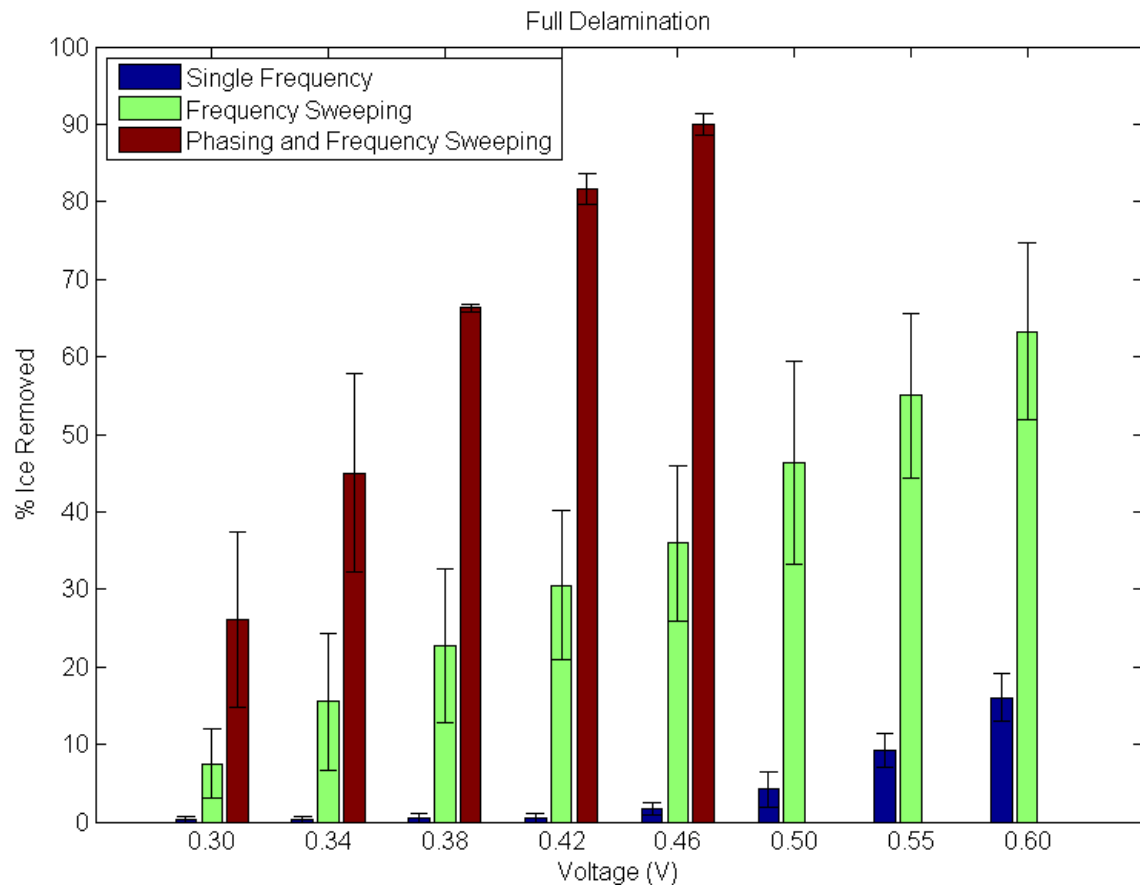


Figure 113 Compiled results of full ice dot delamination for the single frequency, frequency sweeping, and combined phasing and frequency sweeping test schemes versus input voltage.

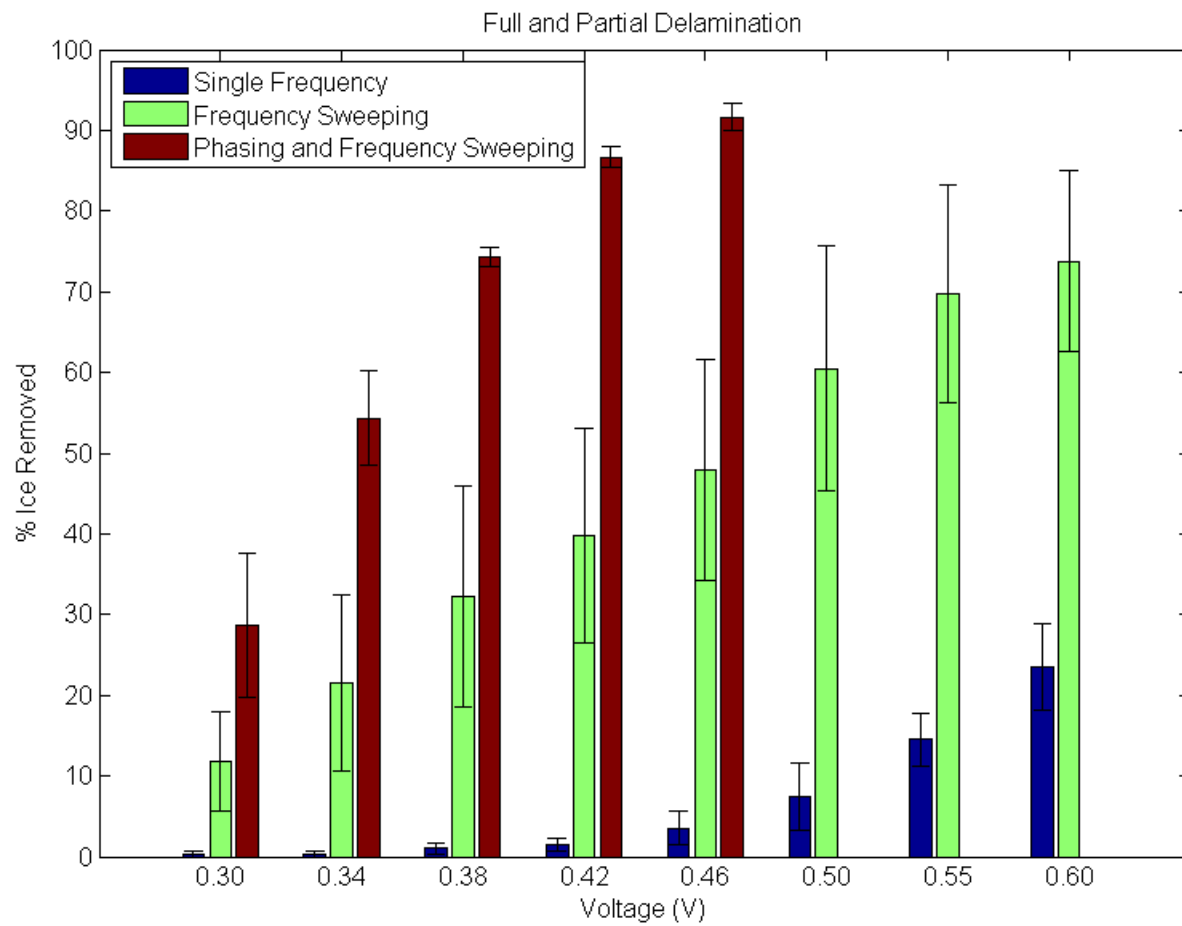


Figure 114 Compiled results of full and partial ice dot delamination for the single frequency, frequency sweeping, and combined phasing and frequency sweeping test schemes versus input voltage.

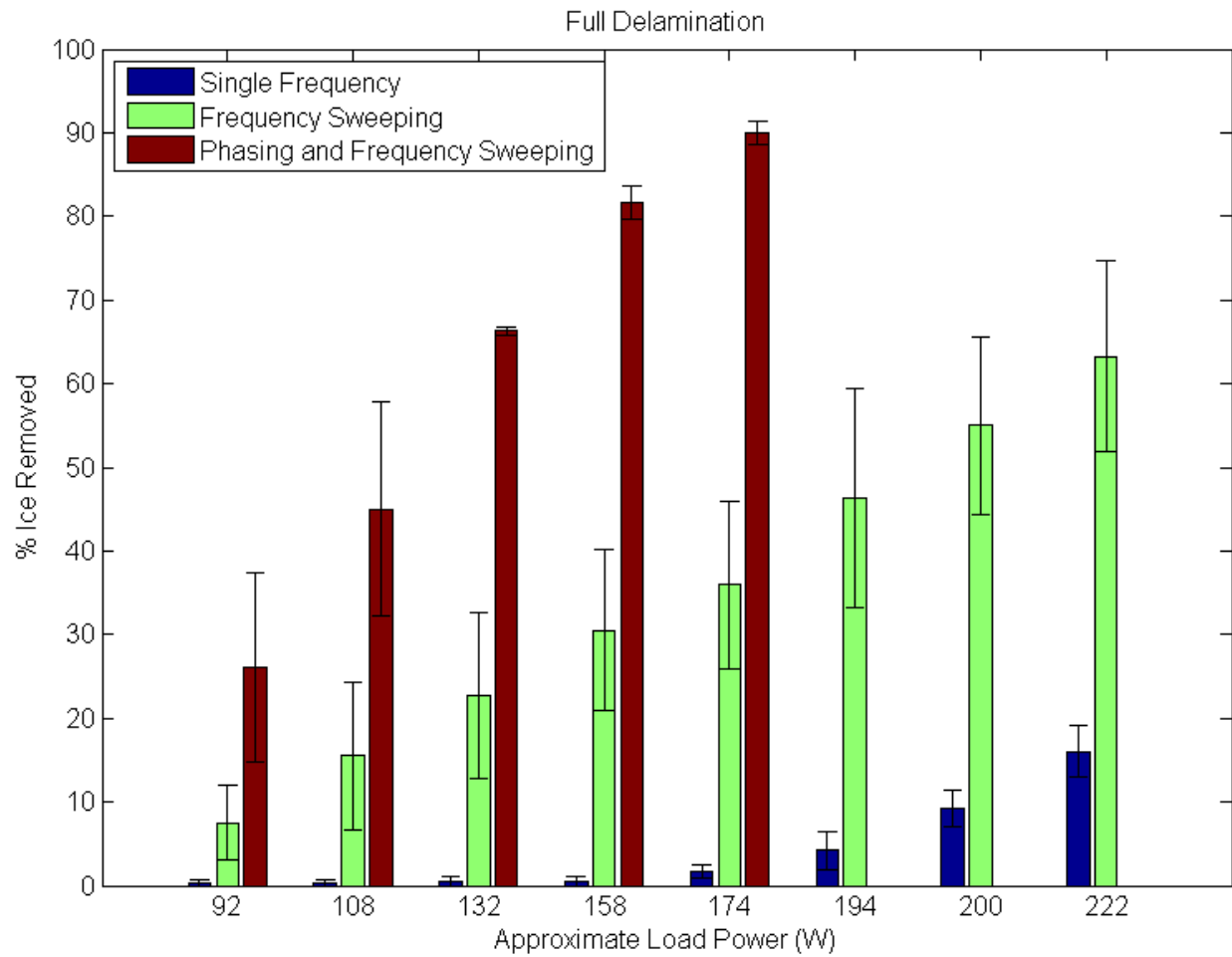


Figure 115 Compiled results of full ice dot delamination for the single frequency, frequency sweeping, and combined phasing and frequency sweeping test schemes versus load power.

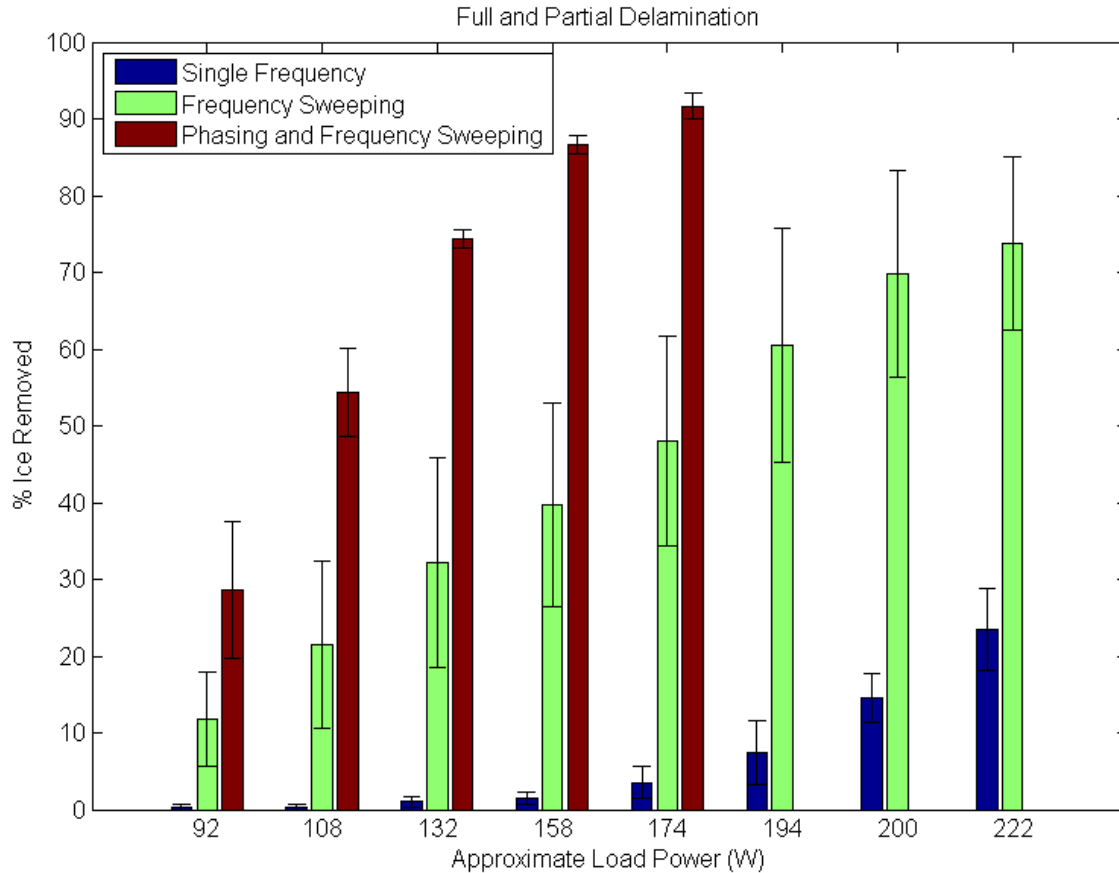


Figure 116 Compiled results of full and partial ice dot delamination for the single frequency, frequency sweeping, and combined phasing and frequency sweeping test schemes versus load power.

Phasing Experiment Conclusions

The results of the de-icing grid phasing experiments directly confirm that actuator phasing can yield dramatic improvements in the efficiency and effectiveness of an ultrasonic de-icing system. In the cases examined here, phasing combined with frequency sweeping provided an improvement of 189% on average at a comparable power level to frequency sweeping alone. To verify that the phasing wasn't simply improving upon the frequency sweeping results due to an increased number of actuation periods, the multiple cycles of frequency sweeping were repeated in several instances. In each case, repeated frequency sweeping provided negligible improvement in ice removal, and generally only served to fully delaminate a small number of the partially delaminated ice dots. It should be noted that the particularly poor performance of the single-frequency actuation was not predicted. However, this is likely due to the fact that the impedance minimum selected during the impedance sweep is often not the optimal resonant frequency for

the system, and frequency sweeping will often show that the best resonance is slightly above or below the predicted resonance. This improper prediction of the resonance can be attributed to the fact that the impedance matching in the system is limited, and thus the true impedance minimum, while it may be the optimal resonance of the actuator-structure system, does not provide the best power transmission from the amplifiers. For instance, if the impedance minimum occurs at 40 kHz with a value of 35Ω , the impedance matching network would be set to 50Ω matching, which is the next closest setting. However, the amplifier will not transmit power into that 35Ω load as well as it will into a slightly off-resonance 40Ω or 50Ω . The balance between electromechanical vibration efficiency and power efficiency is often struck somewhere slightly off the predicted resonance. If these results were collected using the AFT method described early instead of impedance analysis, these effects would have been accounted for by the direct power reflection measurements used in that approach. These results, in conjunction with the finite element and laser vibrometer tests, provide compelling evidence to the benefits of actuator phasing in the ultrasonic de-icing system.

5.7 Composite Sandwich Panel Airfoil De-Icing Experiments

To evaluate the effectiveness of actuator phasing on a realistic and challenging structure, de-icing tests using freezer ice were conducted on an airfoil specimen, shown in Figure 117, which had a construction with two carbon fiber skins sandwiched around a Nomex honeycomb core. Six 2"-dia. actuators were embedded into this structure (three on top and three on bottom), as shown in Figure 117. A layer of freezer ice was created on this specimen by damming up numerous strips of water across the airfoil and allowing them to freeze one-by-one to build up a solid section of freezer ice around the leading edge, as is shown in Figure 118. The ultrasonic de-icing system was first activated with frequency sweeping but with no phasing applied.

Figure 119 shows screenshots from a video made during this de-icing test. These images show cracks and delaminations propagating across the entire ice patch on the leading edge as the ultrasonic de-icing system operates; frequency sweeping and phasing were critical to achieving full de-icing coverage, particularly due to the high attenuation in this structure. Images 1 through 3 in Figure 119 show the ice delamination and cracking on some sections of the airfoil leading edge after several cycles of frequency sweeping. However, the ice fracture would not proceed beyond this point. Actuator phasing using 4 unique phasing combinations (including the

unphased configuration) was then applied; images 4 through 6 show the additional ice fracture and delamination induced by actuator phasing. The last three frames (7 through 9) in Figure 119 show the shattered ice patch being easily removed with a pass from a compressed air nozzle. In real-world conditions, the aerodynamic flow would serve to remove shattered and delaminated ice patches. The power required for these tests was on the order of 600 W due to the highly attenuative and stiff nature of the composite sandwich panel structure. If only the iced section is considered, an area of approximately 400 cm² was protected. This yields a power requirement of approximately 1.5 W/cm², which is much higher than the power required to protect a metallic structure, but still less than half the power required for a typical electro-thermal system [15]. These tests were very successful and confirmed the expectations that actuator phasing would improve the effectiveness of the system when applied to such a structure.

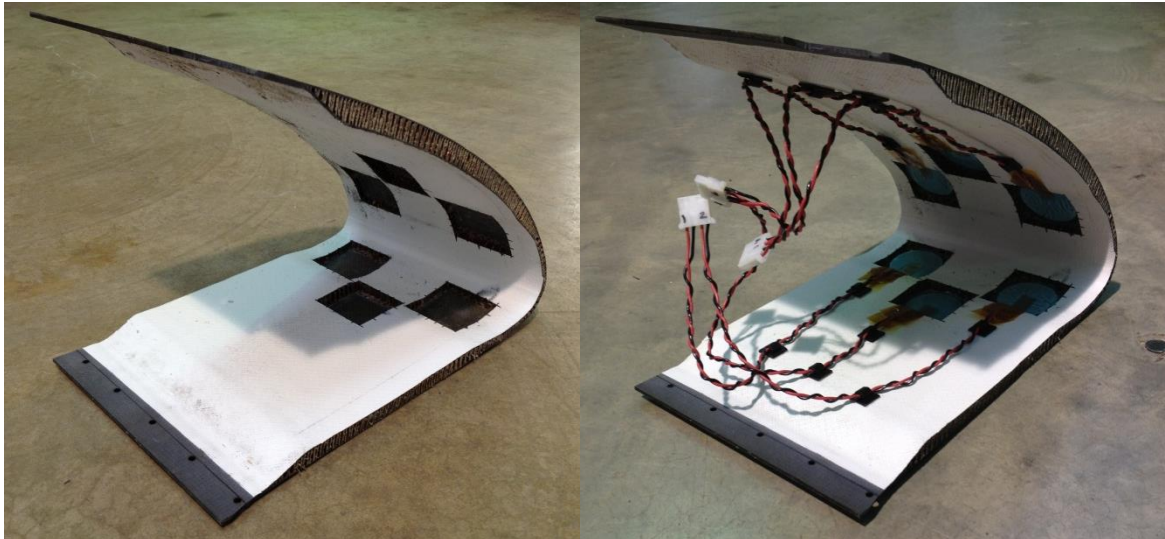


Figure 117 (Left) The composite specimen with sections of honeycomb removed, and the specimen with the actuators bonded into the cavities (right).

It should be noted that the effect of the composite and honeycomb construction of this specimen was an overall increase in the power demands put on the de-icing system. This higher damping of these materials makes de-icing more difficult than on comparable metallic structures. This effect needs to be studied in more detail using FE modeling and more experimentation, but some general conclusions can be drawn. Composite sandwich structures such as this would require

more actuators per linear foot and more system power to provide comparable de-icing performance to a similar structure constructed from metal.



Figure 118 (Left) Strips of ice were created and filled in to cover the leading edge; (middle) top view of leading edge covered with ice; (right) side view of leading edge covered with ice.

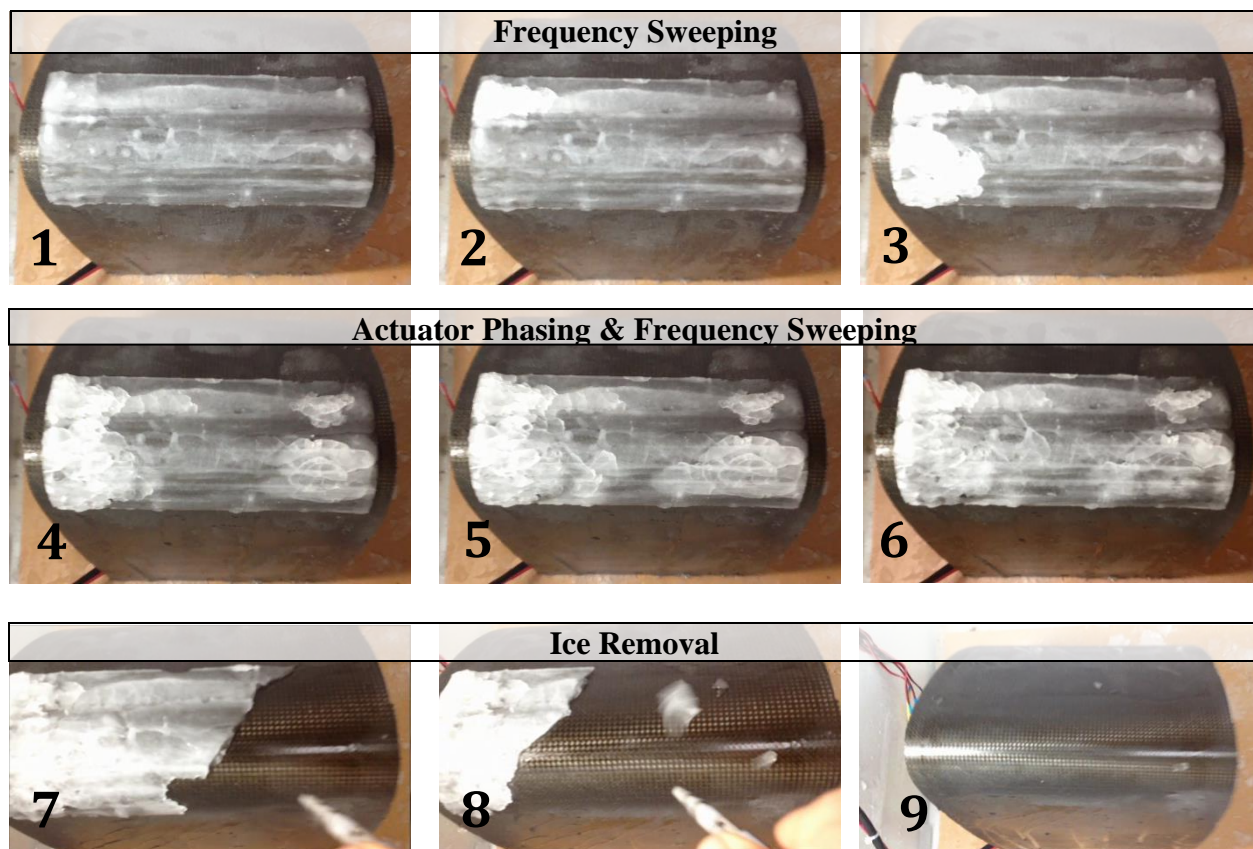


Figure 119 (1-3) Initial cracking and delamination of ice on the airfoil leading edge during de-icing system operation with frequency sweeping and no phasing employed; (4-6) further cracking and delamination of ice on the airfoil leading edge during actuator phasing using 4 unique phasing combinations; (7-9) shattered ice easily being removed from airfoil with a compressed air nozzle.

Chapter 6

ULTRASONIC DE-ICING SYSTEM HARDWARE AND SOFTWARE

6.1 Ultrasonic De-Icing System Functionality

In the previous chapters the concepts upon which the ultrasonic de-icing system operates have been described. However, when it comes to the implementation of these concepts, the only system hardware component that was detailed was the piezoelectric actuator in Chapter 3. In order to fully implement the ultrasonic de-icing system, a number of critical hardware components must be selected or designed and control software must be developed. This chapter will detail the hardware and software components of the ultrasonic de-icing system and will discuss the important parameters that define each component.

The system must be capable of performing the tasks required for successful ultrasonic de-icing, as described in previous chapters:

- generating a high-power sinusoidal signal over a frequency range of 15 – 75 kHz
- delivering the high-power signal to the actuators
- matching the impedance of the power source and the actuators
- monitoring the forward and reflected power between the power source and the actuators
- dynamically applying phase inversion to various actuators
- automatically carrying out the various procedures required for de-icing by accepting various user input parameters, receiving feedback from the system hardware, and controlling the system hardware

6.2 Hardware Components

Arguably the most important part of the de-icing system is its ability to generate and deliver high-power sinusoidal signals to the de-icing actuators. Without a power delivery system, the actuators are useless. The amplification needs of the ultrasonic de-icing system are somewhat different than those of most medical and industrial ultrasonic inspection technologies, which require high-voltage (~300V) spike pulse or tone burst input over short periods of time with a low repetition rate (~10-20 Hz). The de-icing system, on the other hand, requires high-power continuous wave output over longer periods of time (up to several seconds) on much higher duty

cycles (~50% or more). High-power continuous wave amplifiers that meet these specifications are often used in microwave (GHz range) and radio (100s of MHz range) applications, but there are some amplifiers available that operate in the much lower frequency band required for de-icing.

Amplifiers

To meet these needs, the Electronics & Innovation, Ltd. (E&I) 1040L broadband solid state class AB amplifier, shown in Figure 120, was selected. This amplifier operates in the 10 kHz to 5 MHz range and is rated at 400W of RF power. The amplifier is unconditionally stable, which means that it will not oscillate even with significantly mismatched source and/or load [86]. The specifications of the 1040L are provided in Table 15.

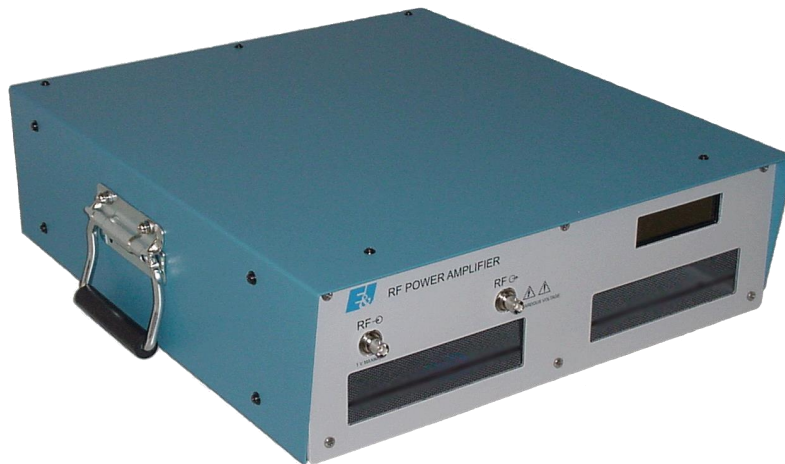


Figure 120 Electronics & Innovation, Ltd. (E&I) 1040L broadband solid state class AB amplifier.

This amplifier is, in fact, significantly larger and heavier than necessary since its capabilities exceed the needs of the de-icing system. By reducing the frequency range of the amplifier, reducing the amount of internal heat sinks (unnecessary due to the duty cycling of the system), and remove the AC-DC converter (unnecessary since it would receive on-board DC power from the aircraft), the amplifier manufacturer, E&I Ltd., has confirmed that the size, weight, and efficiency of the system could be significantly reduced. An amplifier was designed with an output power of 1000W, dimensions of 12" x 12" x 3", and a weight of 10 lbs. One or two of these amplifiers are used in the de-icing system to provide sufficient power and to allow for

phasing, depending on the system setup; the details of these setups will be discussed in a subsequent section. A custom amplifier with both 0° and 180° outputs could also be used to achieve phasing.

Table 15 Specifications of the E&I 1040L amplifier and the new custom amplifier design

SPECIFICATION	E&I 1040L	E&I 1000D01 Custom
CLASS	AB	D
FREQUENCY RANGE	10 kHz to 5 MHz	40 kHz to 100 kHz
GAIN	55 dB nominal	55 dB nominal
QUASI-LINEAR OUTPUT	Nominal 400 W	Nominal 1000W
INPUT IMPEDANCE	50 Ω	50 Ω
OUTPUT IMPEDANCE	50 Ω	50 Ω
PROTECTION	+13dBm (1.0 V _{RMS}) input	+13dBm (1.0 V _{RMS}) input
POWER REQUIREMENTS	100-240 V _{AC} 47-63 Hz	48 V _{DC}
DIMENSIONS	5.25" x 16.5" x 18.1"	3" x 12" x 12"
WEIGHT	52.5 lbs	10 lbs
CONNECTORS	BNC	BNC
OPERATING TEMPERATURE	0 – 40 °C	0 – 45 °C

Impedance Matching Networks

In order to efficiently transmit the power from the amplifier(s) to the actuators, an impedance matching network is required. As was discussed in Chapter 4: Impedance Analysis, the matching network selected for the de-icing system is a single-winding autotransformer. This type of matching network provides loss-less matching for real loads, which is in accordance with the impedance of the actuator system at resonance. One of these networks, shown in Figure 121, is utilized in the de-icing system. A metal housing for this matching network (not shown) serves as a Faraday cage between the network and the rest of the system to avoid electromagnetic interference from the unshielded wires.

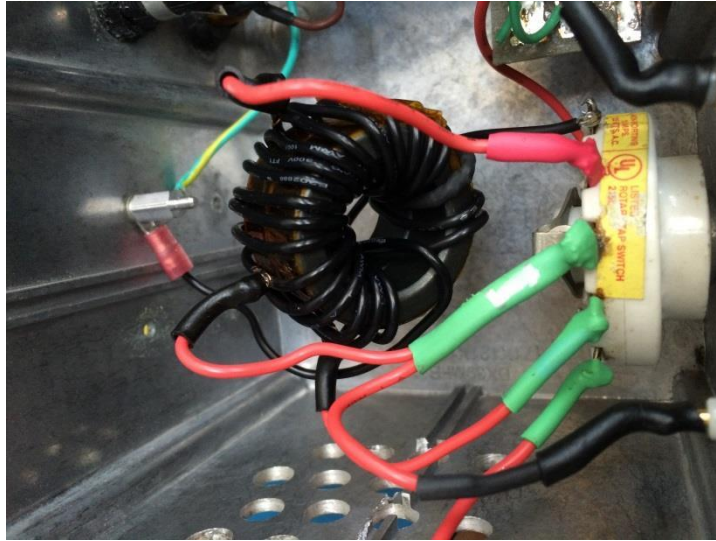


Figure 121 A single-winding autotransformer impedance matching network utilized in the de-icing system.

Cabling

Delivery of the high-power signal between the amplifier and the impedance matching network and the impedance matching network and the actuators requires cabling. Selecting the wrong cabling can lead to cable failure, poor power transmission efficiency, RF interference, and RF emission problems. Due to the high-power transmitted through the cabling and the electronically-sensitive aircraft environment in which the system is intended to operate, shielded cabling is a necessity. Coaxial cabling is sufficient if a cable with the appropriate dimensions is selected. The power output capabilities of the amplifier and the impedance range of the actuator system means that voltages up to 300 V and current up to 9 A could be experienced. RG-8X cabling was selected for this application because it has 50Ω impedance and is rated to 300 V_{RMS} and power levels of over 1000 W below 1 MHz. The core of RG-8X is 16 AWG solid copper (0.058" diameter). This cabling is more than sufficient for the needs of the system and if weight and size issues become a concern, it could be replaced with another type of cabling with more limitations. Since coaxial cabling is difficult to attach to the actuator tabs, 18 AWG twisted shielded pair cabling was used for this purpose. It must be pointed out that RF interference can cause unstable oscillations in the amplifier system and that inadequate shielding of any of the power transmission components can lead to the emission and reception of such noise.

Phasing Relays and Splitter

Several hardware components are required to implement actuator phasing in the de-icing system. As was stated in Section 6.2, either one or two amplifiers can be utilized for actuator phasing, depending on the system setup. For instance, phasing can be achieved with two actuators by providing two input voltages (one in-phase and one out-of-phase) to two separate amplifiers so that one amplifier outputs a sinusoidal signal at frequency f and phase $\varphi = 0^\circ$ and the second amplifier outputs a sinusoidal signal at frequency f and phase $\varphi = 180^\circ$. This may at first seem like the most straight-forward approach to achieving actuator phasing, however it seriously complicates the matters of impedance matching and frequency selection. The forward and reverse power from both amplifiers must be read and added together, and separate impedance matching networks are required for each amplifier. Additionally, since each actuator is only connected to half of the total number of actuators, the impedance measured across each amplifier output is higher than if all of the actuators were connected to a single output port. Finally, two amplifiers will lead to unnecessary equipment components such as housings, displays, AC-DC converters, and other miscellaneous duplicated components that do not contribute to doubling the output power of the amplifiers. Therefore it would be preferable to utilize a single amplifier with sufficient output power instead of two amplifiers half of the sufficient output power. To overcome the issues associated with using two amplifiers to achieve actuator phasing, a method was developed in which a single amplifier can be utilized by employing a phase splitter device. This phase splitter splits an input signal into two components with equal amplitude but opposite phase, as is illustrated in Figure 122.

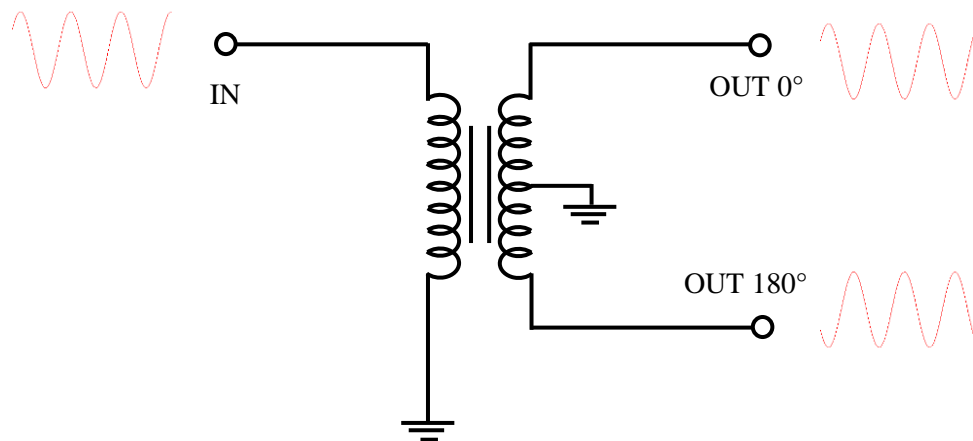


Figure 122 Simplified illustration of a phase splitter circuit using a transformer.

In a system setup that utilizes a phase splitter, such as the one shown in Figure 123, the single amplifier would receive an input voltage at frequency f and output an amplified signal at the same frequency. This output would be transmitted into an impedance matching network and then into the phase splitter device, which would output two signals of equal (but reduced) amplitude at frequency f , one of which has 0° phase and the other has opposite phase relative to this original signal. These two anti-phase signals can be transmitted into the phasing PCB that controls which actuators receive which signal through a series of relays; the PCB used for the de-icing system phasing is detailed in a subsequent section.

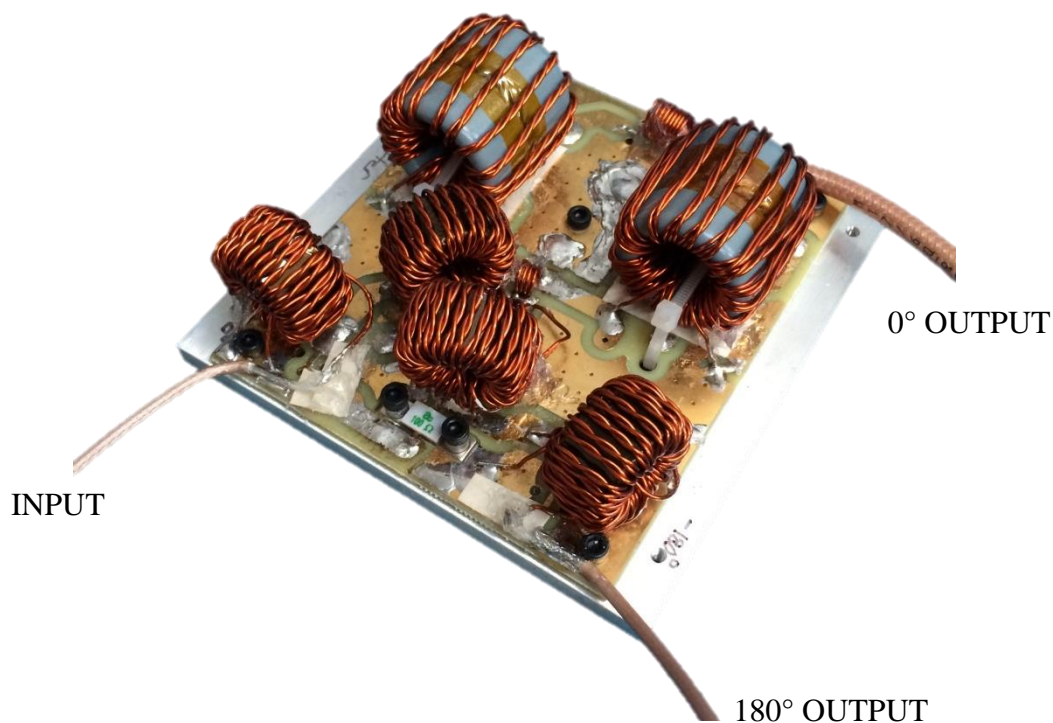


Figure 123 Phase splitter circuit employed in the ultrasonic de-icing system.

In order to implement a variety of phasing combinations, the actuators must be able to be dynamically switched between the two amplifiers. This switching requires a series of relays. The relays selected for the de-icing system are miniature TE Connectivity PT270012 double-pole double-throw relays that are rated for 400 V_{RMS} and 12 A. The relays are substantially smaller than standard industrial relays but feature similar specifications that meet the needs of the de-

icing system; these relays are compared in Figure 124. The dimensions of the miniature relay are 29mm x 28mm x 22.5mm.

Analog and Digital I/O

Operating the phasing relays requires a 12 V_{DC} power source, a transistor switching circuit, and a low-voltage digital I/O device. The circuit diagram for these relay switching circuits and associated relay hardware is provided in Figure 125. The voltage source utilized for this purpose is a National Instruments USB-6361 analog and digital I/O. This device has 24 digital I/O lines that are used to supply the digital signals to the transistor switching circuits after boosting the voltage with a pull-up resistor and the 5V line of the device. The two analog output channels of the device are used to generate the low-voltage sine wave signals supplied to the input of the amplifiers, and the analog input lines are used to read the forward and reflected power signals from the amplifier bi-directional couplers. This device, shown in Figure 126, has dimensions of 26.4 cm x 17.3 cm x 3.6 cm.



Figure 124 Comparison of the miniature relay and socket (left) and standard relay and socket (right).

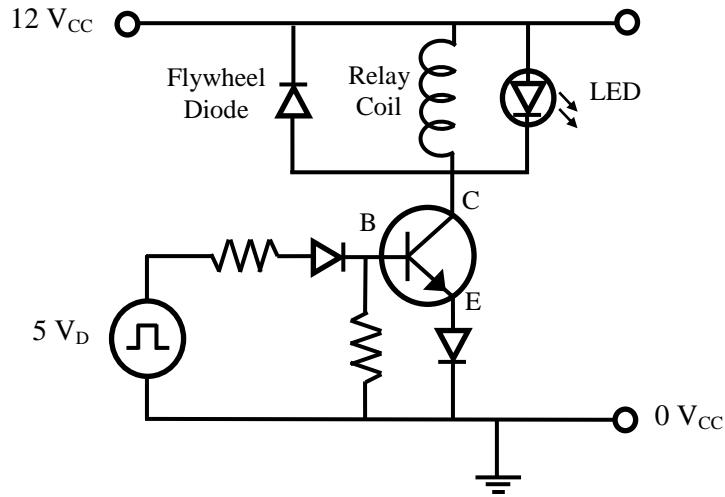


Figure 125 Transistor switching circuit used to control the relays.



Figure 126 National Instruments USB-6361 analog and digital I/O device [89].

Relay Control PCB

In an effort to minimize the size, weight, and complexity of the de-icing system hardware required for phasing, a four-layer printed circuit board (PCB), shown in Figure 127, was designed to contain the relays, transistor switching circuits, digital I/O connections, and output to the actuators. A design image of the circuit board is provided in Figure 129, in which the bottom layer signal traces are solid blue, the top layer signal traces are solid red, the second layer ground plane is hashed blue, the third layer DC power plane is hashed red, and the vias are green. The

gray markings are for silk screening or reference purposes only. The individual layers of the PCB are shown in Figure 130 through Figure 132.

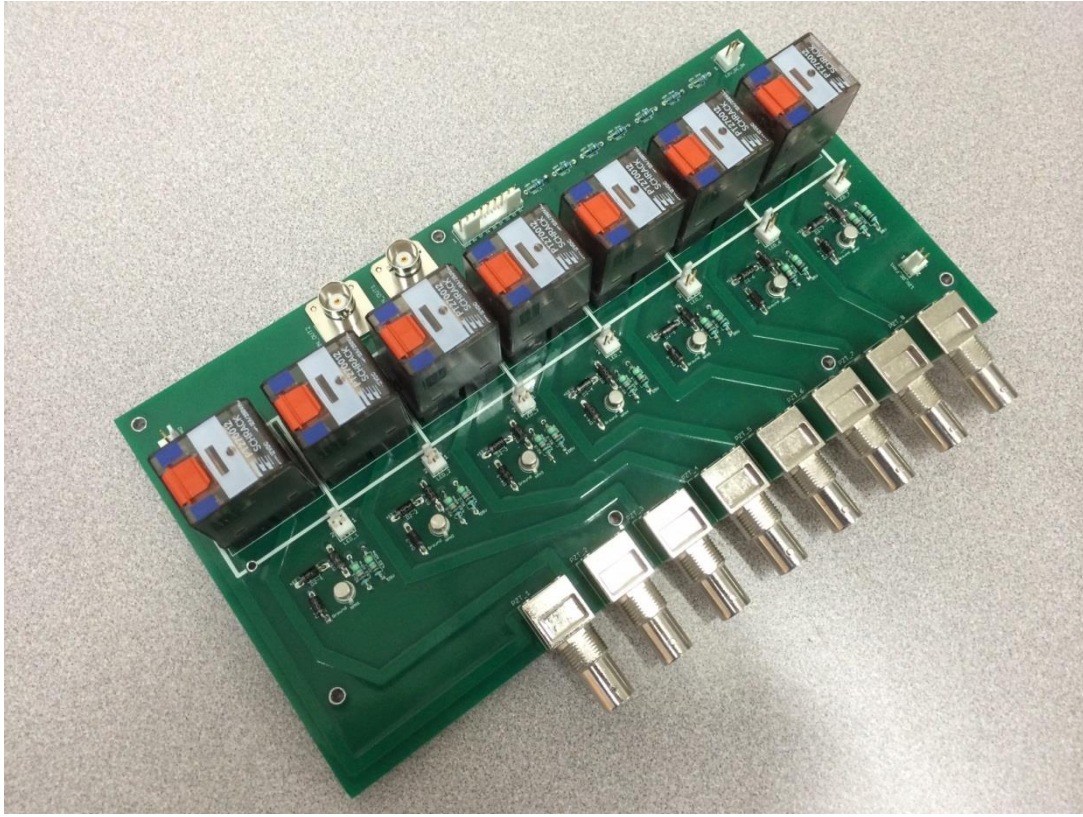


Figure 127 Photograph of the four-layer PCB used to control the relays for actuator phasing.

Properly designing the PCB for high-power signals requires careful consideration of a number of factors including current limitations, short-circuit protection, proper grounding, transmission line impedances, and trace crosstalk. Each of these factors must be balanced while minimizing the size and cost of the PCB and assuring that it will meet the requirements of the board hardware and housing. In order to address these requirements, a four-layer PCB was designed, because it allows for improved trace decoupling and signal routing.

The impedance of a PCB surface microstrip (Figure 128) can be calculated using

$$Z_0 = \frac{87}{\sqrt{\epsilon_r + 1.41}} \ln \left(\frac{5.98h}{0.8w + t} \right), \quad (5.41)$$

in which ϵ_r is the relative dielectric constant of the board material, h is the thickness of the board between the strip and the plane, w is the width of the trace, and t is the thickness of the trace. The high-power signal line impedances must be matched to 50Ω along the entire length of the trace, if possible, to optimally match these transmission lines to the rest of the system. The impedance can be adjusted by altering the three geometric parameters shown in Figure 128.

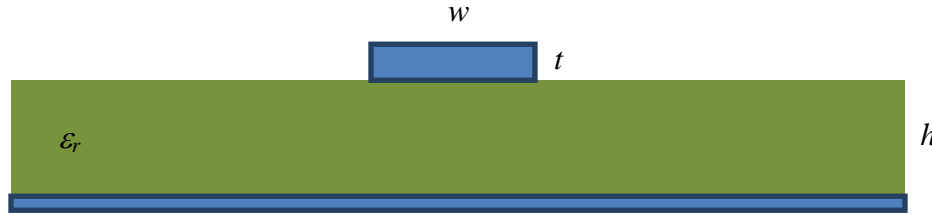


Figure 128 A microstrip PCB trace above a plane.

However, the geometry of the trace itself, specifically the width and thickness, also must be tuned to reduce resistance and temperature rise due to the large currents that can be generated by the de-icing system amplifiers. The equation describing this relationship for external microstrip traces like the one shown in Figure 128 is [90, 91]

$$I = 0.048 \cdot \Delta T^{0.44} \cdot A^{0.725}, \quad (11.42)$$

in which I is the transmitted current, A is the cross-sectional area of the trace, and ΔT is the temperature rise in $^{\circ}\text{C}$.

Cross-coupling of traces must also be taken into consideration, especially with the high voltages that will be applied across the two signal traces. Cross-coupling of the electromagnetic fields between traces can lead to unwanted voltages and, due to the out-of-phase nature of the two amplified signals in the de-icing system, signal power loss. Cross-coupling is minimized by utilizing the two interior layers for the ground plane and DC power plane, respectively. These mostly-continuous planes shield the signal traces from one another. Cross-coupling is further reduced by separating any parallel traces, even on separate planes, as much as possible and

reducing the length of any parallel segments. The cross-coupling CT_{dB} between two short (relative to the wavelength) parallel traces on an outer layer can be calculated by

$$CT_{dB} = 20 \log \left[\frac{1}{1 + \left(\frac{s}{h} \right)^2} \frac{T_{RT}}{T_R} \right], \quad (11.43)$$

$$T_{RT} = 2.034 \cdot L \cdot \sqrt{0.475\epsilon_r + 0.67}, \quad (11.44)$$

in which s is minimum trace separation, h is the height of the traces above the nearest plane, T_R is the fastest rise time of the signal, and L is the parallel trace length.

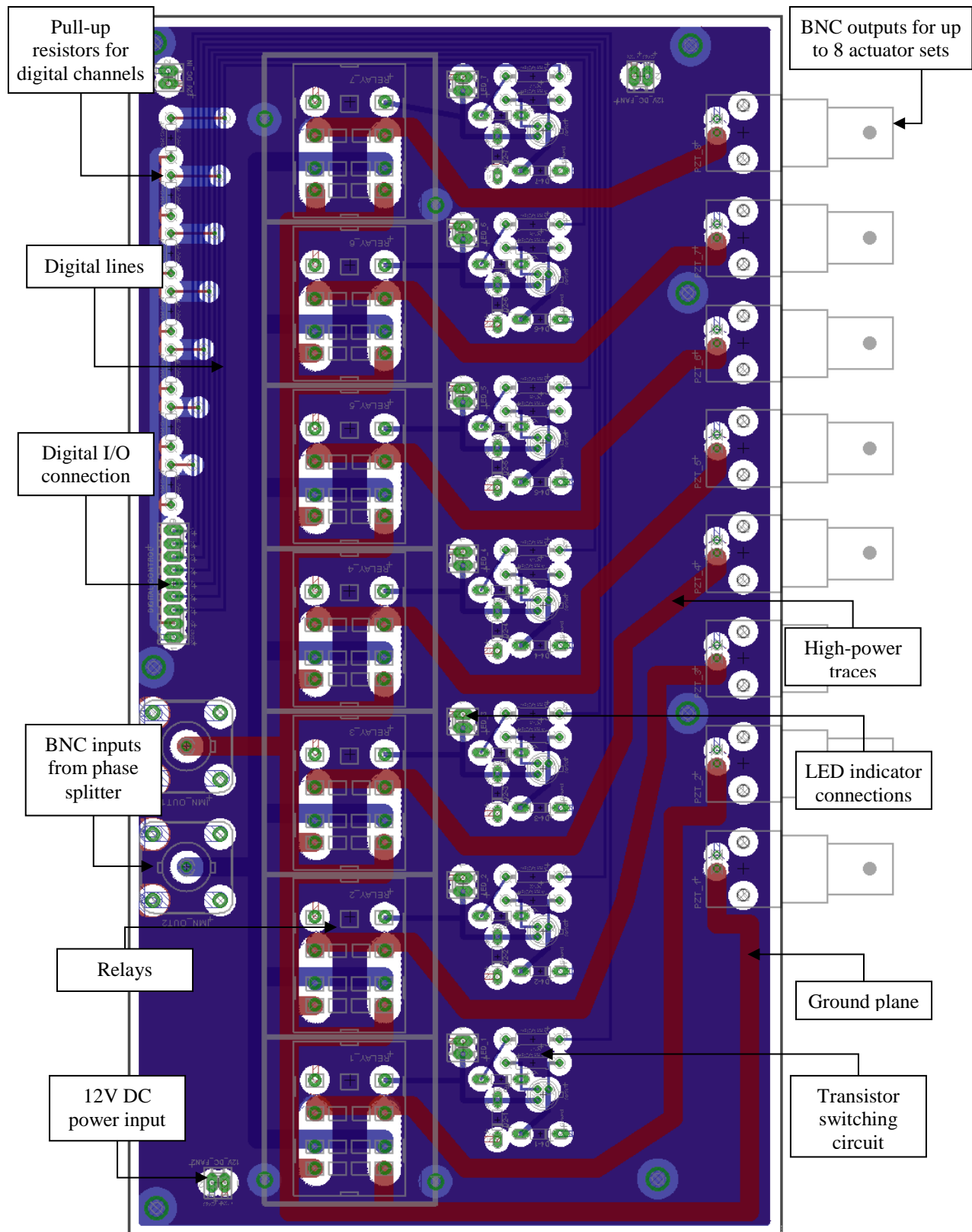


Figure 129 Design of the de-icing PCB for phasing.

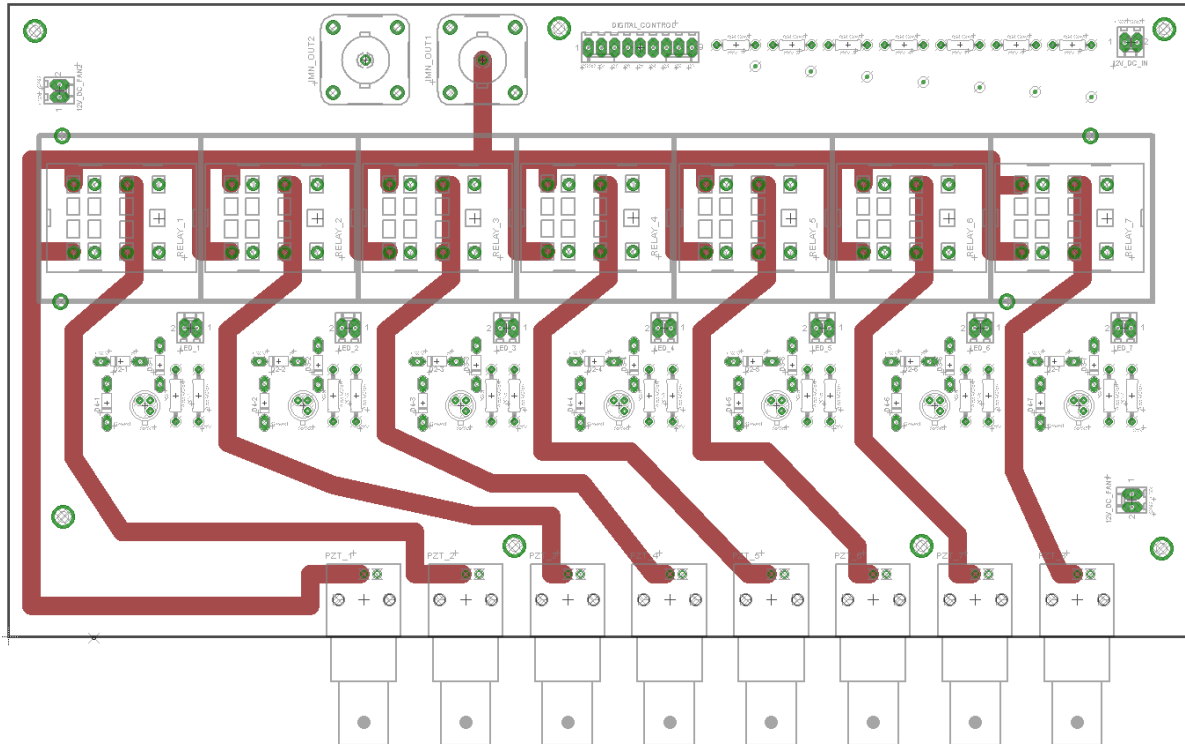


Figure 130 PCB signal layer 1.

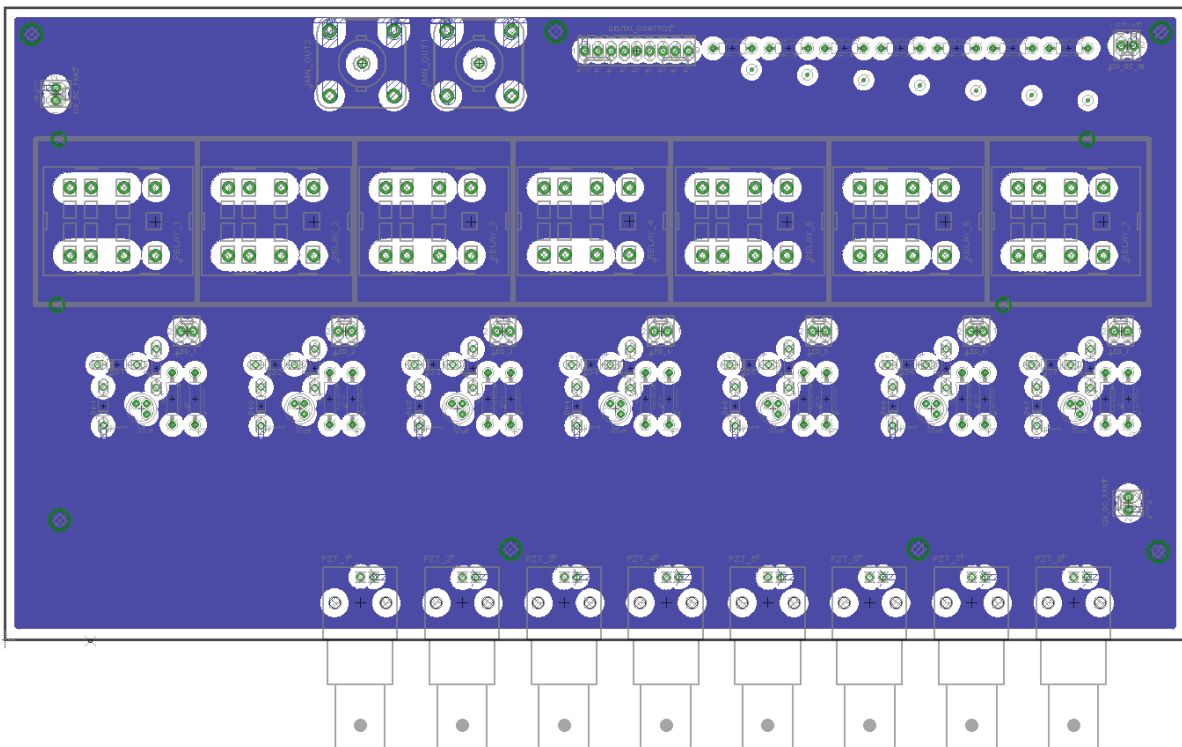


Figure 131 PCB ground plane.

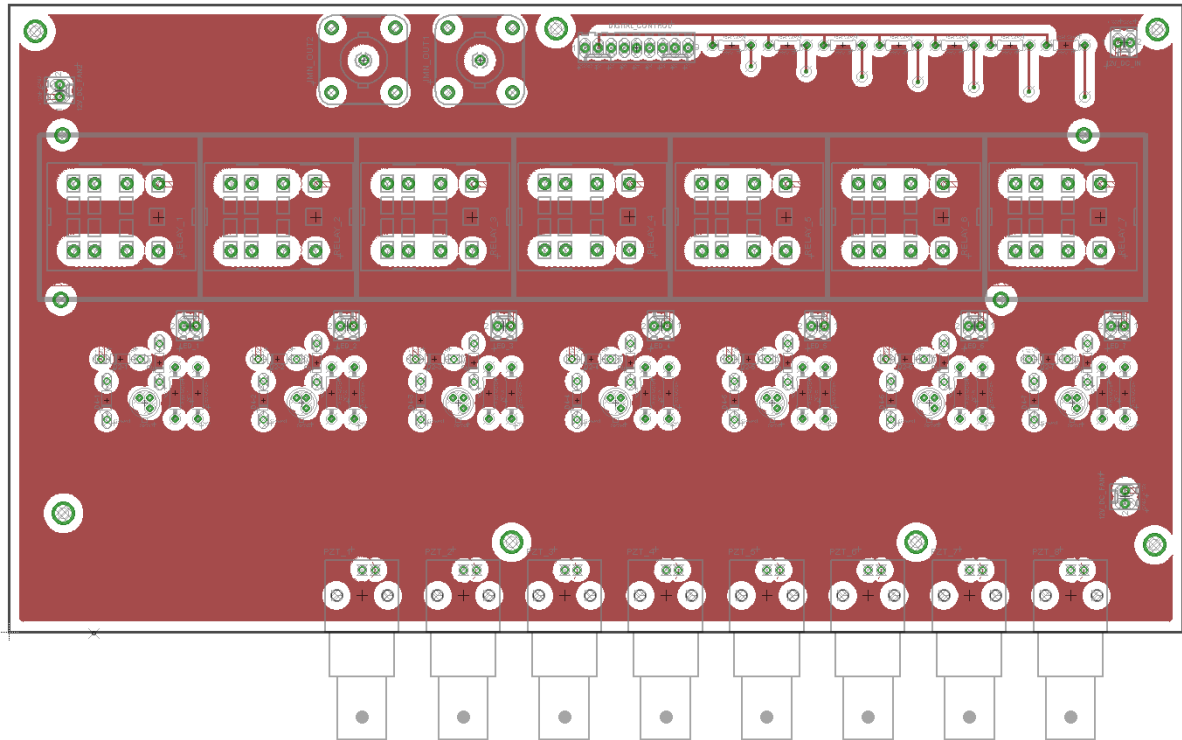


Figure 132 PCB DC power plane.

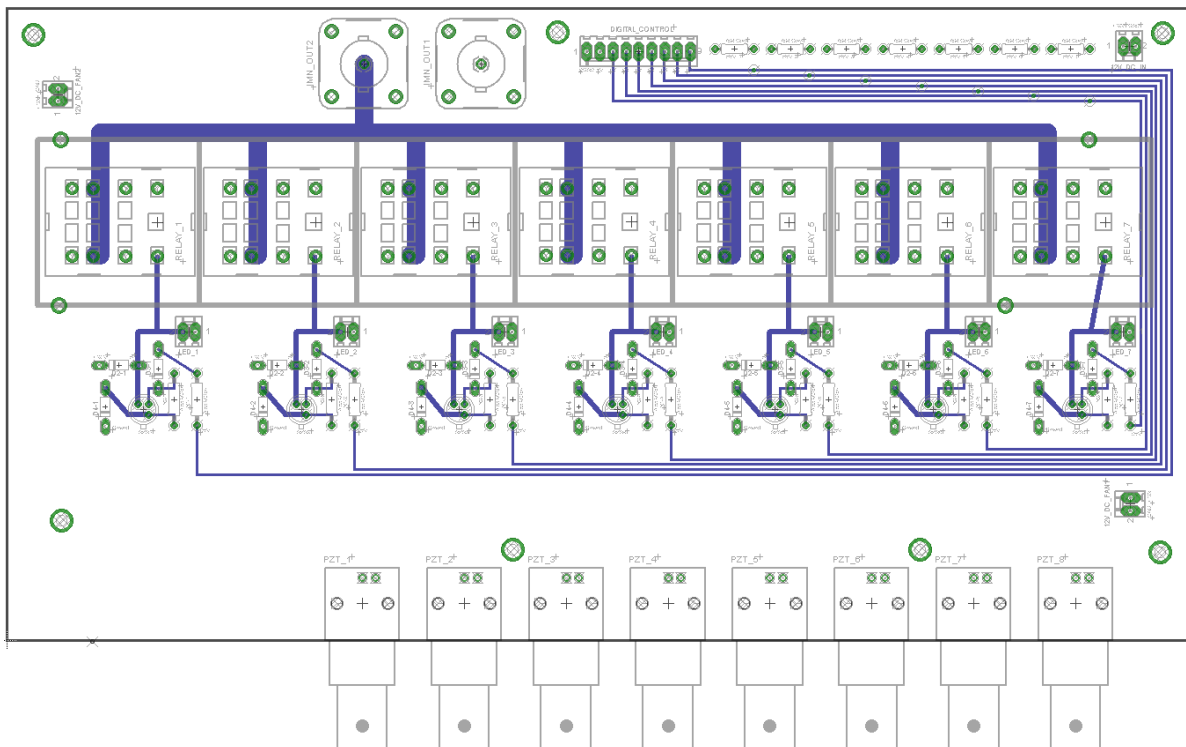


Figure 133 PCB signal layer 2.

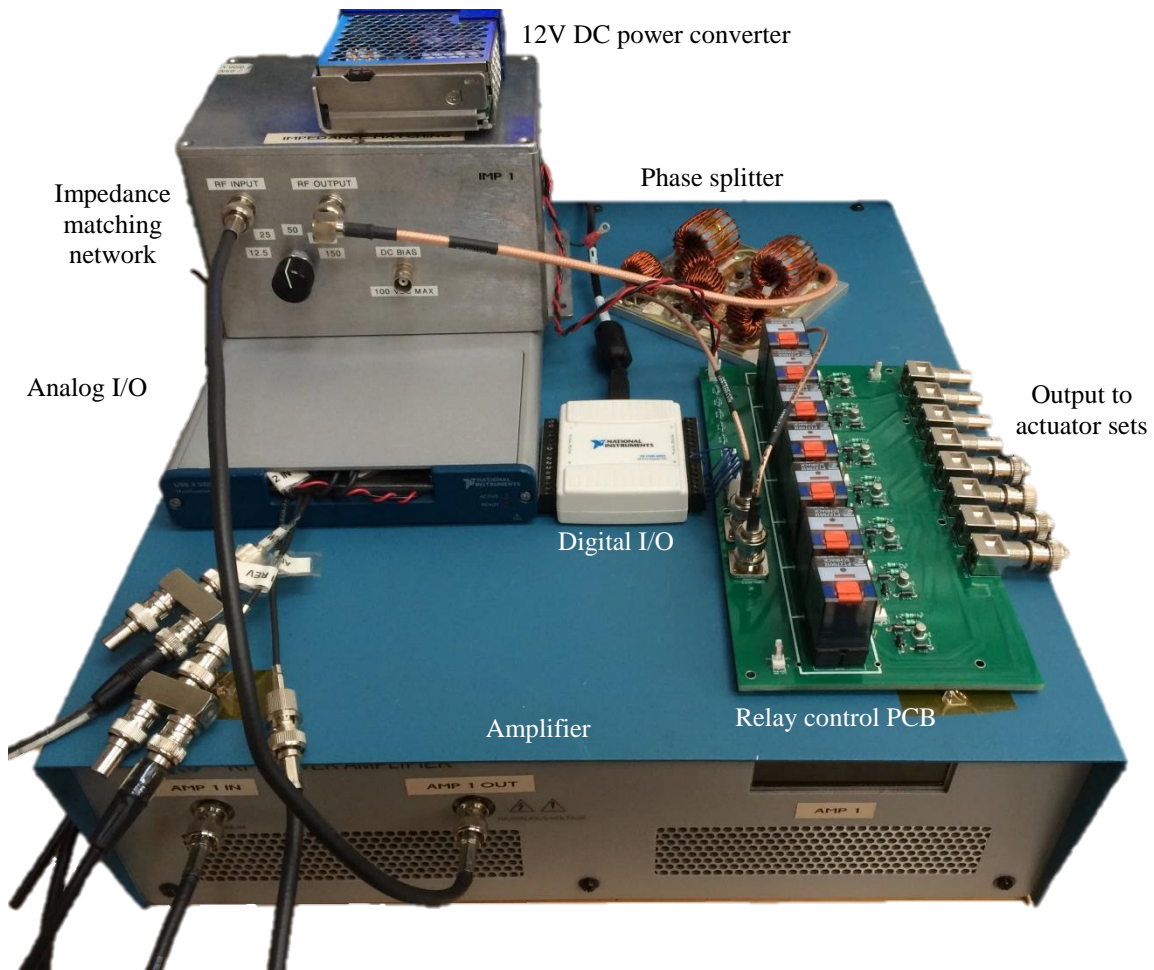


Figure 134 The various components of the ultrasonic de-icing system with actuator phasing and power monitoring. Note that the overall size of the system could be reduced by combining the components into a single housing.

6.3 Control Software

LabView-based control software was designed for use with the ultrasonic de-icing system. This software controls the operation of the phasing relays, the amplifier input signal (including frequency, amplitude, and duty cycling), and the monitoring of the forward and reverse power data from the amplifier. Basic input parameters such as the bandwidth and increment for frequency sweeping, the various pre-determined phasing combinations, the output amplitude, the duty cycling details, the number of de-icing cycles to execute, etc. can be entered by the user prior to engaging the system. Once the system is engaged, it can operate without requiring any additional operations by the user, as long as the general operation parameters listed above remain unchanged.

Chapter 7

CONCLUDING REMARKS

7.1 Summary of Research

Aircraft icing is a critical concern for commercial and military rotorcraft and fixed-wing aircraft. The accretion of ice on airfoil and control surfaces can lead to dramatic decreases in lift and increases in drag that have led to thousands of deaths and hundreds of accidents in the United States in the past three decades alone. Current technologies to address airfoil icing include anti-icing fluids, hot bleed air systems, pneumatic boots, and electro-thermal blankets; however, each of these technologies has substantial drawbacks due to weight, power consumption, and/or incompatibility with particular structures. In the early 2000s, research into a non-thermal low-power ultrasonic vibration de-icing system began at Penn State University, primarily under the efforts of Palacios, Smith, and Rose [1]. This technique showed promise in its ability to achieve de-icing on metallic plates and airfoils using piezoelectric actuators.

In this research, an actuator phasing method for ultrasonic de-icing of aircraft structures was developed and tested using a series of finite element models, 3D scanning laser Doppler vibrometer measurements, and experimental de-icing tests on metallic and composite structures including plates and airfoils. It was demonstrated that this novel method can greatly improve the efficiency and effectiveness of the ultrasonic de-icing system by effectively redistributing the shear stress fields at the ice-structure interface. This is achieved by inverting the phase of the amplified excitation signal applied to certain actuators in the piezoelectric de-icing actuator set during system operation. A series of finite element models on a plate geometry were employed in conjunction with a genetic optimization algorithm to demonstrate that this phase inversion approach can yield improvements comparable to arbitrarily-selected phasing with phasing increments smaller than 180° . Several methods by which phase inversion can be practically implemented were explored, including a two-amplifier approach as well as a single-amplifier approach with a phase splitter. Finite element modeling of an airfoil geometry demonstrated that actuator phasing can improve the 90% coverage threshold shear stress levels by 90-150%. 3D scanning laser Doppler vibrometer experiments showed that de-icing coverage on a composite sandwich panel structure using actuator phasing were improved by as much as 30% over

frequency sweeping; note that frequency sweeping was not used in conjunction with actuator phasing in this experiment due to limitations on the access time for the equipment and it is expected that including frequency sweeping while phasing would further improve the performance of the system. De-icing tests were also performed on an ice grid of 100 ice dots to compare the effectiveness of frequency sweeping and phasing at various system power levels. These tests showed that actuator phasing dramatically improved the effectiveness of the system and allowed for comparable or better de-icing coverage at substantially lower power levels. For instance, on average, the system with actuator phasing was able to de-ice 90% of the ice grid at a power level at which the system with frequency sweeping alone was unable to de-ice even 50% of the grid. On average, phasing improved ice removal by 189% compared to frequency sweeping alone (a ratio of 1:2.89). Finally, a freezer de-icing experiment on a composite sandwich-construction airfoil was carried out in which it was demonstrated that actuator phasing allowed the ultrasonic de-icing system to fully fracture and delaminate the accreted ice layer while frequency sweeping without phasing only achieved insufficient partial fracture and delamination.

An independent actuator analysis method of electromechanical impedance predictions for a multi-actuator system with phasing was developed in which the complex direct- and cross-impedances of individual actuators are recombined based on a model of a multi-port electrical network. This phased actuator impedance formulation was verified using a series of finite element models. This phased impedance calculation method allowed for the efficient prediction of phased impedances and phased stress fields on a complex airfoil (based on a subset of unphased finite element models), which would have otherwise required an impractical amount of computational time to run individually. Using this method, a series of 432 models was completed, which required a total of 10,800 hours of computational time. However, the results of implementing any arbitrary phasing combination at any one of the frequencies considered was possible based on these unphased results using the independent actuator analysis method.

Methods for identifying the optimum driving frequency of the system while phasing is applied were also explored. Finite element models of an airfoil were used to show that dynamic frequency selection, in which the system is operated at the phased impedance minimum for each new actuator phasing configuration, is superior to the static frequency selection approach, in

which the system is simply operated at the impedance minimum measured without phasing. In the three actuator configurations studied, dynamic frequency selection yielded improvements in the average shear stress field of 57% on average and as high as 115% in one case. The dynamic frequency selection approach, however, requires that the phased impedance curve be known, which cannot be easily measured directly during system operation. To overcome this issue and to improve the method of optimal frequency selection overall, an automatic frequency tuning approach was adopted.

A method of automatic frequency tuning, in which the forward and reflected power between the amplifier(s) and actuators is monitored to determine the frequency at which an electrical system is operating most efficiently, was applied to the ultrasonic de-icing system. The E&I 1040L amplifier was retrofitted with two data ports that output signals from a bi-directional coupler; these signals could then be analyzed and forward, reverse, and load power curves could be measured as a function of frequency. One of the benefits of this approach over the impedance analyzer approach used in prior ultrasonic de-icing research is that it accounts for all variables in the system including the impedance matching network to deliver the information that is explicitly of interest, that is, the load power successfully delivered to the actuators. This approach is also applicable regardless of the phasing applied to the actuators and thus solves the issue of dynamic frequency selection during actuator phasing. Additional benefits of this approach to frequency selection are that it eliminates the need for an impedance analyzer and the associated switching hardware and it can be applied during actuation.

In addition to developing and verifying the actuator phasing approach both numerically and experimentally, a series of hardware improvements were made to practically implement the phasing method and improve the overall operation of the de-icing system while decreasing its size and weight. A small 4.9" x 9.1" custom four-layer printed circuit board with miniature relays was designed and successfully implemented to control the actuator phasing configurations of up to 8 independent actuator sets without cross-talk, impedance mismatch, overheating, or other issues. A phase splitter device was implemented in the system to reduce the number of amplifiers and impedance matching networks required by the system and to make impedance matching and dynamic frequency selection simpler.

In summary, the concept of actuator phasing for improving the efficiency and effectiveness of the ultrasonic vibration de-icing system for aircraft structures was taken from a potential theoretical concept, investigated in various forms using finite element modeling, implemented with new developments in system hardware and de-icing system procedure, and numerically and experimentally verified on a number of structures using various methods to demonstrate that actuator phasing is, in fact, feasible and greatly beneficial in an ultrasonic de-icing system.

The benefits of actuator phasing as applied to ultrasonic de-icing have been shown to include the following:

- Improved ability to achieve high shear stress coverage over large areas of a structure
- The opportunity to exploit resonances that are not available with the unphased configuration
- The ability to vary the stress field while staying near the strongest resonance of the system
- The ability to de-ice regions of a structure that would otherwise require increased power output using the unphased configuration

It has also been shown that these improvements can be efficiently implemented using the hardware and procedural techniques developed during this research.

7.2 Research Contributions

The primary contributions of this research are:

1. A novel actuator phasing method for improving the efficiency and effectiveness of the ultrasonic vibration de-icing system was introduced, developed, and verified using a variety of numerical and experimental techniques and analyses.
2. Finite element models of a metallic airfoil demonstrated that actuator phasing can improve the 90% coverage threshold shear stresses by 90-150% over frequency sweeping alone.

3. 3D scanning laser Doppler vibrometer experiments demonstrated that, on a composite sandwich panel specimen, actuator phasing (even without frequency sweeping) offered an increase in average in-plane surface vibration coverage thresholds by more than 30%.
4. De-icing experiments on a grid of freezer ice demonstrated that actuator phasing can improve the de-icing coverage of an ultrasonic de-icing system by a factor of 2.89 on average and that 90% de-icing coverage was achieved at a power level of 174 W, for which frequency sweeping alone yielded less than 50% de-icing coverage.
5. A freezer de-icing experiment was carried out on a carbon fiber honeycomb sandwich airfoil, in which it was demonstrated that actuator phasing allowed the ultrasonic de-icing system to fully fracture and delaminate the accreted ice layer while frequency sweeping without phasing only achieved insufficient partial fracture and delamination.
6. Through a series of finite element models of a metallic plate and a genetic algorithm optimization analysis, it was shown that phase inversion, in which only in-phase and anti-phase signals are utilized for actuator phasing, can yield improvements comparable to arbitrarily-selected phasing with phasing increments smaller than 180° . Phase inversion is simpler to implement than arbitrary phasing, so this is an important factor to understand.
7. Finite element models of an airfoil were used to show that dynamic frequency selection, in which the system is operated at the phased impedance minimum for each new actuator phasing configuration, is superior to the static frequency selection approach, in which the system is simply operated at the impedance minimum measured for the unphased system. It was shown that dynamic frequency selection yielded improvements in average interface shear stress of as much as 115%, depending on the actuator configuration.
8. An independent actuator analysis method of electromechanical impedance predictions for a multi-actuator system with phasing was developed in which the complex direct- and cross-impedances of individual actuators are recombined based on a model of a multi-port electrical network. The phased actuator impedance calculations were verified using a series of finite element models. This method allows for the efficient analysis of arbitrary actuator phasing configurations by predicting the phased impedances and phased stress

fields of a finite element model based on a subset of unphased finite element model results.

9. A method of automatic frequency tuning, in which the forward and reflected power between the amplifier(s) and actuators is monitored to determine the frequency at which an electrical system is operating most efficiently, was applied to the ultrasonic de-icing system by monitoring the output signals from a bi-directional coupler in the amplifier. This approach to frequency selection is more explicit and direct than the method of impedance measurements employed in prior research; it also eliminates the need for an impedance analyzer and associated switching hardware in the system while simultaneously solving the difficulty of dynamically selecting the frequency during actuator phasing.
10. An improved method of actuator fabrication and integration was developed in which copper tabs and low-viscosity non-conductive epoxy are used to electrode the actuators, several film epoxy layers are used to insulate and bond the actuators, and a special fabrication procedure is used to integrate the ultrasonic de-icing actuators into composite honeycomb sandwich structures. This method provided more reliability and a simpler, neater fabrication method than previous approaches.
11. Several system hardware components were developed and integrated into the system to allow for practical implementation of actuator phasing and automatic frequency tuning and to reduce the overall size and weight of the ultrasonic de-icing system. These components included a custom-designed 4-layer printed circuit board with miniature relays and a phase splitter device for phasing purposes.

7.3 Recommendations for Further Research

Several recommendations for continued research in this area are:

- An investigation of the optimum actuator diameter (and thus frequency range) for various structures could be carried out. Increasing actuator size increases the weight and the structural stiffness added by these actuators, but also reduces the radial resonance frequency, which appears to lead to more efficient de-icing in general.

- Discussion with the amplifier manufacturer E&I, Ltd. have yielded an improved custom amplifier design that would greatly reduce the size and weight of the current amplifier setup while increasing the power output and efficiency. This customized amplifier design should be executed and tested with the de-icing system. Certain features of the de-icing system could also be built into this amplifier to reduce the overall bulk of the system.
- Form-fitting mediator wedges made from metal were designed to mount the flat actuators to a complex structure such as an airfoil in order to improve the coupling and reduce the damping in the system compared to the epoxy fill method currently employed. This method was used with success during this research, but a strict comparison of these two techniques could be performed and the wedge material could be optimized to yield maximum energy transfer from the actuator to the structure.
- Various icephobic coatings could be tested in conjunction with the ultrasonic de-icing system to investigate the potential benefits of using a joint coating-ultrasound system. The reduced ice adhesion strength afforded by the coatings could reduce the required input power of the ultrasound system, but the effects of coatings on shear stress transmission efficiency at ultrasonic frequencies could vary greatly between coatings.

REFERENCES

1. Leary, W.M., “We Freeze to Please: A History of NASA’s Icing Research Tunnel and the Quest for Flight Safety,” NASA History Series, 2002.
2. Gent, R.W., Dart, N.P., and Cansdale, J.T., “Aircraft Icing,” *Philosophical Transactions of the Royal Society of London Series A*, Vol. 358, pp. 2873 – 2911, 2000.
3. Petty, K.R. and Floyd, C.D.F., “A Statistical Review of Aviation Airframe Icing Accidents in the U.S.,” *11th Conference on Aviation, Range, and Aerospace Meteorology*, 2004, pp. 623 – 628.
4. Cole, J. and Sand, W., “Statistical Study of Aircraft Icing Accidents,” *29th Aerospace Sciences Meeting and Exhibit*, Reno, NV, AIAA, AIAA Paper 91-0558, 1991.
5. Goraj, Z., “An Overview of the Deicing and Anti-Icing Technologies with Prospects for the Future,” *24th International Congress of the Aeronautical Sciences*, 2004.
6. Simpson, M.P. and Render, P.M., “Investigation into the Effectiveness of Certification and Operational Icing Procedures for Helicopters,” *36th Aerospace Sciences Meeting and Exhibit*, AIAA Paper 1998-750, Reno, NV, 1998.
7. Thomas, S., Cassoni, R., and McArthur, C., “Aircraft Anti-Icing and De-Icing Techniques and Modeling,” *Journal of Aircraft*, Vol. 33, NO. 5, pp. 841 – 854, Sep. 1996.
8. Palacios, J., Szefti, J., Wolfe, D., and Bailey, M., “Ice Testing of a Centrifugally Powered Pneumatic Deicing System for Helicopter Rotor Blades,” *70th American Helicopter Society Annual Forum and Technology Display*, Montreal, Quebec, 2014.
9. Bradley, J.J., Sivier, K.R., Anderson, A.E., and Schiller, J.L., “The Impact of Smart Icing Systems on Commuter Aircraft,” *38th AIAA Aerospace Sciences Meeting and Exhibit*, AIAA Paper 2000-0362, Jan. 2000.
10. Addy Jr., H.E., Potapczuk, M.G., and Sheldon, D.W., “Modern Airfoil Ice Accretions,” *Cross Sections*, NASA, Jan. 1997.
11. Gray, V.H., “Prediction of Aerodynamic Penalties Caused by Ice Formations on Various Airfoils,” NASA Technical Note, NASA TN D-2166, Feb. 1964.

12. Brouwers, E., Palacios, J., Smith, E.C., “The Experimental Investigation of a Rotor Hover Icing Model with Shedding,” *Journal of America Helicopter Society*, 2010.
13. In-flight icing on turboprop airplane wing, photograph, Our Airspace, accessed 17 October 2014, <<http://www.ourairspace.org/Risk-Icing.html>>.
14. Grounded Sea King helicopter, digital image, BBC News – In Pictures, accessed 17 June 2014, <http://news.bbc.co.uk/2/hi/in_pictures/4768180.stm>.
15. Palacios, J., “Design, Fabrication, and Testing of an Ultrasonic De-Icing System for Helicopter Rotor Blades”, *PhD Thesis*, Penn State University, May 2008.
16. Cornell, J.S., Pillard, D.A., and Hernandez, M.T., “Comparative Measures of the Toxicity of Component Chemicals in Aircraft Deicing Fluid,” *Environmental Toxicology and Chemistry*, Vol. 19, Issue 6, pp. 1465 – 1472, June 2000.
17. Coffman, H.J., “Helicopter Rotor Icing Protection Methods,” *Journal of the American Helicopter Society*, Vol. 32, No. 2, pp. 34 – 39, April 1987.
18. Flight Learnings, “Anti-Ice and Deice Systems (Part One),” accessed 7 July 2014, <<http://www.flightlearnings.com/2010/04/15/anti-ice-and-deice-systems-part-one>>
19. Zumwalt, G.W., “Electro-Impulse De-Icing Research: Fatigue and Electromagnetic Interference Tests,” FAA Technical Document, DOT/FAA/CT-88/27, Mar. 1989.
20. Feher, L.E. and Thumm, M., “High Frequency Microwave Anti-/De-icing Systems for Carbon Reinforced Airfoil Structures,” *Proceedings of SPIE*, Vol. 4371, pp. 99 – 110, 2001.
21. Feher, L.E. and Thumm, M., “Design of Avionic Microwave De-/Anti-Icing Systems,” *Advances in Microwave and Radio Frequency Processing*, part X, pp. 695 – 702, 2006.
22. Ingram, R.B., Gerardi, J.J., “Shape Memory Alloy De-Icing Technology,” U.S. Patent 5,686,003, issued Nov. 11, 1997.
23. Gerardi, J.J., Ingram, R.B., and Catarella, R.A., “Wind Tunnel Test Results for a Shape Memory Alloy Based De-Icing System for Aircraft,” *AHS and SAE International Icing Symposium '95*, Montreal, Canada, pp. 103 – 112, Sep. 1995.

24. Zhu, Y., "Structural Tailoring and Actuation Studies for Low Power Ultrasonic De-Icing of Aluminum and Composite Plates", *PhD Thesis*, Penn State University, December 2010.
25. Ramanathan, S., "An Investigation on the Deicing of Helicopter Blades Using Shear Horizontal Guided Waves", *PhD Thesis*, Penn State University, May 2005.
26. Venna, S., Lin, Y., and Botura, G., "Piezoelectric Transducer Actuated Leading Edge De-Icing with Simultaneous Shear and Impulse Forces," *Journal of Aircraft*, Vol. 44, No 2, pp. 509 – 515, Apr. 2007.
27. Palacios, J., Smith, E., Rose, J., and Royer, R., "Ultrasonic Deicing of Wind Tunnel Impact Icing," *Journal of Aircraft*, Vol. 28, No. 3pp. 1020 – 1027, 2011.
28. Palacios, J., Smith, E., Rose, J., and Royer, R., "Instantaneous Deicing of Freezer Ice via Ultrasonic Actuation," *AIAA Journal*, Vol. 49, No. 6, pp. 1158 – 1167, 2011.
29. DiPlacido, N., Soltis, J., Smith, E., and Palacios, "Enhancement of Ultrasonic De-icing via Transient Excitation ," *4th International Basic Research Conference on Rotorcraft Technology*, Tianjin, China, 2013.
30. , "70th American Helicopter Society Annual Forum and Technology Display, Montreal, Quebec, 2014.
31. Marks, P. 2011, "Cold fronts", digital image, New Scientist, accessed 17 June 2014, <<http://www.newscientist.com/article/mg21028106.100-freeze-airframe-targeting-an-icy-killer-in-flight.html>>.
32. Ryzhkin, I. and Petrenko, V., "Physical Mechanisms Responsible for Ice Adhesion," *Journal of Physical Chemistry B*, Vol. 101, No. 32, pp. 6267 – 6270, Aug. 1997.
33. Petrie, E.M., "Strategies for Combating Ice Adhesion," *Metal Finishing*, 2009.
34. Sonwalker, N., Sunder, S., and Sharma, S.K., "Ice/Solid Adhesion Analysis Using Low-Temperature Rama Microprobe Shear Apparatus," *Applied Spectroscopy*, Vol. 47, No. 10, pp. 1585 – 1593, 1993.
35. Isaacs, E.D., Shukla, A., Platzman, P.M., Hamann, D.R.m Barbiellini, B, and Tulk, C.A., "Covalency of the Hydrogen Bond in Ice: A Direct X-Ray Measurement," *Physical Review Letters*, Vol. 82, No. 3, 600 – 603, Jan. 1993.

36. Model of hydrogen bonds in water in English, digital image, Wikimedia Commons, accessed 14 June 2014, <http://en.wikipedia.org/wiki/File:3D_model_hydrogen_bonds_in_water.svg>.
37. Crystal structure of hexagonal ice, digital image, Wikimedia Commons, accessed 14 June 2014, <http://en.wikipedia.org/wiki/File:Hex_ice.GIF>.
38. Wilen, L.A., Wettlaufer, J.S., Elbaum, M., and Schick, M., “Dispersion-Force Effects in Interfacial Premelting of Ice,” *Physical Review B*, Vol. 52, No. 16, pp. 52 – 59, Oct. 1995.
39. Adhesives and Sealant Council 2014, “Adhesion and Cohesion,” accessed 17 June 2014, <<http://www.adhesives.org/adhesives-sealants/science-of-adhesion/adhesion-cohesion>>.
40. Xian, X., Chu, M.L., Scavuzzo, R.J., and Srivatsan, T.S., “An Experimental Evaluation of the Tensile Strength of Impact Ice,” *Journal of Materials Science Letters*, Issue 8, pp. 1205 – 1208, 1989.
41. Archer, P. and Gupta, V., “Measurement and Control of Ice Adhesion to Aluminum 6061 Alloy,” *Mech. Phys. Solids*, Vol. 46, No. 10, pp. 1745 – 1771, 1998.
42. Javan-Mashmool, M., “A New Method for Measuring Ice Adhesion Strength at an Ice-Substrate Interface,” *Hydrological Processes*, Vol. 20, No. 4, *Eastern Snow Conference/Western Snow Conference*, pp. 645 – 655, Mar. 2006.
43. Kraj, A.G., and Bibeau, E.L., “Measurement Method and Results of Ice Adhesion Force on the Curved Surface of a Wind Turbine Blade,” *Renewable Energy*, Issue 35, pp. 741 – 746, 2010.
44. Laforte, C. and Laforte, J.L., “Tensile, Torsional, and Bending Strain at the Adhesive Rupture of an Iced Substrate,” *Proceedings of the ASME 28th International Conference on Ocean, Offshore, and Arctic Engineering*, Honolulu, HI, June 2009.
45. Chu, M.C. and Scavuzzo, R.J., “Adhesive Shear Strength of Impact Ice,” *AIAA Journal*, Vol. 29, No. 11, pp. 1921 – 1926, Nov. 1991.

46. Loughborough, D.L. and Hass, E.G., "Reduction of Adhesion of Ice to De-Icer Surfaces," *Journal of the Aeronautical Sciences*, Vol. 13, No. 3, pp. 126 – 134, Mar. 1946.
47. Raraty, L. and Tabor, D., "The Adhesion and Strength Properties of Ice," *Royal Society Proceedings*, Vol. 245, No. 1241, pp. 184 – 201, Jun. 1958.
48. Bascom, W., Cottington, R., and Singleterry, C., "Ice Adhesion to Hydrophilic and Hydrophobic Surfaces," *Journal of Adhesion*, Vol. 1, pp. 246 – 263, Oct. 1969.
49. Stallabrass, J. and Price, R., "On the Adhesion of Ice to Various Materials," *Canada National Research Council -- Aeronautical Report*, pp. 199 – 219, Jul. 1962.
50. Scavuzzo, R. J. and Chu, M. L., "Structural Properties of Impact Ices Accreted on Aircraft Structures," NASA CR-179580, 1987.
51. Itagaki, K., "Adhesion of Ice to Polymers and Other Surfaces," *Physicochemical Aspects of Polymer Surfaces*, p. 241, 1983.
52. Reich, A., "Interface Influences Upon Ice Adhesion to Airfoil Materials," 32nd *Aerospace Sciences Meeting and Exhibit*, AIAA, AIAA Paper 94-0714, Reno, NV, 1994.
53. Ford, T.F. and Nichols, O.D., "Shear Characteristics of Ice in Bulk, at Ice/Solid Interfaces, and at Ice/Lubricant/Solid Interfaces in a Laboratory Device," Naval Research Lab Report 5662, 1961.
54. Venna, S.V. and Lin, Y.J., "PZT-Actuated In-Flight Deicing with Simultaneous Shear and Impulse Forces," *Proceedings of the ASME International Mechanical Engineering Congress and Exposition*, Anaheim, CA, Nov. 2004.
55. Brouwers, E., Palacios, J., Smith, E.C., "The Experimental Investigation of a Rotor Hover Icing Model with Shedding," *Journal of America Helicopter Society*, 2010.
56. Cook, R.D. and Young, W.C., *Advanced Mechanics of Materials*, 2nd Ed., Prentice Hall, NJ, 1999.
57. Cauchy tetrahedron, digital image, Wikimedia Commons, accessed 14 June 2014, <http://en.wikipedia.org/wiki/File:Cauchy_tetrahedron.svg>
58. Meirovitch, L., *Principles and Techniques of Vibration*, Prentice Hall, NJ, 2000.

59. Rao, S.S., *Mechanical Vibrations 4th Ed.*, Pearson, 2009.
60. Cleaning Technologies Group 2009, Magnetostrictive Versus Piezoelectric Transducers for Power Ultrasonic Applications, accessed 16 January 2014,
<<http://www.ctgclean.com/blog/technology-library/articles/magnetostrictive-versus-piezoelectric-transducers-for-power-ultrasonic-applications/>>.
61. Claeysen, F., Lhermet, N., and Maillard, T., “Magnetostrictive Actuators Compared to Piezoelectric Actuators,” *ASSET* 2002.
62. Pons, J.L., “A Comparative Analysis of Piezoelectric and Magnetostrictive Actuators in Smart Structures,” *Bol. Soc. Esp. Ceram. V.*, Vol. 44, No. 3, pp. 146 – 154, 2005.
63. Overmeyer, A., Palacios, J., Smith, E., “Ultrasonic De-Icing Bondline Design and Rotor Ice Testing,” *AIAA Journal*, Vol. 51, No. 12, pp. 2965 – 2976, 2013.
64. *Piezoelectric Ceramics: Principles and Applications*, American Piezo Ceramics International, Ltd., 2002.
65. Giurgiutiu, V., *Structural Health Monitoring with Piezoelectric Wafer Active Sensors*, Academic Press, Elsevier, Burlington, MA, 2008.
66. Overmeyer, A., “Actuator Bondline Optimization and Experimental De-Icing of a Rotor Blade Ultrasonic De-Icing System”, *PhD Thesis*, Penn State University, May 2012.
67. Cawley, P. “The Impedance Method of Non-Destructive Inspection,” *NDT International*, Vol. 17, No. 2, pp. 59 – 65, 1984.
68. Meirovitch, L., *Principles and Techniques of Vibrations*, Prentice Hall, New Jersey, 1997.
69. Thomas, D. “Mechanical Impedances for Thin Plates,” *Journal of the Acoustical Society of America*, Vol. 32, No. 10, pp. 1302 – 1304, 1960.
70. Bowick, C., Blyler, J., and Ajluni, C., *RF Circuit Design, 2nd Ed.*, Elsevier, Burlington, MA, 2008.
71. Gottlieb, I.M., *Practical RF Power Design Techniques*, TAB Books, Blue Ridge Summit, PA, 1993.

72. Ludwig, R. and Bretchko, P., *RF Circuit Design: Theory and Applications*, Prentice Hall, New Jersey, 2000.
73. Frenzel, L. 2011, Electronic Design, “Back to Basics: Impedance Matching (Part 1),” accessed 17 January 2014, < <http://electronicdesign.com/communications/back-basics-impedance-matching-part-1> >.
74. Zagrai, A. and Giurgiutiu, V., “The Electro-Mechanical Impedance Method for Damage Identification in Circular Plates,” *142nd Meeting of the Acoustical Society of America*, Fort Lauderdale, FL, Dec. 2001.
75. MKS Instruments 2014, “Impedance matching option for RF Plasma Generators,” accessed 20 January 2014, < <http://www.mksinst.com/docs/ur/eniaft.aspx> >.
76. Smith, J.L. “R.F. Amplifier Automatic Frequency Tuning,” U.S. Patent 3,106,681, issued Oct. 8, 1963.
77. Vizmuller, P., *RF Design Guide: Systems, Circuits, and Equations*, Artech House Publishers, 1995.
78. *Electronic Warfare and Radar Systems Engineering Handbook*, NAWCWPNS TP 8347, Naval Air Systems Command and Naval Air Warfare Center, 2006.
79. Fish, J. and Belytschko, T., *A First Course in Finite Elements*, John Wiley & Sons, Ltd., West Sussex, England, 2007.
80. Cook, R.D., Malkus, D.S., Plesha, M.E., and Witt, R.J., *Concepts and Applications of Finite Element Analysis*, John Wiley & Sons, Ltd., West Sussex, England, 2002.
81. *ABAQUS 6.13 User Manual*, Dassault Systems, 2013.
82. *ABAQUS 6.13 Theory Manual*, Dassault Systems, 2013.
83. Rowland, T. 2014, Wolfram MathWorld, “Genetic Algorithm,” accessed 17 June 2014, <<http://mathworld.wolfram.com/GeneticAlgorithm.html>>.
84. Holland, J., *Adaptation in Natural and Artificial Systems: An Introductory Analysis with Applications to Biology, Control, and Artificial Intelligence*, The MIT Press, Cambridge MA, 1998.

85. The MathWorks, Inc. 2014, “MATLAB Documentation Center – Global Optimization Toolbox, Genetic Algorithm,” accessed 17 June 2014, <<http://www.mathworks.com/help/gads/genetic-algorithm.html>>.
86. Polytec, Inc. 2014, “PSV-500-3D Scanning Vibrometer,” accessed 17 June 2014, <<http://www.polytec.com/us/products/vibration-sensors/scanning-vibrometers/psv-500-3d-scanning-vibrometer>>.
87. Polytec, Inc. 2014, “Basic Principles of Vibrometry,” accessed 17 June 2014, <<http://www.polytec.com/us/solutions/vibration-measurement/basic-principles-of-vibrometry>>.
88. *1040L Broadband Power Amplifier System Manual*, Rev. E, Electronics & Innovation, Ltd., 2011.
89. National Instruments Corporation 2014, “White Paper: What is NI X Series?,” accessed 17 June 2014, <<http://www.ni.com/white-paper/9376/en>>.
90. IPC-2141A-2004, “Design Guide for High-Speed Controlled Impedance Circuit Boards with Errata”, ANSI Standard, 2004.
91. IPC-2221B, “Generic Standard on Printed Board Design,” ANSI Standard, 2012.

Appendix A

MATLAB CODES FOR AIRFOIL FINITE ELEMENT MODEL PHASING ANALYSIS

A description of the general method used for creating, processing, and analyzing the finite element airfoil models for the purposes of ultrasonic de-icing phasing analysis is provided here. This description is a high-level procedure that is intended for a user already familiar with ABAQUS.

A.1 Part

1. Import airfoil part in .iges format from a drawing program
2. Cut airfoil in half lengthwise if symmetry will be applied
 - a. Create plane at halfway point
 - b. Extrude cut from plane
3. Partition clamped boundary region at edge as needed
4. Extrude epoxy on airfoil inner surface
 - a. Create datum points along edge using length parameter for top and bottom edges of actuators
 - b. Create datum axes along airfoil inner surface at top and bottom edges of actuators
 - c. Create datum plane between these two axes for each actuator row
 - d. Sketch epoxy/actuator circle onto each plane and extrude to airfoil inner surface
5. Extrude actuators on airfoil inner surface
 - a. Extrude from back of the epoxy circle outward to thickness of actuator + 0.25 mm for epoxy corner thickness (for meshing purposes)
 - b. Partition actuator/epoxy extrusions from airfoil by sweeping airfoil inner edge
 - c. Partition between actuators and epoxy
 - i. Create datum planes offset by actuator thickness referenced from actuator top face
 - ii. Partition using these datum planes
 - d. Repeat for all actuators
6. Extrude ice on airfoil outer surface
 - a. Create datum points on airfoil outer surface at top and bottom edges of ice.

- b. Create datum points at some horizontal distance forward of these points, beyond leading edge
 - c. Connect outer surface point and forward point with horizontal datum axis
 - d. Create a datum plane facing airfoil using the two forward points and the datum axis (point and normal)
 - e. Sketch rectangular ice section onto this datum plane and extrude to airfoil outer surface.
 - f. Create datum plane along one side of ice sheet
 - g. Sketch ice profile on this datum plane by offsetting from airfoil outer surface and cut ice using this sketch along airfoil length
 - h. Partition ice from airfoil by sweeping airfoil outer edge
7. Create part sections.
- a. Create airfoil part set named ('Airfoil_Part_Cells')("set" of all airfoil cells).
 - b. Create airfoil surface named ('Surf-1') ("surface" covering at least a full top-to-bottom strip of the airfoil outer surface).

A.2 Materials

8. Create and assign material parameters.
- a. Create all materials.
 - b. Create all sections.
 - c. Assign sections to partitioned model regions.
 - d. Create datum point on edge of each disk by offsetting from center
 - e. Create Cartesian datum coordinate systems on each actuator by using three points on disk top face, with z-axis outward
 - f. Assign local PZT material orientations
9. Create material orientation for airfoil regions.
- a. Discrete orientation
 - b. "Define" "normal vectors" from airfoil surface (previously defined 'Surf-1') in 3-direction
 - c. "Define" "primary vector" by selecting long edge of airfoil

A.3 Assembly

10. Create assembly from single independent part instance
11. Partition the airfoil as needed to achieve an acceptable structured mesh
 - a. Partition edges where clamped BCs will be applied
 - i. Create datum points on inner top and bottom airfoil edges at distance in from ends
 - ii. Create datum point offset from inner bottom airfoil edge datum point on opposite end of airfoil length
 - iii. Partition by defining cutting plane with these three points
 - b. Partition through peak of leading edge of airfoil (approximate)
 - c. Partition around ice edges through airfoil as needed
 - d.
 - e. Partition actuators through airfoil and ice by extending circumferential face of actuators
 - f. Partition a cross through each actuator
 - g. Partition midway between each actuator (top to bottom) as needed to control mesh
12. Create through-thickness sets for seeding
 - a. Create actuator thickness set (all through-thickness edges in actuators)
 - b. Create epoxy thickness set (all through-thickness edges in epoxy)
 - c. Create ice thickness set (all through-thickness edges in ice)
 - d. Create airfoil thickness set (all through-thickness edges in airfoil)
13. Create TP (top point), BP (bottom point), TS (top surface), and BS (bottom surface) sets for each actuator
14. Create “interface” set of airfoil outer face in contact with ice

A.4 Step

15. Create calculation step.
 - a. Steady-state, dynamic, direct
 - b. Linear frequency steps
 - c. Define min, max, and increment frequencies
16. Modify or add history and field output settings as required

A.5 Boundary Conditions

17. Apply mechanical boundary conditions
 - a. Apply symmetry boundary conditions on cut edge if needed
 - b. Apply clamped boundary conditions around edge regions as needed
18. Apply electrical boundary conditions
 - a. Create “ground” boundary conditions of voltage = 0 for each actuator BP set during initial step
 - b. Create “voltage” boundary conditions of voltage = 100 for each actuator TP set during calculation step
19. Create top and bottom electrode constraints
 - a. Create equation constraints
 - b. 1,-1 TS,TP 9,9
 - c. 1,-1 BS,BP 9,9

A.6 Meshing

20. Assign element types to all regions
21. Check mesh controls. If not all structured, partitioning further may help, but will require revision of the through-thickness edge sets
22. Assign edge seeds for each through-thickness set as needed, assigning by element size or number
23. Assign global seeds
24. Mesh assembly
25. Check mesh for quality and re-partition and/or re-mesh as needed

A.7 Modify Imported Model

26. Write temporary input file for importing
27. Import temporary input file as a new model
28. Create material orientation for airfoil regions
 - a. Discrete orientation
 - b. “Define” “normal vectors” from airfoil surface (previously defined ‘Surf-1’) in 3-direction

- c. “Define” “primary vector” by selecting datum axis parallel to z-direction
- 29. Delete erroneously-created 0-Volt boundary conditions on TP actuator sets
- 30. Manually delete TP and BP nodes from TS and BS actuator sets
- 31. Write input file for job run

A.8 Input File Modification

- 32. Manually edit input file by adding complex output to .dat file, for example...
 - a. “Node Print, nset=TP1
PHCHG,” - for each actuator top point
 - b. “El Print, elset=INTERFACE, position=nodes
PHS13,PHS23,” - for airfoil interface set
 - c. All node charge prints first, followed by element stress print.
 - d. Save the modified input file.
- 33. Create multiple impedance and frequency range files using ‘inp_file_modifierBB_v2.m’ if necessary
 - a. Note that flag lines and file paths may differ somewhat depending on input file generation
- 34. Create multiple impedance files manually if necessary if automatic generation is not possible
 - a. Below constraints, add short-circuit constraint equations; i.e. to short-circuit actuator 3...

```

** Constraint: short-circuit 3
*Equation
2
TP3, 9, 1.
BP3, 9, -1.

```

- b. Repeat for each short-circuited actuator (i.e. for impedance ij , all actuators other than i and j should be short-circuited
- c. Below boundary conditions under Step-1, add electric potential for the driving actuator (i) and a zero electric potential for the receiving actuator (j); if $i=j$, omit the zero potential command...

```

** Name: voltage 1 Type: Electric potential
*Boundary, load case=1
TP1, 9, 9, 100.
*Boundary, load case=2
TP1, 9, 9
** Name: voltage 2 Type: Electric potential
*Boundary, load case=1
TP2, 9, 9,
*Boundary, load case=2
TP2, 9, 9

```

35. Create multiple frequency range files, if necessary, using MATLAB script
“input_file_modifierBB.m” if not already done during impedance file generation
36. Create a .pbs script for job submission using MATLAB script “pbs_writer_BBairfoil.m”
 - a. Note that file paths and pbs script lines may differ and need to be altered

A.9 Job Submission and Analysis

37. Submit job(s) for completion
38. Copy and save .odb and .dat files as needed
39. Extract data from output files
 - a. Run MATLAB script “FEanalysis_initial.m”
 - b. Copy and save extracted .mat files as needed
40. Analyze data
 - a. Run MATLAB script “FEanalysis.m”
 - b. Run other analysis scripts as needed
 - c. Copy and save data as needed

Appendix B

MATLAB CODES FOR AIRFOIL FINITE ELEMENT MODEL PHASING ANALYSIS

The following sections provide examples of the MATLAB codes utilized to process the finite element airfoil models used for the ultrasonic de-icing phasing analysis. Each code is preceded by a brief description of its function.

B.1 datFileReader_v5_pt1.m

This code reads data from the .dat file generated by ABAQUS and extracts information about the model mesh that will be used by another script, datFileReader_v5_pt2.m, to extract the field data from the .dat file.

```
function
[UPartNodes,SPartNodes,Unum_nodes,Snum_nodes,USetNodes,SSetNodes,num_elem,Uglobal_num,Sglobal_num] = datFileReader_v5_pt1(filelist, outvarlist, setlist)

%% datFileReader_v5_pt1
% Cody Borigo
% 5-14-11
%-----
% Reads data from .dat file generated from ABAQUS with multiple outputs,
% then sorts and saves this data to a .mat file.
%
% %%%%%%%%%%%%%%%%%%%%%%%%%%%%%%%%%%%%%%%%%%%%%%%%%%%%%%%%%%%%%%%%%%%%%%%%%
% Input Parameter Lists:
% -----
% filelist:      {datfolder, datfilename, inpfolder, inpfilename, savefolder}
% outvarlist:    [var1, var2, var3, var4]
% setlist:       {Uset, Upart, Sset, Spart}
% optlist:       [Zmin_option, rectmesh_option]
% elem_nodes:    elem_nodes
% num_act:       num_act
% V:             V
%
% %%%%%%%%%%%%%%%%%%%%%%%%%%%%%%%%%%%%%%%%%%%%%%%%%%%%%%%%%%%%%%%%%%%%%%%%%
% Input Parameter Descriptions:
% -----
% datfilename:    .dat file name (omit file extension)
% inpfilename:    .inp file name (omit file extension)
% datfolder:      folder in which .dat file exists
% inpfolder:      folder in which .inp file exists
% savefolder:     folder to save .mat file with data
% var1:           'PHU' displacement - '1' if requested
% var2:           'PHS13' S13 stress - '1' if requested
% var3:           'PHS23' S23 stress - '1' if requested
% var4:           'PHCHG' charge - '1' if requested
% Uset:           name of set in model for which displacement values were
requested
```

```

% Upart:          name of part in model in which displacement set exists
% Sset:          name of set in model for which stress values were
requested
% Spart:         name of part in model in which stress set exists
% num_act:       number of actuators for which charge output was requested
% V:            voltage applied to actuators
% elem_nodes:    number of nodes per element
% Zmin_option:   set to '1' if field output is only desired at impedance
minimum
% rectmesh_option: set to '1' if rectangular mesh is used for specified set,
and output sorted by x-y location is desired
%
%%%%%%%%%%%%%%%%%%%%%%%%%%%%%%%%%%%%%%%%%%%%%%%%%%%%%%%%%%%%%%%%%%%%%%%%
% Input Parameter Examples:
% -----
% datfilename = 'ind_act1a_phase_method2';
% inpfilename = 'ind_act1a_phase_method2';
% datfolder = 'E:\Deicing ABAQUS Files\Actuator Phasing\Individual Phasing
Output Data\Ind_Act1_Data';
% inpfolder = 'E:\Deicing ABAQUS Files\Actuator Phasing';
% savefilename = 'OutputData';
% var1 = 1;
% var2 = 1;
% var3 = 0;
% var4 = 1;
% Uset = ['PLATE_SET'];
% Upart = ['PLATE-1'];
% Sset = 'INTERFACE';
% Spart = 'PLATE-1';
% num_act = 3;
% V = 100;
% elem_nodes = 8;
% Zmin_option = 1;
% rectmesh_option = 0;
%
%%%%%%%%%%%%%%%%%%%%%%%%%%%%%%%%%%%%%%%%%%%%%%%%%%%%%%%%%%%%%%%%%%%%%%%%

%% File Parameters
% Parameters required to be input by user, including file names and
% directories, set and part names, and variable names.
%%%%%%%%%%%%%%%%%%%%%%%%%%%%%%%%%%%%%%%%%%%%%%%%%%%%%%%%%%%%%%%%%%%%%%%%

datfolder = filelist{1};
datfilename = filelist{2};
inpfolder = filelist{3};
inpfilename = filelist{4};

var1 = outvarlist(1);
var2 = outvarlist(2);
var3 = outvarlist(3);

Uset = setlist{1};
Upart = setlist{2};
Sset = setlist{3};
Spart = setlist{4};

```



```

%% Data Line Indicators and Formats
% Specific strings used to locate values and parameters in .inp and .dat
% files, as well specific data formats used to extract values from these
% files.
%%%%%%%%%%%%%%%%%%%%%%%%%%%%%%%%%%%%%%%%%%%%%%%%%%%%%%%%%%%%%%%%%%%%%%%%
flagline3 = ['      ' Sset ':'];
flagline4 = ['      number of elements:'];
flagline6 = ['*Part, name=' Spart];
flagline7 = ['*Element, type='];
flagline8 = ['GLOBAL TO LOCAL NODE AND ELEMENT MAPS'];
flagline9 = ['*Nset, nset=' Sset ', instance=' Spart];
flagline10 = ['*Elset, elset=' Sset ', instance=' Spart];
flagline11 = ['*Nset, nset=' Uset ', instance=' Upart];
flagline12 = ['*Elset, elset=' Uset ', instance=' Upart];
flagline14 = ['      ' Uset ':'];
flagline15 = ['*Part, name=' Upart];
flagline16 = ['      number of nodes:'];

format2 = ['      number of nodes: %d' sprintf('\n')];
format3 = ['      number of elements: %d' sprintf('\n')];
format5 = ['      %d, %f, %f, %f' sprintf('\n')];
format6 = ['      %d          %d          %s
' sprintf('\n')];
format7 = ['      %d, %d, %d, %d, %d, %d, %d, %d, %d, %d, %d, %d, %d, %d, %d, %d'
sprintf('\n')];
format12 = ['      number of nodes: %d' sprintf('\n')];

%% Initialize All Potential Output Variables
UPartNodes = [];
SPartNodes = [];
Unum_nodes = [];
Snum_nodes = [];
USetNodes = [];
SSetNodes = [];
num_elem = [];
Uglobal_num = [];
Sglobal_num = [];

%% Open .dat and .inp Files
% Open .dat and .inp files and assign them file identifiers to access them
% later.
%%%%%%%%%%%%%%%%%%%%%%%%%%%%%%%%%%%%%%%%%%%%%%%%%%%%%%%%%%%%%%%%%%%%%%%%
OldFolder=cd;
cd(datfolder);
fid=fopen([datfilename '.dat']);
fseek(fid,0,'bof');

cd(inpfolder);
fid_inp=fopen([inpfilename '.inp']);
fseek(fid_inp,0,'bof');

%% Determine Nodal Coordinates for Part(s)
% Read all node numbers and spatial coordinates for the specified part(s)
from
% the .inp file.
%%%%%%%%%%%%%%%%%%%%%%%%%%%%%%%%%%%%%%%%%%%%%%%%%%%%%%%%%%%%%%%%%%%%%%%%

```

```

% The following will execute if 'PHU' displacement output was requested
if var1==1
    eofflag = 0;
    nodeinx=1;
    wbh=waitbar(0,['Determining Nodal Coordinates for Part "' Upart '"']);
    while eofflag == 0
        currentline = fgetl(fid_inp);
        if currentline == -1
            eofflag = 1;
        elseif strcmp(currentline,flagline15,length(flagline15))==1
            currentline = fgetl(fid_inp);
            while strcmp(currentline,flagline7,length(flagline7))==0
                UPartNodes(nodeinx,:)=fscanf(fid_inp,format5,4); %#ok<AGROW>
                nodeinx=nodeinx+1;
                prevline=ftell(fid_inp);
                currentline = fgetl(fid_inp);
                fseek(fid_inp,prevline,'bof');
            end
            eofflag = 1;
        end
    end
    close(wbh)
end

% The following will execute if 'PHS13' or 'PHS23' shear stress output was
requested
if var2==1 || var3==1
    fseek(fid_inp,0,'bof');
    eofflag = 0;
    nodeinx=1;
    wbh=waitbar(0,['Determining Nodal Coordinates for Part "' Spart '"']);
    while eofflag == 0
        currentline = fgetl(fid_inp);
        if currentline == -1
            eofflag = 1;
        elseif strcmp(currentline,flagline6,length(flagline6))==1
            currentline = fgetl(fid_inp);
            while strcmp(currentline,flagline7,length(flagline7))==0
                SPartNodes(nodeinx,:)=fscanf(fid_inp,format5,4); %#ok<AGROW>
                nodeinx=nodeinx+1;
                prevline=ftell(fid_inp);
                currentline = fgetl(fid_inp);
                fseek(fid_inp,prevline,'bof');
            end
            eofflag = 1;
        end
    end
    close(wbh)
end

%% Determine Number of Nodes in Set(s)
% Determine the total number of elements in the specified set(s),
% from the .dat file.
%%%%%%%%%%%%%%%%%%%%%%%%%%%%%%%%%%%%%%%%%%%%%%%%%%%%%%%%%%%%%%%%%%%%%%%%

```

```

% The following will execute if 'PHU' displacement output was requested
if var1==1
    eofflag = 0;
    wbh=waitbar(0,['Determining Number of Nodes in Set "' Uset "'']);
    while eofflag == 0
        currentline = fgetl(fid);
        if currentline == -1
            eofflag = 1;
        elseif strcmp(currentline,flagline14,length(flagline14))==1
            fgetl(fid);
            prevline=ftell(fid);
            currentline = fgetl(fid);
            if strcmp(currentline,flagline16,length(flagline16))==1
                fseek(fid,prevline,'bof');
                Unum_nodes=fscanf(fid,format12,2);
                eofflag = 1;
            end
        end
    end
    close(wbh)
end

% The following will execute if 'PHS13' or 'PHS23' shear stress output was
requested
if var2==1 || var3==1
    fseek(fid,0,'bof');
    eofflag = 0;
    wbh=waitbar(0,['Determining Number of Nodes in Set "' Sset "'']);
    while eofflag == 0
        currentline = fgetl(fid);
        if currentline == -1
            eofflag = 1;
        elseif strcmp(currentline,flagline3,length(flagline3))==1
            fgetl(fid);
            prevline=ftell(fid);
            currentline = fgetl(fid);
            if strcmp(currentline,flagline16,length(flagline16))==1
                fseek(fid,prevline,'bof');
                Snum_nodes=fscanf(fid,format2,2);
                eofflag = 1;
            end
        end
    end
    close(wbh)
end

%% Compile Node List for Set(s)
% Read the list of nodes that comprise the specified set(s), from the
% .inp file.
%%%%%%%%%%%%%%%%%%%%%%%%%%%%%%%%%%%%%%%%%%%%%%%%%%%%%%%%%%%%%%%%%%%%%%%%

% The following will execute if 'PHU' displacement output was requested
if var1==1
    eofflag = 0;
    USetNodes=zeros(Unum_nodes,1);
    wbh=waitbar(0,['Determining Nodes in Set "' Uset "'']);

```

```

while eofflag == 0
    currentline = fgetl(fid_inp);
    if currentline == -1
        eofflag = 1;
    elseif strncmp(currentline,flagline11,length(flagline11))==1
        setinx1 = 1;
        while strncmp(currentline,flagline12,length(flagline12))==0
            tempread = fscanf(fid_inp,format7);
            setinx2 = setinx1 + length(tempread)-1;
            USetNodes(setinx1:setinx2) = tempread;
            prevline=ftell(fid_inp);
            currentline = fgetl(fid_inp);
            fseek(fid_inp,prevline,'bof');
            setinx1 = setinx2 + 1;
        end
        eofflag = 1;
        clear tempread
    end
end
if length(USetNodes) == 3
    USetNodes = USetNodes(1):USetNodes(3):USetNodes(2);
end
close(wbh)
end

% The following will execute if 'PHS13' or 'PHS23' shear stress output was
requested
if var2==1 || var3==1
    fseek(fid_inp,0,'bof');
    eofflag = 0;
    SSetNodes=zeros(Snum_nodes,1);
    wbh=waitbar(0,['Determining Nodes in Set ' Sset '']);
    while eofflag == 0
        currentline = fgetl(fid_inp);
        if currentline == -1
            eofflag = 1;
        elseif strncmp(currentline,flagline9,length(flagline9))==1
            setinx1 = 1;
            while strncmp(currentline,flagline10,length(flagline10))==0
                tempread = fscanf(fid_inp,format7);
                setinx2 = setinx1 + length(tempread)-1;
                SSetNodes(setinx1:setinx2) = tempread;
                prevline=ftell(fid_inp);
                currentline = fgetl(fid_inp);
                fseek(fid_inp,prevline,'bof');
                setinx1 = setinx2 + 1;
            end
            eofflag = 1;
            clear tempread
        end
    end
end
if length(SSetNodes) == 3
    SSetNodes=SSetNodes(1):SSetNodes(3):SSetNodes(2);
end
close(wbh)
end
fclose(fid_inp);

```

```

%% Determine Number of Elements in Set
% Determine the total number of elements in the specified set for stresses,
% from the .dat file.
%%%%%%%%%%%%%%%%%%%%%%%%%%%%%%%%%%%%%%%%%%%%%%%%%%%%%%%%%%%%%%%%%%%%%%%%
if var2==1 || var3==1
    eofflag = 0;
    wbh=waitbar(0,['Determining Number of Elements in Set ' Sset '']);
    while eofflag == 0
        currentline = fgetl(fid);
        if currentline == -1
            eofflag = 1;
        elseif strcmp(currentline,flagline3,length(flagline3))==1
            fgetl(fid);
            prevline=ftell(fid);
            currentline = fgetl(fid);
            if strcmp(currentline,flagline4,length(flagline4))==1
                fseek(fid,prevline,'bof');
                num_elem=fscanf(fid,format3,2);
                eofflag = 1;
            end
        end
    end
    close(wbh)
end

%% Determine Global to Local Node Mapping
% Determine the relationship between local and global node
% numbering from the list in the .dat file in order to directly compare
% nodal coordinates (using local node numbering) and output variable
% values (using global node numbering).
%%%%%%%%%%%%%%%%%%%%%%%%%%%%%%%%%%%%%%%%%%%%%%%%%%%%%%%%%%%%%%%%%%%%%%%%

% The following will execute if 'PHU' displacement output was requested
if var1==1
    eofflag = 0;
    partname=[];
    wbh=waitbar(0,['Global to Local Node Mapping for Part ' Upart '']);
    while eofflag == 0
        currentline = fgetl(fid);
        if currentline == -1
            eofflag = 1;
        elseif strcmp(currentline,flagline8,length(flagline8))==1
            for ii=1:4
                fgetl(fid);
            end
            while strcmp(partname,Upart,length(Upart))==0
                tempread=fscanf(fid,format6,3);
                partname=char(tempread(3:end));
            end
            Uglobal_num = tempread(1)-1;
            eofflag = 1;
        end
    end
    close(wbh)
end

```

```

% The following will execute if 'PHS13' or 'PHS23' shear stress output was
requested
if var2==1 || var3==1
    fseek(fid,0,'bof');
    eofflag = 0;
    partname=[];
    wbh=waitbar(0,['Global to Local Node Mapping for Part "' Spart '"']);
    while eofflag == 0
        currentline = fgetl(fid);
        if currentline == -1
            eofflag = 1;
        elseif strcmp(currentline,flagline8,length(flagline8))==1
            for ii=1:4
                fgetl(fid);
            end
            while strcmp(partname,Spart,length(Spart))==0
                tempread=fscanf(fid,format6,3);
                partname=char(tempread(3:end));
            end
            Sglobal_num = tempread(1)-1;
            eofflag = 1;
        end
    end
    close(wbh)
end

cd(OldFolder)

```

B.2 datFileReader_v5_pt2.m

This code extracts the impedance, displacement, and stress data from the .dat file generated by ABAQUS.

```

function [] = datFileReader_v5_pt2(filelist, outvarlist, setlist, optlist,
elem_nodes, num_act, V, UPartNodes, SPartNodes, Unum_nodes, USetNodes,
SSetNodes, num_elem, Uglobal_num, Sglobal_num)

%% datFileReader_v5_pt2
% Cody Borigo
% 5-14-11
%-----
% Reads data from .dat file generated from ABAQUS with multiple outputs,
% then sorts and saves this data to a .mat file.
%
%%%%%%%%%%%%%%%%%%%%%%%%%%%%%%%%%%%%%%%%%%%%%%%%%%%%%%%%%%%%%%%%%%%%%%%%
% Input Parameter Lists:
% -----
% filelist:      {datfolder, datfilename, inpfolder, inpfilename, savefolder}
% outvarlist:    [var1, var2, var3, var4]
% setlist:       {Uset, Upart, Sset, Spart}
% optlist:       [Zmin_option, rectmesh_option]
% elem_nodes:    elem_nodes

```

```

% num_act:      num_act
% V:            V
%
%%%%%%%%%%%%%%%%%%%%%%%%%%%%%%%%%%%%%%%%%%%%%%%%%%%%%%%%%%%%%%%%%%%%%%%%
% Input Parameter Descriptions:
% -----
% datfilename:   .dat file name (omit file extension)
% inpfilename:  .inp file name (omit file extension)
% datfolder:    folder in which .dat file exists
% inpfolder:    folder in which .inp file exists
% savefolder:   folder to save .mat file with data
% var1:         'PHU'      displacement - '1' if requested
% var2:         'PHS13'   S13 stress - '1' if requested
% var3:         'PHS23'   S23 stress - '1' if requested
% var4:         'PHCHG'   charge - '1' if requested
% Uset:         name of set in model for which displacement values were
requested
% Upart:        name of part in model in which displacement set exists
% Sset:        name of set in model for which stress values were
requested
% Spart:        name of part in model in which stress set exists
% num_act:     number of actuators for which charge output was requested
% V:           voltage applied to actuators
% elem_nodes:  number of nodes per element
% Zmin_option: set to '1' if field output is only desired at impedance
minimum
% rectmesh_option: set to '1' if rectangular mesh is used for specified set,
and output sorted by x-y location is desired
%
%%%%%%%%%%%%%%%%%%%%%%%%%%%%%%%%%%%%%%%%%%%%%%%%%%%%%%%%%%%%%%%%%%%%%%%%
% Input Parameter Examples:
% -----
% datfilename = 'ind_act1a_phase_method2';
% inpfilename = 'ind_act1a_phase_method2';
% datfolder = 'E:\Deicing ABAQUS Files\Actuator Phasing\Individual Phasing
Output Data\Ind_Act1_Data';
% inpfolder = 'E:\Deicing ABAQUS Files\Actuator Phasing';
% savefilename = 'OutputData';
% var1 = 1;
% var2 = 1;
% var3 = 0;
% var4 = 1;
% Uset = ['PLATE_SET'];
% Upart = ['PLATE-1'];
% Sset = 'INTERFACE';
% Spart = 'PLATE-1';
% num_act = 3;
% V = 100;
% elem_nodes = 8;
% Zmin_option = 1;
% rectmesh_option = 0;
%
%%%%%%%%%%%%%%%%%%%%%%%%%%%%%%%%%%%%%%%%%%%%%%%%%%%%%%%%%%%%%%%%%%%%%%%%

%% File Parameters
% Parameters required to be input by user, including file names and
% directories, set and part names, and variable names.

```

```

%%%%%%%%%%%%%%%%%%%%%%%%%%%%%%%%%%%%%%%%%%%%%%%%%%%%%%%%%%%%%%%%%%%%%%%%

datfolder = filelist{1};
datfilename = filelist{2};
inpfolder = filelist{3};
inpfilename = filelist{4};
savefolder = filelist{5};

var1 = outvarlist(1);
var2 = outvarlist(2);
var3 = outvarlist(3);
var4 = outvarlist(4);

Uset = setlist{1};
Upart = setlist{2};
Sset = setlist{3};
Spart = setlist{4};

Zmin_option = optlist(1);
rectmesh_option = optlist(2);

%% Data Line Indicators and Formats
% Specific strings used to locate values and parameters in .inp and .dat
% files, as well specific data formats used to extract values from these
% files.
%%%%%%%%%%%%%%%%%%%%%%%%%%%%%%%%%%%%%%%%%%%%%%%%%%%%%%%%%%%%%%%%%%%%%%%%
flagline1 = '          INCREMENT NUMBER';
flagline2 = '          NOTE ' ;
flagline3 = ['      ' Sset ':'];
flagline4 = '          number of elements:';
flagline5 = '          FREQUENCY RANGE DEFINITIONS (CYCLES/TIME)';
flagline6 = ['*Part, name=' Spart];
flagline7 = '*Element, type=';
flagline8 = 'GLOBAL TO LOCAL NODE AND ELEMENT MAPS';
flagline9 = ['*Nset, nset=' Sset ', instance=' Spart];
flagline10 = ['*Elset, elset=' Sset ', instance=' Spart];
flagline11 = ['*Nset, nset=' Uset ', instance=' Upart];
flagline12 = ['*Elset, elset=' Uset ', instance=' Upart];
flagline13 = '  ALL VALUES IN THIS TABLE ARE ZERO';
flagline14 = ['      ' Uset ':'];
flagline15 = ['*Part, name=' Upart];
flagline16 = '          number of nodes:';
flagline17 = '          NODE FOOT-   PHCHG   ' ;
flagline18 = '          NODE FOOT-   PU';
flagline19 = '          ELEMENT          ND   FOOT-   PHS';
flagline20 = '          THE FOLLOWING TABLE IS PRINTED FOR NODES BELONGING TO NODE
SET';
flagline21 = ['          THE FOLLOWING TABLE IS PRINTED FOR NODES BELONGING TO NODE
SET ASSEMBLY_' Uset];
flagline22 = '          THE FOLLOWING TABLE IS PRINTED AT THE NODES FOR ELEMENT
TYPE';

format1 = ['          INCREMENT NUMBER          %d  AT FREQUENCY (CYCLES/TIME) =
%f          ' sprintf('\n')];
format2 = ['          %d          %d          %e  %e' sprintf('\n')...
          %d          %d SSD          %f          %f' sprintf('\n')];

```



```

format3 = ['          number of elements: %d' sprintf('\n')];
format4 = ['          %e      %e          %d          %f          %f
Linear          ' sprintf('\n')];
format5 = ['          %d,   %f,   %f, %f' sprintf('\n')];
format6 = ['          %d          %d          %s
' sprintf('\n')];
format7 = [' %d, %d, %d, %d, %d, %d, %d, %d, %d, %d, %d, %d, %d, %d, %d, %d'
sprintf('\n')];
format8 = ['          THE FOLLOWING TABLE IS PRINTED FOR NODES BELONGING TO NODE
SET ASSEMBLY_20c' sprintf('\n')];
format9 = ['          %d          %e' sprintf('\n')...
          %d SSD %f' sprintf('\n')];
format10 = ['          %d          %d          %e' sprintf('\n')...
          %d          %d SSD          %f' sprintf('\n')];
format11 = ['          %d          %e %e %e' sprintf('\n')...
          %d SSD %f          %f          %f' sprintf('\n')];
format12 = ['          number of nodes: %d' sprintf('\n')];

skip1 = 8;      % values for data formatting, for displacement output
skip2 = 8;      % values for data formatting, for both S13 and S23 output
skip3 = 6;      % values for data formatting, for single S13 or S23 output
skip4 = 4;      % values for data formatting, for charge output

%% Open .dat and .inp Files
% Open .dat and .inp files and assign them file identifiers to access them
% later.
%%%%%%%%%%%%%%%%%%%%%%%%%%%%%%%%%%%%%%%%%%%%%%%%%%%%%%%%%%%%%%%%%%%%%%%%
OldFolder=cd;
cd(datfolder);
fid=fopen([datfilename '.dat']);
fseek(fid,0,'bof');

cd(inpfolder);
fid_inp=fopen([inpfilename '.inp']);
fseek(fid_inp,0,'bof');

%% Determine Number of Frequency Increments in Step
% Determine the total number of frequency increments in the .dat file.
%%%%%%%%%%%%%%%%%%%%%%%%%%%%%%%%%%%%%%%%%%%%%%%%%%%%%%%%%%%%%%%%%%%%%%%%
listflag = 0;
wbh=waitbar(0,'Determining Number of Frequency Increments in Step');
while listflag == 0
    currentline = fgetl(fid);
    if strcmp(currentline,flagline5,length(flagline5))==1
        for ii=1:3
            fgetl(fid);
        end
        tempread = fscanf(fid,format4,5);
        numinc = tempread(3);
        clear tempread
        listflag = 1;
    end
end
close(wbh)

```

```

%% Extract Data at Impedance Minimum Only (if Zmin_option selected)
% Extract the charge and frequency data from the .dat file, determine the
% frequency at which the impedance minimum occurs, and then extract the
requested
% field output variable data from the tables in the .dat file at that
frequency.
%%%%%%%%%%%%%%%%%%%%%%%%%%%%%%%%%%%%%%%%%%%%%%%%%%%%%%%%%%%%%%%%%%%%%%%%
if Zmin_option==1 && var4==1
    wbh=waitbar(0,'Extracting Charge Data from .dat File...');
    finx=1;
    prevline=0;
    eofflag = 0;
    FData=zeros(numinc,1);
    Qdata=zeros(numinc,num_act*2);

    % Extract all frequency and charge data
    while eofflag == 0
        currentline = fgetl(fid);
        if currentline == -1
            eofflag = 1;
        elseif strcmp(currentline,flagline1,length(flagline1))==1
            if FData(1) == 0
                startline = prevline;
            end
            fseek(fid,prevline,'bof');
            tempread=fscanf(fid,format1,2);
            FData(finx)=tempread(2);
            clear tempread

            ai=1;
            while ai <= num_act
                while strcmp(currentline,flagline20,length(flagline20))==0
                    currentline=fgetl(fid);
                end
                while strcmp(currentline,flagline17,length(flagline17))==0
                    currentline=fgetl(fid);
                end
                currentline=fgetl(fid);
                currentline=fgetl(fid);
                prevline2=ftell(fid);
                currentline=fgetl(fid);
                if strcmp(currentline,flagline13,length(flagline13))==0
                    fseek(fid,prevline2,'bof');
                    tempread=fscanf(fid,format9,skip4);
                    Qdata(finx,(ai-1)*2+1:ai*2)=[tempread(2) tempread(4)];
                end
                ai=ai+1;
            end
            clear tempread

            waitbar(finx/numinc,wbh)
            finx=finx+1;
        end
        prevline=ftell(fid);
    end
    close(wbh)

```

```

% Calculate impedance curve and determine minimum
wbh=waitbar(0,'Calculating Impedance Minimum...');
Qmag = Qdata(:,1:2:num_act*2-1);
Qphase = Qdata(:,2:2:num_act*2);
Q = Qmag.*exp(1i*Qphase/180*pi);
Zind=zeros(length(FData),num_act);
cnt=1;
for ai=1:num_act
    if Q(:,ai) == zeros(length(FData),1)
        Zind(:,ai) = NaN*ones(length(FData),1);
    else
        Zind(:,ai) = V./((2*pi*FData).*Q(:,ai));
        ZindCalc(:,cnt) = Zind(:,cnt); %#ok<AGROW>
        cnt=cnt+1;
    end
end
Z = 1./(sum(1./ZindCalc,2));
[~,min_inx] = min(abs(Z));
close(wbh)
clear aa

% Extract field variable output at frequency of impedance minimum
wbh=waitbar(0,'Extracting Output Data at Impedance Minimum...');
eofflag = 0;

if var1==1
    RawUData=zeros(Unum_nodes,7);
end
if var2==1 && var3==1
    RawSData=zeros(num_elem*elem_nodes,5);
elseif var2==1 || var3==1
    RawSData=zeros(num_elem*elem_nodes,3);
end

finx = 1;
fseek(fid,startline,'bof');
while eofflag == 0
    currentline = fgetl(fid);
    if currentline == -1
        eofflag = 1;
    elseif strcmp(currentline,flagline1,length(flagline1))==1
        if finx == min_inx
            % The following will execute if 'PHU' displacement output was
            % requested
            if var1==1
                eovflag=0;
                while nodeinx <= Unum_nodes
                    currentline = fgetl(fid);
                    if currentline == -1
                        eofflag = 1;
                    elseif
                        strcmp(currentline,flagline18,length(flagline18))==1
                            fgetl(fid);
                            nodeinx=1;
                            DataTemp=zeros(Unum_nodes,7);

```

```

        while nodeinx <= Unum_nodes
            tempread=fscanf(fid,format11,skip1);
            DataTemp(nodeinx,:)=[tempread(1) tempread(2)
tempread(6) tempread(3) tempread(7) tempread(4) tempread(8)];
            nodeinx=nodeinx+1;
        end
    end
end
RawUData=sortrows(DataTemp);
clear tempread DataTemp
end

% The following will execute if 'PHS13' and/or 'PHS23'
shear stress
% output was requested
if var2==1 || var3==1
    nodeinx=1;
    if var2==1 && var3==1
        DataTemp=zeros(num_elem*elem_nodes,5);
    else
        DataTemp=zeros(num_elem*elem_nodes,3);
    end

    while nodeinx <= num_elem*elem_nodes
        currentline = fgetl(fid);
        if currentline == -1
            eofflag = 1;
        elseif
strncmp(currentline,flagline19,length(flagline19))==1
            fgetl(fid);
            while nodeinx <= num_elem*elem_nodes
                if var2==1 && var3==1
                    tempread=fscanf(fid,format2,skip2);
                    DataTemp(nodeinx,:)=[tempread(2)
tempread(3) tempread(7) tempread(4) tempread(8)];
                else
                    tempread=fscanf(fid,format10,skip3);
                    DataTemp(nodeinx,:)=[tempread(2)
tempread(3) tempread(6)];
                end
                nodeinx=nodeinx+1;
            end
        end
    end
end
RawSData=sortrows(DataTemp);
clear tempread DataTemp
end

end
finx=finx+1;
end
end
close(wbh)
fclose(fid);
end

```

```

%% Extract Data at All Frequencies
% Extract the requested output variable data from the tables in the
% .dat file for all frequencies.
%%%%%%%%%%%%%%%%%%%%%%%%%%%%%%%%%%%%%%%%%%%%%%%%%%%%%%%%%%%%%%%%%%%%%%%%
if Zmin_option ~= 1
    wbh=waitbar(0,'Extracting Output Data from .dat File...');
    finx=1;
    prevline=0;
    eofflag = 0;
    FData=zeros(numinc,1);

    if var1==1
        RawUData=zeros(Unum_nodes,7,numinc);
    end
    if var2==1 && var3==1
        RawSData=zeros(num_elem*elem_nodes,5,numinc);
    elseif var2==1 || var3==1
        RawSData=zeros(num_elem*elem_nodes,3,numinc);
    end
    if var4==1
        Qdata=zeros(numinc,num_act*2);
    end

    while eofflag == 0
        currentline = fgetl(fid);
        if currentline == -1
            eofflag = 1;
        elseif strcmp(currentline,flagline1,length(flagline1))==1
            fseek(fid,prevline,'bof');
            tempread=fscanf(fid,format1,2);
            FData(finx)=tempread(2);
            clear tempread

            % The following will execute if 'PHU' displacement output was
            % requested
            if var1==1
                nodeinx=1;
                DataTemp=zeros(Unum_nodes,7);

                while strcmp(currentline,flagline21,length(flagline21))==0
                    currentline=fgetl(fid);
                end
                while strcmp(currentline,flagline18,length(flagline18))==0
                    currentline=fgetl(fid);
                end
                currentline=fgetl(fid);
                currentline=fgetl(fid);
                while nodeinx <= Unum_nodes
                    tempread=fscanf(fid,format11,skip1);
                    DataTemp(nodeinx,:)= [tempread(1) tempread(2) tempread(6)
tempread(3) tempread(7) tempread(4) tempread(8)];
                    nodeinx=nodeinx+1;
                end
                RawUData(:, :, finx)=sortrows(DataTemp);
                clear tempread DataTemp
            end
        end
    end
end

```

```

end

% The following will execute if 'PHS13' and/or 'PHS23' shear
stress
% output was requested
if var2==1 || var3==1
    nodeinx=1;
    if var2==1 && var3==1
        DataTemp=zeros(num_elem*elem_nodes,5);
    else
        DataTemp=zeros(num_elem*elem_nodes,3);
    end

    while strcmp(currentline,flagline22,length(flagline22))==0
        currentline=fgetl(fid);
    end
    while strcmp(currentline,flagline19,length(flagline19))==0
        currentline=fgetl(fid);
    end
    currentline=fgetl(fid);
    currentline=fgetl(fid);
    while nodeinx <= num_elem*elem_nodes
        if var2==1 && var3==1
            tempread=fscanf(fid,format2,skip2);
            DataTemp(nodeinx,:)=[tempread(2) tempread(3)
tempread(7) tempread(4) tempread(8)];
        else
            tempread=fscanf(fid,format10,skip3);
            DataTemp(nodeinx,:)=[tempread(2) tempread(3)
tempread(6)];
        end
        nodeinx=nodeinx+1;
    end
    RawSData(:, :, finx)=sortrows(DataTemp);
    clear tempread DataTemp
end

% The following will execute if 'PHCHG' charge output
was
% requested
if var4==1
    ai=1;
    while ai <= num_act
        while
strcmp(currentline,flagline20,length(flagline20))==0
            currentline=fgetl(fid);
        end
        while
strcmp(currentline,flagline17,length(flagline17))==0
            currentline=fgetl(fid);
        end
        currentline=fgetl(fid);
        currentline=fgetl(fid);
        prevline2=ftell(fid);
        currentline=fgetl(fid);
        if strcmp(currentline,flagline13,length(flagline13))==0

```

```

        fseek(fid,prevline2,'bof');
        tempread=fscanf(fid,format9,skip4);
        Qdata(finx,(ai-1)*2+1:ai*2)=[tempread(2)
tempread(4)];

        end
        ai=ai+1;
    end
    clear tempread
end

waitbar(finx/numinc,wbh)

    finx=finx+1;
end
prevline=ftell(fid);
end
close(wbh)
fclose(fid);
end

%% Calculate Impedance Values from Charge Data
% Rewrite charge magnitude and phase for each actuator into complex charge
% values, and calculate the complex impedance for each actuator. The net
% complex impedance of the entire actuator system is calculated as a
% combination of the individual impedances.
if var4==1 && Zmin_option~=1
    Qmag = Qdata(:,1:2:num_act*2-1);
    Qphase = Qdata(:,2:2:num_act*2);
    Q = Qmag.*exp(1i*Qphase/180*pi);

    Zind=zeros(length(FData),num_act);
    cnt=1;
    for ai=1:num_act
        if Q(:,ai) == zeros(length(FData),1)
            Zind(:,ai) = NaN*ones(length(FData),1);
        else
            Zind(:,ai) = V./((2*pi*FData).*Q(:,ai));
            ZindCalc(:,cnt) = Zind(:,ai); %#ok<AGROW>
            cnt=cnt+1;
        end
    end
    Z = 1./(sum(1./ZindCalc,2));
end

%% Rewrite Field Value Arrays in Terms of Complex Values
% Rewrite the output variable data from separate magnitude and phase columns
to
% single complex value columns.
%%%%%%%%%%%%%%%%%%%%%%%%%%%%%%%%%%%%%%%%%%%%%%%%%%%%%%%%%%%%%%%%%%%%%%%%%%%%%%
if var1==1
    if Zmin_option == 1
        RawUDataComp(:,1) = RawUData(:,1);
        RawUDataComp(:,2) = RawUData(:,2).*exp(1i*RawUData(:,3)/180*pi);
        RawUDataComp(:,3) = RawUData(:,4).*exp(1i*RawUData(:,5)/180*pi);
        RawUDataComp(:,4) = RawUData(:,6).*exp(1i*RawUData(:,7)/180*pi);
    else

```

```

        RawUDataComp(:,1,:) = RawUData(:,1,:);
        RawUDataComp(:,2,:) =
RawUData(:,2,:).*exp(1i*RawUData(:,3,:)/180*pi);
        RawUDataComp(:,3,:) =
RawUData(:,4,:).*exp(1i*RawUData(:,5,:)/180*pi);
        RawUDataComp(:,4,:) =
RawUData(:,6,:).*exp(1i*RawUData(:,7,:)/180*pi);
    end
    clear RawUData
end

if var2==1 || var3==1
    if Zmin_option == 1
        RawSDataComp(:,1) = RawSData(:,1);
        RawSDataComp(:,2) = RawSData(:,2).*exp(1i*RawSData(:,3)/180*pi);
        if var2==1 && var3==1
            RawSDataComp(:,3) = RawSData(:,4).*exp(1i*RawSData(:,5)/180*pi);
            RawSDataComp(:,4) = sqrt(RawSDataComp(:,2).^2 +
RawSDataComp(:,3).^2);
        end
    else
        RawSDataComp(:,1,:) = RawSData(:,1,:);
        RawSDataComp(:,2,:) =
RawSData(:,2,:).*exp(1i*RawSData(:,3,:)/180*pi);
        if var2==1 && var3==1
            RawSDataComp(:,3,:) =
RawSData(:,4,:).*exp(1i*RawSData(:,5,:)/180*pi);
            RawSDataComp(:,4,:) = sqrt(RawSDataComp(:,2,:).^2 +
RawSDataComp(:,3,:).^2);
        end
    end
    clear RawSData
end

%% Average at Unique Nodes
% Average complex output variable values at each unique nodes. Since nodes
% are shared by up to 4 adjacent elements, multiple output values will
% exist for various nodes. These values may be different from one another
% due to inaccuracies in extrapolation from the integration point(s).
%%%%%%%%%%%%%%%%%%%%%%%%%%%%%%%%%%%%%%%%%%%%%%%%%%%%%%%%%%%%%%%%%%%%%%%%
if var1==1
    if Zmin_option == 1
        RawUDataComp(:,1)=RawUDataComp(:,1) - Uglobal_num;
        uniq_nodes=unique(RawUDataComp(:,1));
        SortedUData=zeros(length(uniq_nodes),4);
        wbh=waitbar(0,['Averaging at Unique Nodes in Set ' Uset '']);
        for uni=1:length(uniq_nodes)
            node_inx=find(squeeze(RawUDataComp(:,1))==uniq_nodes(uni));
            if length(node_inx) == 1
                SortedUData(uni,:)=RawUDataComp(node_inx,:);
            else
                SortedUData(uni,:)=mean(squeeze(RawUDataComp(node_inx,:)),1);
            end
        end
        close(wbh)
        DispData=SortedUData;
    end
end

```



```

else
    RawUDDataComp(:,1,:)=RawUDDataComp(:,1,:) - Uglobal_num;
    uniq_nodes=unique(RawUDDataComp(:,1,1));
    SortedUDData=zeros(length(uniq_nodes),4,numinc);
    wbh=waitbar(0,['Averaging at Unique Nodes in Set "' Uset "'"]);
    for uni=1:length(uniq_nodes)
        node_inx=find(squeeze(RawUDDataComp(:,1,1))==uniq_nodes(uni));
        if length(node_inx) == 1
            SortedUDData(uni,,:)=RawUDDataComp(node_inx,,:);
        else
            SortedUDData(uni,,:)=mean(squeeze(RawUDDataComp(node_inx,,:),1));
        end
    end
    close(wbh)
    DispData=SortedUDData;
end
clear RawUDDataComp SortedUDData
end

if var2==1 || var3==1
    if Zmin_option == 1
        RawSDataComp(:,1)=RawSDataComp(:,1) - Sglobal_num;
        uniq_nodes=unique(RawSDataComp(:,1));
        SortedSData=zeros(length(uniq_nodes),4);
        wbh=waitbar(0,['Averaging at Unique Nodes in Set "' Sset "'"]);
        for uni=1:length(uniq_nodes)
            node_inx=find(squeeze(RawSDataComp(:,1))==uniq_nodes(uni));
            if length(node_inx) == 1
                SortedSData(uni,:)=RawSDataComp(node_inx,:);
            else
                SortedSData(uni,:)=mean(squeeze(RawSDataComp(node_inx,:),1));
            end
        end
        close(wbh)
    else
        RawSDataComp(:,1,:)=RawSDataComp(:,1,:) - Sglobal_num;
        uniq_nodes=unique(RawSDataComp(:,1,1));
        SortedSData=zeros(length(uniq_nodes),4,numinc);
        wbh=waitbar(0,['Averaging at Unique Nodes in Set "' Sset "'"]);
        for uni=1:length(uniq_nodes)
            node_inx=find(squeeze(RawSDataComp(:,1,1))==uniq_nodes(uni));
            if length(node_inx) == 1
                SortedSData(uni,,:)=RawSDataComp(node_inx,,:);
            else
                SortedSData(uni,,:)=mean(squeeze(RawSDataComp(node_inx,,:),1));
            end
        end
        close(wbh)
    end
    clear RawSDataComp
end

%% Remove Nodes not in Specified Node Set
% Remove any nodal values that are not part of the specified node set.

```

```

% Since stress is an element value, nodal output for nodes contained in the
% element set but not the node set exist in the extracted stress data.
%%%%%%%%%%%%%%%%%%%%%%%%%%%%%%%%%%%%%%%%%%%%%%%%%%%%%%%%%%%%%%%%%%%%%%%%
if var1==1
    [~, ia, cc] = intersect(UPartNodes(:,1), USetNodes);
    USetNodeCoords(:,1) = USetNodes;
    USetNodeCoords(:,2:4) = UPartNodes(ia,2:4);
    clear aa cc
end

if var2==1 || var3==1
    if Zmin_option == 1
        [~, ia, cc] = intersect(squeeze(SortedSData(:,1)), SSetNodes);
        StressData = SortedSData(ia,:);
        clear aa cc
    else
        [~, ia, cc] = intersect(squeeze(SortedSData(:,1,1)), SSetNodes);
        StressData = SortedSData(ia,,:);
        clear aa cc
    end
    [~, ia, cc] = intersect(SPartNodes(:,1), SSetNodes);
    SSetNodeCoords(:,1) = SSetNodes;
    SSetNodeCoords(:,2:4) = SPartNodes(ia,2:4);
    clear SortedSData aa cc
end

%% Rearrange Stresses in Terms of X-Y Location
% For simple plates in which the nodes exist on a rectangular mesh, the
% output can be sorted x and y location. If a rectangular mesh is not used
% for the specified set, the this step is skipped.
%%%%%%%%%%%%%%%%%%%%%%%%%%%%%%%%%%%%%%%%%%%%%%%%%%%%%%%%%%%%%%%%%%%%%%%%
if var1==1 && rectmesh_option == 1 && strcmp(Uset,Sset,max([length(Uset)
length(Sset)])) == 1
    xvals=sort(unique(USetNodeCoords(:,2)));
    yvals=sort(unique(USetNodeCoords(:,3)));

    U1_xy=zeros(length(xvals),length(yvals),numinc);
    U2_xy=zeros(length(xvals),length(yvals),numinc);
    U3_xy=zeros(length(xvals),length(yvals),numinc);

    wbh=waitbar(0,'Sorting Stresses by Location');
    if Zmin_option == 1
        for ni=1:size(USetNodeCoords,1)
            pos=USetNodeCoords(ni,2:3);
            xnum=find(xvals == pos(1));
            ynum=find(yvals == pos(2));

            U1_xy(xnum,ynum,:) = squeeze(DispData(ni,2));
            U2_xy(xnum,ynum,:) = squeeze(DispData(ni,3));
            U3_xy(xnum,ynum,:) = squeeze(DispData(ni,4));
        end
    else
        for ni=1:size(USetNodeCoords,1)
            pos=USetNodeCoords(ni,2:3);
            xnum=find(xvals == pos(1));
            ynum=find(yvals == pos(2));

```

```

        U1_xy(xnum, ynum, :) = squeeze(DispData(ni, 2, :));
        U2_xy(xnum, ynum, :) = squeeze(DispData(ni, 3, :));
        U3_xy(xnum, ynum, :) = squeeze(DispData(ni, 4, :));
    end
end
close(wbh)
end

if (var2==1 || var3==1) && rectmesh_option == 1
    xvals=sort(unique(SSetNodeCoords(:,2)));
    yvals=sort(unique(SSetNodeCoords(:,3)));

    S13_xy=zeros(length(xvals),length(yvals),numinc);
    S23_xy=zeros(length(xvals),length(yvals),numinc);
    Smag_xy=zeros(length(xvals),length(yvals),numinc);

    wbh=waitbar(0, 'Sorting Stresses by Location');
    if Zmin_option == 1
        for ni=1:size(SSetNodeCoords,1)
            pos=SSetNodeCoords(ni,2:3);
            xnum=find(xvals == pos(1));
            ynum=find(yvals == pos(2));

            S13_xy(xnum, ynum, :) = squeeze(StressData(ni,2));
            S23_xy(xnum, ynum, :) = squeeze(StressData(ni,3));
            Smag_xy(xnum, ynum, :) = squeeze(StressData(ni,4));
        end
    else
        for ni=1:size(SSetNodeCoords,1)
            pos=SSetNodeCoords(ni,2:3);
            xnum=find(xvals == pos(1));
            ynum=find(yvals == pos(2));

            S13_xy(xnum, ynum, :) = squeeze(StressData(ni,2,:));
            S23_xy(xnum, ynum, :) = squeeze(StressData(ni,3,:));
            Smag_xy(xnum, ynum, :) = squeeze(StressData(ni,4,:));
        end
    end
    close(wbh)
end

%% Average Shear Stress Values over Set when at Local Maximum
% Calculate average shear stress values over the interface, for each node
% when the stress field is at a maximum locally.
%%%%%%%%%%%%%%%%%%%%%%%%%%%%%%%%%%%%%%%%%%%%%%%%%%%%%%%%%%%%%%%%%%%%%%%%
if var2==1 || var3==1
    if Zmin_option == 1
        S13_avg = mean(squeeze(abs(StressData(:,2))),1).';
        S23_avg = mean(squeeze(abs(StressData(:,3))),1).';
        Smag_avg = mean(squeeze(abs(StressData(:,4))),1).';
    else
        S13_avg = mean(squeeze(abs(StressData(:,2,:))),1).';
        S23_avg = mean(squeeze(abs(StressData(:,3,:))),1).';
        Smag_avg = mean(squeeze(abs(StressData(:,4,:))),1).';
    end
end

```

```

        end
    end

    %% Save Data to .mat Files
    % Save extracted and sorted data to .mat file named after .dat file name.
    %%%%%%%%%%%%%%%%%%%%%%%%%%%%%%%%%%%%%%%%%%%%%%%%%%%%%%%%%%%%%%%%%%%%%%%%%
    wbh=waitbar(0,'Saving Data to File');
    cd(savefolder)
    save(['FOutputData_' datfilename '.mat'],'FData');

    if var1==1
        UNodeData=struct('Headings',[ 'Node
Numbers,x,y,z'],'Data',USetNodeCoords); %#ok<*NBRAK,*NASGU>
        if rectmesh_option == 1
            UData=struct('Headings',[ 'Node Numbers,U1,U2,U3'],'Data',DispData,
...
'SortedU1',U1_xy,'SortedU2',U2_xy,'SortedU3',U3_xy,'SortedXYcoords',[xvals
yvals]);
        else
            UData=struct('Headings',[ 'Node Numbers,U1,U2,U3'],'Data',DispData);
        end
        save(['UOutputData_' datfilename '.mat'],'UNodeData','UData');
    end

    if var2==1 && var3==1
        SNodeData=struct('Headings',[ 'Node
Numbers,x,y,z'],'Data',SSetNodeCoords);
        if rectmesh_option == 1
            SData=struct('Headings',[ 'Node
Numbers,S13,S23,Smag'],'Data',StressData, ...
'SortedS13',S13_xy,'SortedS23',S23_xy,'SortedSmag',Smag_xy,'SortedXYcoords',[
xvals yvals]);
        else
            SData=struct('Headings',[ 'Node
Numbers,S13,S23,Smag'],'Data',StressData);
        end
        SavgData=struct('Headings',[ 'S13 avg,S23 avg,Smag avg'],'Data',[S13_avg
S23_avg Smag_avg]);
        save(['SOutputData_' datfilename '.mat'],'SNodeData','SData','SavgData');
    elseif var2==1
        SNodeData=struct('Headings',[ 'Node
Numbers,x,y,z'],'Data',SSetNodeCoords);
        if rectmesh_option == 1
            SData=struct('Headings',[ 'Node
Numbers,S13'],'Data',StressData,'SortedS13',S13_xy,'SortedXYcoords',[xvals
yvals]);
        else
            SData=struct('Headings',[ 'Node Numbers,S13'],'Data',StressData);
        end
        SavgData=struct('Headings',[ 'S13 avg'],'Data',S13_avg);
        save(['SOutputData_' datfilename '.mat'],'SNodeData','SData','SavgData');
    elseif var3==1
        SNodeData=struct('Headings',[ 'Node
Numbers,x,y,z'],'Data',SSetNodeCoords);

```

```

    if rectmesh_option == 1
        SData=struct('Headings',[ 'Node
Numbers,S23'], 'Data',StressData,'SortedS23',S23_xy,'SortedXYcoords',[xvals
yvals]);
    else
        SData=struct('Headings',[ 'Node Numbers,S23'], 'Data',StressData);
    end
    SavgData=struct('Headings',[ 'S23 avg'], 'Data',S23_avg);
    save(['SOutputData_' datfilename '.mat'],'SNodeData','SData','SavgData');
end

if var4==1
    ZData=struct('Individual_Impedance_Data',Zind,'System_Impedance_Data',Z);
    save(['ZOutputData_' datfilename '.mat'],'ZData');
end

close(wbh)
cd(OldFolder)

```

B.3 FEspeccimen_analysis_initial.m

This code calls the previous two functions, datFileReader_v5_pt1.m and datFileReader_v5_pt2.m to extract and organize the appropriate information from the .dat file generated by ABAQUS.

```

clear all
close all
clc

%%%%%%%%%%%%%%%%%%%%%%%%%%%%%%%%%%%%%%%%%%%%%%%%%%%%%%%%%%%%%%%%%%%%%%%%%%%%%%
%%%%%%%%%%%%%%%%%%%%%%%%%%%%%%%%%%%%%%%%%%%%%%%%%%%%%%%%%%%%%%%%%%%%%%%%%%%%%%
% Variable Definitions:
%-----
% filelist:      {datfolder, datfilename, inpfolder, inpfilename, savefolder}
% outvarlist:    [var1, var2, var3, var4]
% setlist:       {Uset, Sset}
% optlist:       [Zmin_option, rectmesh_option]
% elem_nodes:    elem_nodes
% num_act:       num_act
% V:             V
%-----
% datfilename:   .dat file name (omit file extension)
% inpfilename:   .inp file name (omit file extension)
% datfolder:     folder in which .dat file exists
% inpfolder:     folder in which .inp file exists
% savefolder:    folder to save .mat file with data
% var1:          'PHU' displacement - '1' if requested
% var2:          'PHS13' S13 stress - '1' if requested
% var3:          'PHS23' S23 stress - '1' if requested
% var4:          'PHCHG' charge - '1' if requested

```

```

% Uset:          name of set in model for which displacement values were
requested
% Sset:          name of set in model for which stress values were
requested
% num_act:       number of actuators for which charge output was requested
% V:            voltage applied to actuators
% elem_nodes:    number of nodes per element
% Zmin_option:   set to '1' if field output is only desired at impedance
minimum
% rectmesh_option: set to '1' if rectangular mesh is used for specified
% set, and output sorted by x-y location is desired

%% Input Parameters
datfolder = '/gpfs/home/cjb286/scratch/BBPhasingFE_Data';
inpfolder = '/gpfs/home/cjb286/scratch/BBPhasing_Inp_Files';
savefolder = '/gpfs/home/cjb286/scratch/BBPhasingFE_Data';

prefix = 'BBconfig2_250';
% suffix =
{'impedance_11','impedance_22','impedance_33','impedance_44','impedance_55','i
impedance_66','impedance_77','impedance_88', ...
%
'impedance_12','impedance_13','impedance_14','impedance_15','impedance_16','i
mpedance_17','impedance_18', ...
%
'impedance_23','impedance_24','impedance_25','impedance_26','impedance_27','i
mpedance_28', ...
%
'impedance_34','impedance_35','impedance_36','impedance_37','impedance_38',
...
%      'impedance_45','impedance_46','impedance_47','impedance_48', ...
%      'impedance_56','impedance_57','impedance_58', ...
%      'impedance_67','impedance_68', ...
%      'impedance_78'};
suffix =
{'impedance_57','impedance_58','impedance_67','impedance_68','impedance_78'};
file_prefix = cell(length(suffix),1);
for fsi = 1:length(suffix)
    file_prefix{fsi} = [prefix '_' suffix{fsi}];
end

numfinc = 4;
outvarlist = [0, 1, 1, 1];
setlist = {'','INTERFACE'};
optlist = [0, 0];
elem_nodes = 4;
num_act = 8;
V = 100;

%% Extract Data from Files
OldFolder=cd;
fileslist = {datfolder, [file_prefix{1} '_f1'], inpfolder, [file_prefix{1}
'_f1'], savefolder};
[ModelNodes,Unum_nodes,Snum_nodes,USetNodes,SSetNodes,num_elem] =
datFileReader_v5onepart_pt1(fileslist, outvarlist, setlist);
cd(OldFolder)

```

```

maxiter = numfinc*length(file_prefix);
wbh = waitbar(0, 'Data Extraction Progress:');
for phi = 1:length(file_prefix)
    for fli = 1:numfinc
        inpfilename = [file_prefix{phi} '_f' num2str(fli)];
        datfilename = [file_prefix{phi} '_f' num2str(fli)];
        filelist = {datfolder, datfilename, inpfolder, inpfilename,
savefolder};

        datFileReader_v5onepart_pt2(filelist, outvarlist, setlist, optlist,
elem_nodes, num_act, V, ModelNodes, Unum_nodes, USetNodes, SSetNodes,
num_elem);

        iter = (phi-1)*numfinc + fli;
        waitbar(iter/maxiter,wbh)
    end
end
close(wbh)
cd(OldFolder)

```

B.4 FEspecimen_analysis_phasing.m

This code accesses and analyzes the data extracted from the ABAQUS .dat file output.

```

clear all
close all
clear memory
clc

%% File Parameters
numfinc=4;
actN = 8;
selectphvec = [1 2 11 16 21 24 26 27];

prefix = 'BBconfig3_250';
suffix =
{'impedance_11','impedance_22','impedance_33','impedance_44','impedance_55','i
impedance_66','impedance_77','impedance_88', ...

'impedance_12','impedance_13','impedance_14','impedance_15','impedance_16','i
mpedance_17','impedance_18', ...

'impedance_23','impedance_24','impedance_25','impedance_26','impedance_27','i
mpedance_28', ...

'impedance_34','impedance_35','impedance_36','impedance_37','impedance_38',
...
'impedance_45','impedance_46','impedance_47','impedance_48', ...
'impedance_56','impedance_57','impedance_58', ...
'impedance_67','impedance_68', ...

```

```

    'impedance_78'};
conds = cell(length(suffix),1);
for fsi = 1:length(suffix)
    conds{fsi} = [prefix '_' suffix{fsi}];
end

savefolder = 'G:\BRAIT Analysis\Boeing Phased Result Figures';

%% Determine Phasing Combinations
n = actN/2;
combos = combntns(2:actN,n);
phvec = zeros(size(combos,1),actN);
for phi = 1:size(combos,1)
    phvec(phi,combos(phi,:)) = 180;
end
phvec = unique(phvec,'rows');
wbh = waitbar(0,'Checking for Symmetry...');
for phi = 1:size(phvec,1)
    temp = [phvec(phi,n+1:actN) phvec(phi,1:n)];
    syminx = find(ismember(phvec,temp,'rows'));
    if numel(syminx)>0 && syminx~=phi
        phvec(syminx,:) = NaN*ones(1,actN);
    end

    if mod(phi,floor(size(phvec,1)/200)) == 0
        waitbar(phi/size(phvec,1),wbh)
    end
end
close(wbh)
NaNinx = isnan(phvec);
NaNrows = find(ismember(NaNinx,ones(1,actN),'rows') == 0);
phvec = [zeros(1,actN); phvec(NaNrows,:)];

%% Import Data from MAT Files
OldFolder=cd;
wbh=waitbar(0,'Loading Data...');
cd('G:\BRAIT Analysis')
maxiter=length(conds)*numfinc;
iter=1;
for ci=1:length(conds)
    freq = [];
    tempSData = [];
    tempZInd = [];
    tempZnet = [];

    for fli=1:numfinc
        load(['SOutputData_' conds{ci} '_f' num2str(fli) '.mat']);
        load(['ZOutputData_' conds{ci} '_f' num2str(fli) '.mat']);
        load(['FOutputData_' conds{ci} '_f' num2str(fli) '.mat']);

        if ci==1 && fli==1
            NodeData = SNodeData.Data;
        end

        freq = [freq; FData(find(FData))]; %#ok<AGROW>
    end
end

```



```

tempSData = cat(3,tempSData,SData.Data);
tempZInd = [tempZInd; ZData.Individual_Impedance_Data]; %#ok<AGROW>

waitbar(iter/maxiter,wbh)
iter=iter+1;
end
clear SData SNodeData ZData FData

if ci==1
    SDataMat =
zeros(size(tempSData,1),size(tempSData,2),size(tempSData,3),length(conds));
    ZInd = zeros(size(tempZInd,1),size(tempZInd,2),length(conds));
end

SDataMat(:,:,ci) = tempSData;
ZInd(:,:,ci) = tempZInd;
clear -regexp '^temp'

end
close(wbh)
cd(OldFolder)

SData = SDataMat;
clear SDataMat

fnum=length(freq);
freq=freq/1000;

%% Predict System Impedance
crossmat = zeros(actN);
sensormat = zeros(actN);
for ii = 1:actN
    for jj = 1:actN
        if ii==jj
            crossmat(ii,jj) = ii;
            sensormat(ii,jj) = ii;
        elseif jj > ii
            crossmat(ii,jj) = sum((actN-ii+1):actN) + jj-ii;
            sensormat(ii,jj) = jj;
        elseif jj < ii
            crossmat(ii,jj) = sum((actN-jj+1):actN) + ii-jj;
            sensormat(ii,jj) = ii;
        end
    end
end

% crossmat = [1 9 10 11 12 13 14 15; 9 2 16 17 18 19 20 21; 10 16 3 22 23 24
25 26; 11 17 22 4 27 28 29 30; 12 18 23 27 5 31 32 33; 13 19 24 28 31 6 34
35; 14 20 25 29 32 34 7 36; 15 21 26 30 33 35 36 8];
% sensormat = [1 2 3 4 5 6 7 8; 2 2 3 4 5 6 7 8; 3 3 3 4 5 6 7 8; 4 4 4 4 5 6
7 8; 5 5 5 5 5 6 7 8; 6 6 6 6 6 6 7 8; 7 7 7 7 7 7 7 8; 8 8 8 8 8 8 8 8];

ZSys = zeros(fnum,size(phvec,1));
ZSysP = zeros(fnum,size(phvec,1));
wbh = waitbar(0,'Calculating Phased Impedance...');
for phi = 1:size(phvec,1)

```

```

Vphase = phvec(phi,:);

ZIndph = cell(actN);
for ii = 1:actN
    for jj = 1:actN
        ZIndph{ii,jj} =
ZInd(:,sensormat(ii,jj),crossmat(ii,jj))*exp(1i*Vphase(ii)/180*pi);
    end
end

ZSysInd = zeros(size(ZInd,1),size(ZInd,2));
for ii = 1:size(ZInd,2)
    for jj = 1:size(ZInd,2)
        ZSysInd(:,ii) = ZSysInd(:,ii) + 1./ZIndph{jj,ii};
    end
end
ZSysInd = 1./ZSysInd;

for ii = 1:size(ZInd,2)
    ZSysInd(:,ii) = ZSysInd(:,ii)*exp(1i*Vphase(ii)/180*pi);
end

ZSys(:,phi) = abs(1./sum(1./ZSysInd,2));
ZSysP(:,phi) = angle(1./sum(1./ZSysInd,2))/pi*180;

waitbar(phi/size(phvec,1),wbh)
end
close(wbh)

%% Calculate Stress Fields for each Frequency and Phasing Combination
SSysTemp = zeros(size(SData,1),2,fnum,size(phvec,1));
wbh = waitbar(0,'Calculating Phased Stress Fields...');
for phi = 1:size(phvec,1)
    for ii = 1:actN
        SSysTemp(:, :, :, phi) = SSysTemp(:, :, :, phi) +
squeeze(SData(:,2:3, :, ii)*exp(1i*phvec(phi,ii)/180*pi));
    end
    waitbar(phi/size(phvec,1),wbh)
end
close(wbh)
SSys = abs(sqrt(squeeze(SSysTemp(:,1, :, :)).^2 +
squeeze(SSysTemp(:,2, :, :)).^2));
clear SSysTemp

%% Analyze Stress Fields for each Frequency and Phasing Combination
meanS = zeros(fnum,size(phvec,1));
maxS = zeros(fnum,size(phvec,1));
wbh = waitbar(0,'Analyzing Phased Stress Fields...');
for phi = 1:size(phvec,1)
    for fi = 1:fnum
        meanS(fi,phi) = mean(SSys(:,fi,phi));
        maxS(fi,phi) = max(SSys(:,fi,phi));
    end
    waitbar(phi/size(phvec,1),wbh)
end

```

```

close(wbh)

meanS_sel = meanS(:,selectphvec);
maxS_sel = maxS(:,selectphvec);

% Analyze Stress Fields at Zmin Frequency for each Phasing Combination
SSys_fmin = zeros(size(SSys,1),size(phvec,1));
meanS_fmin = zeros(1,size(phvec,1));
maxS_fmin = zeros(1,size(phvec,1));
for phi = 1:size(phvec,1)
    [aaa,inx] = min(ZSys(:,phi));
    SSys_fmin(:,phi) = SSys(:,inx,phi);
    meanS_fmin(phi) = mean(SSys(:,inx,phi));
    maxS_fmin(phi) = max(SSys(:,inx,phi));
end
meanS_fmin_sel = meanS_fmin(selectphvec);
maxS_fmin_sel = maxS_fmin(selectphvec);

threshvec = [.75 .80 .85 .90 .95 .99];
legendstr = cell(1,length(threshvec));
for thi = 1:length(threshvec)
    legendstr{thi} = [num2str(threshvec(thi)*100) '% coverage threshold'];
end

N = size(SData,1);
clear SData
covthresh_fmin = zeros(length(threshvec),size(phvec,1));
for phi = 1:size(phvec,1)
    Ssort_fmin = sort(abs(SSys_fmin(:,phi)), 'descend');
    for thi = 1:length(threshvec)
        threshinx = floor(N*threshvec(thi));
        covthresh_fmin(thi,phi) = Ssort_fmin(threshinx);
    end
end
covthresh_fmin_sel = covthresh_fmin(:,selectphvec);

% Analyze Stress Fields at Zmin Frequency for all Phasing Combinations
SSys_fmin_ph = max(SSys_fmin,[],2);
SSys_fmin_selph = max(SSys_fmin(:,selectphvec),[],2);
SSys_fmin_noph = SSys_fmin(:,1);

covthresh_fmin_ph = zeros(length(threshvec),1);
covthresh_fmin_selph = zeros(length(threshvec),1);
covthresh_fmin_noph = zeros(length(threshvec),1);
Ssort_fmin_ph = sort(SSys_fmin_ph, 'descend');
Ssort_fmin_selph = sort(SSys_fmin_selph, 'descend');
Ssort_fmin_noph = sort(SSys_fmin_noph, 'descend');
for thi = 1:length(threshvec)
    threshinx = floor(N*threshvec(thi));
    covthresh_fmin_ph(thi) = Ssort_fmin_ph(threshinx);
    covthresh_fmin_selph(thi) = Ssort_fmin_selph(threshinx);
    covthresh_fmin_noph(thi) = Ssort_fmin_noph(threshinx);
end

meanS_fmin_ph = mean(SSys_fmin_ph);

```

```

maxS_fmin_ph = max(SSys_fmin_ph);

%% Analyze Stress Fields at Each Frequency for all Phasing Combinations
SSys_f_ph = max(SSys,[],3);
SSys_f_selph = max(SSys(:, :, selectphvec), [], 3);

covthresh_f_ph = zeros(length(threshvec),1);
covthresh_f_selph = zeros(length(threshvec),1);
covthresh_f_noph = zeros(length(threshvec),1);
for fi = 1:fnum
    Ssort_f_ph = sort(SSys_f_ph(:,fi), 'descend');
    Ssort_f_selph = sort(SSys_f_selph(:,fi), 'descend');
    Ssort_f_noph = sort(SSys(:,fi,1), 'descend');
    for thi = 1:length(threshvec)
        threshinx = floor(N*threshvec(thi));
        covthresh_f_ph(thi,fi) = Ssort_f_ph(threshinx);
        covthresh_f_selph(thi,fi) = Ssort_f_selph(threshinx);
        covthresh_f_noph(thi,fi) = Ssort_f_noph(threshinx);
    end
end

%% Analyze Stress Fields for Frequency Sweeping with and without Phasing
fsweepnum = 7; % number of frequency sweep points, including Zmin frequency
SSys_fswp_ph_all = zeros(size(SSys,1), fsweepnum, size(phvec,1));
for phi = 1:size(phvec,1)
    for fi = 1:(fsweepnum-1)/2
        [aaa,fz] = min(ZSys(:,phi)); clear aaa
        fsweepinx = fz + (-(fsweepnum-1)/2:(fsweepnum-1)/2);
        SSys_fswp_ph_all(:,fi,phi) = SSys(:,fsweepinx(fi),phi);
    end
end

SSys_fswp_ph = max(max(SSys_fswp_ph_all,[],3), [], 2);
SSys_fswp_selph = max(SSys_fswp_ph_all(:, :, selectphvec), [], 3), [], 2);
SSys_fswp_noph = max(squeeze(SSys_fswp_ph_all(:, :, 1)), [], 2);

covthresh_fswp_ph = zeros(length(threshvec),1);
covthresh_fswp_selph = zeros(length(threshvec),1);
covthresh_fswp_noph = zeros(length(threshvec),1);
Ssort_fswp_ph = sort(SSys_fswp(:,fi), 'descend');
Ssort_fswp_selph = sort(SSys_fswp(:,fi), 'descend');
Ssort_fswp_noph = sort(SSys_fswp(:,fi), 'descend');
for thi = 1:length(threshvec)
    threshinx = floor(N*threshvec(thi));
    covthresh_fswp_ph(thi) = Ssort_fswp_ph(threshinx);
    covthresh_fswp_selph(thi) = Ssort_fswp_selph(threshinx);
    covthresh_fswp_noph(thi) = Ssort_fswp_noph(threshinx);
end

figure(1)
set(gcf, 'Position', [975 225 639 723])
bar(90, [covthresh_fmin_noph(4) covthresh_fmin_selph(4) covthresh_fmin_ph(4)
covthresh_fswp_noph(4) covthresh_fswp_selph(4) covthresh_fswp_ph(4)]*1e-6)
title('Stress Coverage Thresholds at Z_m_i_n for All Phases')
xlabel('Coverage Threshold (%)')
ylabel('Threshold Stress Level (MPa)')

```

```

ylim([0 1.2*max(covthresh_fmin_ph)*1e-6])
legend('No Phasing','Selective Phasing','All Phasing','Freq Sweep & No
Phasing','Freq Sweep & Selective Phasing','Freq Sweep & All Phasing')
saveas(gcf,['Threshold_fswp_allph ' prefix'],'fig')
saveas(gcf,['Threshold_fswp_allph ' prefix'],'png')

%% Plot Results
clc
disp(['Average Stress from Phased Fields at Zmin: '
num2str(meanS_fmin_ph*1e-6) ' MPa'])
disp(' ')
disp(['Peak Stress from Phased Fields at Zmin: ' num2str(maxS_fmin_ph*1e-6)
' MPa'])
disp(' ')

OldFolder = cd;
cd(savefolder)

figure(1)
set(gcf,'Position',[975 225 639 723])
bar(threshvec*100,[covthresh_fmin_noph covthresh_fmin_selph
covthresh_fmin_ph]*1e-6)
title('Stress Coverage Thresholds at Z_m_i_n for All Phases')
xlabel('Coverage Threshold (%)')
ylabel('Threshold Stress Level (MPa)')
ylim([0 1.2*max(covthresh_fmin_ph)*1e-6])
legend('No Phasing','Selective Phasing','All Phasing')
saveas(gcf,['Threshold_fmin_allph ' prefix'],'fig')
saveas(gcf,['Threshold_fmin_allph ' prefix'],'png')

figure(2)
set(gcf,'Position',[454 90 922 859])
subplot 311
plot(freq*1e-3,covthresh_f_ph*1e-6)
title('Stress Coverage Thresholds at Each Frequency for All Phases')
xlabel('Frequency (kHz)')
ylabel('Threshold Stress Level (MPa)')
xlim([min(freq*1e-3) max(freq*1e-3)])
ylim([0 1.2*max(max(covthresh_f_ph*1e-6))])
legend(legendstr,'Location','EastOutside')
subplot 312
plot(freq*1e-3,covthresh_f_selph*1e-6)
title('Stress Coverage Thresholds at Each Frequency for Selective Phases')
xlabel('Frequency (kHz)')
ylabel('Threshold Stress Level (MPa)')
xlim([min(freq*1e-3) max(freq*1e-3)])
ylim([0 1.2*max(max(covthresh_f_ph*1e-6))])
legend(legendstr,'Location','EastOutside')
subplot 313
plot(freq*1e-3,covthresh_f_noph*1e-6)
title('Stress Coverage Thresholds at Each Frequency with No Phasing')
xlabel('Frequency (kHz)')
ylabel('Threshold Stress Level (MPa)')
xlim([min(freq*1e-3) max(freq*1e-3)])
ylim([0 1.2*max(max(covthresh_f_ph*1e-6))])

```

```

legend(legendstr, 'Location', 'EastOutside')
saveas(gcf, ['Threshold_vs_f_allph ' prefix], 'fig')
saveas(gcf, ['Threshold_vs_f_allph ' prefix], 'png')

figure(3)
set(gcf, 'Position', [454 225 1160 573])
plot(1:size(phvec,1), covthresh_fmin*1e-6)
title('Stress Coverage Thresholds at Z_m_i_n vs. Phase')
xlabel('Phasing Combination #')
ylabel('Threshold Stress Level (MPa)')
legend(legendstr, 'Location', 'EastOutside')
xlim([1 size(phvec,1)])
ylim([0 1.2*max(max(covthresh_fmin*1e-6))])
saveas(gcf, ['Threshold_fmin_vs_ph ' prefix], 'fig')
saveas(gcf, ['Threshold_fmin_vs_ph ' prefix], 'png')

figure(4)
set(gcf, 'Position', [454 225 1160 573])
bar(1:size(phvec,1), meanS_fmin*1e-6, 'b')
hold on
bar(selectphvec, meanS_fmin_sel*1e-6, 'r')
title('Average Stress at Z_m_i_n vs. Phase')
xlabel('Phasing Combination #')
ylabel('Average Shear Stress (MPa)')
xlim([0 size(phvec,1)+1])
ylim([0 1.2*max(max(meanS_fmin*1e-6))])
legend('All Phases', 'Select Phases')
saveas(gcf, ['Avg_fmin_vs_ph ' prefix], 'fig')
saveas(gcf, ['Avg_fmin_vs_ph ' prefix], 'png')

figure(5)
set(gcf, 'Position', [454 225 1160 573])
bar(1:size(phvec,1), maxS_fmin*1e-6, 'b')
hold on
bar(selectphvec, maxS_fmin_sel*1e-6, 'r')
title('Peak Stress at Z_m_i_n vs. Phase')
xlabel('Phasing Combination #')
ylabel('Peak Shear Stress (MPa)')
xlim([0 size(phvec,1)+1])
ylim([0 1.2*max(max(maxS_fmin*1e-6))])
legend('All Phases', 'Select Phases')
saveas(gcf, ['Peak_fmin_vs_ph ' prefix], 'fig')
saveas(gcf, ['Peak_fmin_vs_ph ' prefix], 'png')

figure(6)
set(gcf, 'Position', [454 74 967 724])
subplot 211
plot(freq*1e-3, meanS.*1e-6)
title('Average Stress vs. Frequency & Phase')
xlabel('Frequency (kHz)')
ylabel('Average Shear Stress (MPa)')
ylim([0 1.2*max(max(meanS))*1e-6])
subplot 212
plot(freq*1e-3, meanS_sel.*1e-6)
title('Average Stress vs. Frequency & Select Phases')
xlabel('Frequency (kHz)')

```

```

ylabel('Average Shear Stress (MPa)')
ylim([0 1.2*max(max(meanS))*1e-6])
saveas(gcf,['Avg_vs_f-ph ' prefix],'fig')
saveas(gcf,['Avg_vs_f-ph ' prefix],'png')

figure(7)
set(gcf,'Position',[454 74 967 724])
subplot 211
plot(freq*1e-3,maxS.*1e-6)
title('Peak Stress vs. Frequency & Phase')
xlabel('Frequency (kHz)')
ylabel('Peak Shear Stress (MPa)')
ylim([0 1.2*max(max(maxS))*1e-6])
subplot 212
plot(freq*1e-3,maxS_sel.*1e-6)
title('Peak Stress vs. Frequency & Select Phases')
xlabel('Frequency (kHz)')
ylabel('Peak Shear Stress (MPa)')
ylim([0 1.2*max(max(maxS))*1e-6])
saveas(gcf,['Peak_vs_f-ph ' prefix],'fig')
saveas(gcf,['Peak_vs_f-ph ' prefix],'png')

figure(8)
set(gcf,'Position',[454 74 967 724])
subplot 211
plot(freq*1e-3,ZSys)
title('Impedance vs. Frequency & Phase')
xlabel('Frequency (kHz)')
ylabel('Impedance (\Omega)')
ylim([0 1.2*max(max(ZSys))])
subplot 212
plot(freq*1e-3,ZSys(:,selectphvec))
title('Impedance vs. Frequency & Select Phases')
xlabel('Frequency (kHz)')
ylabel('Impedance (\Omega)')
ylim([0 1.2*max(max(ZSys))])
saveas(gcf,['Z_vs_f-ph ' prefix],'fig')
saveas(gcf,['Z_vs_f-ph ' prefix],'png')

%% Prepare Stress Fields for 3D Plotting
rfactor = 200;
rNodeData = [round(rfactor*NodeData(:,2))/rfactor
round(rfactor*NodeData(:,3))/rfactor round(rfactor*NodeData(:,4))/rfactor];
[y,iaY,aaa] = unique(rNodeData(:,2));
[z,iaZ,aaa] = unique(rNodeData(:,3));

x = NaN*ones(length(y),length(z));
Sgrid = NaN*ones(length(y),length(z),length(selectphvec));
Sgrid_phmax = NaN*ones(length(y),length(z));
Sgrid_selphmax = NaN*ones(length(y),length(z));
Sgrid_nophmax = NaN*ones(length(y),length(z));
wbh = waitbar(0,'Determining Airfoil Surface');
maxiter = length(y)*length(z);
iter = 1;
for yi = 1:length(y)

```

```

for zi = 1:length(z)
    yzpos = [y(yi) z(zi)];
    zinx = find(ismember(rNodeData(:,2:3),yzpos,'rows'));
    if numel(zinx) > 1
        x(yi,zi) = mean(rNodeData(zinx,1));
        Sgrid(yi,zi,:) = mean(SSys_fmin(zinx,selectphvec),1);
        Sgrid_phmax(yi,zi) = mean(SSys_fmin_ph(zinx),1);
        Sgrid_selphmax(yi,zi) = mean(SSys_fmin_selph(zinx),1);
        Sgrid_nophmax(yi,zi) = mean(SSys_fmin_noph(zinx),1);
    elseif numel(zinx) == 1
        x(yi,zi) = rNodeData(zinx,1);
        Sgrid(yi,zi,:) = SSys_fmin(zinx,selectphvec);
        Sgrid_phmax(yi,zi) = SSys_fmin_ph(zinx);
        Sgrid_selphmax(yi,zi) = SSys_fmin_selph(zinx);
        Sgrid_nophmax(yi,zi) = SSys_fmin_noph(zinx);
    end

    if mod(iter,floor(maxiter/300)) == 0
        waitbar(iter/maxiter,wbh)
    end
    iter = iter + 1;
end
end
close(wbh)
clear SSys

YIt = min(y):.0005:max(y);
ZIt = min(z):.0005:max(z);
[YI,ZI] = meshgrid(YIt,ZIt);

XI = interp2(z,y,x,ZI,YI);
SgridInt = zeros(size(XI,1),size(XI,2),length(selectphvec));
SgridInt_phmax = zeros(size(XI,1),size(XI,2));
SgridInt_selphmax = zeros(size(XI,1),size(XI,2));
SgridInt_nophmax = zeros(size(XI,1),size(XI,2));
wbh = waitbar(0,'Interpolating Fields for Plotting...');
for fi = 1:length(selectphvec)
    SgridInt(:, :, fi) = interp2(z,y,Sgrid(:, :, fi),ZI,YI);
    waitbar(fi/length(freq),wbh)
end
SgridInt_phmax = interp2(z,y,Sgrid_phmax,ZI,YI);
SgridInt_selphmax = interp2(z,y,Sgrid_selphmax,ZI,YI);
SgridInt_nophmax = interp2(z,y,Sgrid_nophmax,ZI,YI);
close(wbh)
clear Sgrid Sgrid_phmax Sgrid_selphmax Sgrid_nophmax

SgridInt_phmaxThr = 100*ones(size(SgridInt_phmax));
SgridInt_phmaxThr(SgridInt_phmax <= covthresh_fmin_ph(1)) = 25;
SgridInt_phmaxThr(SgridInt_phmax <= covthresh_fmin_ph(2)) = 20;
SgridInt_phmaxThr(SgridInt_phmax <= covthresh_fmin_ph(3)) = 15;
SgridInt_phmaxThr(SgridInt_phmax <= covthresh_fmin_ph(4)) = 10;
SgridInt_phmaxThr(SgridInt_phmax <= covthresh_fmin_ph(5)) = 5;
SgridInt_phmaxThr(SgridInt_phmax <= covthresh_fmin_ph(6)) = 1;
SgridInt_selphmaxThr = 100*ones(size(SgridInt_selphmax));
SgridInt_selphmaxThr(SgridInt_selphmax <= covthresh_fmin_selph(1)) = 25;
SgridInt_selphmaxThr(SgridInt_selphmax <= covthresh_fmin_selph(2)) = 20;

```



```

SgridInt_selphmaxThr(SgridInt_selphmax <= covthresh_fmin_selph(3)) = 15;
SgridInt_selphmaxThr(SgridInt_selphmax <= covthresh_fmin_selph(4)) = 10;
SgridInt_selphmaxThr(SgridInt_selphmax <= covthresh_fmin_selph(5)) = 5;
SgridInt_selphmaxThr(SgridInt_selphmax <= covthresh_fmin_selph(6)) = 1;
SgridInt_nophmaxThr = 100*ones(size(SgridInt_nophmax));
SgridInt_nophmaxThr(SgridInt_nophmax <= covthresh_fmin_noph(1)) = 25;
SgridInt_nophmaxThr(SgridInt_nophmax <= covthresh_fmin_noph(2)) = 20;
SgridInt_nophmaxThr(SgridInt_nophmax <= covthresh_fmin_noph(3)) = 15;
SgridInt_nophmaxThr(SgridInt_nophmax <= covthresh_fmin_noph(4)) = 10;
SgridInt_nophmaxThr(SgridInt_nophmax <= covthresh_fmin_noph(5)) = 5;
SgridInt_nophmaxThr(SgridInt_nophmax <= covthresh_fmin_noph(6)) = 1;

%% Plot Stress Fields on 3D Airfoils for Individual Phases
% close all
% for fi = 1:length(selectphvec)
%     figure(fi)
%     set(gcf,'Position',[654 388 576 420])
%     aa = squeeze(SgridInt(:,:,fi));
%     cmax = 1e6;
%     warp(ZI,YI,XI,aa,jet(cmax))
%     title(['Shear Stress at Z_m_i_n for Phase #' num2str(selectphvec(fi))])
%     axis equal
%     view(-112,48)
%     xlim([-0.6 0])
%     ylim([-0.1 0.1])
%     zlim([0 0.15])
%     set(gca,'XTick',-0.6:0.1:0,'YTick',-0.1:0.05:0.1,'ZTick',0:0.15:0.15)
%     xlabel('Z (m)')
%     ylabel('Y (m)')
%     zlabel('X (m)')
%     colorbar
%     saveas(gcf,['Stress_Field_fmin_SelPhase_1MPaNorm' num2str(fi) ' '
prefix'],'fig')
%     saveas(gcf,['Stress_Field_fmin_SelPhase_1MPaNorm' num2str(fi) ' '
prefix'],'png')
% end
%
% close all
% for fi = 1:length(selectphvec)
%     figure(fi)
%     set(gcf,'Position',[654 388 576 420])
%     aa = squeeze(SgridInt(:,:,fi));
%     cmax = ceil(max(max(SgridInt(:,:,1))));
%     warp(ZI,YI,XI,aa,jet(cmax))
%     title(['Shear Stress at Z_m_i_n for Phase #' num2str(selectphvec(fi))])
%     axis equal
%     view(-112,48)
%     xlim([-0.6 0])
%     ylim([-0.1 0.1])
%     zlim([0 0.15])
%     set(gca,'XTick',-0.6:0.1:0,'YTick',-0.1:0.05:0.1,'ZTick',0:0.15:0.15)
%     xlabel('Z (m)')
%     ylabel('Y (m)')
%     zlabel('X (m)')
%     colorbar
%     saveas(gcf,['Stress_Field_fmin_SelPhase_NoPhaseNorm' num2str(fi) ' '
prefix'],'fig')

```

```

%      saveas(gcf,['Stress_Field_fmin_SelPhase_NoPhaseNorm' num2str(fi) ' '
prefix'],'png')
% end

%% Plot Stress Fields on 3D Airfoils for Sets of Phases
close all
figure(1)
set(gcf,'Position',[654 388 576 420])
aa = SgridInt_phmax;
cmax = 1e6;
warp(ZI,YI,XI,aa,jet(cmax))
title('All Phases')
axis equal
view(-112,48)
xlim([-0.6 0])
ylim([-0.1 0.1])
zlim([0 0.15])
set(gca,'XTick',-0.6:0.1:0,'YTick',-0.1:0.05:0.1,'ZTick',0:0.15:0.15)
xlabel('Z (m)')
ylabel('Y (m)')
zlabel('X (m)')
colorbar
set(gcf,'Renderer','zbuffer')
saveas(gcf,['Max_Stress_Field_fmin_AirfoilPlot1Mpa_allphases ' prefix'],'fig')
saveas(gcf,['Max_Stress_Field_fmin_AirfoilPlot1Mpa_allphases ' prefix'],'png')

figure(2)
set(gcf,'Position',[654 388 576 420])
aa = SgridInt_selphmax;
cmax = 1e6;
warp(ZI,YI,XI,aa,jet(cmax))
title('Select Phases')
axis equal
view(-112,48)
xlim([-0.6 0])
ylim([-0.1 0.1])
zlim([0 0.15])
set(gca,'XTick',-0.6:0.1:0,'YTick',-0.1:0.05:0.1,'ZTick',0:0.15:0.15)
xlabel('Z (m)')
ylabel('Y (m)')
zlabel('X (m)')
colorbar
set(gcf,'Renderer','zbuffer')
saveas(gcf,['Max_Stress_Field_fmin_AirfoilPlot1Mpa_selphases ' prefix'],'fig')
saveas(gcf,['Max_Stress_Field_fmin_AirfoilPlot1Mpa_selphases ' prefix'],'png')

figure(3)
set(gcf,'Position',[654 388 576 420])
aa = SgridInt_nophmax;
cmax = 1e6;
warp(ZI,YI,XI,aa,jet(cmax))
title('No Phasing')
axis equal
view(-112,48)
xlim([-0.6 0])
ylim([-0.1 0.1])

```

```

zlim([0 .15])
set(gca,'XTick',-0.6:0.1:0,'YTick',-0.1:0.05:0.1,'ZTick',0:0.15:0.15)
xlabel('Z (m)')
ylabel('Y (m)')
zlabel('X (m)')
colorbar
set(gcf,'Renderer','zbuffer')
saveas(gcf,['Max_Stress_Field_fmin_AirfoilPlot1Mpa_nophases ' prefix], 'fig')
saveas(gcf,['Max_Stress_Field_fmin_AirfoilPlot1Mpa_nophases ' prefix], 'png')

close all
figure(1)
set(gcf,'Position',[654 388 576 420])
aa = SgridInt_phmax;
cmax = 2e6;
warp(ZI,YI,XI,aa,jet(cmax))
title('All Phases')
axis equal
view(-112,48)
xlim([-0.6 0])
ylim([-0.1 0.1])
zlim([0 .15])
set(gca,'XTick',-0.6:0.1:0,'YTick',-0.1:0.05:0.1,'ZTick',0:0.15:0.15)
xlabel('Z (m)')
ylabel('Y (m)')
zlabel('X (m)')
colorbar
set(gcf,'Renderer','zbuffer')
saveas(gcf,['Max_Stress_Field_fmin_AirfoilPlot2Mpa_allphases ' prefix], 'fig')
saveas(gcf,['Max_Stress_Field_fmin_AirfoilPlot2Mpa_allphases ' prefix], 'png')

figure(2)
set(gcf,'Position',[654 388 576 420])
aa = SgridInt_selphmax;
cmax = 2e6;
warp(ZI,YI,XI,aa,jet(cmax))
title('Select Phases')
axis equal
view(-112,48)
xlim([-0.6 0])
ylim([-0.1 0.1])
zlim([0 .15])
set(gca,'XTick',-0.6:0.1:0,'YTick',-0.1:0.05:0.1,'ZTick',0:0.15:0.15)
xlabel('Z (m)')
ylabel('Y (m)')
zlabel('X (m)')
colorbar
set(gcf,'Renderer','zbuffer')
saveas(gcf,['Max_Stress_Field_fmin_AirfoilPlot2Mpa_selphases ' prefix], 'fig')
saveas(gcf,['Max_Stress_Field_fmin_AirfoilPlot2Mpa_selphases ' prefix], 'png')

figure(3)
set(gcf,'Position',[654 388 576 420])
aa = SgridInt_nophmax;
cmax = 2e6;
warp(ZI,YI,XI,aa,jet(cmax))

```

```

title('No Phasing')
axis equal
view(-112,48)
xlim([-0.6 0])
ylim([-0.1 0.1])
zlim([0 0.15])
set(gca,'XTick',-0.6:0.1:0,'YTick',-0.1:0.05:0.1,'ZTick',0:0.15:0.15)
xlabel('Z (m)')
ylabel('Y (m)')
zlabel('X (m)')
colorbar
set(gcf,'Renderer','zbuffer')
saveas(gcf,['Max_Stress_Field_fmin_AirfoilPlot2Mpa_nophases ' prefix],'fig')
saveas(gcf,['Max_Stress_Field_fmin_AirfoilPlot2Mpa_nophases ' prefix],'png')

close all
figure(1)
set(gcf,'Position',[654 388 576 420])
aa = SgridInt_phmaxThr;
cmax = 100;
warp(ZI,YI,XI,aa,jet(cmax))
title('All Phases')
axis equal
view(-112,48)
xlim([-0.6 0])
ylim([-0.1 0.1])
zlim([0 0.15])
set(gca,'XTick',-0.6:0.1:0,'YTick',-0.1:0.05:0.1,'ZTick',0:0.15:0.15)
xlabel('Z (m)')
ylabel('Y (m)')
zlabel('X (m)')
colorbar
set(gcf,'Renderer','zbuffer')
saveas(gcf,['Max_Stress_Field_fmin_AirfoilPlotThresholds_allphases '
prefix],'fig')
saveas(gcf,['Max_Stress_Field_fmin_AirfoilPlotThresholds_allphases '
prefix],'png')

figure(2)
set(gcf,'Position',[654 388 576 420])
aa = SgridInt_selphmaxThr;
cmax = 100;
warp(ZI,YI,XI,aa,jet(cmax))
title('Select Phases')
axis equal
view(-112,48)
xlim([-0.6 0])
ylim([-0.1 0.1])
zlim([0 0.15])
set(gca,'XTick',-0.6:0.1:0,'YTick',-0.1:0.05:0.1,'ZTick',0:0.15:0.15)
xlabel('Z (m)')
ylabel('Y (m)')
zlabel('X (m)')
colorbar
set(gcf,'Renderer','zbuffer')

```

```

saveas(gcf,['Max_Stress_Field_fmin_AirfoilPlotThresholds_selphases '
prefix'],'fig')
saveas(gcf,['Max_Stress_Field_fmin_AirfoilPlotThresholds_selphases '
prefix'],'png')

figure(3)
set(gcf,'Position',[654 388 576 420])
aa = SgridInt_nophmaxThr;
cmax = 100;
warp(ZI,YI,XI,aa,jet(cmax))
title('No Phasing')
axis equal
view(-112,48)
xlim([-0.6 0])
ylim([-0.1 0.1])
zlim([0 0.15])
set(gca,'XTick',-0.6:0.1:0,'YTick',-0.1:0.05:0.1,'ZTick',0:0.15:0.15)
xlabel('Z (m)')
ylabel('Y (m)')
zlabel('X (m)')
colorbar
set(gcf,'Renderer','zbuffer')
saveas(gcf,['Max_Stress_Field_fmin_AirfoilPlotThresholds_nophases '
prefix'],'fig')
saveas(gcf,['Max_Stress_Field_fmin_AirfoilPlotThresholds_nophases '
prefix'],'png')

```

Appendix C

MATLAB CODES FOR GENETIC ALGORITHM FINITE ELEMENT MODEL PHASING OPTIMIZATION

The following sections provide examples of the MATLAB codes utilized to process the finite element model data from the four-actuator plate used to carry out genetic algorithm optimization of various phasing combinations and methods.

C.1 PhasingGA_Optimization_Master.m

This code calls the other functions listed below to carry out the genetic algorithm optimization.

```
clear all
close all
clc
clear memory

%% Specify Parameters
global N ph_inc fsweepnum Zmin_opt Pnorm_opt Npop StallGenLim

Zmin_opt = 1;
Pnorm_opt = 1;

N = 4;
ph_inc = 15;
nmax = 8;

Npop = 50;
StallGenLim = 4;

%% Specify Parameters
fmin = 30000;
fmax = 60000;
finc = 200;
fseq = fmin:finc:fmax;

if Zmin_opt == 1
    fsrange = fmax-fmin;
    fwidth = 800;
    fsweepnum = fwidth/2/finc;
elseif Zmin_opt == 0
    fsrange = 1000;
end
dfi = fsrange/finc;

savefolder = ['/gpfs/home/cjb286/work/Phasing_Optimization/Optimization
Results/Z' num2str(Zmin_opt) ' P' num2str(Pnorm_opt) ' ' num2str(ph_inc)
'deg'];
```

```

%% Import Data from MAT File
OldFolder='/gpfs/home/cjb286/work/Phasing_Optimization';
cd('/gpfs/home/cjb286/work/Phasing_Optimization/Phasing_FE_Compiled_Data')
load('FData.mat')
cd(OldFolder)

%% Genetic Algorithm Optimization
global f1 f2 SInterp fvec fnum

maxiter = nmax*(floor((length(fseq)-1)/dfi));
ga_iter = 1;
wbh = waitbar(0,'Performing Genetic Algorithm Optimization...');
set(wbh,'Position',[84.8 377.6 288.0 60.0])

for fi = 1:floor((length(fseq)-1)/dfi)
    % Determine frequency sweep limits
    f1 = fseq((fi-1)*dfi+1);
    f2 = fseq(fi*dfi+1);

    % Identify frequency components
    [~,f1inx] = min(abs(fseq-f1));
    [~,f2inx] = min(abs(fseq-f2));
    fvec = f1inx:f2inx;
    fnum = length(fvec);

    % Load appropriate field data

    cd('/gpfs/home/cjb286/work/Phasing_Optimization/Phasing_FE_Compiled_Data')
    temp = load(['SInterpData_f_' num2str(freq(fvec(1))) '.mat']);
    SInterp =
zeros(size(temp.SInterp_f,1),size(temp.SInterp_f,2),size(temp.SInterp_f,3),fnum,size(temp.SInterp_f,5));
    SInterp(:,:,,1,:) = temp.SInterp_f;
    wbh2 = waitbar(1/fnum,'Loading Field Data...');
    for fsubi = 2:fnum
        temp = load(['SInterpData_f_' num2str(freq(fvec(fsubi))) '.mat']);
        SInterp(:,:,,fsubi,:) = temp.SInterp_f;
        waitbar(fsubi/fnum,wbh2)
    end
    clear temp
    close(wbh2)
    cd(OldFolder)

    % Perform optimization
    for ni = 1:nmax

        if ni > 1
            [phfinal{ni},phvec{ni},fval(ni),output{ni},exitflag(ni)] =
PhasingGA_Optimization_Function(ni-1); %#ok<*SAGROW>
        else
            [fval(ni)] = PhasedFieldFunction([]);
            phfinal{ni} = zeros(1,length(N));
            phvec{ni} = 0;
            output{ni} = NaN;
        end
    end
end

```

```

        exitflag(ni) = NaN;
    end

    if mod(ga_iter,floor(maxiter/300))==0 || floor(maxiter/300)==0
        waitbar(ga_iter/maxiter,wbh)
    end
    ga_iter = ga_iter + 1;
    close all

    if Zmin_opt == 1
        cd(savefolder)
        save(['GAoptim_data_f' num2str(f1) '_' num2str(f2) '_N'
num2str(ni)]);
        cd(OldFolder)
    end
end

% Save results for each frequency
if Zmin_opt ~= 1
    cd(savefolder)
    save(['GAoptim_data_f' num2str(f1) '_' num2str(f2)]);
    cd(OldFolder)
end

end
close(wbh)

%% Plot Results
cd(savefolder)
fval_mat = zeros(nmax,floor((length(freq)-1)/dfi));
if Zmin_opt ~= 1
    for ffi = 1:floor((length(freq)-1)/dfi)
        f1 = freq((ffi-1)*dfi+1);
        f2 = freq(ffi*dfi+1);
        load(['GAoptim_data_f' num2str(f1) '_' num2str(f2)]);
        fval_mat(:,ffi) = fval;
    end
else
    f1 = freq(1);
    f2 = freq(end);
    for ni = 1:nmax
        load(['GAoptim_data_f' num2str(f1) '_' num2str(f2) '_N'
num2str(ni)]);
        fval_mat(ni) = fval(ni);
    end
end

fseqplot = freq(1:dfi:dfi*floor((length(freq)-1)/dfi))/1000;
figure(1)
plot(1:nmax,-fval_mat)
xlabel('Number of Phasing Combinations','FontSize',12)
ylabel('90% Coverage Stress Level (MPa)','FontSize',12)
title(['Genetic Algorithm Phasing Optimization for \delta f = '
num2str(fsrage) ' kHz'],'FontSize',13)
ylim([0 1])
saveas(gcf,'results1','fig')

```



```

if length(fseqplot) ~= 1
    figure(2)
    surf(fseqplot,1:nmax,-fval_mat)
    xlabel('Start Frequency (kHz)','FontSize',12)
    ylabel('Number of Phasing Combinations','FontSize',12)
    zlabel('90% Coverage Stress Level','FontSize',12)
    title(['Genetic Algorithm Phasing Optimization for \delta f = '
num2str(fsrage) ' kHz'],'FontSize',13)
    zlim([0 1])
    saveas(gcf,'results2','fig')
end
cd(OldFolder)

```

C.2 PhasingGA_Optimization_Function.m

This code is called by the preceding function and controls the genetic algorithm component of the analysis.

```

function [phfinal,phvec,fval,output,exitflag] =
PhasingGA_Optimization_Function(Nphi)

%% System Parameters
global N ph_inc GAval iter Npop StallGenLim

nphAll = (360/ph_inc)^(N-1);
GAval = [];
iter = 1;

%% Optimization Parameters
fitnessfcn = @PhasedFieldFunction;
nonlcon = []; % @PhasingGA_ConstraintFunction;
nvars = Nphi;
LB(1:nvars) = 2;
UB(1:nvars) = nphAll;

%% Run Optimization
options =
gaoptimset('Display','iter','StallGenLimit',StallGenLim,'PopulationSize',Npop
);
[phvec,fval,exitflag,output] =
ga(fitnessfcn,nvars,[],[],[],[],LB,UB,nonlcon,options);

%% Save Results
inp_vec = [];
for ni = 1:N-1
    inp_vec = cat(2,inp_vec,0:ph_inc:(360-ph_inc));
end
combs = unique(combnk(inp_vec,3),'rows');
AllPerms = [];
for ii = 1:size(combs,1)

```

```

        combperms = perms(combs(ii,:));
        AllPerms = cat(1,AllPerms,combperms);
    end
    phvecAll = zeros(nphAll,N);
    phvecAll(:,2:N) = unique(AllPerms,'rows');

    phfinal = phvecAll([1 round(phvec)],:);
    disp(phfinal)
    clear combs AllPerms combperms phvecAll

    save('GAresults2')

```

C.3 PhasedFieldFunction.m

This code generates the value that the genetic algorithm is attempting to optimize, which is the percent surface area coverage of the shear stresses that exceed a preset threshold.

```

function [FuncOutput] = PhasedFieldFunction(x)

phvar = round(x);

global N ph_inc SInterp fvec fnum GAval iter Zmin_opt Pnorm_opt fsweepnum

%% Determine Phasing Values
nph = length(phvar) + 1;
nphAll = (360/ph_inc)^(N-1);

inp_vec = [];
for ni = 1:N-1
    inp_vec = cat(2,inp_vec,0:ph_inc:(360-ph_inc));
end
combs = unique(combnk(inp_vec,3),'rows');
AllPerms = [];
for ii = 1:size(combs,1)
    combperms = perms(combs(ii,:));
    AllPerms = cat(1,AllPerms,combperms);
end
phvecAll = zeros(nphAll,N);
phvecAll(:,2:N) = unique(AllPerms,'rows');

phvec = phvecAll([1 phvar],:);

clear combs AllPerms combperms phvecAll

%% Determine phased impedance curves
OldFolder='/gpfs/home/cjb286/work/Phasing_Optimization';
cd('/gpfs/home/cjb286/work/Phasing_Optimization/Phasing_FE_Compiled_Data')
load('ZData.mat')
cd(OldFolder)

```

```

crossmat = [1 5 6 7; 5 2 8 9; 6 8 3 10; 7 9 10 4];
sensormat = [1 2 3 4; 2 2 3 4; 3 3 3 4; 4 4 4 4];

ZInd = ZInd(fvec, :, :);
ZSys = zeros(fnum, np);
for phi = 1:np
    for ii = 1:size(ZInd, 2) %#ok<*NODEF>
        for jj = 1:size(ZInd, 2)
            ZIndph{ii, jj} =
ZInd(:, sensormat(ii, jj), crossmat(ii, jj)) * exp(1i * phvec(phi, ii) / 180 * pi);
%#ok<AGROW, *SAGROW>
        end
    end

    ZSysInd = zeros(size(ZInd, 1), size(ZInd, 2));
    for ii = 1:size(ZInd, 2)
        for jj = 1:size(ZInd, 2)
            ZSysInd(:, ii) = ZSysInd(:, ii) + 1 ./ ZIndph{jj, ii};
        end
    end
    ZSysInd = 1 ./ ZSysInd;

    for ii = 1:size(ZInd, 2)
        ZSysInd(:, ii) = ZSysInd(:, ii) * exp(1i * phvec(phi, ii) / 180 * pi);
    end
    ZSys(:, phi) = abs(1 ./ sum(1 ./ ZSysInd, 2));
end
clear ZInd ZIndph ZSysInd

if Zmin_opt == 1
    [~, ZminInx] = min(ZSys, [], 1);
    fZvec = zeros(fsweepnum * 2 + 1, length(ZminInx));
    fsweep = -fsweepnum:fsweepnum;
    for fi = 1:length(fsweep)
        fZvec(fi, :) = ZminInx + fsweep(fi);
    end
    fZvec(fZvec < 1) = 1;
    fZvec(fZvec > fnum) = fnum;
end

%% Predict Power-Normalized Phased Field Values
if Zmin_opt == 1
    Smag = zeros(size(SInterp, 1), size(SInterp, 2), fsweepnum * 2 + 1, np);
elseif Zmin_opt == 0
    Smag = zeros(size(SInterp, 1), size(SInterp, 2), fnum, np);
end

for phi = 1:np
    SphTemp = zeros(size(SInterp, 1), size(SInterp, 2), 3, fnum);
    for ci = 1:4
        SphTemp = SphTemp + SInterp(:, :, :, ci) * exp(1i * phvec(phi, ci) / 180 * pi);
    end
    SphTemp = squeeze(abs(SphTemp));
    if Zmin_opt == 1
        Smag(:, :, :, phi) = sqrt(SphTemp(:, :, 1, fZvec(:, phi)).^2 +
SphTemp(:, :, 2, fZvec(:, phi)).^2);

```

```

elseif Zmin_opt == 0
    Smag(:,:,phi) = sqrt(SphTemp(:,:,1,:).^2 + SphTemp(:,:,2,:).^2);
end
clear SphTemp
end

if Pnorm_opt == 1
    V = 100;
    P = 400;
    Vp = sqrt(P*ZSys);
    Vp(Vp > 250) = 250;
    Vrel = Vp/V;
    SmagNorm = zeros(size(Smag));
    for phi = 1:nph
        for fi = 1:size(Smag,3)
            SmagNorm(:,:,fi,phi) = Smag(:,:,fi,phi)*Vrel(fi,phi);
        end
    end
elseif Pnorm_opt == 0
    SmagNorm = Smag;
end

%% Determine Percent Coverage
sLimMin = 0;
sLimMax = 3e6;
sLimInc = .0001e6;
slimits = sLimMin:sLimInc:sLimMax;

SmagVec = SmagNorm(:);
n_counts = histc(SmagVec,slimits);
c_counts = cumsum(n_counts)/length(SmagVec);
Slim = slimits(find(c_counts < 0.10,1,'last'));
FuncOutput = -Slim*1e-6;

% figure(1)
% bar(slimits,n_counts,'barwidth',1)
% figure(2)
% bar(fliplr(slimits),c_counts,'barwidth',1)
% xlabel('Stress Value')
% ylabel('% Area Above Stress Value')
% xlim([0 sLimMax])

%% Output Updated Plot
if Pnorm_opt == 1
    ymax = 1;
elseif Pnorm_opt == 0
    ymax = 1;
end

if isempty(x) == 0
    GAval = [GAval FuncOutput];

    figure(1)
    set(gcf,'position',[585 277 1052 420])
    plot(-GAval,'-b.','MarkerSize',18)

```

```

xlim([0 length(GAval)+1])
ylim([0 ymax])
set(gca,'XTick',0:1:length(GAval) + 1)
ylabel('90% Coverage Stress Threshold','FontSize',14)
xlabel('Genetic Algorithm Iteration (MPa)','FontSize',14)
title(['Genetic Algorithm Phasing Optimization Z' num2str(Zmin_opt) ' P'
num2str(Pnorm_opt)], 'FontSize',15)
text(0.5*length(GAval),0.85,{'Current state: [' num2str(phvar)
'],''},['Current Stress: ' num2str(-GAval(end)) ' MPa'],['Iteration:
' num2str(iter)]}, ...
'FontSize',12,'EdgeColor',[0 0 0],'BackgroundColor',[.7 .9 .7])

iter = iter + 1;
end

```

C.4 PhasingGA_ConstraintFunction.m

This code controls the constraint function by which the genetic algorithm selects phasing combinations to consider.

```

function [c,ceq] = PhasingGA_ConstraintFunction(x)

% Phasing combinations are integer values
ceq(1) = length(find(round(x) - x));

% All phasing combinations are unique
ceq(2) = length(unique(x))-length(x);

% No inequality constraints
c = [];

```

Appendix D

POWER-NORMALIZED VERSIONS OF AIRFOIL FEM RESULTS

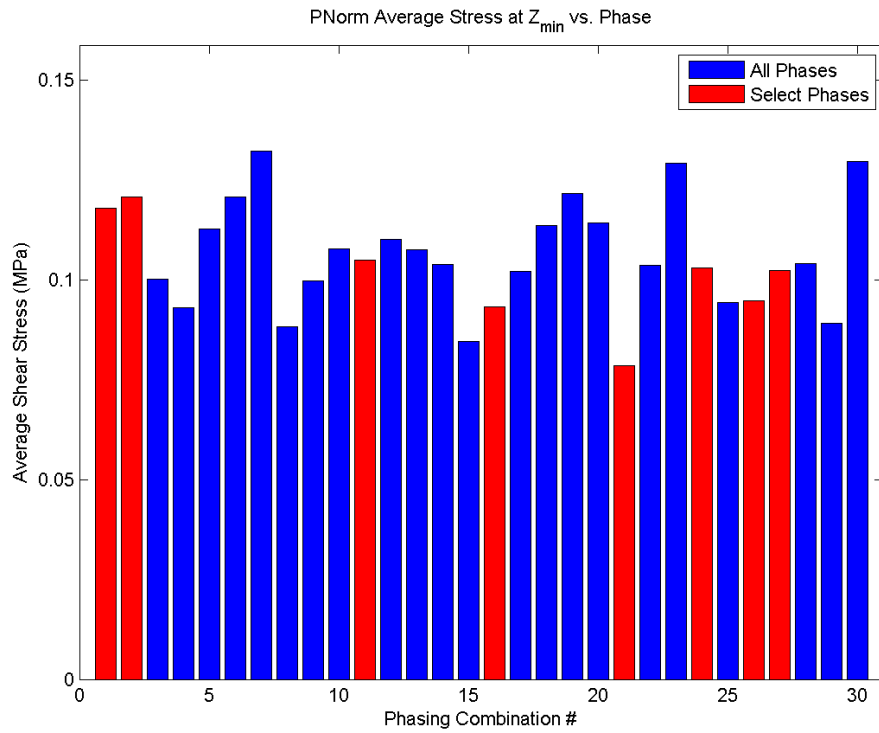


Figure 135 Power-normalized version average interface shear stress at the phased impedance minimum for all 30 phasing combinations for actuator configuration 1.

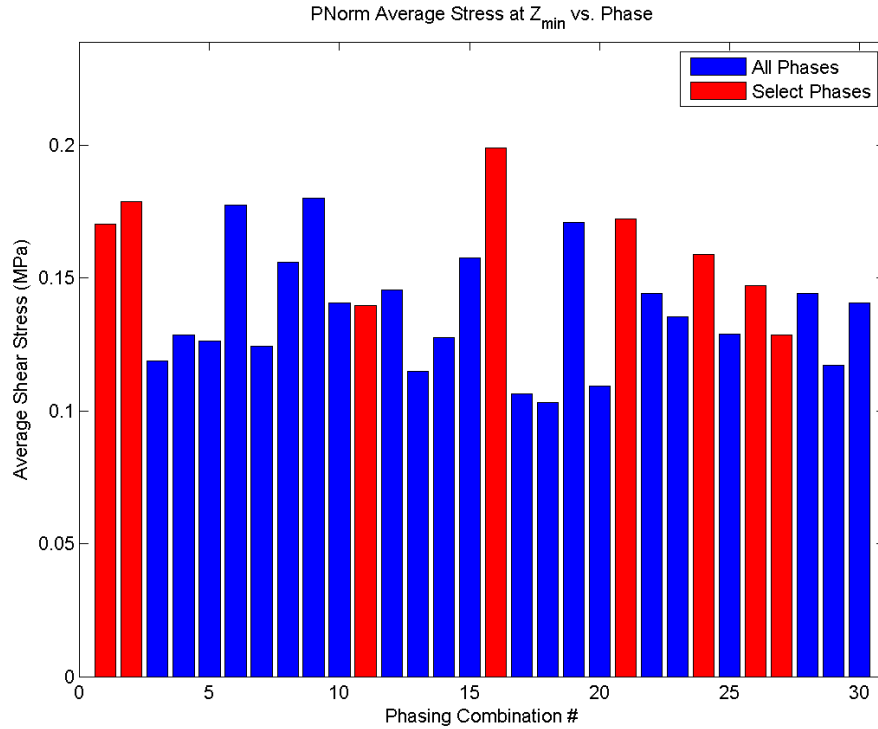


Figure 136 Power-normalized average interface shear stress at the phased impedance minimum for all 30 phasing combinations for actuator configuration 2.

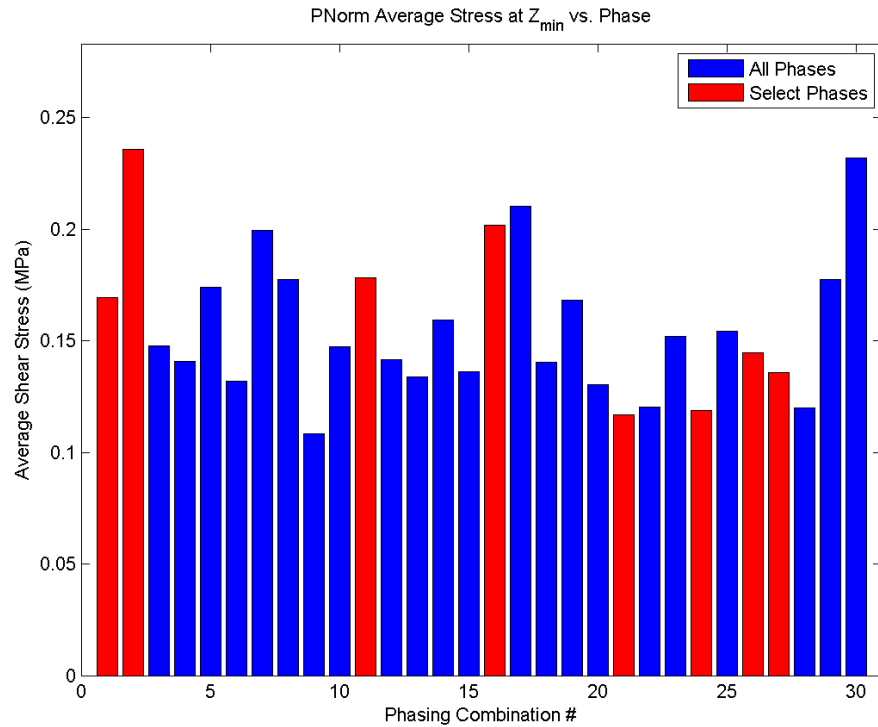


Figure 137 Power-normalized average interface shear stress at the phased impedance minimum for all 30 phasing combinations for actuator configuration 3.

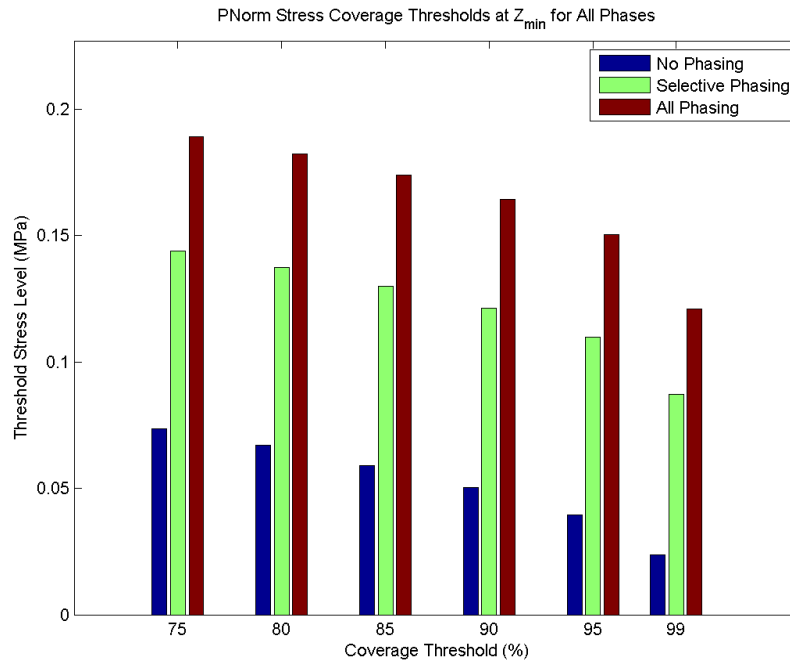


Figure 138 Power-normalized coverage threshold shear stress levels for various phasing groups, actuator configuration 1.

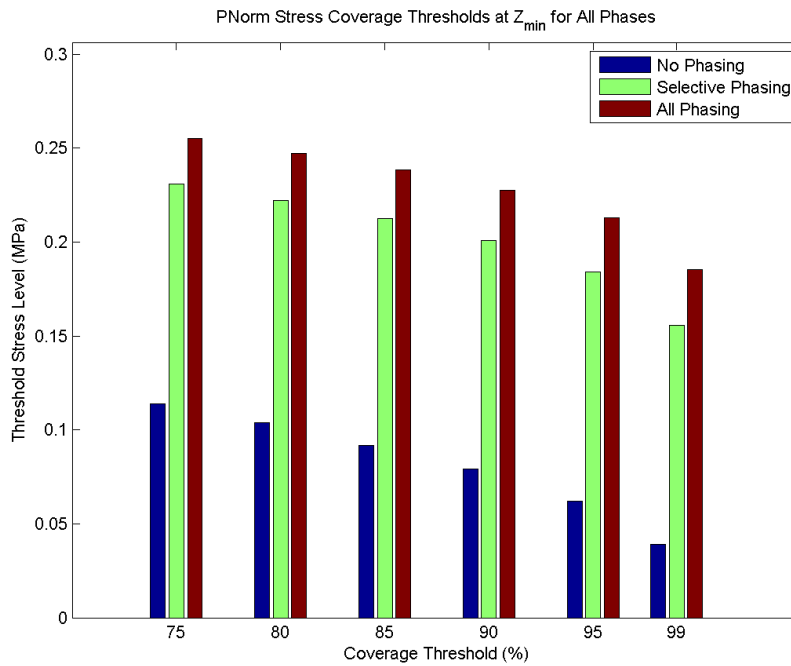


Figure 139 Power-normalized coverage threshold shear stress levels for various phasing groups, actuator configuration 2.

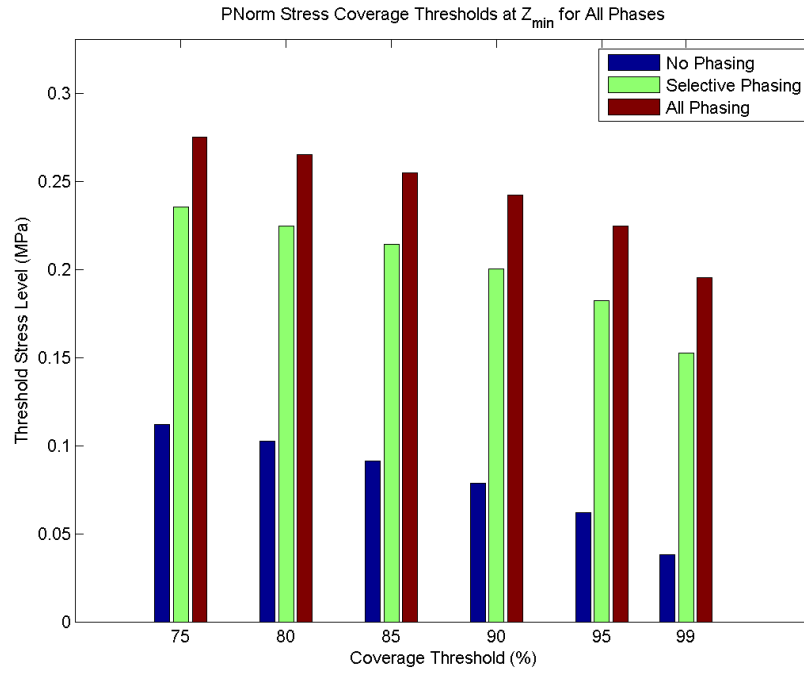


Figure 140 Power-normalized coverage threshold shear stress levels for various phasing groups, actuator configuration 3.

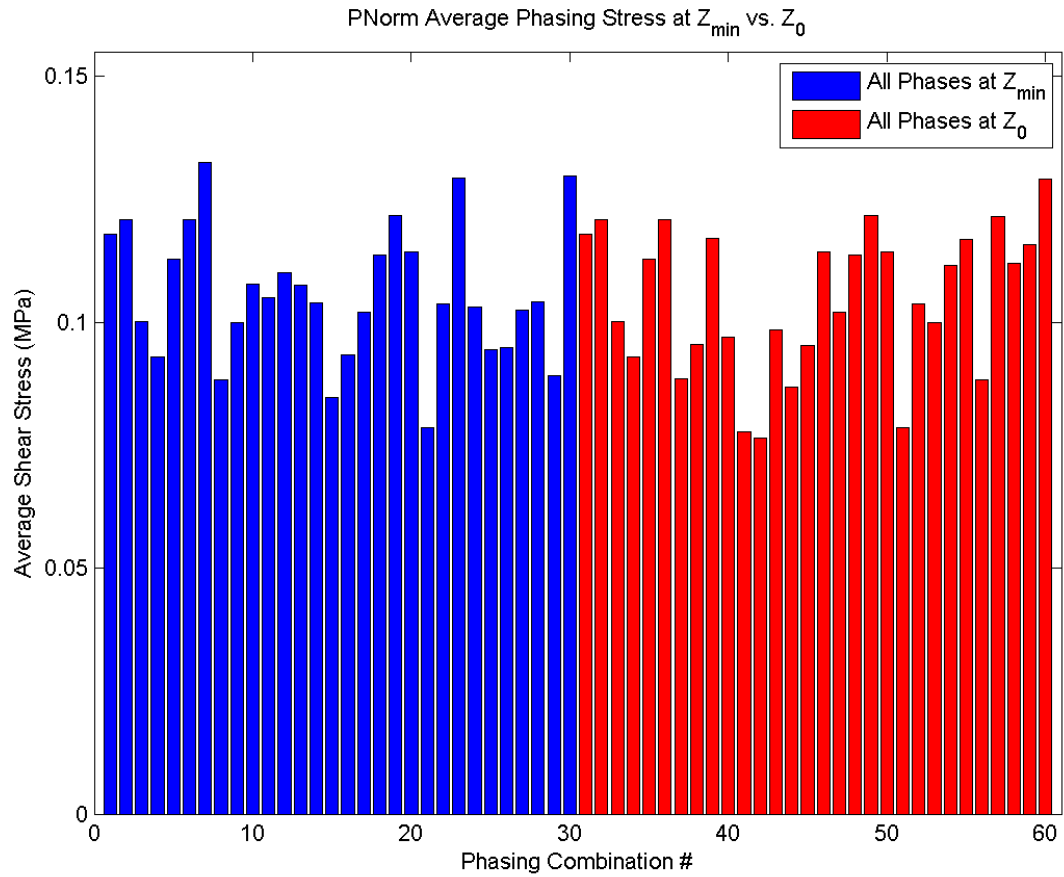


Figure 141 Power-normalized average shear stress field values for each phasing combination using the dynamic frequency selection approach (blue) and the static frequency selection approach (red) for actuator configuration 1.

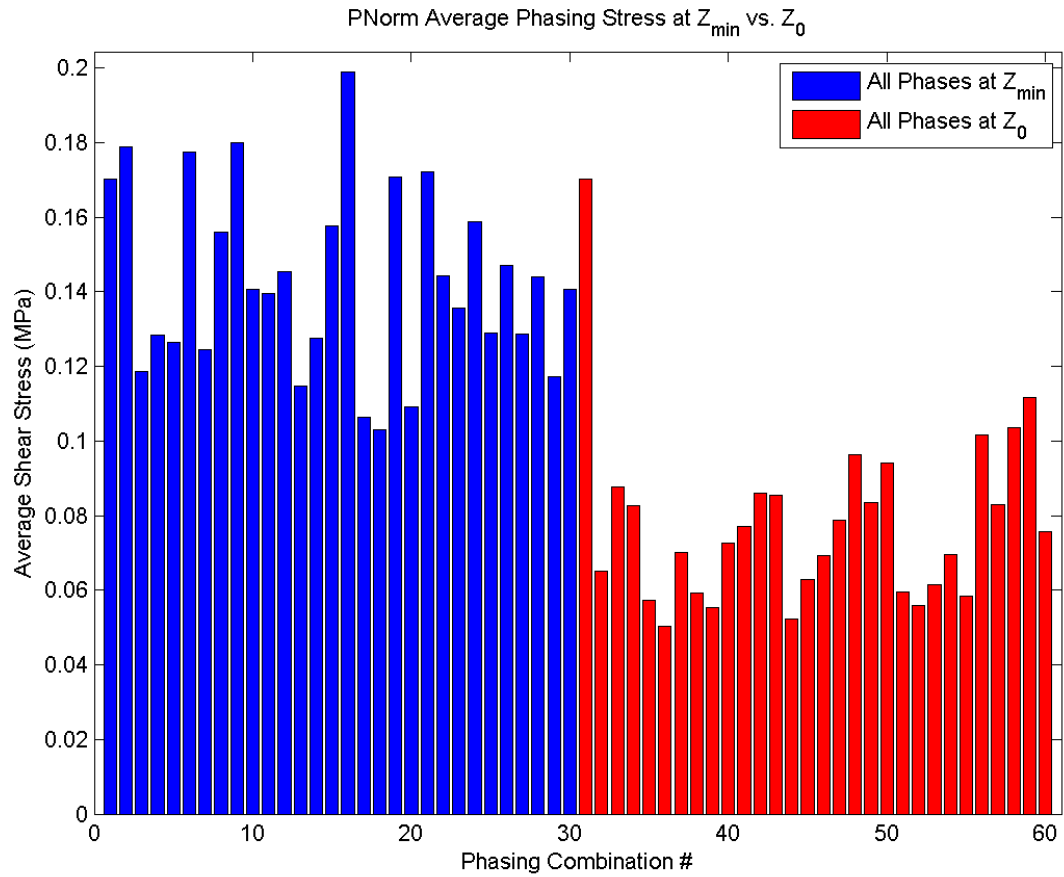


Figure 142 Power-normalized average shear stress field values for each phasing combination using the dynamic frequency selection approach (blue) and the static frequency selection approach (red) for actuator configuration 2.

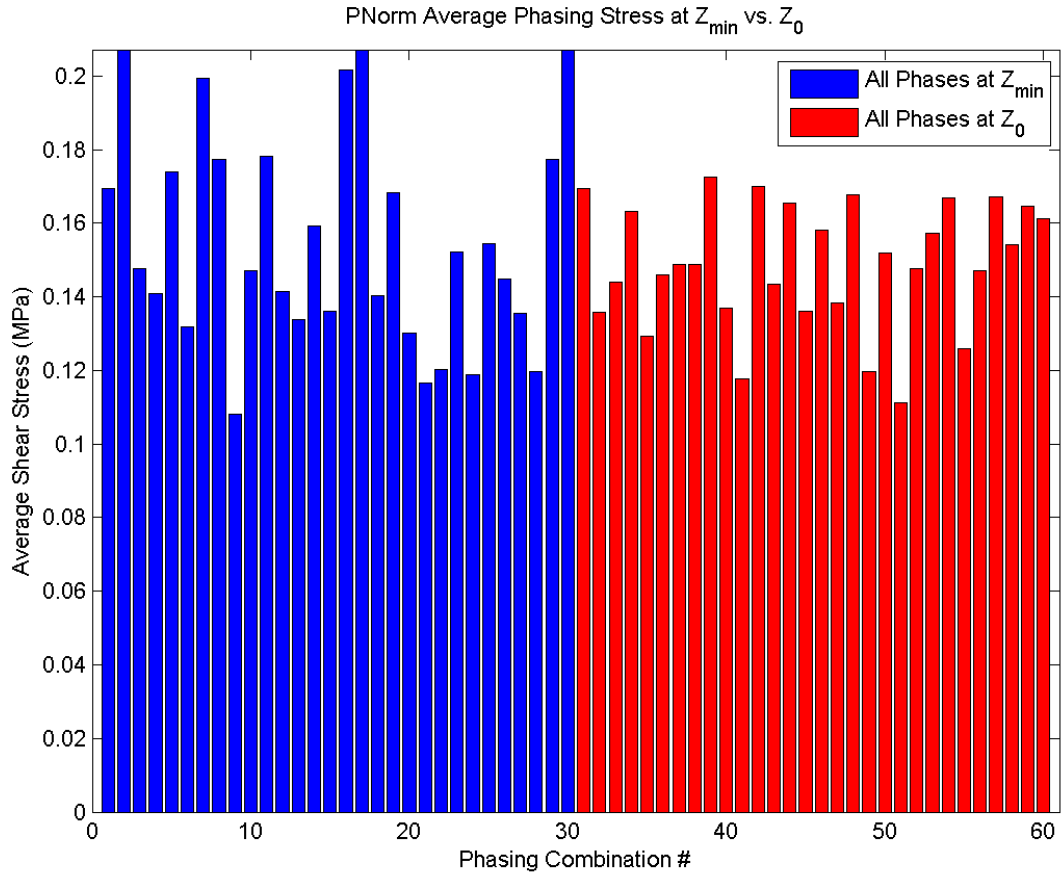


Figure 143 Power-normalized average shear stress field values for each phasing combination using the dynamic frequency selection approach (blue) and the static frequency selection approach (red) for actuator configuration 3.

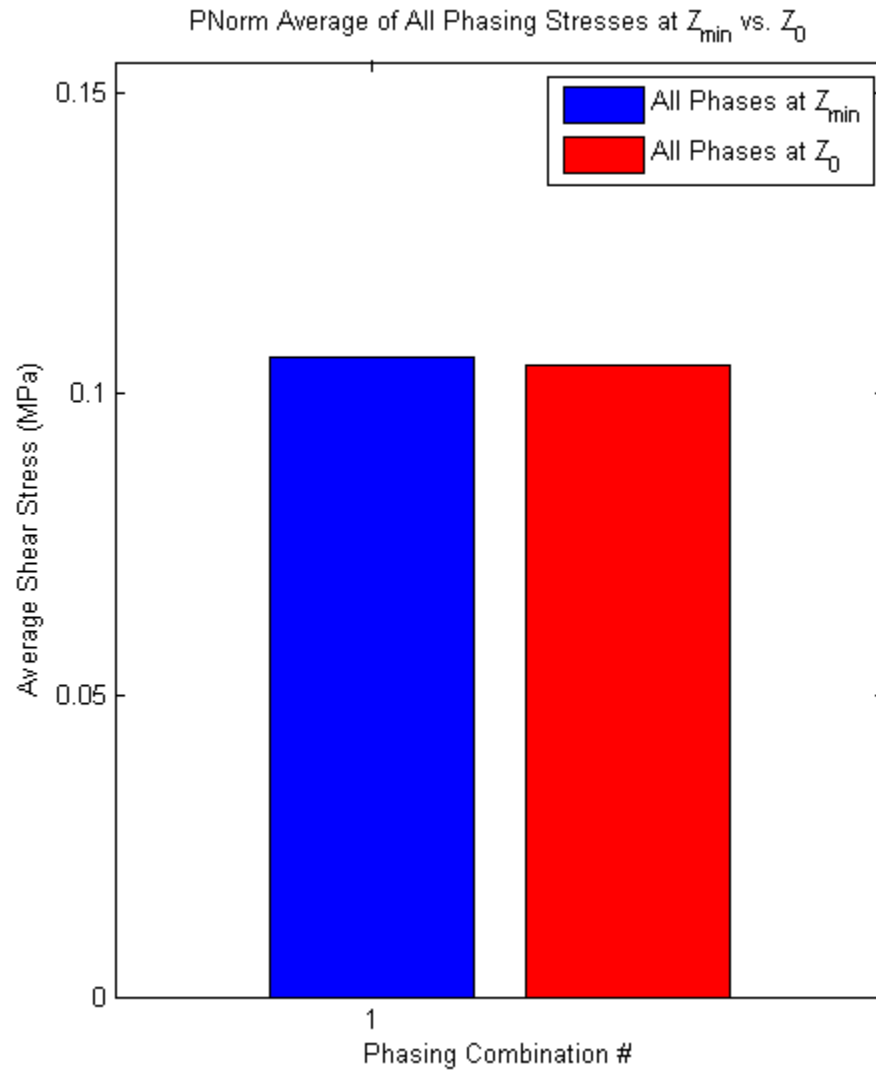


Figure 144 Power-normalized average of the average shear stress values across all phasing combinations using the dynamic frequency selection approach (blue) and the static frequency selection approach (red) for actuator configuration 1.

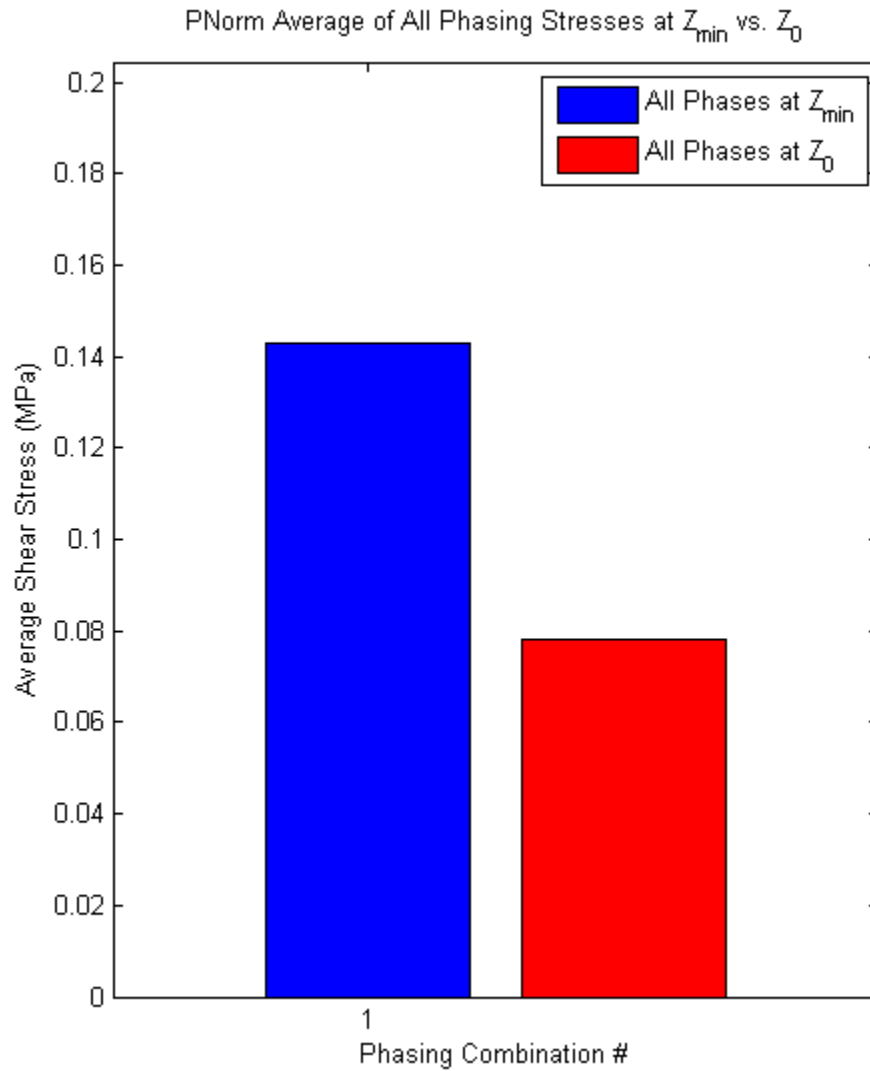


Figure 145 Power-normalized average of the average shear stress values across all phasing combinations using the dynamic frequency selection approach (blue) and the static frequency selection approach (red) for actuator configuration 2.

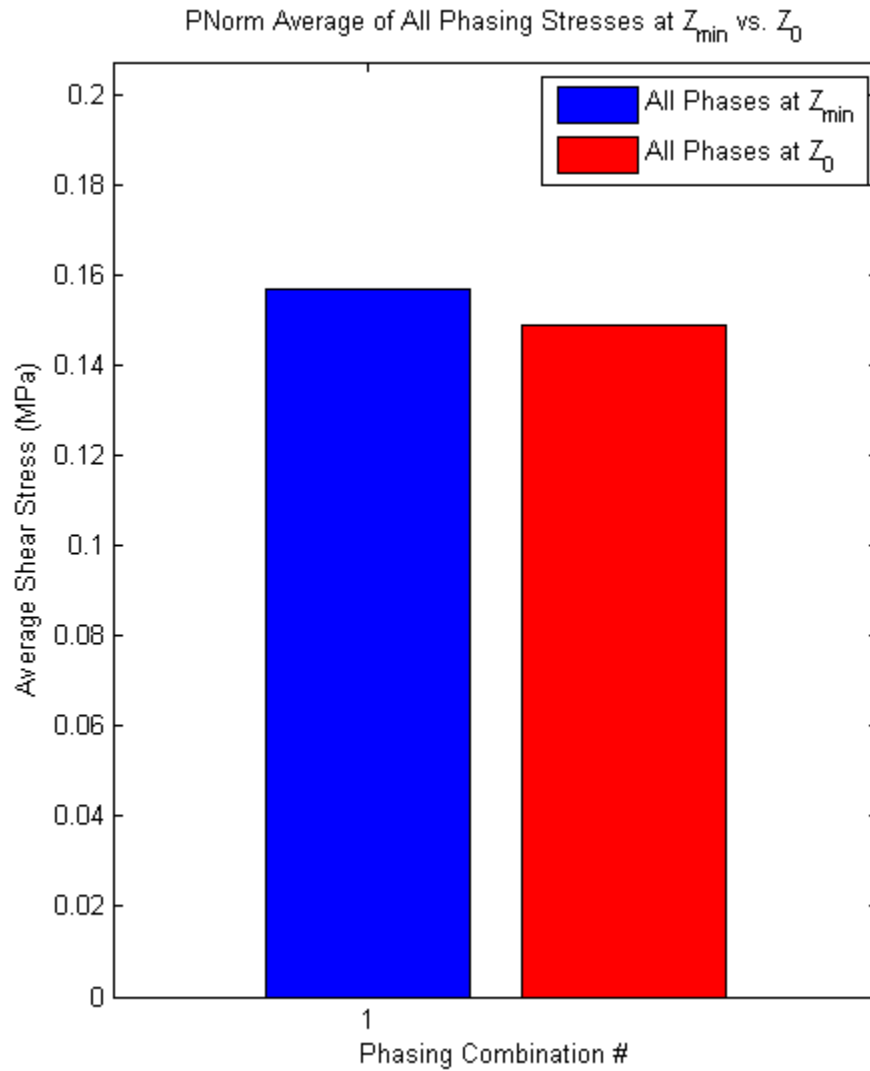


Figure 146 Power-normalized average of the average shear stress values across all phasing combinations using the dynamic frequency selection approach (blue) and the static frequency selection approach (red) for actuator configuration 3.

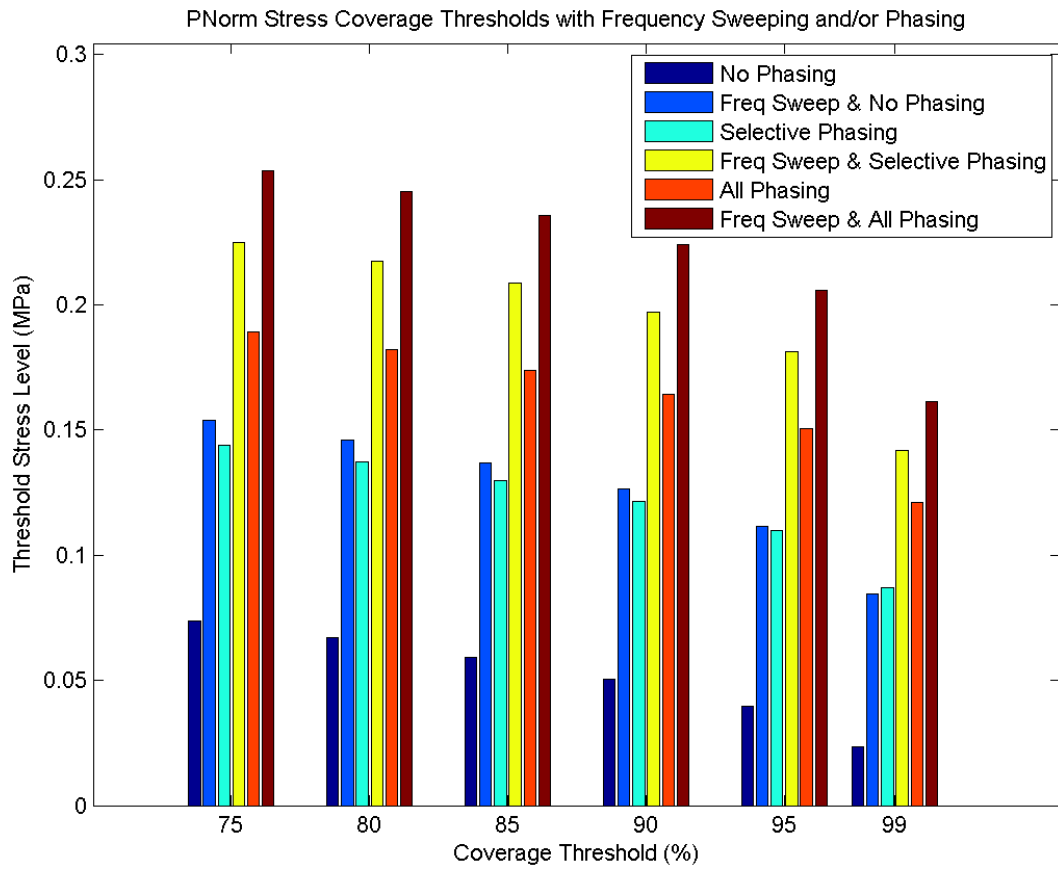


Figure 147 Power-normalized shear stress coverage threshold levels for six combinations of phasing and frequency sweeping for actuator configuration 1.

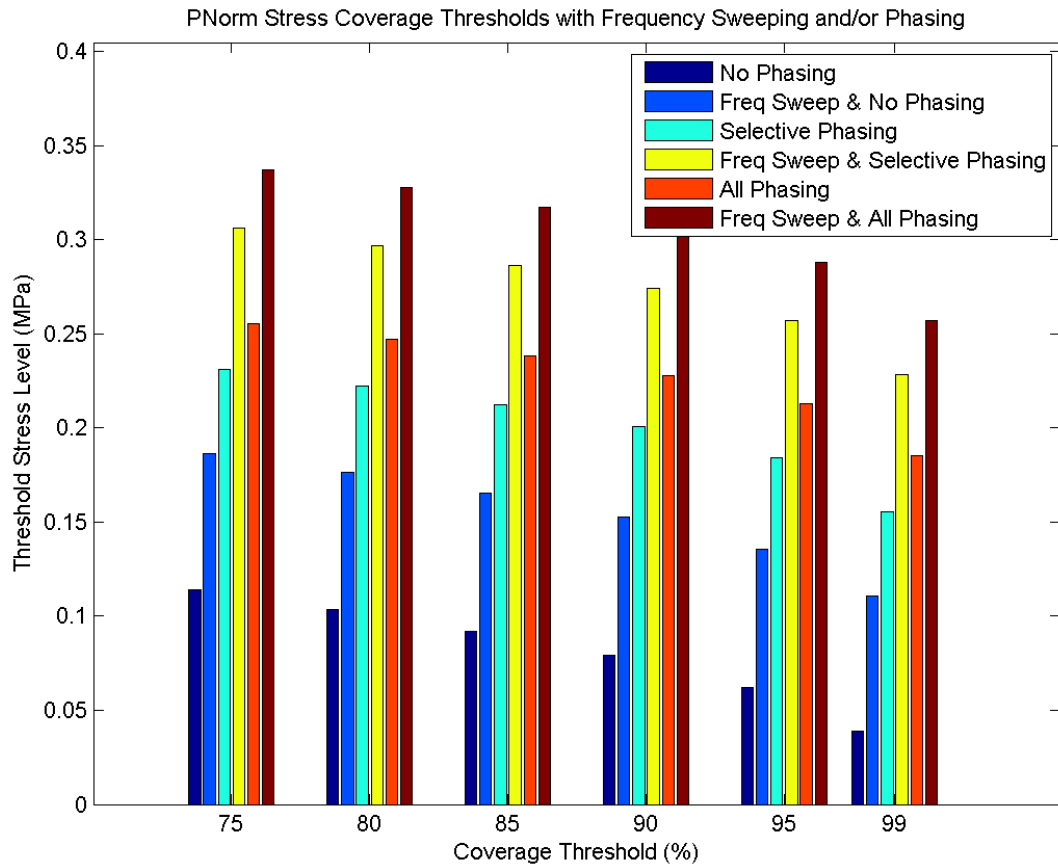


Figure 148 Power-normalized shear stress coverage threshold levels for six combinations of phasing and frequency sweeping for actuator configuration 2.

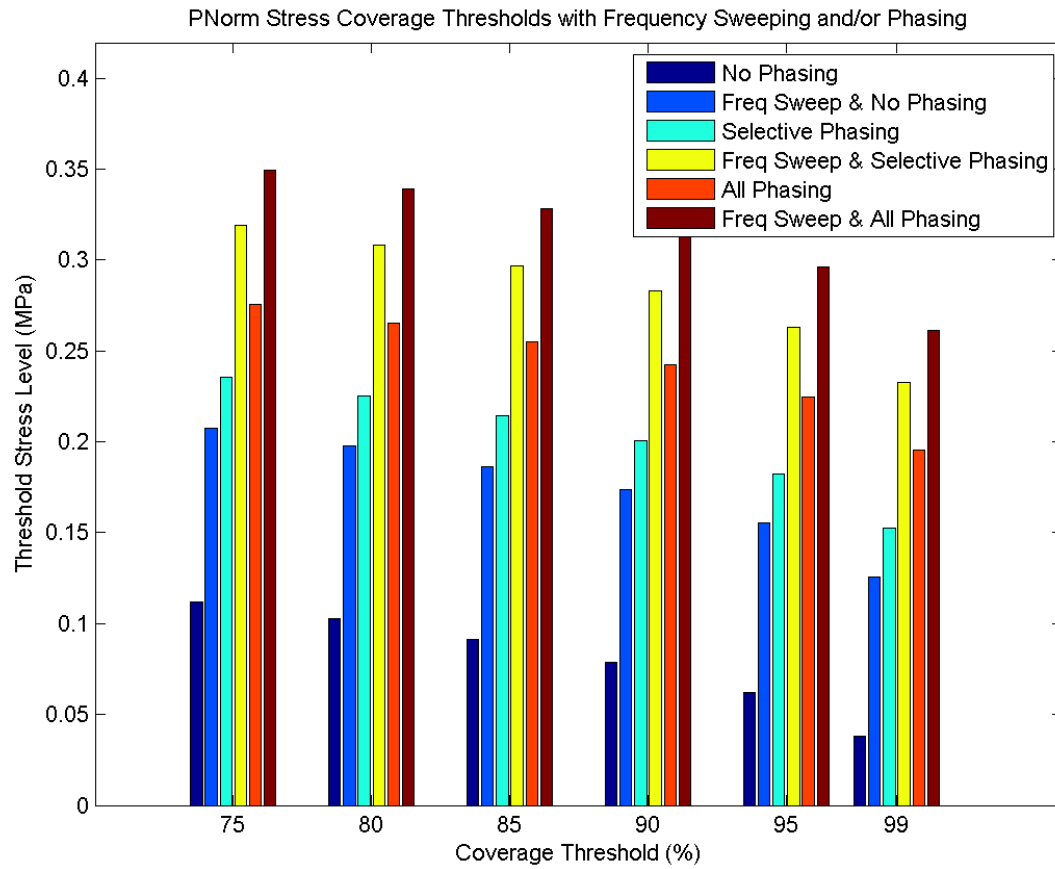


Figure 149 Power-normalized shear stress coverage threshold levels for six combinations of phasing and frequency sweeping for actuator configuration 3.

NON-TECHNICAL ABSTRACT

Aircraft icing is a critical concern for commercial and military rotorcraft and fixed-wing aircraft. In-flight icing dramatically reduces an aircraft's ability to maintain flight and has caused more than a thousand deaths and hundreds of accidents over the past three decades alone. Current ice protection technologies have substantial drawbacks due to weight, power consumption, environmental concerns, or incompatibility with certain structures. In this research, an ultrasonic actuator phasing method for ultrasonic de-icing of aircraft structures was developed and tested using numerical and experimental methods applied to metallic and carbon fiber composite plates and airfoils. It was demonstrated that this novel method can greatly improve the efficiency and effectiveness of the ultrasonic de-icing system by redistributing the vibration energy at the interface between the ice and the aircraft. Additional contributions were made to facilitate the actuator phasing method and to advance the state-of-the-art in ultrasonic de-icing technology. These contributions include the development of improved frequency optimization, reduction in the system size and weight, and improvements in actuator bonding techniques.

VITA

Cody Borigo

EDUCATION

Ph.D., Engineering Science and Mechanics, 2014

The Pennsylvania State University, University Park, PA, USA

M.S., Engineering Mechanics, 2011

The Pennsylvania State University, University Park, PA, USA

B.S., Physics (Departmental Honors, Magna cum Laude), 2009

Millersville University, Millersville, PA, USA

EMPLOYMENT

Research & Development Engineer, 2012 – present

FBS, Inc., State College, PA, USA

SELECTED PUBLICATIONS

1. **C. Borigo**, F. Yan, Y. Liang, J.L. Rose (2013) "A Novel Ultrasonic Vibration Analysis Technique for Defect Detection," 2013 ASNT Fall Conference, Las Vegas.
2. **C. Borigo**, F. Yan, Y. Liang, J.L. Rose (2013) "A Novel Ultrasonic Vibration Analysis Technique for Defect Detection," *Mat. Eval.*, Vol. 71, No. 10.
3. **C. Borigo**, F. Yan, J.L. Rose (2013) "A Spacing Compensation Factor for the Optimization of Guided Wave Annular Array Transducers," *J. Acoust. Soc. Am.*, Vol. 133, No. 1, pp. 127-135.
4. **C. Borigo**, F. Yan, Y. Liang, J.L. Rose (2012) "Ultrasonic Guided Wave Vibration Formulation," *Review of Progress in QNDE*, Vol. 31, pp. 225-232.
5. J.L. Rose, F. Yan, Y. Liang, **C. Borigo** (2012) "Ultrasonic Vibration Method for Damage Detection in Composite Aircraft Components," *Topics in Modal Analysis II*, Vol. 6, Proc. of the 30th IMAC Conference on Structural Dynamics, 2012, pp. 359-367.
6. J.L. Rose, F. Yan, **C. Borigo**, Y. Liang (2012) "Ultrasonic Vibration Modal Analysis Technique (UMAT) for Defect Detection," *Advanced Aerospace Applications Vol. 1*, Proc. of the Society for Experimental Mechanics Series, Vol. 4, pp. 25-32.
7. F. Yan, **C. Borigo**, Y. Liang, J. Koduru, J.L. Rose (2011) "Phased Annular Array Transducers for Ultrasonic Guided Wave Applications," *Proc. SPIE 7984*, Health Monitoring of Structural and Biological Systems 2011.
8. **C. Borigo**, F. Yan, J.L. Rose (2011) "Analysis of the Excitation Spectra of Annular and Comb Arrays for Ultrasonic Guided Wave Applications", ASNT Spring Research Symposium 2011, San Francisco.

PATENTS

1. **C. Borigo**, S. Owens, J. Rose, Ultrasonic Vibration System and Method for Removing/Avoiding Unwanted Build-up on Structures (patent pending)
2. **C. Borigo**, S. Owens, J. Rose, J. Van Velsor, System and Method for Testing Shell and Tube Heat Exchangers for Defects (patent pending)
3. **C. Borigo**, S. Owens, J. Rose, Systems and Methods for Damage Detection in Plate-Like Structures Using Guided Wave Phased Arrays (patent pending)
4. P. Zombo, J. Landy, J. Rose, S. Owens, F. Yan, **C. Borigo**, Guided Wave Thermography System and Methods for Damage Detection in Various Structures (patent pending)
5. F. Yan, S. Owens, J. Rose, **C. Borigo**, An Ultrasonic Guided Wave Monitoring System for Storage Tank Floors and Plate-Like Structures (patent pending)